論文 / 著書情報
Article / Book Information

題目(和文)	
Title(English)	Thermal History of Small Bodies in the Early Solar System
著者(和文)	荒川創太
Author(English)	Sota Arakawa
出典(和文)	学位:博士(理学), 学位授与機関:東京工業大学, 報告番号:甲第11380号, 授与年月日:2020年3月26日, 学位の種別:課程博士, 審査員:中本 泰史,井田 茂,奥住 聡,太田 健二,玄田 英典
Citation(English)	Degree:Doctor (Science), Conferring organization: Tokyo Institute of Technology, Report number:甲第11380号, Conferred date:2020/3/26, Degree Type:Course doctor, Examiner:,,,,
学位種別(和文)	博士論文
Type(English)	Doctoral Thesis

Thermal History of Small Bodies in the Early Solar System

THESIS

submitted in partial fulfillment of the
requirements for the degree of

DOCTOR OF SCIENCE
in
PLANETARY SCIENCE

Sota Arakawa

Tokyo, Japan, February 22, 2020

Thermal History of Small Bodies in the Early Solar System

Sota Arakawa

Department of Earth and Planetary Sciences,
Tokyo Institute of Technology
2-12-1 Ookayama, Meguro, Tokyo 152-8551, Japan

February 22, 2020

Abstract

The planets in the solar system formed approximately 4.6 billion years ago. In the solar nebula, km-sized small bodies are thought to form via accretion of small dust grains as a first step of the planet formation. The evolution of dust grains in the protoplanetary disks is the key to understanding the first step of the planet formation. Submicron-sized interstellar dust grains are incorporated into the gaseous solar nebula and grow into km-sized planetesimals. The pathways of dust growth from submicron-sized grains to km-sized planetesimals are not yet fully understood, however. In this thesis, we discussed what the building blocks of planetesimals are and how planetesimals formed in the solar nebula, from the thermal history of small bodies.

In the inner region of the solar nebula, chondrules, mm-sized spherical igneous grains, would be formed in the first a few million years of the solar nebula, although the heating and cooling processes of the igneous spherules are still under debate. Some chondrules are composed of two or more chondrules fused, called compound chondrules. We can interpret the presence of compound chondrules as the result of collisions between crystallized chondrules and supercooled precursors. We focused on the shock-wave heating within the solar nebula, which is one of the leading candidates for the source of chondrule-forming events. In Chapters 2 and 3, we evaluated whether compound chondrules can form via the collision of supercooled chondrule precursors in the framework of the shock-wave heating model. We found that chondrule precursors immediately turn into supercooled droplets when the shock waves are optically thin, and they can maintain supercooling until the condensation of evaporated fine dust grains. Owing to the large viscosity of supercooled melts, supercooled chondrule precursors can survive high-speed collisions on the order of 1 km s^{-1}. We also showed that optically thin shock waves with a spatial scale of $\sim 10^4$ km could reproduce the fraction, size ratio, and textural feature of compound chondrules observed in ordinary chondrites.

The thermal and mechanical properties of dust aggregates depend on

their internal structure. In Chapters 4 and 5, we numerically calculated the thermal conductivity of dust aggregates. We found that the thermal conductivity of dust aggregates through the solid network follows a power-law function of the filling factor and the coordination number of dust aggregates. We also give a theoretical explanation for why a power-law gives it from the fractal structure of dust aggregates in Chapter 6.

The *Rosetta* mission to comet 67P/Churyumov–Gerasimenko has provided plenty of data to understand what comets are made of. The thermal and mechanical properties of dust aggregates depend on their internal structure, i.e., whether homogeneous or hierarchical. In Chapter 7, we calculated the thermal inertia, tensile strength, and compressive strength of dust aggregates using formulae derived in Chapters 4–6. We found that we cannot explain the tensile strength of the comet if it is a homogeneous aggregate of μm-sized dust grains. On the other hand, the thermal inertia, tensile strength, and compressive strength of the comet are consistent with those of hierarchical aggregates of cm- or dm-sized constituent aggregates. Our findings indicate that the icy planetesimals may form via accretion of cm- or dm-sized compressed dust aggregates in the solar nebula.

Recent observational studies have revealed that all 1000 km-sized large trans-Neptunian objects form satellite systems. However, their origins are still under debate. The largest Plutonian satellite, Charon, is thought to be an intact fragment of an impactor directly formed via a giant impact, although whether giant impacts can explain the characteristics of other satellite systems, e.g., the secondary-to-primary mass ratios, the spin/orbital periods, and their small eccentricities, remains to be determined. In Chapter 8, we found that hydrodynamic simulations of giant impacts can reproduce the secondary-to-primary mass ratio of the satellite systems of large trans-Neptunian objects when the impact velocity is approximately the same as the escape velocity. We also revealed that the satellite systems' current distribution of spin/orbital periods and small eccentricity could be explained when their spins and orbits tidally evolve, initially as fluid-like bodies, and finally as rigid bodies. These results suggest that all satellites of large trans-Neptunian objects were formed via giant impacts before the outward migration of Neptune and that they were fully or partially molten during the giant impact era. Recent studies proposed that accretion of cm-sized dust aggregates onto pre-existing planetesimals can form 100–1000 km-sized large trans-Neptunian objects within a few million years.

Thus, we concluded that rapid accretion of cm-sized dust aggregates is a strong candidate for the origin of small icy bodies including comets and trans-Neptunian objects. This planet formation scenario is recently featured, and we revealed that the thermal histories of small icy bodies are also consistent with the hypothesis. The rapid formation of icy planetesimals in the gaseous solar nebula might support our scenario for chondrule formation in shock waves caused by pre-existing eccentric planetesimals. Although understanding of the physical properties of hierarchical dust aggregates is still limited, we will reveal the nature of hierarchical dust aggregates in future experiments and simulations.

Acknowledgments

My heartfelt appreciation goes to my supervisor, Taishi Nakamoto, for his helpful advice and constant encouragement. The many discussions we had together are my life treasure, and without your support, my first five years as an academic would have been much less productive, and much less exciting. I would like to express my great appreciation to Hidenori Genda of Earth-Life Science Institute, who taught me the skills for the numerical simulations and discussed my study of satellite formation. I much appreciate Makiko Nagasawa of Kurume University, who taught me the basics of celestial mechanics and planetary science when I was an undergraduate student.

I also owe a lot to my collaborators and colleagues. My studies on the physical properties of dust aggregates cannot start without the help of Hidekazu Tanaka of Tohoku University and Akimasa Kataoka of National Astronomical Observatory of Japan. The collaboration with Naoya Sakatani of Japan Aerospace Exploration Agency and Misako Tastuuma of the University of Tokyo developed our understanding of the nature of dust aggregates. Many discussions with Masaki Takemoto, a member of our laboratory, qualitatively changes my understanding of the fractal aggregates. I learned many things from Ryuki Hyodo of Japan Aerospace Exploration Agency and Daigo Shoji of Earth-Life Science Institute through your collaboration. I hope we can keep collaborating in the future. Our approachable alumnus, Yuhito Shibaike, is now at Universität Bern. I really enjoyed our collaborating work on circumplanetary disks. Constructive and critical comments from my colleague, Kazumasa Ohno, always improve my study. I am glad to have met him in my Ph.D. life and to start our cooperation.

I thank all members and alumni of Department of Earth and Planetary Sciences, Tokyo Institute of Technology. They gave me a lot of comments and suggestions, and we had a wonderful time together in our old building. Finally, I thank my family for their warm encouragement.

Contents

Chapter 1

Introduction

The planets in the solar system formed approximately 4.6 billion years ago. In protoplanetary disks (PPDs), km-sized small bodies are thought to be formed via accretion of small dust grains as a first step of the planet formation. This standard scenario of planet formation is called the planetesimal hypothesis (Safronov, 1969; Hayashi et al., 1985).

The evolution of dust grains in the protoplanetary disks is the key to understanding the first step of the planet formation. Submicron-sized interstellar dust grains (e.g., Mathis et al., 1977; Weingartner and Draine, 2001) are incorporated into gaseous PPDs and grow into km-sized planetesimals. The pathways of dust growth from submicron-sized grains to km-sized planetesimals are not yet fully understood, however. Figure 1.1 shows the schematic of the evolution of small bodies in PPDs, including dust grains, aggregates, and planetesimals.

1.1 Dust growth in the solar nebula

The dust growth from submicron-sized grains to mm- or cm-sized dust aggregates is thought to be driven by collisional sticking (e.g., Blum and Wurm, 2008; Testi et al., 2014). The size of dust aggregates embedded in PPDs is evaluated from astronomical observations. Radio observations of thermal emission from dust suggest that dust grains have been grown to mm-sized aggregates (e.g., Ricci et al., 2010; Natta et al., 2007), and recent observations of millimeter-wave scattering polarization of PPDs also suggest that the size of mass-dominating aggregates in PPDs are (sub)mm-size and they are not highly porous (e.g., Stephens et al., 2017; Tazaki et al., 2019). The dust growth from submicron-sized grains to mm-sized dust aggregates occurred not only observed PPDs but also in the solar nebula. In the inner region of the solar nebula, chondrules, (sub)mm-sized spherical igneous grains, would be the main dust component because the volume fraction of chondrules in ordinary chondrites is 60–80% (Rubin, 2000; Scott, 2007). Although the heating and cooling processes of the igneous spherules are still under debate, the abundance of chondrules in meteorites suggests that mm- or cm-sized dust aggregates, possible chondrule precursors, would float in the first a few million years of the solar nebula (e.g., Connelly et al., 2012; Kita and Ushikubo, 2012).

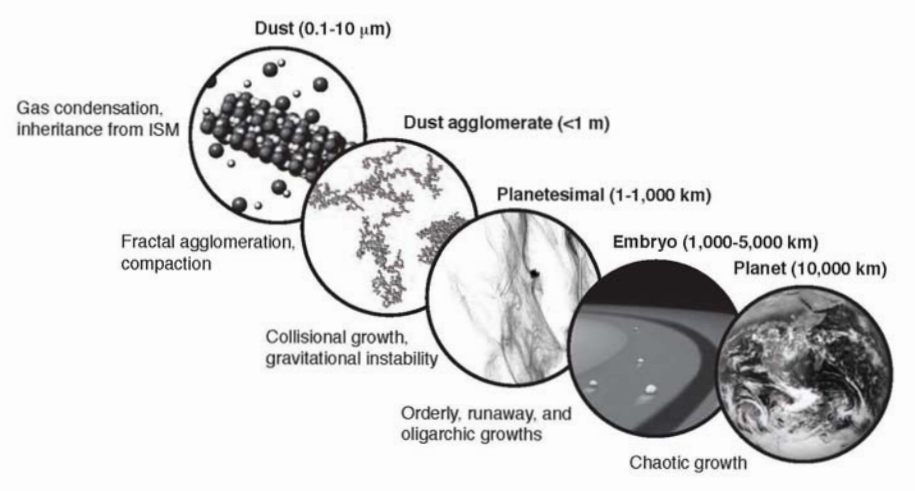

Figure 1.1: Schematics of the evolution of small bodies in protoplanetary disks. Figure taken from Dauphas and Chaussidon (2011).

1.1.1 Outcomes of collision

Both experiments and numerical simulations study the collisional growth of dust aggregates. In the context of planet formation, systematic experimental studies for the dust growth model started with the work by Blum and Münch (1993). When the collisional velocity is higher than the critical velocity for collisional growth, collisions among dust aggregates do not result in sticking, but rather in bouncing of fragmentation (e.g., Blum and Wurm, 2008). Blum and Wurm (2008) summarized the complex diversity of the collisional interaction of dust aggregates, and Güttler et al. (2010) derived a comprehensive collision model. Figure 1.2 shows the classification of collisional outcomes suggested from laboratory experiments.

Sticking. When the collisional energy of dust aggregates is low, a hit-and-stick growth is observed in both laboratory experiments (e.g., Wurm and Blum, 1998; Blum et al., 2000) and numerical simulations (e.g., Dominik and Tielens, 1997; Paszun and Dominik, 2009). When all dust grains exist as monomers at first, the mass distribution during the initial growth stage is quasi-monodisperse, and the collisional energy at this stage is low enough to avoid restructuring (e.g., Suyama et al., 2008; Okuzumi et al., 2012).

In turbulent gaseous PPDs, the collisional energy of dust aggregates increases with increasing aggregate radii (e.g., Cuzzi and Hogan, 2003; Ormel and Cuzzi, 2007). Numerical simulations showed that collisions between large aggregates result in collisional compaction at moderate collision velocities (e.g., Dominik and Tielens, 1997; Wada et al., 2007, 2008). Laboratory experiments also found that colliding aggregates are elastically and plastically deformed at the contact area, which can lead to sticking through surface effects, or sticking by penetration occurred when the target aggregate is porous and larger than the projectile (see Güttler et al., 2010; Zsom et al., 2010).

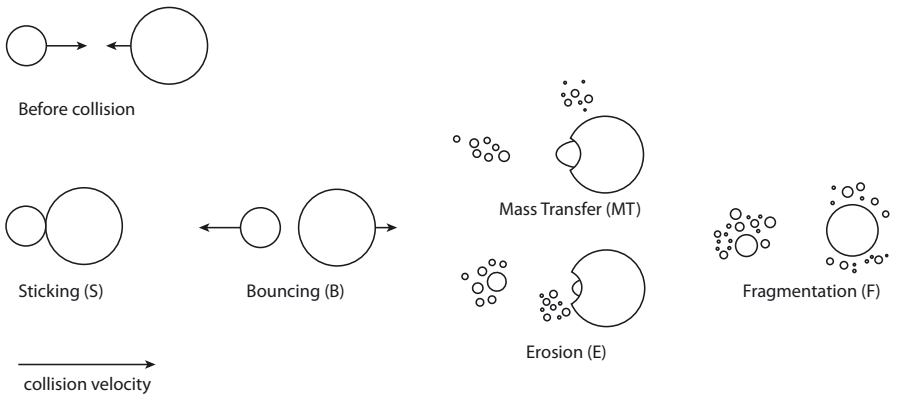

Figure 1.2: Classification of collisional outcomes of dust aggregates (see also Figure 1 of Güttler et al., 2010). Sticking occurs at low collision velocities, and fragmentation occurs when the collision velocity is higher than the threshold velocity. We define mass transfer as the outcome, which leads to net growth for the target, and erosion as the outcome, which leads to net mass loss. Figure taken from Windmark et al. (2012).

Bouncing. When the collision velocity is too high for sticking and also too low for fragmentation of the projectile, the outcome of collision will bounce. Experimental studies revealed that collisions between mm- to cm-sized compressed aggregates result in bouncing at moderate collision velocities (e.g., Langkowski et al., 2008; Weidling et al., 2009). Whether bouncing collisions occur or not mainly depends on the filling factor of aggregates; when the filling factor is lower than 0.1, bouncing collisions hardly occur in laboratory experiments (Langkowski et al., 2008).

Bouncing also occurs in numerical simulations (Wada et al., 2011; Seizinger and Kley, 2013); however, the threshold filling factor for sticking/bouncing obtained from their simulations is inconsistent with experimental results. Whether colliding aggregates stick or bounce is determined by the energy dissipation along with a restructuring of the aggregates, and Wada et al. (2011) found that the critical factor is the mean coordination number: when the mean coordination number is greater than 6, the restructuring of constituting grains are limited, and bouncing will occur. The corresponding filing factor is $\simeq 0.6$ if aggregates were statically compressed before collision (Arakawa et al., 2019c); however, this estimate is significantly larger than the threshold filling factor inferred from experiments ($\simeq 0.1$; Langkowski et al., 2008). Seizinger and Kley (2013) also reported that the threshold filling factor for sticking/bouncing is $\simeq 0.5$, and this discrepancy between numerical simulations and laboratory experiments remains an open question.

Mass transfer. Wurm et al. (2005) studied collisions between mm-sized projectile aggregates and cm-sized target aggregates of μm-sized SiO_2 constituting grains. They found that the outcome of collisions is rebound for collisions below 13 m s^{-1}. However, approximately 50% of the mass of the projectile sticks to the target after the collision at higher collision velocities ($\sim$ 25 m s^{-1}). This growth mechanism, called mass transfer, may help the planetesimal formation

via collisional growth of dust aggregates (e.g., Windmark et al., 2012).

Erosion. Collisions between similar-sized aggregates result in catastrophic fragmentation when they collide above the fragmentation threshold velocity. In contrast, when the projectile-to-target mass ratio is $\ll 1$, we can imagine that the catastrophic fragmentation of the large target aggregate may not occur, but the outcome of collision is erosion with cratering. Experiments by Schräpler and Blum (2011) revealed that macroscopic aggregates of μm-sized constituting grains are eroded via collisions of μm-sized grains at the collision velocities of $\gtrsim 30$ m s^{-1} (see also Schräpler et al., 2018). Monte Carlo simulations suggest that erosion limits dust growth in PPDs, and leads to a steady-state size distribution from μm- to dm-sized inside the H_2O snowline (Schräpler et al., 2018), and from μm- to m-sized outside the snowline when we take into account the density evolution (Krijt et al., 2015).

Using N-body simulations of cohesive particles, Wada et al. (2013) found that, for the case of projectile-to-target mass ratio of $m_{\rm proj}/m_{\rm tar} \geq 1/64$, the critical velocity for collisional growth, $v_{\rm crit}$, is approximately given by

$$v_{\rm crit} \simeq 20\sqrt{\frac{E_{\rm break}}{m_0}}, \tag{1.1}$$

where $m_{\rm proj}$ and $m_{\rm tar}$ are the mass of the projectile and target aggregates, and m_0 is the mass of monomer grains. Based on JKR contact theory (Johnson, Kendall and Roberts, 1971), the breaking energy for a pair of monomers in contact, $E_{\rm break}$, is given by (e.g., Wada et al., 2007, 2013)

$$E_{\rm break} \simeq 23\left(\frac{\gamma^5 {r_0}^4(1-\nu^2)^2}{Y^2}\right)^{1/3}, \tag{1.2}$$

where γ is the surface energy, r_0 is the monomer radius, ν is the Poisson's ratio, and Y is Young's modulus, respectively. This estimate of $v_{\rm crit}$ obtained from numerical simulations is also consistent with the results from laboratory experiments (e.g., Blum and Wurm, 2008; Okuzumi, 2016).

Below this threshold, collisions of dust aggregates generate ejected dust grains and aggregates. The total mass of the ejecta, $m_{\rm eje}$, at the collision velocity of $v_{\rm col} < v_{\rm frag}$ is given by $m_{\rm eje} = m_{\rm proj}(v_{\rm col}/v_{\rm crit})$ (see Wada et al., 2013), and the target aggregate grows by mass transfer in this condition.

Fragmentation. Fragmentation also occurs when dust aggregates collide at a velocity above the fragmentation threshold. Both laboratory experiments (e.g., Blum and Wurm, 2000; Gundlach and Blum, 2015) and numerical simulations (e.g., Dominik and Tielens, 1997; Sirono, 2004; Wada et al., 2009, 2013) intensively study this fragmentation threshold velocity.

1.1.2 Fractal aggregates

The structural evolution of dust aggregates in PPDs is a key for understanding how planetesimals formed. At the beginning of the dust growth, the collisional energy, $E_{\rm roll}$, is lower than the energy needed for restructuring. In this stage,

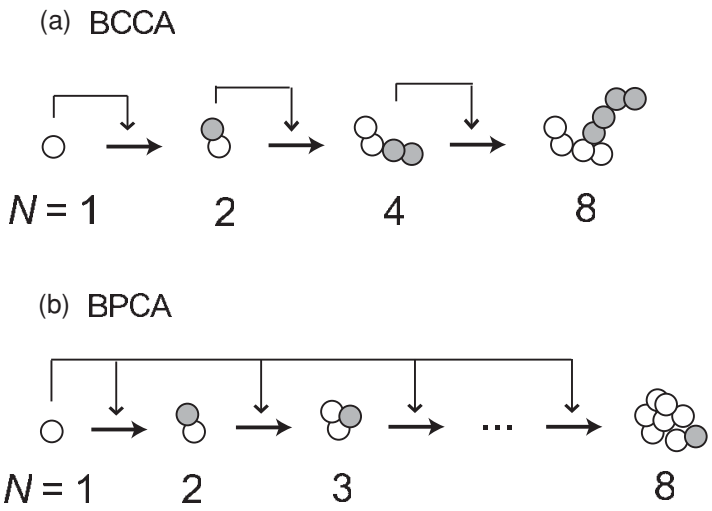

Figure 1.3: Schematic illustrations of (a) the ballistic cluster–cluster aggregation (BCCA), and (b) ballistic particle–cluster aggregation (BPCA). In these collision sequences, we do not consider the restructuring, i.e., compression, of dust aggregates. Figures taken from Okuzumi et al. (2009).

dust aggregates stick without compression, resulting in highly porous aggregates (e.g., Mukai et al., 1992; Wurm and Blum, 1998; Okuzumi et al., 2009).

In the study of dust growth in astrophysical environments, the hit-and-stick processes are usually modeled by (a) the ballistic cluster–cluster aggregation (BCCA), or ballistic particle–cluster aggregation (BPCA) (e.g., Mukai et al., 1992; Ossenkopf, 1993). Figure 1.3 is the schematic description of BCCA and BPCA. Note that, in the early stage of dust growth in PPDs, the mass distribution of aggregates is expected to be (quasi-)monodisperse, then the aggregation process at this stage can approximate BCCA (e.g., Kempf et al., 1999).

Here we introduce the fractal dimension of dust aggregates, D_f, to characterize the structure of aggregates. A simple example of the construction of a fractal aggregate is shown in Figure 1.4 (see also Vicsek, 1983; Meakin, 1991). Aggregates shown in Figure 1.4 are self-similar, and the relation between the number of monomers, N, and the diameter of aggregates, d_agg, is given by

$$\log_5 N = \log_3 \frac{d_\mathrm{agg}}{d_0}, \tag{1.3}$$

where d_0 is the diameter of monomers. We can rewrite Equation (1.3) as

$$N \sim \left(\frac{d_\mathrm{agg}}{d_0}\right)^{D_\mathrm{f}}, \tag{1.4}$$

where $D_\mathrm{f} = \ln 5/\ln 3 \simeq 1.4648$ is the fractal dimension of these self-similar aggregates.

For dust aggregates formed via collision sequence, we define the fractal dimension D_f by the scaling of the number of constituting monomers, N, and

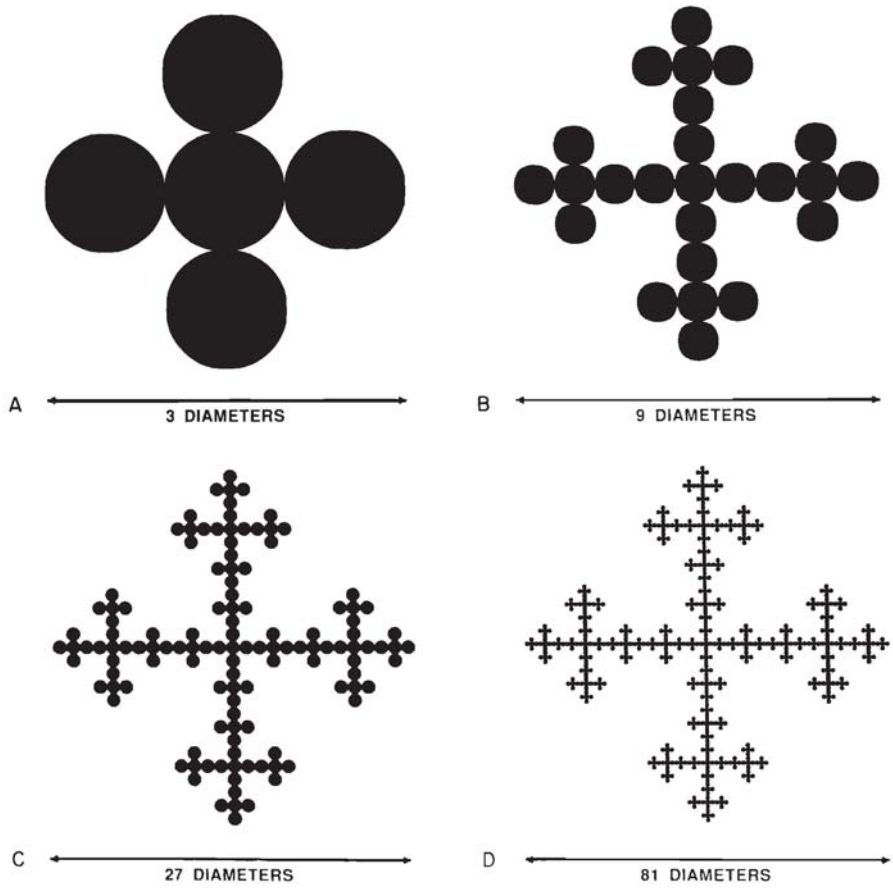

Figure 1.4: An example of the construction of a deterministic model for preparing fractal aggregates (in two-dimensional space). The fractal dimension is given by $D_\mathrm{f} = \ln 5 / \ln 3 \simeq 1.4648$. Figures taken from Meakin (1991).

the gyration radius of aggregates, $r_{\rm gyr}$. The definition of the gyration radius is (e.g., Mukai et al., 1992)

$$r_{\rm gyr} \equiv \sqrt{\frac{1}{2N^2}\sum_{i}^{N}\sum_{j}^{N}\left|\boldsymbol{r}_i - \boldsymbol{r}_j\right|^2}. \tag{1.5}$$

Here $\boldsymbol{r}_i$ is the position of the i-th constituent monomer grain.

Figure 1.5 shows the projections of three-dimensional dust aggregates with the number of constituting monomers of $N = 2^{14} = 16384$. The aggregates shown in Figures 1.5a and 1.5b are formed via BPCA and BCCA, respectively. The fractal dimension of aggregates formed via BPCA is $D_{\rm f} \simeq 3$ (e.g., Mukai et al., 1992; Tazaki et al., 2016). When the fractal dimension is equal to the dimension of space, i.e., $D_{\rm f} = 3$, the aggregates have a constant filling factor ϕ through collisional growth.

In contrast, the fractal dimension of aggregates formed via BCCA is lower than 3; the fractal dimension obtained from numerical simulations is $D_{\rm f} \simeq 1.9$ (e.g., Mukai et al., 1992; Okuzumi et al., 2009). Since larger fractal aggregates naturally have a low filling factor when $D_{\rm f} < 3$, dust aggregates in PPDs are thought to be extremely fluffy. The filling factor of fractal aggregates with a fractal dimension of $D_{\rm f} < 3$ is given by

$$\phi \sim N^{1-3/D_{\rm f}}. \tag{1.6}$$

1.1.3 Compression of dust aggregates

The restructuring of dust aggregates is caused by the rolling at contact points between two monomer grains. Thus the visible collisional compression starts when $E_{\rm col}$ exceeds the energy necessary to roll a particle by 90°, $E_{\rm roll}$ (e.g., Dominik and Tielens, 1997). In the case of dust aggregates formed via BCCA, numerical simulations suggest that the maximum compression is given by (e.g., Wada et al., 2008)

$$\phi_{\rm col,max} \sim N^{-1/5}, \tag{1.7}$$

resulting in that the fractal dimension of collisionally compressed aggregates is $D_{\rm f} \simeq 2.5$ at the maximum. Note that, the collisional compression process of highly porous fractal aggregates is poorly understood from experiments, and future studies on the collisional compression of highly porous aggregates are necessary.

The static compression process of dust aggregates is also studied (e.g., Güttler et al., 2009; Seizinger et al., 2012; Kataoka et al., 2013b; Omura and Nakamura, 2018). Although experiments for highly porous aggregates with filling factor of $\phi \leq 0.1$ are still lacking, and there is no reliable theory for predicting the resulting filling factor in the high-pressure region, both experimental results and numerical simulations are consistent for the case of dust aggregates of μm-sized constituent grains with moderate filling factor (e.g., Seizinger et al., 2012). The filling factor of statically compressed aggregates with the external pressure of P is (Kataoka et al., 2013b)

$$\phi_{\rm static} = \left(\frac{{r_0}^3}{E_{\rm roll}}P\right)^{1/3}. \tag{1.8}$$

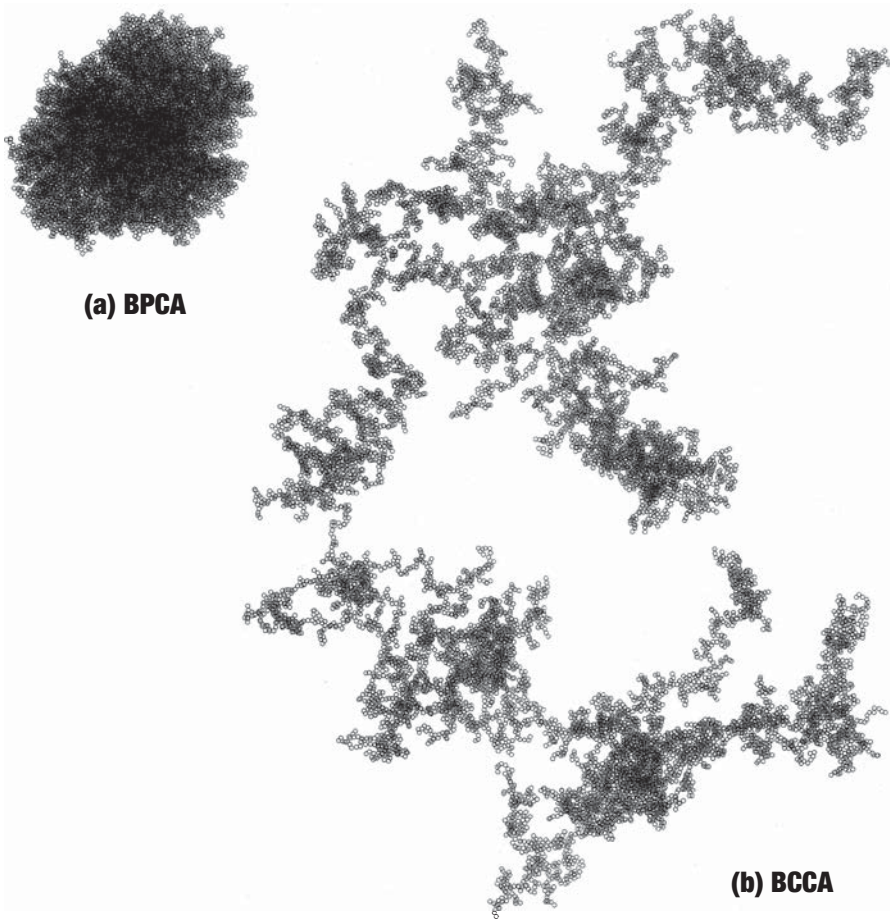

Figure 1.5: Projections of three-dimensional dust aggregates with a number of constituting monomers $N = 2^{14} = 16384$. (a) An aggregate formed via ballistic particle–cluster aggregation (BPCA). (a) An aggregate formed via ballistic cluster–cluster aggregation (BCCA). Figures taken from Mukai et al. (1992).

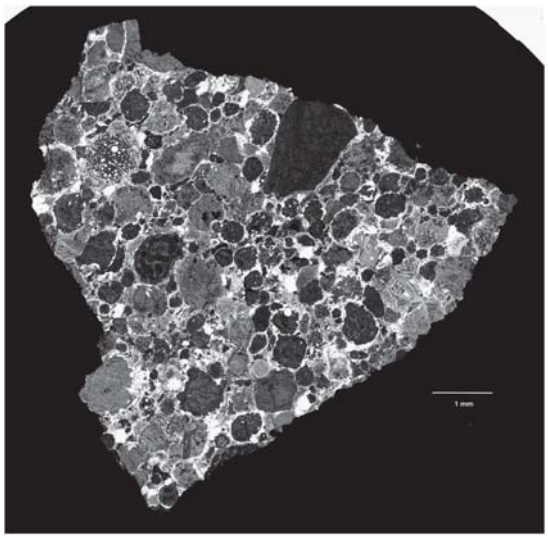

Figure 1.6: A backscatter electron image of a thin section of ordinary chondrite QUE 97008, which is L(LL) (3.05). The abundant circular and fragmented objects in the image are chondrules. Metal grains and sulfide grains is shown as bright white grains, and silicates are grey to almost black in backscatter electron images. Figure taken from Connolly and Jones (2016).

1.2 Chondrites and chondrules

In Section 1.1, we overviewed the dust growth process via collisions in PPDs. It is thought that μm-sized dust grains turn into mm- to cm-sized aggregates in the solar nebula via collisions, and a portion of aggregates have experience of flash heating in the inner solar nebula, resulting in the formation of chondrules, mm-sized spherical igneous dust particles (e.g., Zanda, 2004, and references therein). The heating of dust aggregates would also cause the evaporation of dust aggregates and the formation of nanoparticles (e.g., Miura et al., 2010a). The existence of nanoparticles in PPDs might change the collisional growth pathways toward km-sized planetesimals (Arakawa and Nakamoto, 2016b).

The thermal histories of chondrules before and after accretion onto chondrite parent bodies are the key to understanding how planetesimals formed in the inner solar system. In this section, we briefly summarize the formation and thermal evolution of chondrites and chondrules.

1.2.1 Chondrites

As shown in Figure 1.6, chondrules are the dominant structural component of chondrites; fragments come from undifferentiated rocky planetesimals. German mineralogist Gustav Rose gave the name chondrite in 1863, which comes from the Greek word, χόνδρος (chondros, grain), and it is only slightly later that the word chondrule appears in the literature (see Tschermak et al., 1964; Connolly and Jones, 2016).

Chondrites are pieces of asteroids; however, it is challenging to prove which chondrites come from what asteroids. The Hayabusa sample return mission

revealed that the returned materials from S-type asteroid 25143 Itokawa are identical to LL5 equilibrated ordinary chondrites (Nakamura et al., 2011; Yurimoto et al., 2011). The near-infrared observations of a C-type asteroid, 162173 Ryugu, by Hayabusa2 mission also revealed that the OH feature and low albedo of Ryugu are consistent with thermally- and shock-metamorphosed carbonaceous chondrites (Kitazato et al., 2019). Then we can believe that ordinary chondrite parent bodies were S-type asteroids, and most carbonaceous chondrites came from C-type asteroids.

Chondrites record geological processes, e.g., thermal metamorphism, shock metamorphism, and aqueous alteration. The primary heat source for chondrite parent bodies is possibly the decay of short-lived radionuclides such as ^{26}Al (e.g., Henke et al., 2012a). The meteoritic records of the thermal history of chondrites provide us with the constraints on the accretion age, size of parent bodies, and thermal properties of the interior (see, e.g., Gail et al., 2015).

Cosmochemical measurements revealed that chondrules and matrix in chondrites have chemical (e.g., Palme et al., 2015; Ebel et al., 2016) and isotopic (e.g., Budde et al., 2016a,b) complementarities. These complementarities indicate that the mm-sized chondrules and μm-sized matrix grains must have formed from a single reservoir, and after their formation, neither the chondrules nor matrix grains were lost from the reservoir until planetesimal formation. Arakawa (2017) proposed that the chondrule–matrix complementarity is easily explained when chondrules and matrix grains were formed in the same heating events and that at least some parts of the matrix grains are condensates of evaporated dust.

1.2.2 Chondrules

"Chondrules would not be predicted to exist if they did not exist" (Connolly and Jones, 2016). There are still no chondrule formation models that can explain all observed features of chondrules. Chondrules are igneous spherules, and they were melted and subsequently cooled. Therefore, the fundamental variables to understand how chondrules formed are their thermal history and heating environment (e.g., Desch et al., 2012).

Chondrules are classified by textures and compositions (e.g., Gooding and Keil, 1981). The most abundant type of chondrule texture is porphyritic. Porphyritic chondrules mainly consist of phenocrysts of olivine and/or low-calcium pyroxene. Meteoriticists usually thought that porphyritic chondrules melt incompletely during their formation (e.g., Lofgren and Russell, 1986; Hewins and Radomsky, 1990), although (Connolly and Hewins, 1995) reported that porphyritic textures could be reproduced from completely molten precursors. Nonporphyritic chondrules are minor: 15% of all chondrules in ordinary chondrites (e.g., Wasson et al., 1995) and 5% in CV carbonaceous chondrites (e.g., Akaki and Nakamura, 2005). They are classified into three subtypes: cryptocrystalline, barred, and radial textures (e.g., Gooding and Keil, 1981). Glassy chondrules are extremely rare (e.g., Krot and Rubin, 1994), and this fact might indicate that chondrules were formed together with fine dust particles that aid the nucleation of molten chondrules (e.g., Nagashima et al., 2008).

In chondrites, some chondrules, referred to as compound chondrules, exist as compounds of two or more chondrules which fused. Figure 1.7 is a micrograph of a compound chondrule from a thin section of LL3.00 ordinary chon-

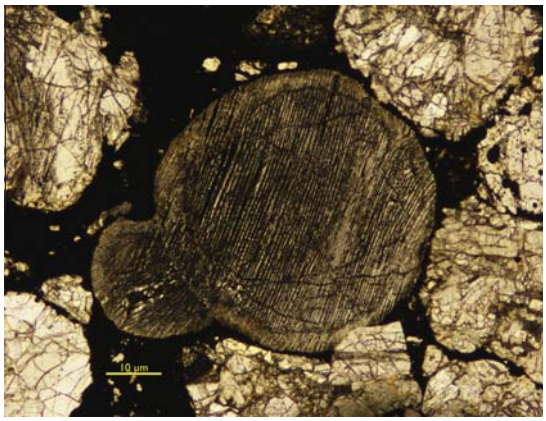

Figure 1.7: A micrograph of a compound chondrule from a thin section of LL3.00 ordinary chondrite Semarkona. Figure taken from Hubbard (2015).

drite Semarkona (Hubbard, 2015). Most compound chondrules are thought to be formed by collisions between chondrules (e.g., Gooding and Keil, 1981; Bischoff et al., 2017); thus, we can give some constraints on the formation environment of chondrules from the observed feature and fraction of compound chondrules. Arakawa and Nakamoto (2016a, 2019) studied the formation process of compound chondrules from the crystallization process and collision dynamics of molten chondrules.

1.3 Comets

Comets are small and irregular-shaped objects composed of ices, organics, and refractory materials. We think that they keep a record of the physical and chemical evolution of the early solar system. Solar system small bodies—asteroids, comets, and trans-Neptunian objects—are leftovers from the planet formation 4.6 billion years ago.

Comets are characterized by activity, i.e., the release of gas and dust from their solid surface, nuclei (see, e.g., Vincent et al., 2019). When they pass through the inner solar system, they have a coma, which is the nebulous envelope of ice and dust particles. Gas and dust tails are also visible features of comets. The *Rosetta* mission of the European Space Agency explored comet 67P/Churyumov–Gerasimenko between 2014 and 2016. Activity from the neck of comet 67P/Churyumov–Gerasimenko is pictured by the Optical, Spectroscopic, and Infrared Remote Imaging System, OSIRIS (Keller et al., 2007). Figure 1.8 shows the jets from the neck region of comet 67P/Churyumov–Gerasimenko (Sierks et al., 2015).

It is thought that cometary activities are driven by sublimation of ices (e.g., H_2O and CO_2; Kührt and Keller, 1994, 1996). However, the cohesion force between dust particles on a cometary surface would be larger than the ice sublimation pressure if comets were made of submicron-sized dust particles (e.g., Tatsuuma et al., 2019). Thus, some "tricks" must be needed to explain how comets work (e.g., Blum, 2018; Fulle et al., 2019). In Chapter 7, we discuss the

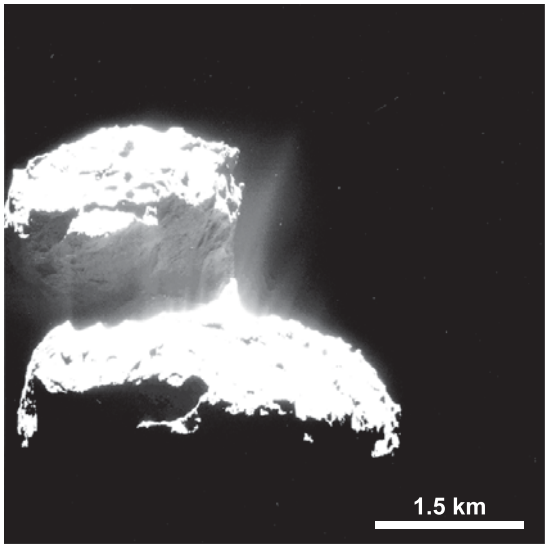

Figure 1.8: Jets from the surface of comet 67P/Churyumov–Gerasimenko as observed on 23 September 2014. Figure taken from Sierks et al. (2015).

structure of the nucleus of comet 67P/Churyumov–Gerasimenko, from the mechanical and thermal properties, which are revealed by the *Rosetta* mission. We also expect that the structure of comets directly associates with the formation process of icy planetesimals in the early solar system.

1.4 Kuiper belt objects

The Kuiper belt is a donut-shaped region of small icy bodies beyond the orbit of Neptune. There is also an outer edge of the classical Kuiper belt* at heliocentric distances of 50 au (Trujillo et al., 2001). The hypothesis of the distant region of leftovers from the planet formation in the early solar system is initially proposed by Edgeworth (1943, 1949), as a source of short-period comets. Kuiper (1951) also proposed that scattering of small icy bodies from the Kuiper belt may be the origin of spherical clouds of long-period comets, which is called the Oort cloud (Oort, 1950).

Excluding Pluto and Charon, the most famous Kuiper belt objects (KBOs), the first observational confirmation of KBOs was in 1992; Jewitt and Luu (1993) discovered the 100 km-sized object, 15760 Albion (provisional designation 1992 QB_1), in the cold classical Kuiper belt. Now we know at least six 1000 km-sized KBOs, and there are approximately 2400 known KBOs (see List Of Transneptunian Objects). KBOs are also referred to as trans-Neptunian objects (TNOs).

Many KBOs exist as binaries or multiples (see Noll et al., 2008a). The binary fraction of $\sim 30\%$ is found for cold classical KBOs by Noll et al. (2008b),

* Classical Kuiper belt objects, also called cubewanos (named from 1992 QB_1), are defined as low-eccentricity KBOs with heliocentric eccentricity lower than 0.24 (Gladman et al., 2008). The majority of classical KBOs are dynamically cold, i.e., whose inclination is lower than 5°. The cold classical KBOs are dynamically unperturbed, and therefore they would preserve the nature of the ancient Kuiper belt.

Figure 1.9: Enhanced color images of Pluto (lower right) and Charon (upper left) taken by NASA's New Horizons spacecraft on July 14, 2015. The color and brightness of both Pluto and Charon have been processed identically. The relative sizes of Pluto and Charon shown in this figure are approximately correct, but their separation is not to scale. Figure credit: NASA/JHUAPL/SwRI.

and possible nearly 100% of the cold classical KBOs were initially formed as binaries (Fraser et al., 2017). There are many models for the origin of binaries (e.g., Goldreich et al., 2002; Nesvorný et al., 2010; Kominami et al., 2011), and Nesvorný et al. (2019) recently proposed that these Kuiper belt binaries may have been formed via streaming instability (e.g., Youdin and Goodman, 2005; Johansen et al., 2012), based on the spatial orientation of binary orbits.

Binaries of 100 km-sized KBOs usually have mass ratios close to unity (e.g., Noll et al., 2008a,b). In contrast, the secondary-to-primary mass ratio of 1000 km-sized large KBOs is typically $\ll 0.1$ (e.g., Brown et al., 2006, except for Pluto–Charon system), suggesting that their origin is different from that of 100 km-sized binaries. Satellite systems around 1000 km-sized KBOs are thought to be formed via giant impacts (e.g., Canup, 2005). The heating of the equatorial region of Pluto by Charon-forming giant impact is a possible explanation of the dark reddish region of Pluto (Sekine et al., 2017, see Figure 1.9). Arakawa et al. (2019a) found that circular orbits of their satellites (typically eccentricity lower than 0.1) can be reproduced when they were tidally evolved initially as dissipative bodies. This suggests that at least 100 km-sized KBOs, which can retain the heat generated from the decay of short-lived radionuclides such as ^{26}Al, should form in the solar nebula within a few million years after the birth of the sun (see Chapter 8). The early formation of 100–1000 km-sized KBOs is consistent with the planetesimal formation scenario proposed by Nesvorný et al. (2019).

1.5 This thesis

The evolution of dust aggregates in the solar nebula is the key to understanding the first step of the planet formation. However, the growth pathway from submicron-sized dust grains to km-sized planetesimals is still unclear. In this thesis, we discuss what the building blocks of planetesimals are and how planetesimals formed in the solar nebula, from the thermal history of small bodies.

Chondrules, the primary component of chondrites, is thought to form via flash-heating events in the solar nebula. Some of them exist as compound chondrules; thus, they would collide in their formation environments. In Chapter 2, we propose a new scenario for compound chondrule formation: the supercooled collision model. The collisions between a crystallized chondrule and a supercooled precursor explain the textural feature and primary-to-secondary size ratio of compound chondrules observed within ordinary chondrites. In Chapter 3, we further develop our model. We propose that chondrules formed via optically thin shock waves, and collisions of supercooled precursors behind shock fronts make compound chondrules. Using semi-analytical calculations, we find that 10^4 km-sized shock waves in the gaseous solar nebula are the possible candidate for chondrule formation, which is consistent with the observed features of single and compound chondrules and their survivability.

The thermal and mechanical properties of dust aggregates provide us plenty of insights into the formation process of small bodies. In Chapter 4, we numerically calculate the thermal conductivity of dust aggregates whose filling factor of lower than 0.1. We reveal that the thermal conductivity through the solid network is approximately proportional to the square of the filling factor. We further work on the thermal conductivity calculation in Chapter 5 and find that the thermal conductivity through the solid network is a function of the filling factor and average coordination number. The average coordination number also depends on the filling factor, and we obtain a simple relation. In Chapter 6, we theoretically derive these equations from the fractal structure of dust aggregates used in our simulations. We introduce a new constant that characterizes the chain length within fractal aggregates. This constant is essential to describe the filling factor dependence of the thermal conductivity, and the compressive strength would also depend on this constant.

Comets are possible survivors of icy planetesimals in the early solar system. The *Rosetta* mission revealed the thermal and mechanical properties of comet 67P/Churyumov–Gerasimenko. In Chapter 7, comparing the observational results and model calculations from our dust aggregate formulae, we find that the structure of dust aggregates on the comet is not a homogeneous aggregate constituted from (sub)micron-sized monomer grains. Instead, the hierarchical aggregate of cm- or dm-sized constituent aggregates well explains the thermal and mechanical features of the comet. This hierarchical structure of comets indicates that icy planetesimals grew via accretion of cm- or dm-sized dust aggregates onto pre-existing planetesimals.

The trans-Neptunian objects are the small icy bodies that resided in the outer edge of the solar system. Recent observations revealed that all 1000 km-sized trans-Neptunian objects form satellite systems. In Chapter 8, we carry out numerical simulations of giant impacts and reveal that not only large satellites but small satellites could form via giant impacts as intact fragments of

impactors when their impact velocities are approximately the same as their escape velocities. We also calculate the tidal evolutions of these satellite systems, which formed after impacts. The observed satellite systems have small eccentricities typically lower than 0.1. We find that low-eccentricity systems formed when satellites are tidally evolved initially as fluid-like dissipative bodies. These results suggest that all satellites of large trans-Neptunian objects formed via giant impacts before the outward migration of Neptune and that they were fully or partially molten during the giant impact era. The rapid formation of large trans-Neptunian objects is also consistent with the scenario that small icy bodies grew via accretion of cm-sized dust aggregates, which is proposed by recnt numerical simulations of planet formation.

Finally, in Chapter 9, we summarize the main results of this thesis and discuss an outlook on future work. Although the accretion of cm-sized dust aggregates is a strong candidate for the planetesimal formation mechanism, we need to understand in detail the physical properties of dust aggregates, the flash-heating process of floating aggregates, which would make chondrules, and the accretion process of dust aggregates in the solar nebula.

Chapter 2

Compound chondrule formation via collision of supercooled droplets

Sota Arakawa and Taishi Nakamoto
Icarus **276**, 102–106 (2016).

Abstract

We present a novel model showing that compound chondrules are formed by collisions of supercooled droplets. This model reproduces two prominent observed features of compound chondrules: the nonporphyritic texture and the size ratio between two components.

2.1 Introduction

Chondrules are spherical particles of 0.1–1 mm in size contained within chondrites, the most common type of meteorites, as a major component. The volume fraction of chondrules in typical chondrites, i.e., ordinary chondrites, is up to 70% (Rubin, 2000). It implies that the total mass of all the chondrules in all the asteroids would be very large. This cannot be ignored compared to the total solid mass in the asteroid belt. The ages of chondrules are about 4.6 Gyr, slightly (probably a few Myr or less) younger than the Calcium-Aluminum-rich Inclusions (CAIs) (e.g., Dauphas and Chaussidon, 2011). Therefore, the formation of chondrules must be related to the formation of the solar system itself, especially to the formation of the asteroids, the rocky planets, and probably Jupiter as well. Revealing the chondrule formation process, therefore, is one of the keys to elucidating the solar system formation. Chondrules are thought to be melted by some heating processes in the early solar nebula and become spherical due to the surface tension. However, heating processes responsible for chondrule formation and their details remain unclear.

Studies of chondrules in thin sections have revealed that some chondrules are composed of two or more chondrules fused together. They are called *compound chondrules*. The presence of compound chondrules is interpreted to be the result of collisions among non-solid precursors. Since the compound chondrule formation includes multiple precursors, it is a more complicated phenomenon than single chondrule formation. It suggests that by studying compound chondrule formation, we can obtain more information on the chondrule formation process itself, since it is likely that compound chondrules and single chondrules are formed by similar mechanisms. Determining the compound chondrule formation process is an important issue to be addressed.

Previous studies on compound chondrule formation mainly analyzed the fraction of compound chondrules among all the chondrules, which is expressed by $f^{\rm ALL}_{\rm compound}$ and is about 4% ($f^{\rm ALL}_{\rm compound} = 4 \times 10^{-2}$) (Gooding and Keil, 1981). Most of the previous studies assume that compound chondrules are formed by collisions of molten precursors (the molten-collision model) (e.g., Ciesla et al., 2004b). The fraction of compound chondrules was estimated from the fraction of chondrules undergoing collisions with other chondrules (Gooding and Keil, 1981; Ciesla et al., 2004b). The fraction of chondrules that underwent collisions with others, $f_{\rm col}$, can be estimated by

$$f_{\rm col} = n\sigma v t_{\rm col}, \tag{2.1}$$

where n is the number density of chondrules, σ is the collisional cross section, v is the collision velocity, and $t_{\rm col}$ is the duration of time when compound chondrule forming collisions take place. Each quantity may be evaluated as follows. A typical radius of chondrules r is about 2×10^{-2} cm (Rubin, 2000), and the collisional cross section of chondrules σ is about $\sigma \sim \pi(2r)^2 = 5 \times 10^{-3}$ cm^2. We assume that the collision velocity is $v = 1 \times 10^2$ cm s^{-1} from hydromechanical constraints (e.g., Ashgriz and Poo, 1990). As for the duration of time when chondrules stay molten, it is suggested to be shorter than 10^4 sec based on the cooling rate estimation of chondrule formation (Desch and Connolly, 2002), or some studies suggest that the duration of time when chondrules stay molten is only a few sec (e.g., Yurimoto and Wasson, 2002). In order to reproduce the observed fraction of compound chondrules, $f^{\rm ALL}_{\rm compound} = 0.04$, the number density n should be 8×10^{-6} cm^{-3} or much higher. Using a similar argument, Ciesla et al. (2004b) inferred that chondrules would have formed in regions of the solar nebula that had highly concentrated solids. However, it is not clear if such a concentrated region can be present in the early solar nebula. For example, when we suppose that compound chondrules are formed in the midplane of the minimum mass solar nebula (Hayashi, 1981) at 2 AU, and suppose that the dust-to-gas mass ratio is raised to be unity due to dust sedimentation, and suppose that all the dust forms chondrule precursor particles, then the estimated number density of chondrule precursor particles would only be about 2×10^{-6} cm^{-3} when the internal density of precursor particles is about 3 g cm^{-3}. Since the values of σ and $v_{\rm c}$ would not be changed significantly, the short duration $t_{\rm col}$ requires a higher number density n to form the large fraction of compound chondrules.

Compound chondrules have some other noteworthy features. A component in a compound chondrule usually holds spherical shape, which is called *primary*. In contrast, the other component is usually deformed and called

secondary. The median size ratio of primary to secondary is approximately four (Wasson et al., 1995); i.e., the spherical primary is typically four times larger than the deformed secondary. In addition, compound chondrules can be grouped into three types according to structure (Wasson et al., 1995): (1) an adhering type, wherein a small secondary is stuck on a large primary, (2) a consorting type, where both primary and secondary have roughly the same size, and (3) an enveloping type, where a secondary encloses a primary. In ordinary chondrites, it is found that enveloping compound chondrules are rare (only eight out of 80 samples or about 10% of all the compound chondrules) (see Wasson et al., 1995), so in this study we consider only the adhering and the consorting types. According to Wasson et al. (1995), the fraction of the adhering type is $66/80 = 82.5\%$ and that of the consorting type is $6/80 = 7.5\%$.

The textures of chondrules contained in compound chondrules have another noteworthy feature. In general, the textures of chondrules are classified into three types: porphyritic, nonporphyritic, and glassy. According to Gooding and Keil (1981), only 16% of all the chondrules are nonporphyritic chondrules, while 84% of them are porphyritic. Glassy chondrules are extremely rare (Krot and Rubin, 1994). In contrast, when we look at components in compound chondrules in ordinary chondrites, we can find that most of them have nonporphyritic texture. Although the majority of compound chondrules in CV chondrites is porphyritic, the trend ($f^{\mathrm{NP}}_{\mathrm{compound}}/f^{\mathrm{ALL}}_{\mathrm{compound}} \gg 1$) is common (Akaki and Nakamura, 2005), where $f^{\mathrm{NP}}_{\mathrm{compound}}$ is the fraction of compound chondrules in nonporphyritic chondrules. Wasson et al. (1995) revealed that 52 primaries and 65 secondaries in 72 adhering and consorting compound chondrules are nonporphyritic, so the fractions of the nonporphyritic type are $52/72 = 81\%$ for the primary and $65/72 = 90\%$ for the secondary, both of which are much higher than the fractions in all the chondrules. Experimental studies showed that nonporphyritic chondrules are formed from completely molten droplets, and porphyritic ones are formed from partially molten particles (e.g., Connolly et al., 1998). Therefore, it is strongly suggested that compound chondrules are formed mainly from completely molten droplets, while single chondrules are formed from partially molten particles.

Experiments (e.g., Nagashima et al., 2006, 2008) showed that completely molten levitated droplets having no contact with any other solids turned into a supercooled state at their liquidus temperature as they are cooled. The supercooled droplets behaved as fluid particles even at a temperature lower than the liquidus. If the temperature is maintained properly, the droplets remained supercooled for a long time. However, when the droplets collide with a solid particle, they immediately crystallize and form a nonporphyritic texture. Since the majority of components in compound chondrules are likely to be formed from completely molten droplets, it seems natural to expect that most of the compound chondrules have experienced a supercooled state in their formation process. However, the supercooling has never been taken into consideration in the context of compound chondrule formation.

In this study, compound chondrule formation with supercooling is examined. Table 2.1 lists some apparent features and the number of observed compound chondrules, which should be explained by a successful compound chondrule formation model. We will address these properties, and we will see that they can be explained by taking the supercooling into account in the

Table 2.1: Three features of compound chondrules that should be explained in this study.

Feature I	textural type of compound chondrule	almost all (90%) are nonporphyritic
Feature II	size ratio between primary to secondary	4:1 (primary is larger)
Fraction	compound chondrule fraction in nonporphyritic (or porphyritic) chondrule	$f^{\mathrm{NP}}_{\mathrm{compound}} = (4\% \times 90\%)/16\% \sim 20\%$ ($f^{\mathrm{P}}_{\mathrm{compound}} = (4\% \times 10\%)/84\% \sim 0.5\%$)

model.

2.2 Crystallization of melts

Understanding the crystallization mechanism is essential for discussing the formation process of compound chondrules. However, in previous studies of compound chondrule formation, the crystallization process was considered incorrectly. For example, Hubbard (2015) assumed that the viscosity of dust particles changed continuously from the liquidus temperature to the glass transition point; however, in reality, the viscosity increases discontinuously at the solidus temperature.

Figure 2.1 shows a schematic phase diagram of dust in stable states (completely molten, solid-liquid equilibrium, and crystallized) and metastable states (supercooled and glass). A metastable state is an unstable equilibrium state of a macroscopic system in which the system can remain for a long period. A supercooled droplet and a glass particle are well-known examples of metastable states.

In stable states, as the temperature decreases, completely molten droplets (colored by red in Figure 2.1) turn into partially molten particles (solid-liquid equilibrium phase, yellow) at their liquidus ($\sim$ 1700–2000 K) (Hewins and Radomsky, 1990), and partially molten particles turn into crystallized particles (gray) at their solidus (e.g., 1830 K for the $MgSiO_3$–Mg_2SiO_4 system) (Bowen and Andersen, 1914). On the other hand, in metastable states, completely molten droplets turn into supercooled droplets (light blue) at the liquidus, and supercooled droplets turn into glass particles (deep blue) at the glass transition point (e.g., 1063 K for enstatite, reviewed by Stebbins et al., 1984).

Previous studies of compound chondrule formation did not take supercooling into consideration. Although partially molten droplets immediately turn into crystallized particles, experimental studies (Nagashima et al., 2006, 2008) revealed that completely molten levitated droplets invariably turn into supercooled droplets. Nagashima et al. (2006) studied supercooling and crystallization of forsterite droplets using levitation experiments, and they revealed that the duration of supercooling is longer than 10^3 sec even if supercooled droplets are kept at low temperature (1160 K). In addition, a theoretical study by Tanaka et al. (2008) suggested that the duration of supercooling can be arbitrarily long if the temperature of these supercooled droplets are kept above their glass transition points. These supercooled droplets turn into crystallized particles by contact (Nagashima et al., 2006). We, therefore, suggest that the crystallization of supercooled droplets is the key for the compound chondrule formation

because almost all the compound chondrules have experienced complete melting.

In this study, we assume that completely molten droplets turn into supercooled droplets as their temperature decreases, and supercooled droplets turn into crystallized particles when they collide with other particles. Even though supercooled droplets may turn into partially molten droplets, we ignore this for simplicity. The outline of our model should hardly change with this transition. More details of the crystallization of supercooled droplets should be studied in the future.

2.3 Supercooled-collision model for compound chondrule formation

We propose a novel compound chondrule formation model, wherein compound chondrules are formed through the collision and the crystallization of supercooled droplets. We call this model a supercooled-collision model. In this model, the heating mechanism for the chondrule formation is not specified. Therefore, this model is a general one that could be applicable to various

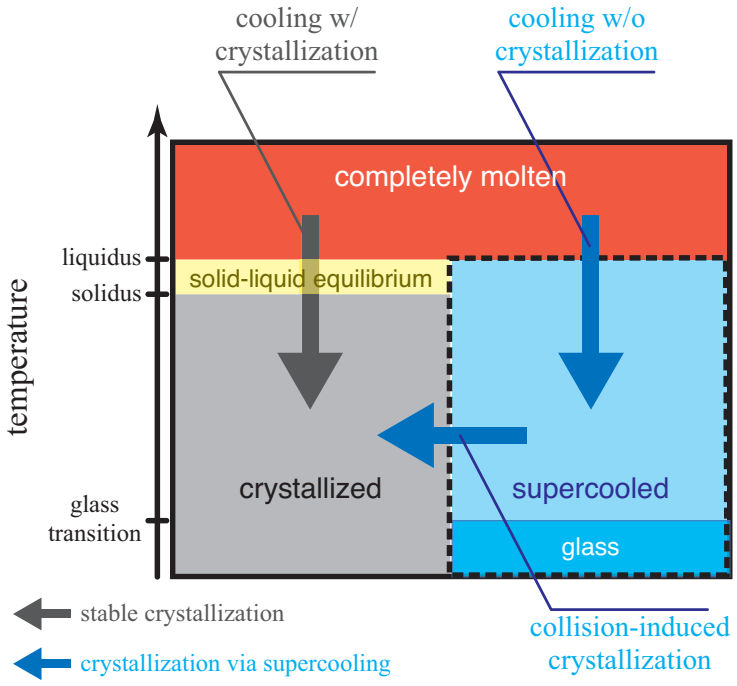

Figure 2.1: A schematic phase diagram of dust particles in stable states (completely molten, solid–liquid equilibrium, and crystallized) and metastable states (supercooled and glass). Previous studies considered that nonporphyritic chondrules are crystallized between their liquidus and solidus (gray arrow). In contrast, completely molten levitated droplets invariably turn into supercooled droplets and these supercooled droplets turn into crystallized particles by contact (blue arrows).

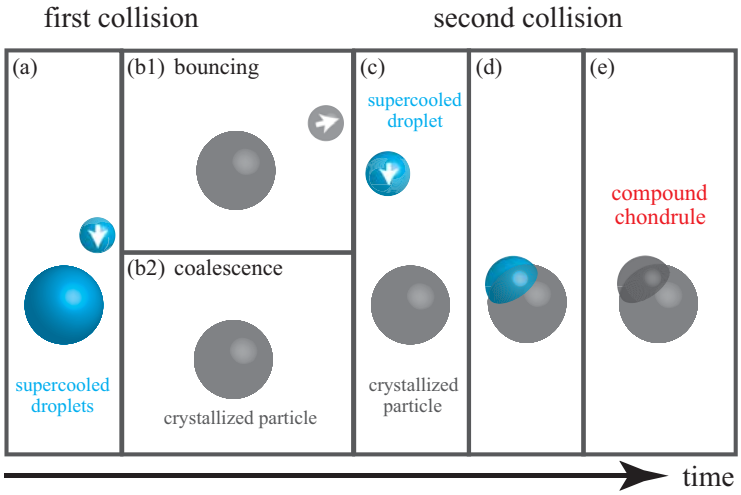

Figure 2.2: An outline of the supercooled-collision model. The compound chondrules are formed by collisions between supercooled droplets and crystallized particles.

chondrule formation models.

Figure 2.2 shows an outline of the supercooled-collision model. We suppose that at first the temperature of the dust particles is above the liquidus, and the particles are completely molten. Afterwards, these particles cool below the liquidus and become supercooled droplets (Figure 2.2a). The supercooled droplets are crystallized by collisions with other particles and change into crystallized particles. When two droplets collide with a large relative velocity, the two droplets fragment into small pieces or separate after the collision and change into two crystallized particles (Figure 2.2b1). On the other hand, when two droplets collide with a small relative velocity, the two droplets coalesce and change into one crystallized particle (Figure 2.2b2). When a supercooled droplet collides with a crystallized particle (Figure 2.2c), the supercooled droplet sticks to the crystallized particle (Figure 2.2d), and a compound chondrule is formed by rapid crystallization (Figure 2.2e).

The supercooled-collision model immediately reproduces two important features of compound chondrules, Feature I and Feature Ⅱ in Table 2.1. The observed Feature I—that most of the compound chondrules are nonporphyritic—can be reproduced, because a complete molten state is supposed first in the supercooled-collision model so that molten droplets can experience supercooling, and complete molten droplets can finally form nonporphyritic chondrules. The observed Feature Ⅱ—that the primaries (spherical-shaped particles in compound chondrules) have larger sizes than the secondaries (deformed particles) in almost all the compound chondrules—can be explained by the size dependence of the collision rate. Larger particles have a larger geometrical cross section for collision, so they collide with other particles more frequently than do the smaller particles. In addition, it is often the case that larger particles have a greater velocity than smaller particles (e.g., Ormel and Cuzzi, 2007), so again they tend to collide with other particles more frequently, though this depends on the chondrule forming mechanism and the environment. Thus, larger su-

percooled droplets are likely to crystallize earlier than smaller droplets and become the primaries of compound chondrules.

It may be not clear what happens after stage (c) in Figure 2.2 for the collision of the supercooled droplet. We need to determine if hydrodynamic motion (Figure 2.2d) or crystallization (Figure 2.2e) occurs, and we do this by evaluating the time scales of these phenomena. Laboratory experiments suggest that the crystallization time scale is of the order of 1 sec (Nagashima et al., 2006, 2008). On the other hand, the time scale of the hydrodynamic motion of the supercooled fluid caused by collision should be about r/v, where r is the radius of the droplet and v is the collision velocity. The size of the colliding droplet, which would become secondary, is of the order of 10^{-2} cm, and the collision velocity should be about 10^2 cm s^{-1}, as will be discussed later. Therefore, the collision time scale would be of the order of 10^{-4} sec. Since the time scale of the hydrodynamic motion is shorter than the crystallization time scale, we can see that the hydrodynamic motion takes place first and the crystallization follows. The supercooled droplet colliding into the crystallized particle behaves as a fluid and deforms first; and after stopping the hydrodynamic motion, it crystallizes. This estimate is consistent with the experimental results (Connolly et al., 1994).

2.4 Quantitative evaluation of the supercooled-collision model

The observed feature named *Fraction* in Table 2.1 (the fraction of compound chondrules among all the nonporphyritic chondrules, $f^{\mathrm{NP}}_{\mathrm{compound}}$) is about 20% (Ciesla et al., 2004b). We need to evaluate if the supercooled-collision model can quantitatively reproduce this observed feature of the compound chondrules.

In the supercooled-collision model, the fraction of the compound chondrules among all the nonporphyritic chondrules $f^{\mathrm{NP}}_{\mathrm{compound}}$ is given by $f^{\mathrm{NP}}_{\mathrm{compound}} = n\sigma v t_{\mathrm{form}}$. Therefore, we suppose that the compound chondrule forming collision velocities v are 1×10^2 cm s^{-1}, the same as the collision velocities in the molten-collision model; and we have

$$nt_{\mathrm{form}} = \frac{f^{\mathrm{NP}}_{\mathrm{compound}}}{\sigma v} = 4 \times 10^{-1}\ \mathrm{cm}^{-3}\ \mathrm{s}. \tag{2.2}$$

Note that the supposed collision velocity v may be different among the compound chondrule formation models, though the cross section σ is independent of the models.

In the molten-collision model, it is supposed that the upper limit of t_{form} is 10^4 sec (or might be a few sec) and v is about 1×10^2 cm s^{-1}, so the number density should be higher than 4×10^{-5} cm^{-3} to reproduce a sufficient amount of the compound chondrules. However, the required number density seems to be too high to be realized in the solar nebula. For example, as discussed in section 2.1, the number density of chondrule sized particles at 2 AU may reach 4×10^{-4} cm^{-3} only if the dust-to-gas mass ratio is about 20:1 in the mid-plane of the minimum mass solar nebula (Hayashi, 1981).

In contrast, in the supercooled-collision model, the duration of the supercooled state, which can be the duration of compound chondrule formation $t_{\rm form}$, can be long. A theoretical study on nucleation (Tanaka et al., 2008) indicated that the duration of the supercooled state can be arbitrarily long depending on the temperature cooling rate. For example, it was shown that the supercooled state could last for 10^5 sec or 10^6 sec, when the cooling rate of the temperature is 10^{-2} K s^{-1} or 10^{-3} K s^{-1}, respectively. In fact, these slow cooling rates are considered to be appropriate as the cooling rates for chondrule formation ($\sim 10^{-3}$–1 K s^{-1}) (Desch et al., 2012). We think that the duration of the supercooled state can be 10^5 sec or 10^6 sec.

Generally, the supercooled-collision model requires a lower number density compared to the molten-collision model, since the duration for formation $t_{\rm form}$ can be long because of the supercooling.

2.5 Discussion: application to chondrule formation models

The supercooled-collision model for compound chondrules proposed in this study is independent of the chondrule formation models. However, it requires certain relationships between the number density of chondrule precursors n and the duration of compound chondrule formation $t_{\rm form}$ as discussed in section 2.4. We now examine if some chondrule formation models studied to date may meet the requirement for compound chondrule formation. The examined chondrule formation models include the planetesimal bow shock model, the lightning model, and the impact jetting model.

The planetesimal bow shock model assumes that some eccentric planetesimals in the solar nebula generate bow shocks around them; and the chondrule precursor particles in the solar nebula are heated by the bow shock, mainly due to the gas frictional heating (e.g., Morris et al., 2012; Nagasawa et al., 2014). According to Morris et al. (2012), chondrules heated in the shocked gas are cooled to the glass transition point about 10 hours ($\simeq 4 \times 10^4$ sec) after heating. This time scale can be regarded as the duration of the supercooled state and the duration of compound chondrule formation $t_{\rm form}$. We then obtain that the required number density of the chondrule precursors is about 1×10^{-5} cm^{-3}, which might be realized in a dust-rich region such as the dust-layer at the mid-plane of the solar nebula. Therefore, the planetesimal bow shock model may be consistent with compound chondrule formation using the supercooled-collision model.

The planetesimal bow shock model may provide another benefit for the compound chondrule formation. Tanaka et al. (2008) showed that supercooled forsterite droplets are crystallized without collision near the transition temperature ($\sim$ 1200 K) and that they do not turn into glass. Forsterite-rich particles crystallize spontaneously. In contrast, enstatite-rich particles never crystallize spontaneously and turn into glass at the transition temperature. To crystallize enstatite-rich particles, some solid particles as nuclei for crystallization are needed (Nagashima et al., 2008). Since natural chondrites do not contain many glass chondrules, some nuclei for crystallization should be supplied for enstatite-rich particles in the chondrule forming. These nuclei may be pro-

vided as tiny solid particles, which are condensates from silicate vapor in the chondrule forming region. Miura et al. (2010a) suggested that nm- and μm-sized dust grains are formed in the shocked region, at the temperature around 1000 K, which is near the glass transition point. Because of the supply of these small grains, enstatite-rich glassy chondrules are not formed frequently.

The lightning model (e.g., Horányi et al., 1995) assumes that charged dust particles in the solar nebula are decoupled with gas, and the motions of the dust particles generate local potential differences in the solar nebula. Electrical charges are released then as lightning. There are several positive (e.g., Muranushi, 2010) and negative (e.g., Güttler et al., 2008) opinions regarding this mechanism. However, from the viewpoint of compound chondrule formation, the lightning model seems to be inappropriate. Horányi et al. (1995) suggests that the duration of melting is extremely short (the temperature of the dust particles decreases at the glass transition point within 10 sec). In this case, the fraction of compound chondrules cannot be reproduced by the lightning model.

The impact jetting model (e.g., Johnson et al., 2015) assumes that chondrules are formed by collisions between planetesimals or protoplanets. According to Johnson et al. (2015), the dust particles ejected by the collisions are mm-sized completely molten droplets, and cooling rates of these particles are of the order of 10^{-1} K s^{-1}. These features are consistent with the constraints of chondrule formation. However, the number of collisions per dust particle calculated by Johnson et al. (2015) is of the order of 10^2, which might be extremely large for reproducing the fraction of compound chondrules. This high frequency of collision leads to the conclusion that not only nonporphyritic chondrules, but also most porphyritic ones, are compound. In reality, the fraction of compound chondrules in porphyritic chondrules is only 0.5%. Therefore, the impact jetting model might not be appropriate at least for the compound chondrules in ordinary chondrites.

2.6 Conclusion

We examined if the supercooled-collision model, a novel model for compound chondrule formation schematically shown in Figure 2.2, can reproduce the observed features of compound chondrules in ordinary chondrites. Compound chondrules have three features: there are nonporphyritic textural types (Feature I), the primary is about four times as large as the secondary (Feature I I), and 20% of the nonporphyritic chondrules are compound (Fraction). Feature I suggests that almost all of the compound chondrules have experienced complete melting (Connolly et al., 1998) and supercooling (Nagashima et al., 2006). Feature Ⅱ can be explained by the supercooling and crystallization of dust particles. Large supercooled droplets tend to collide with other particles frequently compared to small droplets, with large particles tending to turn into the primaries and the small supercooled survivors sticking on the primaries. The fraction of compound chondrule is related to the number density of the dust particles and the duration of supercooling. Because of the long duration of supercooling (Tanaka et al., 2008), the required number density can be low. Therefore, we conclude that compound chondrules are likely to be formed through collisions among supercooled droplets.

Chapter 3

Compound chondrule formation in optically thin shock waves

Sota Arakawa and Taishi Nakamoto
The Astrophysical Journal **877**, 84 (2019).

Abstract

Shock-wave heating within the solar nebula is one of the leading candidates for the source of chondrule-forming events. Here, we examine the possibility of compound chondrule formation via optically thin shock waves. Several features of compound chondrules indicate that compound chondrules are formed via the collisions of supercooled precursors. We evaluate whether compound chondrules can be formed via the collision of supercooled chondrule precursors in the framework of the shock-wave heating model by using semi-analytical methods and discuss whether most of the crystallized chondrules can avoid destruction upon collision in the post-shock region. We find that chondrule precursors immediately turn into supercooled droplets when the shock waves are optically thin and they can maintain supercooling until the condensation of evaporated fine dust grains. Owing to the large viscosity of supercooled melts, supercooled chondrule precursors can survive high-speed collisions on the order of 1 km s^{-1} when the temperature is below $\sim$ 1400 K. From the perspective of the survivability of crystallized chondrules, shock waves with a spatial scale of $\sim 10^4$ km may be potent candidates for the chondrule formation mechanism. Based on our results from one-dimensional calculations, a fraction of compound chondrules can be reproduced when the chondrule-to-gas mass ratio in the pre-shock region is $\sim 2 \times 10^{-3}$, which is approximately half of the solar metallicity.

3.1 Introduction

Chondrules are millimeter-sized spherical igneous grains contained within chondrites, which are the most common type of meteorites, as a major component. The volume fraction of chondrules in ordinary chondrites is 60–80% (e.g., Rubin, 2000; Scott, 2007), and the ages of chondrules are approximately 4.563–4.567 billion years, i.e., they were formed during the first 4 million years of the solar system (e.g., Connelly et al., 2012; Bollard et al., 2017). Therefore, they must contain a wealth of information regarding the evolution of the solar nebula. In the canonical view, small dust grains in the solar nebula grew into millimeter-sized aggregates, after which chondrules were formed by the melting of these aggregates in the early solar nebula and became spherical owing to their surface tension (e.g., Zanda, 2004); however, their precise origin is still unclear.

Some chondrules, referred to as compound chondrules, are composed of two or more chondrules fused together. They comprise a low percentage of all chondrules (e.g., 4% in ordinary chondrites; Gooding and Keil, 1981); however, they may offer crucial information regarding the physical state of solid materials during chondrule formation because they occur not only in ordinary chondrites but also in many classes of chondrites (e.g., Akaki and Nakamura, 2005; Bischoff et al., 2017). Although the formation process of compound chondrules is still under debate, we can interpret the presence of compound chondrules as the result of collisions (e.g., Gooding and Keil, 1981; Ciesla et al., 2004b; Miura et al., 2008b; Bogdan et al., 2019). The ubiquitous existence of cratered chondrules (approximately 10% of all chondrules) also indicates that some of the chondrules have experienced collision when they crystallize (e.g., Gooding and Keil, 1981). Wasson et al. (1995) examined compound chondrules in thin sections and classified each constituent chondrule as primary or secondary. Primary chondrules retain their spherical shape, while secondary chondrules are deformed. Compound chondrules with blurred intrachondrule boundaries are extremely rare within ordinary chondrites (Wasson et al., 1995). Therefore, most compound chondrules are formed by collisions between crystallized chondrules and non-crystallized precursors (Arakawa and Nakamoto, 2016a), or at least two components with a significant viscosity difference to be able to distinguish primary and secondary chondrules (Yasuda et al., 2009).

Chondrules exhibit various textures, reflecting their different compositions and thermal histories (e.g., Gooding and Keil, 1981). In general, the textures of chondrules are classified into three textural types, that is, porphyritic, nonporphyritic, and glassy. Porphyritic chondrules consist of phenocrysts of olivine and/or low-calcium pyroxene, with accessory amounts of sulfides and metal nuggets suspended in mesostasis. Nonporphyritic chondrules are usually classified into three subtypes (e.g., Gooding and Keil, 1981): cryptocrystalline, composed of nanometer- and micrometer-sized fine grains; radial-pyroxene; and barred-olivine chondrules (barred-pyroxene and radial-olivine chondrules also exist but are minor components). Glassy chondrules are extremely rare, and they are only mentioned occasionally (e.g., Krot and Rubin, 1994). It is typically thought that nonporphyritic and glassy chondrules are formed from completely molten precursors, while porphyritic chondrules melt incompletely during their formation (e.g., Lofgren and Russell, 1986; Hewins and Radomsky, 1990), although porphyritic textures can also be reproduced from com-

pletely molten precursors (e.g., Connolly and Hewins, 1995; Srivastava et al., 2010).

Here, we note that the textures of chondrules contained in compound chondrules have noteworthy features. Gooding and Keil (1981) and Wasson et al. (1995) reported that approximately 15% of all chondrules in ordinary chondrites are nonporphyritic, and most of them have porphyritic textures. In contrast, when we observe the components in compound chondrules, most of the constituent chondrules are nonporphyritic (Wasson, 1993; Wasson et al., 1995). For the case of compound chondrules in ordinary chondrites, Wasson et al. (1995) revealed that 81% of primaries and 90% of secondaries are nonporphyritic chondrules, and the same trend is also reported by Akaki and Nakamura (2005) for compound chondrules in CV carbonaceous chondrites. Therefore, compound chondrules selectively form from precursors of nonporphyritic chondrules. Dynamic crystallization experiments (e.g., Tsukamoto et al., 1999; Nagashima et al., 2006, 2008) have revealed that completely molten levitated precursors having no contact turn into supercooled droplets as they are cooled sufficiently below their liquidus temperature. In addition, once these supercooled droplets collide with other particles, they crystallize instantaneously (e.g., Connolly et al., 1994). Therefore, when a crystallized chondrule and a supercooled precursor collide and stick together, a compound chondrule is formed (Arakawa and Nakamoto, 2016a). This supercooled-collision scenario is consistent with the observed feature of the textures of chondrules contained in compound chondrules because the precursors of nonporphyritic chondrules selectively turn into supercooled droplets.

Numerous ideas have been proposed as mechanisms for single-chondrule formation, including shock-wave heating (e.g., Hood and Horányi, 1991; Iida et al., 2001; Boley et al., 2013; Mai et al., 2018), planetesimal collisions (e.g., Asphaug et al., 2011; Dullemond et al., 2014; Johnson et al., 2015; Wakita et al., 2017), and radiative heating by lightning (e.g., Horányi et al., 1995; Desch and Cuzzi, 2000; Muranushi, 2010; Johansen and Okuzumi, 2018). The combination of theoretical calculations and observations of chondrules provides several constraints on the properties of the chondrule formation mechanisms. For example, the shapes of chondrules are usually close to perfect spheres, but some of them have prolate shapes (Tsuchiyama et al., 2003); these prolate shapes can be explained by the rotation of molten chondrules exposed to a fast gas flow in the framework of the shock-wave heating model (Miura et al., 2008a). The maximum and minimum sizes of chondrules are also consistent with the theoretical predictions of shock-wave heating models (e.g., Susa and Nakamoto, 2002; Miura and Nakamoto, 2005).

Shock-wave heating within the solar nebula is one of the leading candidates for the source of chondrule-forming transient events. Shock waves could be created by the eccentric planetesimals/protoplanets perturbed by Jovian resonances and the secular resonance caused by the gravity of the protoplanetary disk (e.g., Weidenschilling et al., 1998; Nagasawa et al., 2019) or by gravitational instabilities in the protoplanetary disk (e.g., Boss and Durisen, 2005; Boley and Durisen, 2008). The process of heating chondrule precursors by shock waves has been investigated in detail in many previous studies. The shock-wave heating model can satisfy various first-order constraints related to chondrule formation, such as the peak temperature and the formation age (e.g., Desch et al., 2012).

One important challenge for shock-wave heating models was noted by Nakamoto and Miura (2004) and Jacquet and Thompson (2014): chondrule precursors of different sizes have different velocities in the post-shock region, and they should collide at a high speed (approximately a few km s^{-1}), which may cause their destruction rather than compound chondrule formation upon collision. However, the critical velocity for collisional sticking/destruction may strongly depend on the physical states of colliding precursors, e.g., phase, temperature, and size ratio. For example, Ciesla (2006) argued that partially molten chondrules with highly viscous outer layers could survive high-speed collisions because energy dissipation in droplet collisions increases as the viscosity of the liquid is increased (e.g., Ennis et al., 1991; Willis and Orme, 2003). We note that the viscosity of silicate melts strongly depends on the temperature, and supercooled droplets must have significantly high viscosity (e.g., Fulcher, 1925); therefore, the collision of supercooled chondrule precursors in post-shock regions can potentially explain the formation of compound chondrules. In addition, for the case of optically thin shock waves, collisions of chondrule precursors mostly occur when they are in the supercooled state.

In this study, we examine the possibility of compound chondrule formation via optically thin shock waves. We evaluate whether compound chondrules can be formed via the collision of supercooled chondrule precursors in the framework of the shock-wave heating model by using semi-analytical methods and discuss whether most of the crystallized chondrules can avoid destruction upon collision in the post-shock region. The objectives of this study are to postulate how the supercooling of chondrule precursors could affect the outcomes of high-speed collisions and suggest a novel scenario for compound chondrule formation.

3.2 Models

3.2.1 Outline

Most of the previous studies on chondrule-forming shock-wave heating models assumed that the shock waves are optically thick and chondrules are thermally coupled with gas in post-shock regions (e.g., Morris and Desch, 2010); however, optically-thick shock waves have a critical issue in the context of compound chondrule formation. Chondrules in optically thick shock waves should maintain a high temperature above their liquidus in post-shock regions (e.g., Morris and Desch, 2010), and molten chondrules cannot avoid collisional destruction if they are in the molten state (e.g., Jacquet and Thompson, 2014). Therefore, in this study, we examine the scenario whereby compound chondrules are formed via optically thin shock waves. The prominent feature of the optically thin shock-wave model is its rapid cooling as a result of radiative cooling (e.g., Ciesla et al., 2004a).

The formation process of single and compound chondrules in an optically thin shock wave is illustrated in Figure 3.1. There are chondrule precursors and fine dust grains in the pre-shock region; the fine dust grains should evaporate immediately after passing the shock front, while the chondrule precursors are converted into molten droplets (e.g., Miura and Nakamoto, 2005). There are no fine dust grains immediately behind the shock front, and these evapo-

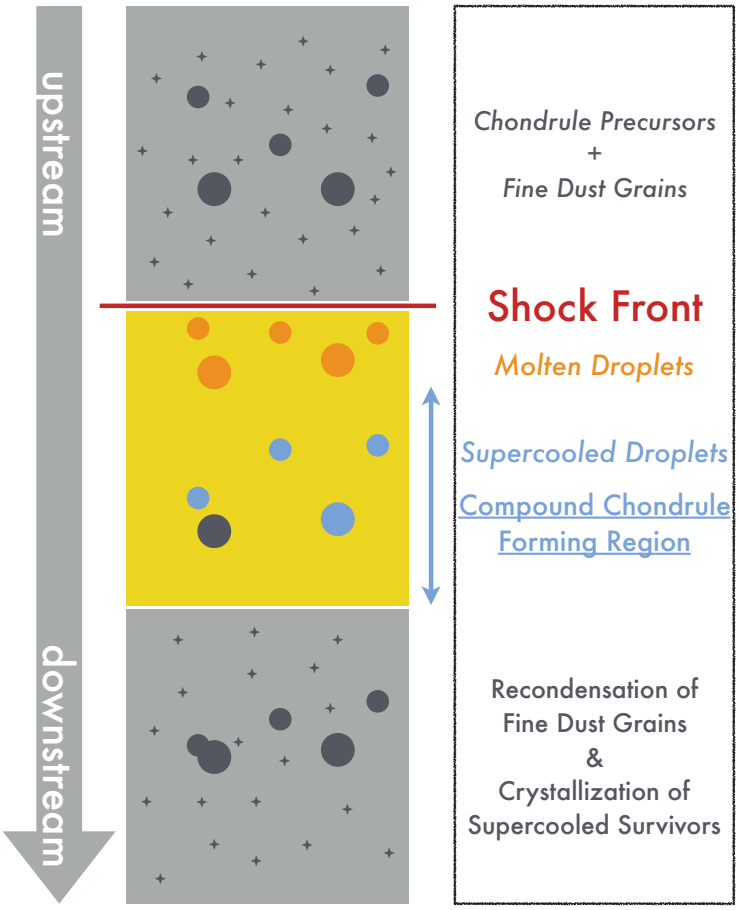

Figure 3.1: Outline of our compound chondrule formation scenario. Molten chondrule precursors formed via passage of the shock front immediately turn into supercooled droplets because of their radiative cooling. Then, some supercooled precursors experience collision and become crystallized chondrules, and if a crystallized chondrule and a supercooled precursor collide and stick together, a compound chondrule is formed.

rated dust grains recondense when the gas temperature drops below the dust condensation temperature T_c (in this study, we assume $T_c = 1600$ K). Molten precursors formed via the passage of the shock front quickly transform into supercooled droplets because of their radiative cooling, and the temperature of supercooled droplets is controlled by the balance between the energy transfer from hot gas molecules to cold droplets and the radiative cooling of droplets (see Equation 3.45). Although most of the precursors are in the supercooled state before the recondensation of fine dust grains, some precursors experience collision and become crystallized chondrules before the recondensation of fine dust grains. Moreover, if a crystallized chondrule and a supercooled precursor collide and stick together, a compound chondrule is formed (Arakawa and Nakamoto, 2016a). Finally, the gas temperature decreases and the recondensation of fine dust grains occurs downstream, after which supercooled survivors collide with fine dust grains and turn into crystallized chondrules.

3.2.2 Chondrule dynamics

In this study, we consider one-dimensional normal shocks, as in previous studies (e.g., Nakamoto and Miura, 2004; Ciesla, 2006; Jacquet and Thompson, 2014). We do not calculate the thermal/dynamical evolution of gas behind the shock front; we assume a simple gas structure, so that the dynamics of chondrules is simulated in the given gas flow. We assume that the gas velocity with respect to the shock front $v_{\rm g}$ and the gas density $\rho_{\rm g}$ change across the shock front as functions of the distance from the shock front x as follows:

$$v_{\rm g} = \begin{cases} v_0 & (x < 0), \\ v_0 + (v_{\rm post} - v_0) \exp(-x/L) & (x \geq 0), \end{cases} \tag{3.1}$$

and

$$\rho_{\rm g} = \begin{cases} \rho_{\rm g,0} & (x < 0), \\ (v_{\rm g}/v_0)^{-1} \rho_{\rm g,0} & (x \geq 0), \end{cases} \tag{3.2}$$

where v_0 is the pre-shock gas velocity with respect to the shock front, $v_{\rm post}$ is the post-shock gas velocity with respect to the shock front, $\rho_{\rm g,0}$ is the pre-shock gas density, and L is the spatial scale of the chondrule-forming shock. The post-shock gas velocity, $v_{\rm post}$, is given by the Rankine–Hugoniot relations as $v_{\rm post} = [(\gamma - 1)/(\gamma + 1)]v_0$, where γ is the ratio of specific heats. In this study, we set $\rho_{\rm g,0} = 3 \times 10^{-9}$ g cm^{-3}, $v_0 = 12$ km s^{-1}, and $\gamma = 1.4$. Similarly, the temperature of the gas $T_{\rm g}$ is assumed as follows:

$$T_{\rm g} = \begin{cases} T_0 & (x < 0), \\ T_0 + (T_{\rm post} - T_0) \exp(-x/L) & (x \geq 0), \end{cases} \tag{3.3}$$

and we assume that the pre-shock gas temperature is $T_0 = 500$ K and the post-shock gas temperature is $T_{\rm post} = 2000$ K. The sound velocity $c_{\rm s}$ is given by $c_{\rm s} \equiv (2k_{\rm B}T_{\rm g}/m_{\rm g})^{1/2}$, where $k_{\rm B} = 1.38 \times 10^{-16}$ erg K^{-1} is the Boltzmann constant, and we set the gas molecule mass $m_{\rm g} = 3.34 \times 10^{-24}$ g, which values correspond to H_2 gas.

The velocity of chondrules with respect to the shock front, v, will change as a function of the distance from the shock front x (e.g., Hood and Horányi, 1991):

$$\frac{4\pi}{3} r^3 \rho \frac{{\rm d}v}{{\rm d}x} = -\frac{C_{\rm D}}{2} \pi r^2 \rho_{\rm g} \frac{|v - v_{\rm g}|}{v} (v - v_{\rm g}), \tag{3.4}$$

where $C_{\rm D}$ is the drag coefficient, r is the chondrule radius, and $\rho = 3.3$ g cm^{-3} is the internal density of chondrules (Ciesla et al., 2004a). The drag coefficient $C_{\rm D}$ is given by

$$C_{\rm D} = \frac{2}{3s} \sqrt{\frac{\pi T}{T_{\rm g}}} + \frac{2s^2 + 1}{\sqrt{\pi} s^3} \exp(-s^2) + \frac{4s^4 + 4s^2 - 1}{2s^4} {\rm erf}(s), \tag{3.5}$$

where the temperature of the chondrule is T, and s is given by $s \equiv |v - v_{\rm g}|/c_{\rm s}$. The drag coefficient $C_{\rm D}$ is a function of the normalized relative velocity s, and we note that $C_{\rm D}$ approaches

$$C_{\rm D} \simeq 2, \tag{3.6}$$

for the supersonic limit (i.e., $s \gg 1$) and

$$C_{\rm D} \simeq \frac{16\sqrt{\pi}}{3s}\left(\sqrt{\frac{T}{T_{\rm g}}}+\frac{1}{8\pi}\right), \tag{3.7}$$

for the subsonic limit (i.e., $s \ll 1$). We can understand the dynamics of chondrules by considering the stopping length $l_{\rm stop}$. For the case in which chondrules move in gas with supersonic velocities, $l_{\rm stop}$ is approximately given by

$$\begin{aligned} l_{\rm stop} &\equiv \left(\frac{1}{v}\frac{{\rm d}v}{{\rm d}x}\right)^{-1} \\ &\simeq \frac{4}{3}\frac{\rho}{\rho_{\rm g}}\left(\frac{v-v_{\rm g}}{v}\right)^{-2} r \\ &\sim 2\times10^2\left(\frac{v}{v-v_{\rm g}}\right)^2\left(\frac{r}{1\ {\rm mm}}\right)\left(\frac{\rho_{\rm g}}{2\times10^{-8}\ {\rm g\ cm^{-3}}}\right)^{-1}\ {\rm km}. \end{aligned} \tag{3.8}$$

If the spatial scale of shock L is much larger than $l_{\rm stop}$, the velocity of a chondrule v reaches $v_{\rm post}$ behind the shock front, while v barely changes when $L \ll l_{\rm stop}$ (see Figure 3.3b).

The equation of energy for a chondrule in gas is given by (e.g., Hood and Horányi, 1991)

$$\frac{4\pi}{3}r^3\rho c_{\rm heat}\frac{{\rm d}T}{{\rm d}x} = \frac{4\pi r^2}{v}(\Gamma-\Lambda), \tag{3.9}$$

where $c_{\rm heat} = 1\times10^7$ erg g^{-1} K^{-1} is the specific heat (Ciesla et al., 2004a), Γ is the heating rate via gas–chondrule energy transfer per unit area, and Λ is the rate of radiative cooling per unit area. In this study, the effects of latent heat and evaporation (e.g., Miura et al., 2002) are not considered for simplicity. The heating rate via gas–chondrule energy transfer Γ is

$$\Gamma = \rho_{\rm g}|v-v_{\rm g}|(T_{\rm rec}-T)C_{\rm H}, \tag{3.10}$$

where $T_{\rm rec}$ is the adiabatic recovery temperature and $C_{\rm H}$ is the heat transfer function, called the Stanton number. The adiabatic recovery temperature $T_{\rm rec}$ and the Stanton number $C_{\rm H}$ are given by (e.g., Gombosi et al., 1986)

$$\begin{aligned} T_{\rm rec} &= \frac{T_{\rm g}}{\gamma+1}\left[2\gamma+2(\gamma-1)s^2\right. \\ &\quad \left.-\frac{\gamma-1}{(1/2)+s^2+(s/\sqrt{\pi})\exp\left(-s^2\right){\rm erf}^{-1}(s)}\right], \end{aligned} \tag{3.11}$$

and

$$C_{\rm H} = \frac{\gamma+1}{\gamma-1}\frac{k_{\rm B}}{8m_{\rm g}s^2}\left[\frac{s}{\sqrt{\pi}}\exp\left(-s^2\right)+\left(\frac{1}{2}+s^2\right){\rm erf}(s)\right]. \tag{3.12}$$

We assume that the optical depth of the chondrule-forming region is not far larger than unity and chondrules are thermally decoupled from the gas. Here, we check the validity of this assumption. We define $\mathcal{R}_{\rm w}$ as the width of the warm region (i.e., the region with a gas temperature of $T_{\rm g} \gg T_0$), and the

width of the heating region whose optical depth is unity, $\mathcal{R}_{w,1}$, can be estimated as follows:

$$\mathcal{R}_{w,1} = \left(\kappa\rho_g\right)^{-1} \sim 10^3 \left(\frac{\rho_g}{3\times10^{-9}\ \mathrm{g\ cm^{-3}}}\right)^{-1} \mathrm{km}, \tag{3.13}$$

where $\kappa \sim 3\ \mathrm{cm^2\ g^{-1}}$ is the opacity of the solar-metallicity protoplanetary disk (e.g., Pollack et al., 1985). Therefore, if the width of the heating region $\mathcal{R}_w$ is not larger than $\mathcal{R}_{w,1}$, and we do not consider significant enrichment of fine dust grains in the solar nebula, we can apply the optically thin approximation for chondrule-forming shock waves. The width of the heating region $\mathcal{R}_w$ is roughly given by the planetary radius $\mathcal{R}_p$ when the shock waves are caused by eccentric planetary bodies (e.g., Boley et al., 2013). Under the optically thin shock assumption, the rate of radiative cooling per unit area of a chondrule Λ is given by

$$\Lambda = \epsilon\sigma_{SB}T^4 - \epsilon\sigma_{SB}T_0^4, \tag{3.14}$$

where $\epsilon = 0.9$ is the Planck mean emission/absorption coefficient (Ciesla et al., 2004a) and $\sigma_{SB} = 5.67\times10^{-5}\ \mathrm{erg\ cm^{-2}\ K^{-4}\ s^{-1}}$ is the Stefan-Boltzmann constant.

3.2.3 Size-frequency distribution

Several studies (e.g., Rubin and Grossman, 1987; Nelson and Rubin, 2002; Metzler, 2018) have focused on chondrule size-frequency distributions. The size-frequency distributions of chondrules usually use $\varnothing$-units, which are defined by,

$$\varnothing \equiv -\log_2 \frac{2r}{1\ \mathrm{mm}}, \tag{3.15}$$

or we can rewrite the above equation as $r = 2^{-(\varnothing+1)}$ mm. The mass of chondrules $m(\varnothing)$ is given by $m(\varnothing) = (4\pi/3)\rho r^3$.

Here, we assume that the size-frequency distribution in the pre-shock region $f_0(\varnothing)$ is similar to the size-frequency distribution in chondrites (Jacquet, 2014); although Kadono and Arakawa (2005) proposed that the size-frequency distribution may originate from the breakup of huge molten precursors. The size-frequency distribution of chondrules in ordinary chondrites is approximately log-normal (e.g., Rubin and Grossman, 1987; Nelson and Rubin, 2002),

$$f_0(\varnothing) \propto \exp\left[-\frac{1}{2}\left(\frac{\varnothing - \varnothing_{mean}}{\varnothing_{SD}}\right)^2\right]; \tag{3.16}$$

although, in reality, it is known that there is a cutoff for small chondrule sizes (e.g., Eisenhour, 1996; Metzler, 2018). In this study, we assume $\varnothing_{mean} = 0.8$ and $\varnothing_{SD} = 0.8$, which are the mean and deviation for chondrules in LL ordinary chondrites (Nelson and Rubin, 2002). The total number density of chondrules in pre-shock region N_0 is given by

$$N_0 = \frac{\rho_{c,0}}{\int_{\varnothing_{min}}^{\varnothing_{max}} \mathrm{d}\varnothing\ f_0(\varnothing)m(\varnothing)}, \tag{3.17}$$

where $\rho_{c,0}$ is the mass density of chondrules in the pre-shock region, and $\varnothing_{min}$ and $\varnothing_{max}$ are the minimum and maximum of $\varnothing$ in the size-frequency distribution, respectively (in this study, we set $\varnothing_{min} = -3$ and $\varnothing_{max} = +3$). The size-frequency distribution in the pre-shock region satisfies $\int_{\varnothing_{min}}^{\varnothing_{max}} d\varnothing\ f_0 = 1$ by definition. The number density of chondrules whose size is $\varnothing$, $n_0(\varnothing)$, is also given by

$$n_0(\varnothing) = f_0(\varnothing) N_0. \tag{3.18}$$

The number density of chondrules in the post-shock region, $n(\varnothing, x)$, changes with changing chondrule velocity $v = v(\varnothing, x)$. Under the one-dimensional normal shock approximation, $n(\varnothing, x)$ is given as follows:

$$n(\varnothing, x) = n_0(\varnothing) \frac{v_0}{v(\varnothing, x)}. \tag{3.19}$$

Using the geometrical optics approximation, the mean opacity of chondrules, κ_c, is given by

$$\kappa_c = \frac{\int_{\varnothing_{min}}^{\varnothing_{max}} d\varnothing\ n(\varnothing, x) \pi r^2}{\int_{\varnothing_{min}}^{\varnothing_{max}} d\varnothing\ n(\varnothing, x) m}, \tag{3.20}$$

and κ_c in the pre-shock region is $\kappa_{c,0} = 3.67\ \mathrm{cm^2\ g^{-1}}$. We found that κ_c is dominated by 0.5 mm-sized chondrules in the pre-shock region. When we take into account the contribution of κ_c, the optical depth of the heating region, τ, is evaluated from

$$\tau = \left(\kappa \rho_g + \kappa_c \rho_c\right) \mathcal{R}_w, \tag{3.21}$$

the latter term, $\kappa_c \rho_c$, is negligibly smaller than the former term, $\kappa \rho_g$, however.

3.2.4 Collision frequency

Here, we describe how to calculate the collision frequency of chondrules. We define $\zeta_{t,p}$ as the collision frequency per unit distance of a target chondrule, whose size is $\varnothing_t$, with a projectile chondrule, whose size is $\varnothing_p$. Then, $\zeta_{t,p}$ is given as follows:

$$\zeta_{t,p}(\varnothing_t, \varnothing_p, x) = n(\varnothing_p, x) \cdot \pi (r_t + r_p)^2 \frac{|v(\varnothing_p, x) - v(\varnothing_t, x)|}{v(\varnothing_t, x)}. \tag{3.22}$$

The collision frequency of a target chondrule with any projectile, Z_t, is therefore given by

$$Z_t(\varnothing_t, x) = \int_{\varnothing_{min}}^{\varnothing_{max}} d\varnothing_p\ \zeta_{t,p}(\varnothing_t, \varnothing_p, x). \tag{3.23}$$

Finally, the expected number of collisions for each target chondrule after passing the shock front, Σ_t, is given by

$$\Sigma_t(\varnothing_t, x) = \int_0^x dx'\ Z_t(\varnothing_t, x'). \tag{3.24}$$

Here, we note that the fraction of compound chondrules among all the non-porphyritic chondrules in ordinary chondrites is approximately 20% (Ciesla

et al., 2004b; Arakawa and Nakamoto, 2016a). Therefore, the expected number of collisions Σ_t should be on the order of 20% for small chondrules whose radii are comparable to that of typical secondaries, and Σ_t may be $\sim$ 1–2 for large chondrules whose radii are comparable to that of typical primaries because primaries have experienced collisions twice (see Section 3.2.1 and Arakawa and Nakamoto, 2016a).

3.2.5 Critical velocity for collisional sticking/merging

When a droplet collides with a solid sphere, the expected collision outcomes are sticking, bouncing, or splashing (e.g., Josserand and Thoroddsen, 2016). Similarly, when two droplets collide, the collision outcomes are merging, bouncing/separation, or splashing (e.g., Qian and Law, 1997). Bouncing usually occurs for grazing collisions. In this study, we examine the critical velocity for compound chondrule formation from the view point of whether supercooled droplets can stick or not. For the description of droplet collisions, it is necessary to consider the physical properties involved: viscosity η, density ρ, and surface tension σ, as well as geometrical properties of the system such as droplet radius r and the impact velocity $v_{\rm imp}$.

Dimensionless parameters for describing droplet collisions

Using dimensional analysis, we can easily identify the relevant dimensionless parameters to describe binary collisions of liquid droplets (e.g., Ashgriz and Poo, 1990). For the case of head-on collision of equal-sized droplets with identical liquids, the basic parameters are the Weber number We, the Reynolds number Re, and the capillary number Ca:

$$\mathrm{We} \equiv \frac{2\rho r {v_{\rm imp}}^2}{\sigma}, \tag{3.25}$$

$$\mathrm{Re} \equiv \frac{2\rho r v_{\rm imp}}{\eta}, \tag{3.26}$$

$$\mathrm{Ca} \equiv \frac{\eta v_{\rm imp}}{\sigma} \equiv \frac{\mathrm{We}}{\mathrm{Re}}. \tag{3.27}$$

For the inviscid fluid limit (i.e., Ca $\ll$ 1), the criteria for collisional sticking should be given by the critical value of the Weber number $\mathrm{We}_{\rm cr,i}$;

$$\mathrm{We} < \mathrm{We}_{\rm cr,i}, \tag{3.28}$$

and, for the viscous fluid limit (i.e., Ca $\gg$ 1), the criteria should be given by the critical value of the Reynolds number $\mathrm{Re}_{\rm cr,v}$;

$$\mathrm{Re} < \mathrm{Re}_{\rm cr,v}. \tag{3.29}$$

This expression can be converted into the expression of the critical Weber number by using the capillary number as follows:

$$\mathrm{We} < \mathrm{Re}_{\rm cr,v}\mathrm{Ca}. \tag{3.30}$$

Therefore, we can imagine that the critical Weber number for collisional sticking, $\mathrm{We}_{\rm cr}$, can be given by the following equation:

$$\mathrm{We}_{\rm cr} \simeq \mathrm{Re}_{\rm cr,v}\mathrm{Ca} + \mathrm{We}_{\rm cr,i}. \tag{3.31}$$

Criteria proposed by Sommerfeld and Kuschel (2016)

Droplets are affected by large deformation and energy dissipation when they collide; therefore, it is logical to use Ca, which is the ratio of viscous forces to surface tension forces, for the expression of $\mathrm{We_{cr}}$. Recently, Sommerfeld and Kuschel (2016) proposed an equation for $\mathrm{We_{cr}}$ as follows:

$$\mathrm{We_{cr}} = \frac{K^3}{3}\mathrm{Ca} + 2K, \tag{3.32}$$

where $K = 6.9451$ is called the structure parameter (Naue and Bärwolff, 1992), and we obtain $\mathrm{We_{cr}} = 111.66\mathrm{Ca} + 13.89$ (see Appendix 3.A).

From Equation (3.32), we can calculate the critical velocity for head-on collision of equal-sized droplets v_{cr} as follows:

$$v_{\mathrm{cr}}(\eta, r) = \frac{K^3}{12}\frac{\eta}{\rho r}\left(1 + \sqrt{1 + \frac{144}{K^5}\frac{\rho\sigma r}{\eta^2}}\right), \tag{3.33}$$

and when v_{cr} are controlled by viscous dissipation, these critical velocities are given by $v_{\mathrm{cr}} \sim 55.8\eta/(\rho r)$. In this case, the critical velocities are proportional to the viscosity and inversely proportional to the droplet radius.

For the case of collisions of different-sized droplets with different viscosities, the critical velocity for collisional merging v_{merge} is not yet understood (Li et al., 2016). In this study, we evaluate v_{merge} from the geometric mean of v_{cr} of the target and projectile:

$$v_{\mathrm{merge}} = \sqrt{v_{\mathrm{cr}}(\eta_{\mathrm{t}}, r_{\mathrm{t}}) \cdot v_{\mathrm{cr}}(\eta_{\mathrm{p}}, r_{\mathrm{p}})}, \tag{3.34}$$

where η_{t} and η_{p} are the viscosities of the target and projectile, respectively. Likewise, when a non-crystallized projectile collides with a solidified target chondrule, we evaluate the critical velocity for collisional sticking v_{stick} from v_{cr} of the projectile (see Appendix 3.B):

$$v_{\mathrm{stick}} = v_{\mathrm{cr}}(\eta_{\mathrm{p}}, r_{\mathrm{p}}). \tag{3.35}$$

The colliding supercooled droplets can turn into compound chondrules when the impact velocity v_{imp} is lower than v_{stick}. We note that our evaluation of v_{merge} and v_{stick} is not more than a rough order-of-magnitude estimate, and future studies on this issue are needed.

To determine the critical velocity for collisional sticking/merging, we need to know the material properties of silicate melts, η and σ. Hubbard (2015) calculated the viscosities of chondrule melts by using the formula of Giordano et al. (2008) which is based on the Vogel–Fulcher–Tammann viscosity equation (Vogel, 1921; Fulcher, 1925; Tammann and Hesse, 1926);

$$\log_{10}\frac{\eta}{1\ \mathrm{P}} = -3.55 + \frac{5084.9\ \mathrm{K}}{T - 584.9\ \mathrm{K}}. \tag{3.36}$$

In contrast, the surface energy is only slightly dependent on the temperature, and we set $\sigma = 400\ \mathrm{erg\ cm^{-2}}$ (Murase and McBirney, 1973).

The calculated v_{cr} is shown in Figure 3.2. There is a strong dependence of v_{cr} on T, and we found that supercooled chondrule precursors could survive high-speed collisions on the order of 1 km $\mathrm{s^{-1}}$ when the temperature is below 1400 K.

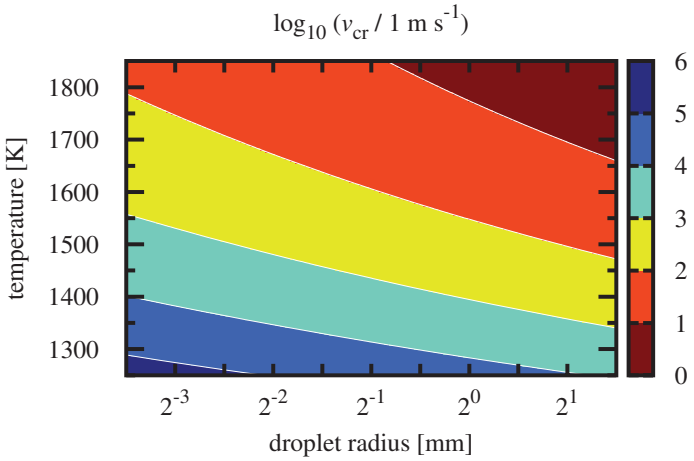

Figure 3.2: The critical velocity $v_{\rm cr}$ as a function of the radius of colliding droplets r and their temperature T. The viscosity of chondrule droplets is obtained from Equation (3.36).

Temperature increase after collision

When a droplet collides and sticks with another chondrule, the kinetic energy of the droplet is converted into thermal energy. The impact energy $E_{\rm imp}$ and the thermal energy $E_{\rm th}$ are given by

$$E_{\rm imp} = \frac{1}{2}\frac{m_{\rm t}m_{\rm p}}{m_{\rm t}+m_{\rm p}}{v_{\rm imp}}^2, \tag{3.37}$$

and

$$E_{\rm th} = m_{\rm p}\rho c_{\rm heat}\Delta T, \tag{3.38}$$

where $m_{\rm t}$ and $m_{\rm p}$ are the masses of the target and the projectile, respectively. By assuming $E_{\rm th} \simeq E_{\rm imp}$, the increase in the droplet temperature ΔT is estimated as follows:

$$\Delta T \sim 1.5\times10^2\left(1+\frac{m_{\rm p}}{m_{\rm t}}\right)^{-1}\left(\frac{v_{\rm imp}}{1\ {\rm km\ s^{-1}}}\right)^2 {\rm K}. \tag{3.39}$$

This order estimation implies that, when the impact velocity $v_{\rm imp}$ is far larger than a few km s^{-1} and the projectile-to-target mass ratio $m_{\rm p}/m_{\rm t}$ is lower than unity, the colliding supercooled droplet would evaporate after collision rather than turn into a compound chondrule because the increase in the droplet temperature would be $\Delta T \gtrsim 1000$ K (although we should consider the effect of the latent heat in reality). Conversely, the effect of ΔT is negligible when $v_{\rm imp} \ll 1$ km s^{-1} or $m_{\rm p}/m_{\rm t} \gg 1$. Hence we do not consider an increase in temperature after collision for simplicity.

3.2.6 Catastrophic disruption criteria

It is known that fragments of chondrules are common in chondrites (Nelson and Rubin, 2002), and fragmentation could have occurred in the solar nebula;

for example, chondrule fragments within enveloping compound chondrules are fragmented in the solar nebula (Wasson et al., 1995). After the crystallization of chondrule precursors, the disruption of chondrules could occur in the post-shock region via high-speed collisions. The catastrophic disruption criteria is $E_{\rm imp} \leq (m_{\rm t} + m_{\rm p}) Q^*_{\rm RD}$, and the critical specific energy for catastrophic disruption $Q^*_{\rm RD}$ is given by (Stewart and Leinhardt, 2009)

$$Q^*_{\rm RD} = q_{\rm s} \left(\frac{r_{\rm C1}}{1 \ {\rm cm}} \right)^{9\mu/(3-2\varphi)} \left(\frac{v_{\rm imp}}{1 \ {\rm cm \ s^{-1}}} \right)^{2-3\mu} {\rm erg \ g^{-1}}, \tag{3.40}$$

where $q_{\rm s}$, μ, and φ are dimensionless material properties, and the normalized radius $r_{\rm C1}$ is given as follows:

$$r_{\rm C1} = \left(\frac{3}{4\pi} \frac{m_{\rm t} + m_{\rm p}}{1 \ {\rm g \ cm^{-3}}} \right)^{1/3}. \tag{3.41}$$

For intact rocks such as basalt and granite, Stewart and Leinhardt (2009) reported that the dimensionless material properties of $q_{\rm s} = 7 \times 10^4$, $\mu = 0.5$, and $\varphi = 8$ provide a reasonable fit for the experimental data. Therefore the critical velocity for catastrophic disruption, $v_{\rm disrupt}$, is given as follows:

$$\begin{aligned} v_{\rm disrupt} &= 5.12 \times 10^3 \left(\frac{m_{\rm t}}{m_{\rm p}} \right)^{2/3} \left(1 + \frac{m_{\rm p}}{m_{\rm t}} \right)^{49/39} \\ &\cdot \left(\frac{m_{\rm t}}{10^{-3} \ {\rm g}} \right)^{-1/13} {\rm cm \ s^{-1}}. \end{aligned} \tag{3.42}$$

Collisional disruption experiments with chondrules in Allende CV3 chondrite have been performed by Ueda et al. (2001), and they revealed that the catastrophic disruption criteria for similar-sized chondrules is approximately 1.5×10^4 cm s^{-1}. This experimental result validates our evaluation of $v_{\rm disrupt}$.

3.3 Results

3.3.1 Chondrule dynamics and thermal history

We first show the chondrule dynamics and thermal history in optically thin shock waves. Here, we consider small and large shock waves whose spatial scales are $L = 100$ km and $L = 10000$ km, respectively. Figure 3.3 shows the velocity of chondrules with respect to the shock front v and gas velocity $v_{\rm g}$. Figure 3.3a clearly shows that v does not approach $v_{\rm post}$ ($= 2$ km s^{-1}) for the small-scale shock wave. In contrast, for the large-scale shock wave (Figure 3.3b), v approaches $v_{\rm post}$ in the post-shock region. This is because the stopping length of chondrules $l_{\rm stop}$ is significantly smaller than the spatial scale L (see Equation 3.8). For the case of Figure 3.3b, both v and $v_{\rm g}$ change simultaneously when the distance from the shock front x is larger than 1000 km. We derive an analytical equation of the chondrule-to-gas relative velocity, $v - v_{\rm g}$, in Section 3.3.5.

Figure 3.4 is the temperature of chondrules T and the gas temperature $T_{\rm g}$. The gray vertical line represents the recondensation line of evaporated fine

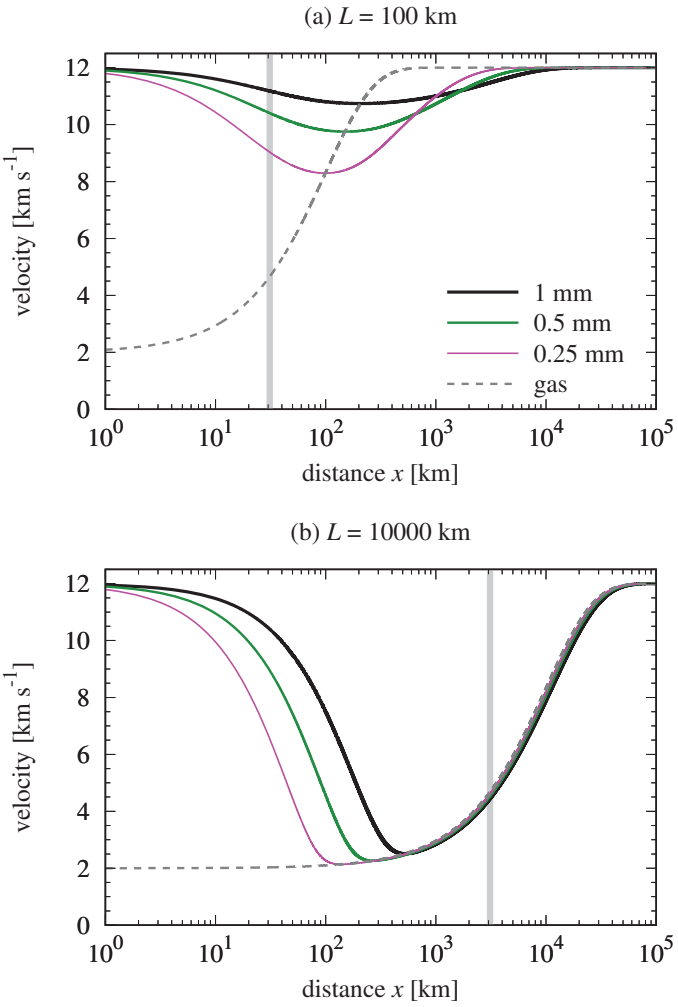

Figure 3.3: The velocity of chondrules with respect to the shock front v and the gas velocity v_g. (a) For the case of the small-scale shock wave ($L = 100$ km). (b) For the case of the large-scale shock wave ($L = 10000$ km). The solid curves represent the velocity of chondrules with radii of $r = 1$ mm (black), $r = 0.5$ mm (green), and $r = 0.25$ mm (magenta), and the gray dashed curve is the gas velocity. The gray vertical line represents the recondensation line of evaporated fine dust grains.

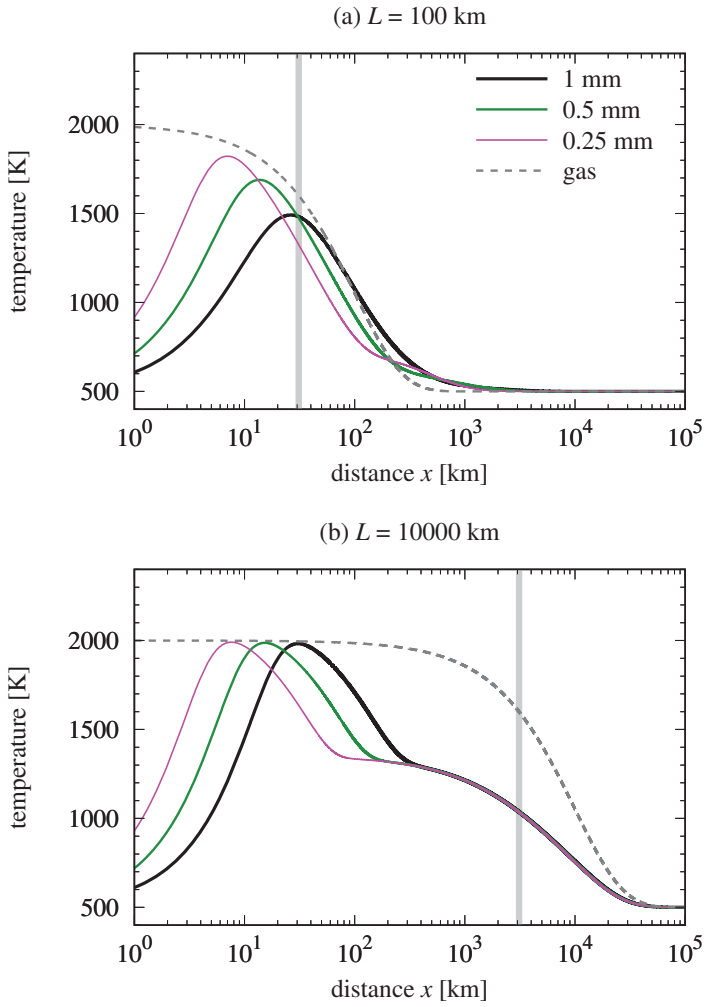

Figure 3.4: The temperature of chondrules T and the gas temperature $T_{\rm g}$. (a) For the case of the small-scale shock wave ($L = 100$ km). (b) For the case of the large-scale shock wave ($L = 10000$ km). The solid curves represent the temperature of chondrules with radii of $r = 1$ mm (black), $r = 0.5$ mm (green), and $r = 0.25$ mm (magenta), and the gray dashed curve is the gas temperature. The gray vertical line represents the recondensation line of evaporated fine dust grains.

dust grains (i.e., the location where the gas temperature is $T_g = T_c$). In this study, we set the condensation temperature to $T_c = 1600$ K.

The liquidus temperature of chondrules is in the range of 1600–2100 K (e.g., Cohen et al., 2000), and the solidus temperature is approximately 1400 K (e.g., Sanders and Scott, 2012), although these temperatures depend on the composition of chondrules and the ambient pressure. When the peak temperature of a chondrule is higher than the solidus temperature but lower than the liquidus temperature, the chondrule turns into a partially molten droplet. In contrast, when the peak temperature is higher than the liquidus temperature, the chondrule becomes a completely molten droplet. For the case of small-scale shock waves (Figure 3.4a), most of the small chondrules with radii of $r < 0.25$ mm turn into completely molten precursors, while almost all large chondrules with radii of $r > 0.5$ mm become partially molten droplets.

Several experimental studies have revealed that completely molten precursors turn into supercooled droplets and finally become glassy chondrules unless they collide with other particles (e.g., Nagashima et al., 2008). However, the observations of chondrules in a thin section revealed that glassy chondrules are extremely rare (e.g., Krot and Rubin, 1994). This fact indicates that the recondensation of evaporated fine dust grains must occur before the temperature of supercooled precursors drops below the glass transition temperature $T_{\rm glass}$. The glass transition temperature is dependent on the chemical composition, but it may be approximately $T_{\rm glass} \sim 900$–1000 K (e.g., Villeneuve et al., 2015). Figure 3.4a shows that the recondensation of evaporated fine dust grains occurs before the temperature of supercooled precursors drops below the glass transition point; therefore, they can turn into crystallized chondrules without a glass transition.

The heating/cooling history of chondrules in the large-scale shock wave is shown in Figure 3.4b. As in Figure 3.4a, recondensation of evaporated fine dust grains occurs before the temperature of supercooled precursors drops below the glass transition temperature, and these supercooled precursors can avoid turning into glassy chondrules. The peak temperature of chondrules only slightly depends on their radii for the case of large-scale shock waves, and they can maintain the supercooling state for a long time.

3.3.2 Equilibrium temperature of chondrules

After the chondrule-to-gas relative velocity reaches zero (i.e., $s \to 0$), the temperature of chondrules in high-temperature gas can be calculated from the balance of the heating via collisions of high-temperature gas molecules and the radiative cooling of chondrules. The heating term is given by

$$\Gamma = \frac{1}{8\sqrt{\pi}} \frac{\gamma + 1}{\gamma - 1} \rho_g c_s^3 \left(1 - \frac{T}{T_g} \right) \equiv \Gamma_g \left(1 - \frac{T}{T_g} \right), \tag{3.43}$$

and the cooling term is

$$\Lambda = \epsilon \sigma_{\rm SB} \left(T^4 - T_0^4 \right) = \Lambda_g \left[\left(\frac{T}{T_g} \right)^4 - \left(\frac{T_0}{T_g} \right)^4 \right], \tag{3.44}$$

where $\Lambda_g \equiv \epsilon\sigma_{SB}T_g^4$. Then, we obtain the equilibrium value of T by solving the equation, $\Gamma - \Lambda = 0$, and we can rewrite this equation as follows:

$$\frac{(T/T_g)^4 - (T_0/T_g)^4}{1 - T/T_g} = \frac{\Gamma_g}{\Lambda_g}. \tag{3.45}$$

We find that there are two limiting cases; one case is that $T/T_g \to 1$ and $\Gamma_g/\Lambda_g \to \infty$, and the other case is that $T/T_g \to T_0/T_g$ and $\Gamma_g/\Lambda_g \to 0$. The dimensionless parameter Γ_g/Λ_g is given by

$$\frac{\Gamma_g}{\Lambda_g} = 0.696\left(\frac{\rho_g}{2\times10^{-8}\ \mathrm{g\ cm^{-3}}}\right)\left(\frac{T_g}{2000\ \mathrm{K}}\right)^{-5/2}. \tag{3.46}$$

Then, we can calculate the equilibrium temperature of chondrules in high-temperature gas as a function of the gas density and the gas temperature, ρ_g and T_g. Figure 3.5 shows that completely molten droplets turn into supercooled droplets with a temperature of 900 K $< T <$ 1400 K when the gas density in the post-shock region is on the order of $\rho_g \sim 10^{-8}$ g cm^{-3}, where $T_{glass} \simeq 900$ K is the glass transition temperature and $T \lesssim 1400$ K is the condition for surviving high-speed collisions (Section 3.2.5). Therefore, the preferred value of the gas density in the pre-shock region, $\rho_{g,0}$, is on the order of 10^{-9}–10^{-8} g cm^{-3} because the gas density increases after the passage of the shock front. We note, however, that the lower limit of ρ_g to maintain the supercooling of chondrule precursors is also dependent on the background temperature (in this study, we simply assume that the background temperature is the same as the pre-shock gas temperature, $T_0 = 500$ K). In addition, the effective background temperature may be affected by the optical depth of the chondrule-forming region when the optical depth is close to unity. We will study the three-dimensional (or axisymmetric two-dimensional) radiative hydrodynamics of planetary bow shocks in the future.

3.3.3 Collision frequency

In Section 3.3.1, we calculated the velocity evolution of chondrules in the post-shock region. The velocity depends on the radius of chondrules, and collision of chondrules occurs towing to the difference in the velocity. Then, we can calculate the collision frequency of chondrules.

Figure 3.6 shows the collision frequency of a target chondrule with any projectiles, Z_t, and Figure 3.7 shows the expected number of collisions for each target chondrule after passing the shock front, Σ_t. Here, we assumed that the chondrule mass density in the pre-shock region is $\rho_{c,0} = 6\times10^{-12}$ g cm^{-3}. The chondrule-to-gas mass ratio in the pre-shock region is therefore $\rho_{c,0}/\rho_{g,0} = 2\times10^{-3}$, and this value is approximately half of the well-assumed silicate-to-gas mass ratio ($= 4.3\times10^{-3}$; Miyake and Nakagawa, 1993). We can imagine that part of the silicate dust may exist as fine dust grains and others exist as chondrules and/or large dust aggregates. Therefore, our estimate of $\rho_{c,0}/\rho_{g,0} = 2\times10^{-3}$ is reasonable to some extent.

As shown in Figures 3.6 and 3.7, the collision of chondrules occurs in two stages; the first stage corresponds to where the velocity of chondrules approaches the gas velocity and larger chondrules have larger values of v, and

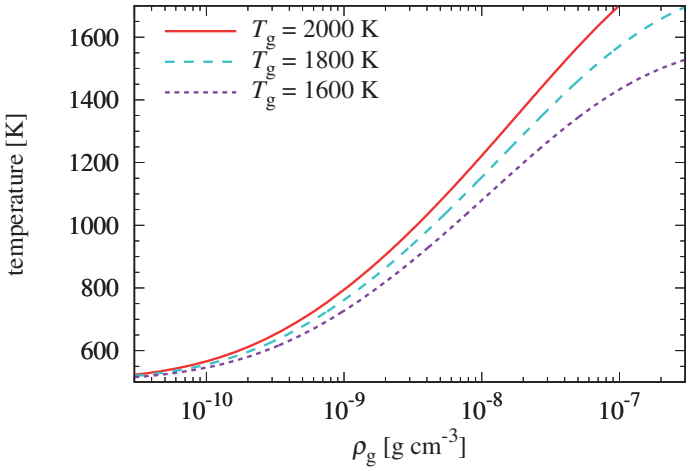

Figure 3.5: The temperature of chondrule precursors T as a function of the gas density and the gas temperature, ρ_g and T_g, under the assumption of $v - v_g = 0$. The temperature of chondrule precursors is calculated from Equation (3.45) and we set $T_0 = 500$ K.

the second stage corresponds to where the velocity of chondrules recover to the pre-shock velocity and smaller chondrules have larger values of v. The frequency of collision depends on the spatial scale L if L is comparable to or smaller than the stopping length of chondrules, i.e., $L \lesssim l_{\rm stop}$. This fact has been previously mentioned by Jacquet and Thompson (2014), and Z_t and Σ_t are small for small-scale shock waves compared with the case of large-scale shock waves.

The expected number of collisions for submillimeter-sized chondrules is lower than unity when we assume $\rho_{c,0}/\rho_{g,0} = 2 \times 10^{-3}$; therefore, most of the chondrule precursors that are heated above their liquidus temperature turn into supercooled droplets and can keep their supercooling state until the recondensation of fine dust grains occurs (see Figure 3.7). Conversely, millimeter-sized large chondrules collide frequently, and for the case of large-scale shock waves, most of the millimeter-sized chondrules experience collision when $\rho_{c,0}/\rho_{g,0} \gtrsim 2 \times 10^{-3}$. After a collision, the supercooled droplet turns into a crystallized chondrule when the collision velocity is below $v_{\rm merge}$, and some of these chondrules have experienced multiple collisions; this is the mechanism of compound chondrule formation (see Figure 2 of Arakawa and Nakamoto, 2016a). We note that the number of collisions Σ_t is proportional to $\rho_{c,0}/\rho_{g,0}$; then, Σ_t for submillimeter-sized chondrules could also exceed unity when $\rho_{c,0}/\rho_{g,0} \gtrsim 10^{-2}$.

Figure 3.8 shows the collision frequency of a target chondrule whose size is $r_t = 0.25$ mm with projectile chondrules whose size is r_p. The peak of the collision frequency distribution is located between $r_p = 0.5$ mm and 1 mm for the whole region. This is due to the balance of the impact velocity, the collisional cross section, and the number density of chondrules; large chondrules have large velocities and large cross sections but small number densities. As shown in Figure 3.7, large chondrules tend to crystallize earlier, and small ones

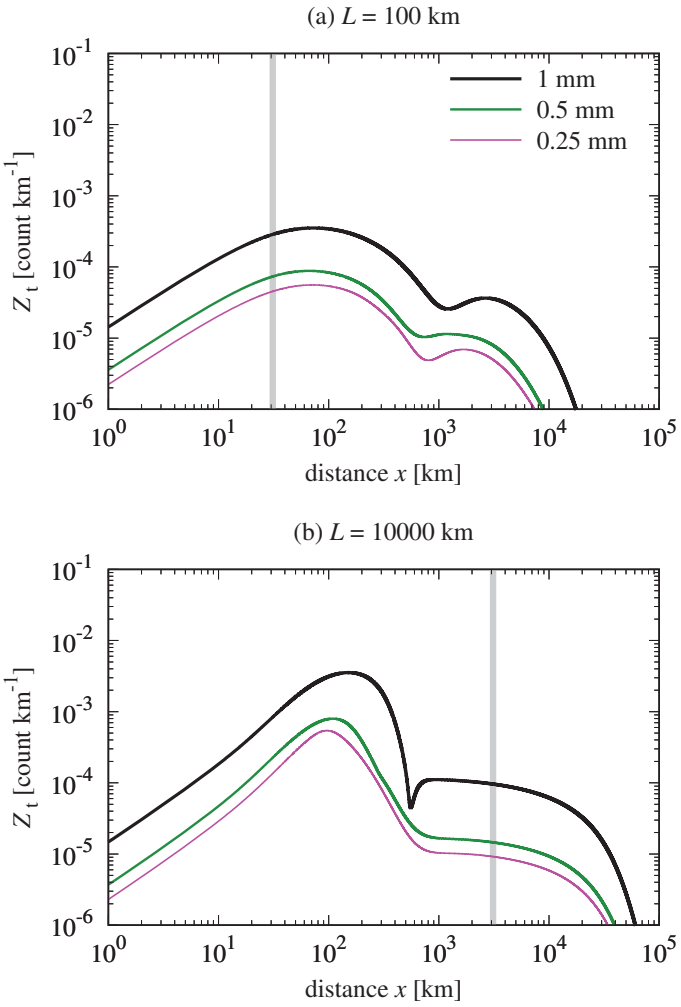

Figure 3.6: The collision frequency of a target chondrule with any projectile, Z_t. (a) For the case of the small-scale shock wave ($L = 100$ km). (b) For the case of the large-scale shock wave ($L = 10000$ km). The solid curves represent Z_t of chondrules with radii of $r = 1$ mm (black), $r = 0.5$ mm (green), and $r = 0.25$ mm (magenta). The gray vertical line represents the recondensation line of evaporated fine dust grains. We assumed that the chondrule mass density in the pre-shock region is $\rho_{c,0} = 6 \times 10^{-12}$ g cm^{-3}.

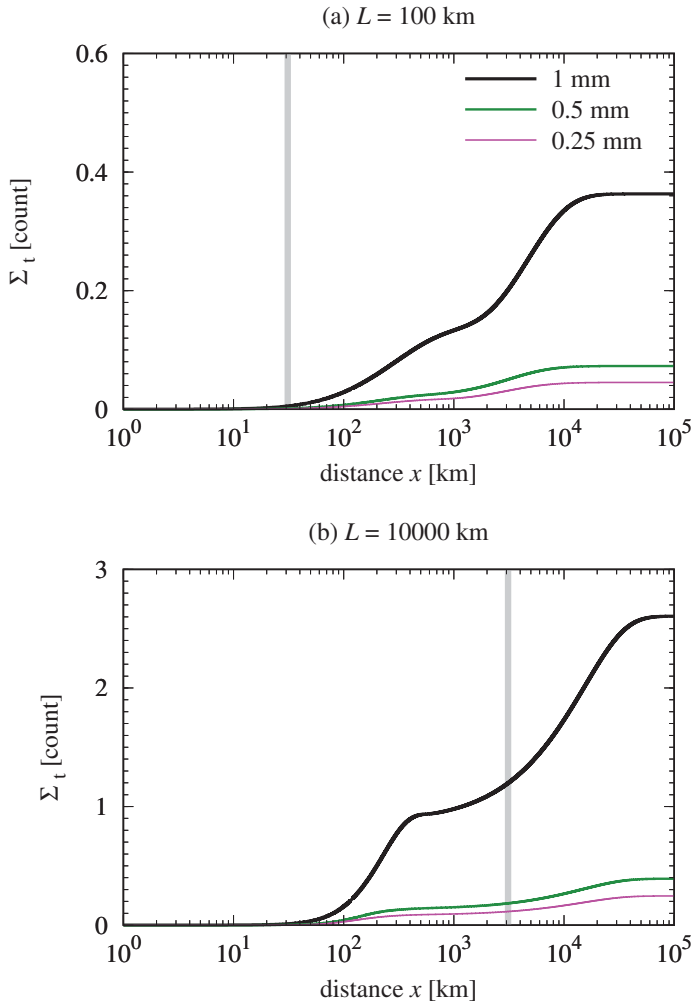

Figure 3.7: The expected number of collisions for each target chondrule after passing the shock front, Σ_t. (a) For the case of the small-scale shock wave ($L = 100$ km). (b) For the case of the large-scale shock wave ($L = 10000$ km). The solid curves represent Σ_t of chondrules with radii of $r = 1$ mm (black), $r = 0.5$ mm (green), and $r = 0.25$ mm (magenta). The gray vertical line represents the recondensation line of evaporated fine dust grains.

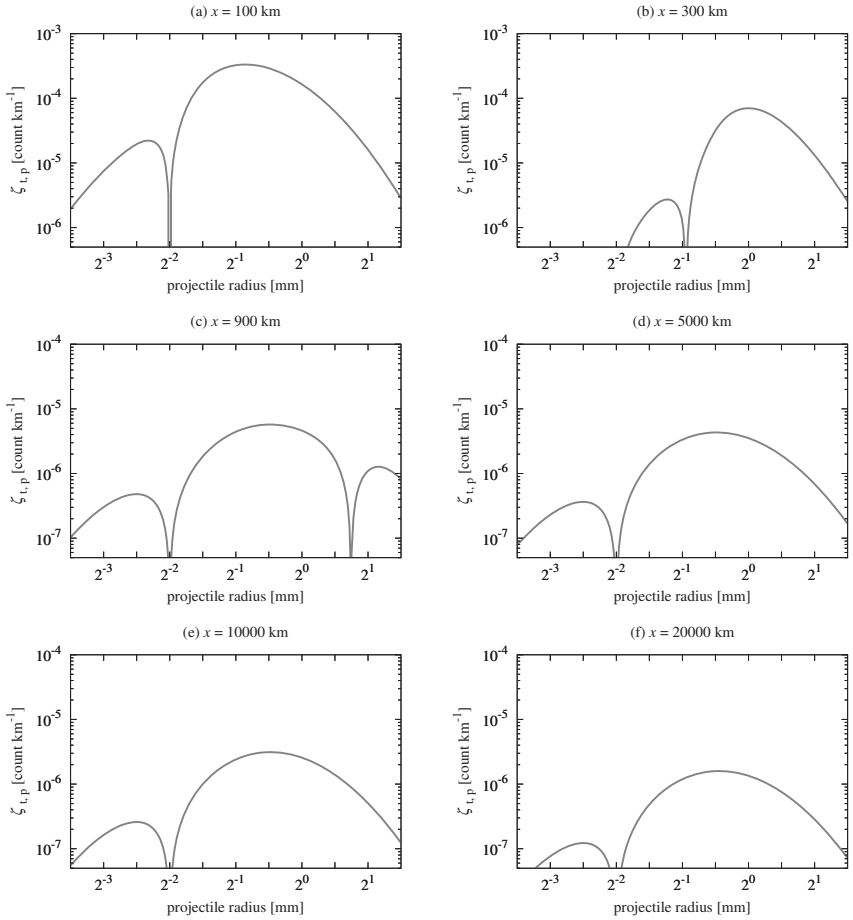

Figure 3.8: The collision frequency of a target chondrule whose size is $r_t = 0.25$ mm with projectile chondrules whose size is r_p at (a) $x = 100$ km, (b) $x = 300$ km, (c) $x = 900$ km, (d) $x = 5000$ km, (e) $x = 10000$ km, and (f) $x = 20000$ km, respectively. The presented results are for the case of the large-scale shock wave ($L = 10000$ km).

tend to be secondaries. In addition, the peak of the size-frequency distribution is located around $r \sim 0.25$ mm. Therefore, the radius of secondaries r_{sec} may be distributed around $r_{sec} \sim 0.25$ mm, and the typical radius of primaries r_{pri} may be $r_{pri} \sim 0.5$–1 mm.

The secondary-to-primary size ratio, $\Delta_{sp} \equiv r_{sec}/r_{pri}$, has been measured in thin sections by a few studies (e.g., Wasson et al., 1995), and the mean value of Δ_{sp} for compound chondrules in ordinary chondrites is ~ 0.3. This value seems to be consistent with the calculated collision frequency distribution shown in Figure 3.8 (see also Figure 3.9); although the observation in the thin section is somewhat biased and the real value of Δ_{sp} may be somewhat larger than 0.3 (see Ciesla et al., 2004b).

3.3.4 Collisions of supercooled droplets

In our calculation, we obtain the temperature and the velocity of chondrules simultaneously. Therefore, we can compare the impact velocity of chondrules with different radius $v_{\rm imp}$ and the critical velocity for collisional merging $v_{\rm merge}$ and sticking $v_{\rm stick}$, which are dependent on the temperature of chondrules. Hereafter, we focus on the case of the large-scale shock wave ($L = 10000$ km).

Figure 3.9 shows the critical velocity for collisional merging $v_{\rm merge}$, sticking $v_{\rm stick}$, and the impact velocity $v_{\rm imp}$ for target chondrules with $r_{\rm t} = 1$ mm. From Figure 3.4a, the temperature of chondrules with $r_{\rm t} = 1$ mm rapidly decreases before the distance from the shock front reaches $x \simeq 300$ km. The critical velocities $v_{\rm merge}$ and $v_{\rm stick}$ are strongly dependent on the temperature of the target and projectile chondrules (see Figure 3.2). Therefore, both $v_{\rm merge}$ and $v_{\rm stick}$ significantly increase before the distance from the shock front reaches $x \simeq 300$ km. In addition, the impact velocity $v_{\rm imp}$ falls below 1 km s^{-1} for $x \gtrsim 200$–300 km; then, $v_{\rm merge}$ and $v_{\rm stick}$ overcome $v_{\rm imp}$.

As a conclusion, compound chondrules with a primary radius of ~ 1 mm would be formed via collisions of supercooled droplets in the post-shock region where the distance from the shock front exceeds $x \gtrsim 300$ km, although the suitable location for compound chondrule formation must depend on the detailed characteristics of the specific chondrule-forming shock waves.

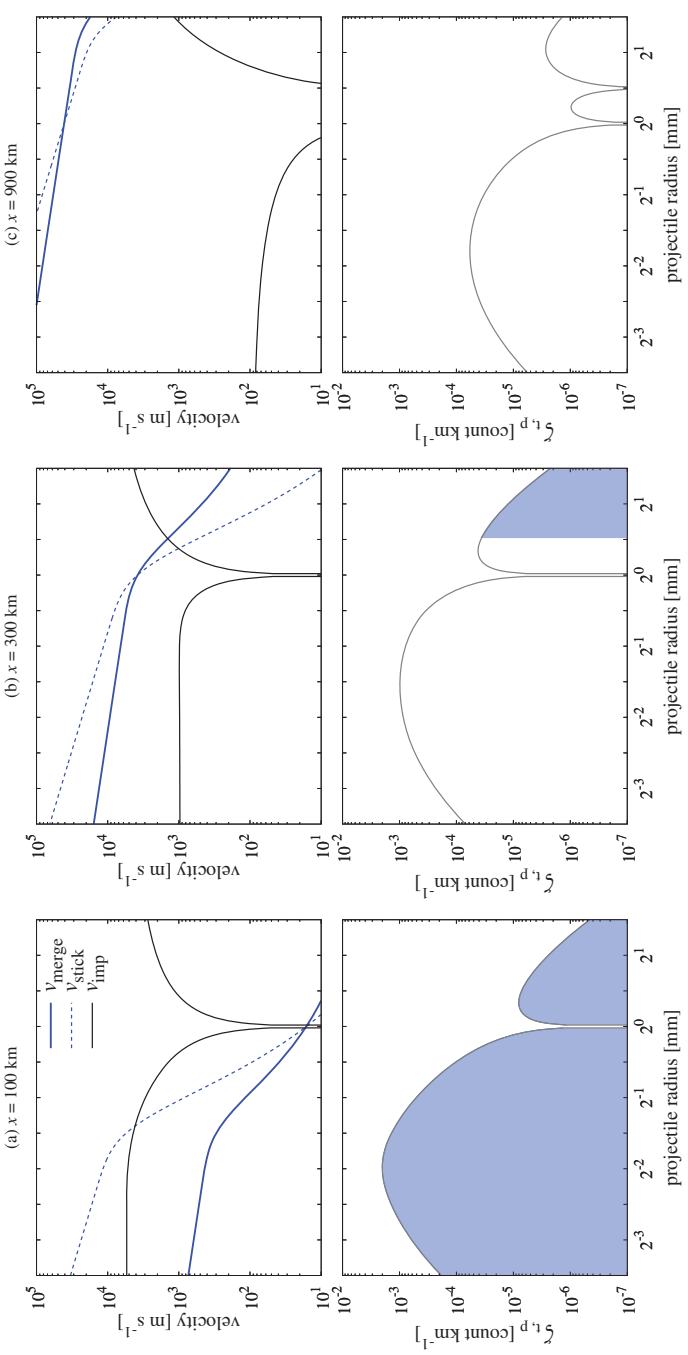

Figure 3.9: *Upper panels*: the critical velocity for collisional merging v_{merge}, sticking v_{stick}, and the impact velocity v_{imp}. *Lower panels*: the collision frequency of a target chondrule whose size is $r_{\mathrm{t}} = 1$ mm with projectile chondrules $\zeta_{\mathrm{tp}}(\varnothing_{\mathrm{t}} = -1, \varnothing_{\mathrm{p}}, x)$. The shaded regions show where non-crystallized targets would disrupt when they collide with projectiles, i.e., $v_{\mathrm{imp}} > v_{\mathrm{merge}}$. The presented results are for the case of the large-scale shock wave ($L = 10000$ km). (a) The snapshot at $x = 100$ km. (b) The snapshot at $x = 300$ km. (c) The snapshot at $x = 900$ km.

The lower panels of Figure 3.9 show the $\zeta_{t,p}(\varnothing_t, \varnothing_p, x)$ of supercooled chondrules with a target radius of $r_t = 1$ mm, i.e., $\varnothing_t = -1$. The size-frequency distribution of projectiles is a maximum at $r_p \sim 0.25$–0.5 mm. As shown in Figure 3.7, the expected number of collisions Σ_t is lower for smaller chondrules. Then, the probability that the small projectile chondrule is supercooled while the large target chondrule is already crystallized is higher than the probability that the small projectile chondrule is crystallized while the large target chondrule is still in the supercooled state. Therefore, compound chondrules whose secondary-to-primary size ratio is $\Delta_{sp} \sim 0.3$ may be formed via a collision between crystallized and supercooled chondrules in the post-shock region, as already mentioned (see Figure 3.8).

Here, we note that some of the collisions must cause the splashing of supercooled droplets when they collide with high speed and/or high temperature, although the fraction of disruption is lower than unity when we assume $\rho_{c,0}/\rho_{g,0} \sim 2 \times 10^{-3}$. Jacquet and Thompson (2014) noted that chondrules can also be destroyed by continuous erosion through the collisions of fragments produced by other catastrophic collision events. In this study, we do not take into consideration this "sandblasting" effect, however. Whether the collisions of fragments would be critical or not is dependent on the size distribution of fragments, and future studies on this point are needed.

3.3.5 Survivability of crystallized chondrules

The evaporated fine dust grains would recondense when the gas temperature decreases below the dust condensation temperature T_c (we assumed $T_c = 1600$ K in this study). The location of the dust condensation line x_c is therefore $x_c \sim 0.3L$ when we assume the gas temperature is determined by Equation (3.3). After the recondensation of fine dust grains, supercooled droplets are crystallized by the accretion of condensates onto chondrule precursors (e.g., Nagashima et al., 2006, 2008).

Here, we investigate whether crystallized chondrules can avoid catastrophic disruption after their crystallization. We compare v_{imp} and $v_{disrupt}$; then, the survivability of crystallized chondrules is evaluated. The upper panels of Figure 3.10 show the critical velocity for catastrophic disruption $v_{disrupt}$ and the impact velocity v_{imp} for target chondrules with $r_t = 1$ mm, and the lower panels show the $\zeta_{t,p}(\varnothing_t, \varnothing_p, x)$ of supercooled chondrules with a target radius of $r_t = 1$ mm.

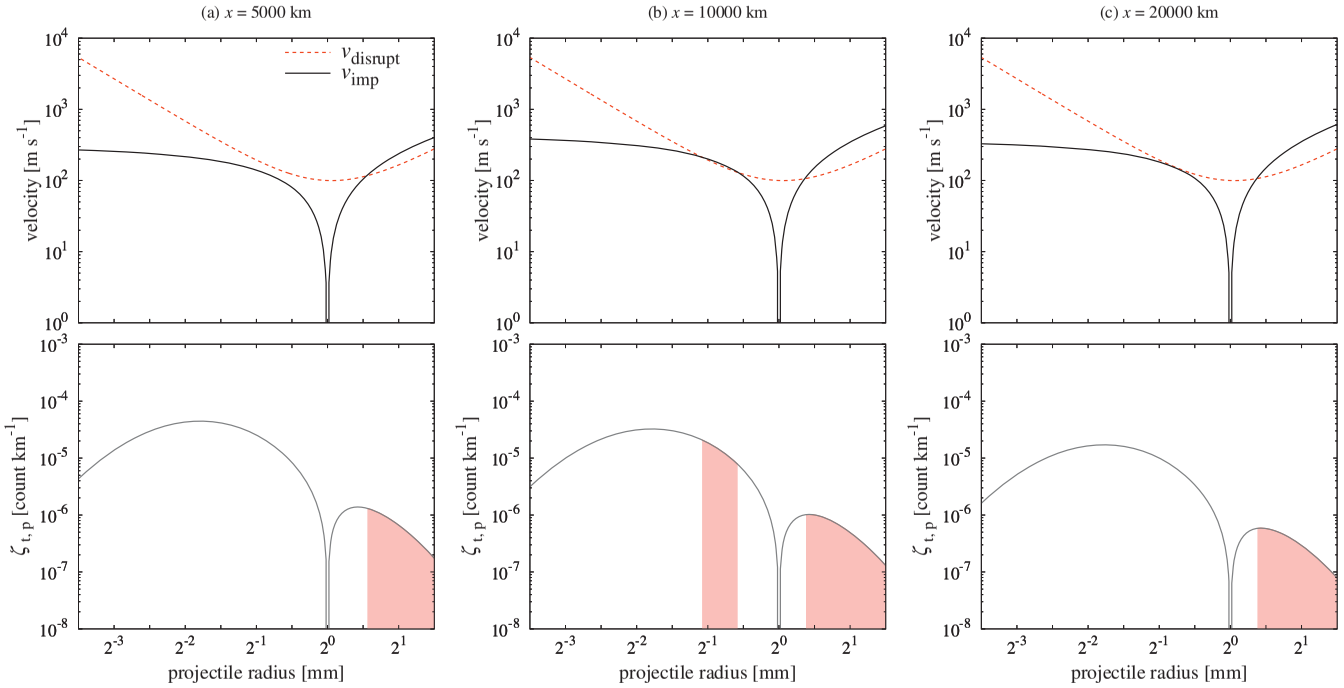

Figure 3.10: *Upper panels*: the critical velocity for catastrophic disruption $v_{\rm disrupt}$ and the impact velocity $v_{\rm imp}$. *Lower panels*: the collision frequency of a target chondrule whose size is $r_{\rm t} = 1$ mm with projectile chondrules $\zeta_{\rm t,p}(\varnothing_{\rm t} = -1, \varnothing_{\rm p}, x)$. The shaded regions show where crystallized targets would disrupt when they collide with projectiles, i.e., $v_{\rm imp} > v_{\rm disrupt}$. The presented results are for the case of the large-scale shock wave ($L = 10000$ km). (a) The snapshot at $x = 5000$ km. (b) The snapshot at $x = 10000$ km. (c) The snapshot at $x = 20000$ km.

49

Without performing numerical simulations, we can roughly evaluate the impact velocity of chondrules by simple analytical calculations. The impact velocity of large and small chondrules is approximately given by the relative velocity of the large chondrule from the gas. The velocity of chondrules with respect to the shock front is given by the following time differential equation:

$$\frac{\mathrm{d}v}{\mathrm{d}t} = -\frac{3}{4}\frac{C_\mathrm{D}}{2}\frac{\rho_\mathrm{g}}{\rho}\frac{|v-v_\mathrm{g}|(v-v_\mathrm{g})}{r} \simeq -3c_\mathrm{s}\frac{\rho_\mathrm{g}}{\rho}\frac{(v-v_\mathrm{g})}{r}, \tag{3.47}$$

where t is the time and we assume $C_\mathrm{D} \sim 8/s$. For the case of large-scale shock waves, the relative velocity of the chondrule from the gas is significantly smaller than the gas velocity, i.e., $|v-v_\mathrm{g}| \ll v_\mathrm{g}$. Then, the differential of $|v-v_\mathrm{g}|$ is also negligible, i.e., $|\mathrm{d}(v-v_\mathrm{g})/\mathrm{d}t| \ll |\mathrm{d}v_\mathrm{g}/\mathrm{d}t|$. This means that the differential of the velocity of chondrules is approximately given by the gas velocity and the spatial scale of the shock wave as follows:

$$\left|\frac{\mathrm{d}v}{\mathrm{d}t}\right| \simeq \left|\frac{\mathrm{d}v_\mathrm{g}}{\mathrm{d}t}\right| \sim \frac{(v_0-v_\mathrm{post})^2}{L}. \tag{3.48}$$

Therefore, from the combination of Equations (3.47) and (3.48), the relative velocity of the chondrule from the gas can be evaluated as follows:

$$\begin{aligned} |v-v_\mathrm{g}| &\simeq \frac{1}{3}\frac{\rho}{\rho_\mathrm{g}}\frac{r}{L}\frac{(v_0-v_\mathrm{post})^2}{c_\mathrm{s}} \\ &\sim 3\times10^2\left(\frac{\rho_\mathrm{g}}{10^{-8}\ \mathrm{g\ cm^{-3}}}\right)^{-1}\left(\frac{L}{10^4\ \mathrm{km}}\right)^{-1} \\ &\quad\cdot\left(\frac{r}{1\ \mathrm{mm}}\right)\mathrm{m\ s^{-1}}. \end{aligned} \tag{3.49}$$

Our numerical simulations also confirmed that the typical impact velocity of chondrules of 1 mm in radius is approximately 300 m s^{-1}, and disruptive collisions are minor among all collisions (see Figure 3.10) when the spatial scale is $L \gtrsim 10000$ km. The expected fraction for catastrophic disruption is, therefore, lower than unity for chondrules whose radius is less than 1 mm in this case. We note that, when the spatial scale is smaller than 100 km (i.e., $L \ll l_\mathrm{stop}$), the expected number of collisions itself is far lower than unity, and neither do we need to consider the catastrophic disruption of chondrules, although it depends on the chondrule-to-gas mass ratio.

The impact velocity is inversely proportional to the spatial scale of the shock L, and the necessary condition for chondrule survival may be $L \gtrsim 10000$ km. When the shock waves are caused by eccentric planetary bodies, the spatial scale of the shock wave L is approximately a few to ten times larger than the planetary radius $\mathcal{R}_\mathrm{p}$ (e.g., Morris et al., 2012; Boley et al., 2013), although $L/\mathcal{R}_\mathrm{p}$ depends on the opacity, the shock velocity, and so on. Therefore, planetary bow shocks caused by 1000 km-sized protoplanets may be potent candidates for the chondrule formation mechanism from the point of view of chondrule survivability.

3.4 Discussion

3.4.1 Chondrule-to-gas mass ratio

It is usually assumed that the silicate-to-gas mass ratio is approximately 4.3×10^{-3} (Miyake and Nakagawa, 1993), and part of the silicate dust can exist as fine dust grains, while others formed chondrules and/or much larger dust aggregates. Therefore, we assume that the chondrule-to-gas mass ratio in the pre-shock region is 2×10^{-3}. However, when chondrules sediment at the midplane of the solar nebula, the chondrule-to-gas mass ratio at the midplane ρ_c/ρ_g becomes significantly higher than the chondrule-to-gas surface density ratio χ. Here, we evaluate whether the sedimentation of chondrules would occur.

When the radius of a chondrule is smaller than the mean-free path of gas molecules, i.e., the gas drag force on the chondrule is determined by Epstein's law, the dimensionless stopping time called the Stokes number St is given by

$$\begin{aligned} \mathrm{St} &= \sqrt{\frac{\pi}{8}} \frac{\rho r \Omega_K}{\rho_g c_s} \\ &\sim 7 \times 10^{-5} \left(\frac{r}{1\ \mathrm{mm}} \right) \left(\frac{\rho_g}{3 \times 10^{-9}\ \mathrm{g\ cm^{-3}}} \right)^{-1} \\ &\quad \cdot \left(\frac{T_0}{500\ \mathrm{K}} \right)^{-1/2} \left(\frac{R}{1\ \mathrm{au}} \right)^{-3/2}, \end{aligned} \tag{3.50}$$

where Ω_K is the Kepler frequency and R is the distance from the sun (Weidenschilling, 1977). The gas scale height h_g is given by $h_g = c_s/\Omega_K$, and the chondrule scale height h_c is given by (Youdin and Lithwick, 2007):

$$\frac{h_c}{h_g} = \left(1 + \frac{\mathrm{St}}{\alpha_t} \frac{1 + 2\mathrm{St}}{1 + \mathrm{St}} \right)^{-1/2}, \tag{3.51}$$

where α_t is a dimensionless turbulent parameter. Then, the chondrule-to-gas mass ratio at the midplane is given by $\rho_c/\rho_g = \left(h_c/h_g\right)^{-1} \chi$.

The value of the dimensionless parameter α_t for our solar nebula is unclear; however, some protoplanetary disks (e.g., the disk around HL Tau) have a turbulent viscosity that is equivalent to α_t in the range of 10^{-4} to 10^{-3} (e.g., Pinte et al., 2016; Okuzumi et al., 2016) in the outer regions. Conversely, the dimensionless parameter α_t for the inner region of the disk has not yet been revealed by astronomical observations. Theoretical studies suggest that α_t is up to 10^{-3} or higher when the magneto-rotational instability is active, while α_t may be on the order of 10^{-4} if the magneto-rotational instability is inactive (e.g., Balbus and Hawley, 1991). Therefore, the scale heights of gas and chondrules, h_g and h_c, should be almost the same when the gas density at the midplane is $\rho_g \sim 3 \times 10^{-9}$ g cm^{-3}. In this case, ρ_c/ρ_g is approximately given by $\rho_c/\rho_g \simeq \chi$ and we do not need to consider the enrichment of chondrules at the disk midplane.

3.4.2 Location of the chondrule-forming region

We give a constraint on the location of the chondrule formation from the point of view of the gravitational stability of the solar nebula. The stability of the

disk is measured by Toomre's Q value, defined by (Toomre, 1964),

$$Q = \frac{c_{\rm s}\Omega_{\rm K}}{\pi G \cdot \left(\sqrt{2\pi} h_{\rm g} \rho_{\rm g}\right)} \simeq 25 \left(\frac{R}{1\ {\rm au}}\right)^{-3} \left(\frac{\rho_{\rm g}}{3 \times 10^{-9}\ {\rm g\ cm^{-3}}}\right), \tag{3.52}$$

and the gas disk becomes unstable when $Q \lesssim 2$ and the above equation gives the upper limit of the gas density.

As shown in Figure 3.5, the favored gas density to keep molten chondrules in the supercooled state is $\rho_{\rm g} \sim 10^{-8}$ g cm^{-3} in the post-shock region. This value corresponds to $\rho_{\rm g,0} \sim 10^{-9}$–$10^{-8}$ g cm^{-3} in the pre-shock region. Then, the location of the chondrule-forming region may be within a few astronomical units from the sun if chondrules are formed by optically thin shock waves. This region overlaps with the location of the inner part of the asteroid belt, which is mostly dominated by S-type asteroids (e.g., DeMeo and Carry, 2014), and this coincidence may indicate that chondrules in ordinary chondrites are formed via shock-wave heating in the inner solar nebula because S-type asteroids are the parent bodies of ordinary chondrites (Nakamura et al., 2011), while chondrules in carbonaceous chondrites may be linked to different events and locations.

3.4.3 Volatile retention

Chondrules contain volatile elements such as sodium, potassium, and sulfur in their interiors. This implies that chondrules are formed by flash-heating/rapid-cooling events (e.g., Tachibana and Huss, 2005; Rubin, 2010; Wasson, 2012) or the ambient environments where chondrules melted under a high partial pressure of lithophile elements (e.g., Alexander et al., 2008; Fedkin and Grossman, 2013). The latter hypothesis, called "dust enrichment", originates from the assumption that porphyritic chondrules, which are the main type among all chondrules, may be formed with a low cooling rate ($\sim 10^{-3}$–1 K s^{-1}; Desch et al., 2012, and references therein). This assumption originates from the results of classical furnace-based crystallization experiments (e.g., Radomsky and Hewins, 1990); however, several estimations based on some chondrule features, such as overgrowth thicknesses on relict grains (e.g., Wasson and Rubin, 2003) and rim formation for barred olivine chondrules (Miura et al., 2010b), give much higher cooling rates ($\sim$ 200–2000 K s^{-1}; Miura and Yamamoto, 2014). Moreover, porphyritic textures may be reproduced by multiple melting processes (e.g., Rubin, 2010) and they can also be formed via supercooled precursors (e.g., Srivastava et al., 2010; Seto et al., 2017). Therefore, dust enrichment is not necessarily needed for volatile retainment when the heating/cooling rates around their liquidus temperature are high enough.

In addition, chondrules in different chondrite groups have different average sizes (e.g., Scott, 2007), and chondrite groups with large average chondrule sizes (e.g., CV chondrites) tend to have less bulk sodium than groups with small average chondrule sizes (Wasson and Kallemeyn, 1988) and low proportions of nonporphyritic chondrules (Rubin, 2010). These features can be interpreted as a result of multiple flash-melting events (e.g., Rubin, 2010), and the constraint on the cooling rate can be mitigated.

3.4.4 Metal grains

Recently, Libourel and Portail (2018) found a notable absence of metal grains in barred olivine chondrules. The absence of metal grains in completely molten chondrule precursors was theoretically predicted by Uesugi et al. (2005, 2008). In addition, the unique occurrence of metal grains in the core region of magnesium-rich olivine crystals of porphyritic chondrules suggests that the metal grains act as seeding agents during the crystal growth of the olivine crystals in porphyritic chondrules (Libourel and Portail, 2018), and the difference in the textures of porphyritic or barred olivine chondrules is linked to the presence/absence of iron-nickel metal grains.

After the ejection of metal grains from molten chondrule precursors, metal grains may collide and merge with other metal grains. Okabayashi et al. (2019) measured the abundances of highly siderophile elements on metal grains from type 3 ordinary chondrites and found that larger metal grains have relatively homogeneous abundances of highly siderophile elements that are close to the bulk metal composition. This observed trend is consistent with the idea that some of the metal grains collided and merged with other metal grains (Okabayashi et al., 2019). For iron and nickel, Leliwa-Kopystynski et al. (1984) performed collision experiments by using 8 mm-sized projectiles. The threshold velocity for collisional sticking/bouncing is $\sim$ 500 m s^{-1} when the temperature is 290 K, and the estimated threshold velocity at 1800 K is approximately 300 m s^{-1}. Therefore, collisional sticking of ejected metal grains could occur in the post-shock region.

3.4.5 Early formation of Jupiter

If chondrules are formed by bow shocks caused by eccentric planetary bodies, the existence of both Jupiter and the nebular gas in the chondrule-forming era is a necessary condition. Although the onset of chondrule formation is still debated (e.g., Kita and Ushikubo, 2012; Bollard et al., 2017; Pape et al., 2019), both lead-lead ages and aluminum-magnesium ages show that the onset of chondrule formation is approximately 2 million years after the formation of calcium-aluminum-rich inclusions, or much earlier. Therefore, Jupiter must be formed within 2 million years in the solar nebula. We note that the early formation of proto-Jupiter is also favored in the context of the chemical dichotomy between carbonaceous and non-carbonaceous meteorite groups (e.g., Kruijer et al., 2017) and the preservation of calcium-aluminum-rich inclusions in the carbonaceous chondrite formation region (Desch et al., 2018).

3.4.6 Accretion of chondrules

There are many studies of the accretion process of chondrules, and some of these studies focus on the effect of fine dust grains accreted onto chondrules. It is known that some of the chondrules in ordinary and carbonaceous chondrites are rimmed by fine dust grains ($\sim$ 15% for chondrules in Allende CV3 chondrite, Simon et al., 2018). Theoretical studies have also revealed that free-floating chondrules in a protoplanetary disk can obtain porous dust layers (e.g., Xiang et al., 2019), which help dust-rimmed chondrules stick together when they collide (Beitz et al., 2012; Gunkelmann et al., 2017).

Evaporation and recondensation by shock-wave heating events change the size-frequency distribution of fine dust grains (e.g., Miura et al., 2010a). When the cooling rate of evaporated dust is large, the condensates could be nanograins, which would be beneficial for the direct aggregation of silicate dust aggregates (Arakawa and Nakamoto, 2016b). However, when fluffy aggregates constituted by chondrules and fine dust grains collide at large velocities, the chondrules in fluffy matrices may be ejected to the solar nebula again (Arakawa, 2017). Then, the growth of dust-rimmed chondrules may be impeded when they reach a few centimeters in radius.

Meanwhile, these centimeter-sized aggregates have the potential to turn into planetesimals via the streaming instability driven by differences in the motions of the gas and dust particles in the disk (Carrera et al., 2015; Yang et al., 2017). In addition, the typical radius of planetesimals formed via the streaming instability is $\sim 10^2$ km (Simon et al., 2016), which is roughly consistent with the estimated radius of the ordinary chondrite parent bodies (e.g., Henke et al., 2012a,b).

The other idea is that chondrules accrete onto planetesimals that already exist in the gaseous solar nebula (e.g., Hasegawa et al., 2016; Matsumoto et al., 2017). Matsumoto et al. (2017) calculated the chondrule accretion onto a protoplanet and planetesimals in the oligarchic growth stage (e.g., Kokubo and Ida, 1998) and found that approximately half of the chondrules accrete onto the protoplanet, while the other half accrete onto planetesimals with an accretion timescale of $\sim 10^6$ years. In this case, some of the chondrules should have stayed in the solar nebula for a few million years; this timescale is consistent with the fact that some of the chondrules have experienced multiple melting events with the time interval of $\sim 10^6$ years (e.g., Akaki et al., 2007).

Planetary bodies with moderate eccentricities ($e_\mathrm{p} \sim 10^{-2}$–$10^{-1}$) accrete chondrule-sized particles more efficiently than planetary bodies in circular orbits; however, the accretion efficiency drops drastically when the eccentricity becomes far larger than 10^{-1} (Liu and Ormel, 2018). Therefore, it may be difficult to grow eccentric planetesimals/protoplanets into terrestrial planets when they have a large eccentricity. The excitation of eccentricity increases the gas drag; then, the eccentricity and semimajor axis are quickly damped around 1 au (Nagasawa et al., 2014, 2019), although the location is dependent on the physical properties of the disk. The migration of planetesimals may cause the concentration of circular planetesimals around $R \sim 1$ au. This concentration of planetesimals could have the potential to explain why two large terrestrial planets, Venus and Earth, formed at approximately 1 au (e.g., Hansen, 2009; Walsh and Levison, 2016).

3.5 Conclusion

We explored the possibility that compound chondrules are formed via the collisions of supercooled precursors in shock waves. The shock-wave heating model is one of the prime candidates to explain the origin of chondrules. However, there is one challenge to this model: chondrule precursors of different sizes must have different velocities in the post-shock region and they should collide with high speed (approximately a few km s^{-1}), which may lead to their destruction upon collision rather than compound chondrule formation if they

were completely molten.

As it is, Arakawa and Nakamoto (2016a) revealed that compound chondrules may be formed via collisions of supercooled precursors. Supercooling is the state where liquids do not solidify even below their solidus temperature. Supercooled chondrule precursors have large viscosity, and their critical velocity for collisional sticking is higher than that of completely molten precursors. Therefore, the destruction of chondrules could be avoided when we consider the supercooling of chondrule precursors.

We calculated the velocity and the temperature of chondrule precursors in optically thin shock waves. We found that, in optically thin shock waves, chondrule precursors can maintain their supercooling until the fine dust grains condense and supercooled precursors crystallize via accretion of fine dust grains. As a first step toward more comprehensive modeling, we considered one-dimensional normal shocks and we assumed a simple gas structure; subsequently, the dynamics of chondrules was simulated in the given gas flow.

Our key findings are summarized as follows.

1. Because supercooled chondrule precursors have a large viscosity, the critical velocity for collisional sticking/merging could be as large as 1 km s^{-1} when the temperature of supercooled droplets is below 1400–1500 K (Figure 3.2).

2. Behind the shock front of the shock wave, recondensation of evaporated fine dust grains occurs before the temperature of supercooled precursors drops below the glass transition temperature, and these supercooled precursors can avoid turning into glassy chondrules (Figure 3.4).

3. The expected number of collisions for submillimeter-sized chondrules is lower than unity when we assume $\rho_{c,0}/\rho_{g,0} = 2 \times 10^{-3}$; therefore, most of the chondrule precursors that are heated above their liquidus temperature turn into supercooled droplets and can maintain their supercooling state until the recondensation of fine dust grains occurs. Conversely, millimeter-sized large chondrules collide frequently, and for the case of large-scale shock waves with $L \gg l_{\rm stop}$, most of the millimeter-sized chondrules have experienced collision when $\rho_{c,0}/\rho_{g,0} \gtrsim 2 \times 10^{-3}$ (Figure 3.7).

4. With respect to the survivability of crystallized chondrules, shock waves with a spatial scale of $L \gtrsim 10^4$ km may be desirable because the impact velocity of chondrules is inversely proportional to the spatial scale of the shock wave (Section 3.3.5).

Appendix

3.A Droplet–droplet collision experiments

The dynamics of droplet–droplet collisions has been studied for a long time because of its complexity as a fluid dynamics phenomenon. In particular, understanding the effect of viscosity and surface energy on binary droplet collisions is of great importance for understanding the outcomes of binary equal-sized droplet collision. The dynamics of binary equal-sized droplet collision has been investigated by numerous experimental and numerical studies (e.g., Ashgriz and Poo, 1990; Finotello et al., 2017). Sommerfeld and Kuschel (2016) proposed the criteria for collisional sticking as follows:

$$\mathrm{We_{cr}} = 111.66\mathrm{Ca} + 13.89. \tag{3.53}$$

In Figure 3.11, we checked the validity of the formula given by Sommerfeld and Kuschel (2016) by using the experimental data reported by Ashgriz and Poo (1990), Willis and Orme (2003), and Finotello et al. (2018).

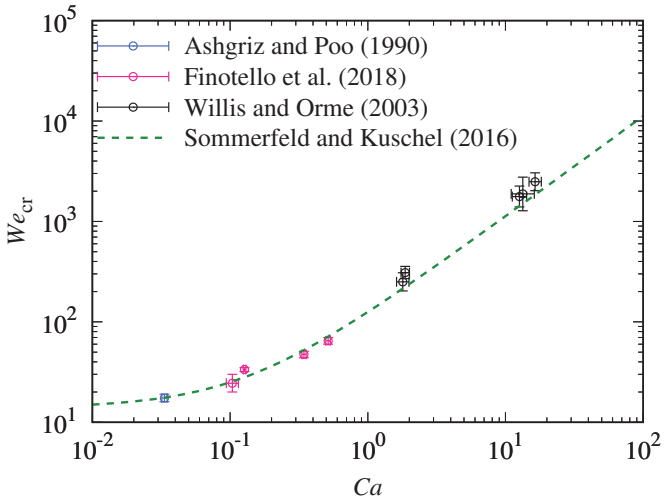

Figure 3.11: Experimental data of head-on collisions for equal-sized droplets (Ashgriz and Poo, 1990; Willis and Orme, 2003; Finotello et al., 2018) and the proposed equation of the critical Weber number (Sommerfeld and Kuschel, 2016). In these experiments, the Ohnesorge number Oh is given and the range of the critical Weber number $\mathrm{We_{cr}}$ is reported. Then, we can evaluate the capillary number Ca from $\mathrm{Ca} = \mathrm{Oh}\sqrt{\mathrm{We_{cr}}}$.

Several previous studies (e.g., Qian and Law, 1997; Gotaas et al., 2007) have proposed utilizing the dependence of $\mathrm{We_{cr}}$ on the Ohnesorge number Oh. The Ohnesorge number Oh is given by

$$\mathrm{Oh} \equiv \frac{\eta}{\sqrt{2\rho\sigma r}} \equiv \frac{\mathrm{Ca}}{\sqrt{\mathrm{We}}}. \tag{3.54}$$

Gotaas et al. (2007) proposed a relationship between $\mathrm{We_{cr}}$ and Oh as follows:

$$\mathrm{We_{cr}} = \begin{cases} 14.8 + 643.1\mathrm{Oh} & (\mathrm{Oh} < 0.04), \\ 9309\mathrm{Oh}^{1.7056} & (\mathrm{Oh} \geq 0.04). \end{cases} \tag{3.55}$$

We can rewrite the latter part of Equation (3.55) by using Ca instead of Oh:

$$\mathrm{We_{cr}} = 138.7\mathrm{Ca}^{0.9206}. \tag{3.56}$$

The coefficient and the exponent in Equation (3.56) are quite close to the coefficient and the exponent in the first term of Equation (3.53). In addition, both Equations (3.53) and (3.55) asymptote to $\mathrm{We_{cr}} \simeq 14$ for the inviscid limit ($\mathrm{Ca} \to 0$ and $\mathrm{Oh} \to 0$). These facts support the validity of the criteria for collisional sticking proposed by Sommerfeld and Kuschel (2016).

Recently, Li et al. (2016) investigated the collisions of two droplets with different viscosities, and they revealed that penetration and encapsulation are the typical outcomes for droplet collisions with a high relative viscosity ratio. These collision outcomes may have the potential to form enveloping compound chondrules. Our numerical results also suggest that collision of chondrule precursors frequently occurs with two precursors with different temperature, i.e., different viscosities (see Figure 3.4).

Compared with equal-size droplet collisions, unequal-size droplet collisions are more relevant to the practical situation of compound chondrule formation. For the case of collision with low-viscosity droplets, Ashgriz and Poo (1990) and Tang et al. (2012) found that the critical impact velocity significantly increases as the size ratio $\Delta \equiv r_{\mathrm{small}}/r_{\mathrm{large}}$ decreases, where r_{small} and r_{large} are the radii of smaller and larger droplets, respectively. This size-ratio dependence of the critical Weber number may be due to the decrease in the relative kinetic energy determined by the total mass, and a theoretical model that is based on energy balance generally reproduces the experimental trend (Tang et al., 2012). Although we expect that this trend is also shown for collisions between highly viscous droplets, we have no reliable experimental data yet. Future studies on this topic are therefore essential.

3.B Droplet–solid collision experiments

The outcome of a droplet impact on a solid surface also depends on the physical properties of the liquid, and there have been several studies on the sticking/splashing criteria of a droplet–solid collision (e.g., Walzel, 1980; Mundo et al., 1995; Josserand and Thoroddsen, 2016). Considering the equations of energy conservation, Mundo et al. (1995) analytically derived the criteria for collisional sticking/splashing as follows (see also Chandra and Avedisian, 1991):

$$\mathrm{We_{cr}} = \frac{9}{2}\beta^4\mathrm{Ca} + 3(1-\cos\Theta)\beta^2 - 12, \tag{3.57}$$

where β is the maximum spreading diameter of the droplet scaled with the initial diameter and Θ is the contact angle. Chandra and Avedisian (1991) revealed that the maximum spreading diameter is $\beta \simeq 2$–3, and this relation matches the experimentally obtained correlation between $\mathrm{We_{cr}}$ and Ca (Mundo et al., 1995). This equation is a special case of Equation (3.31), implying that the energy dissipation mechanism in droplet–solid collisions may be similar to that of a droplet–droplet collision. In addition, the equivalent critical Reynolds number is $\mathrm{Re_{cr,v}} = (9/2)\beta^4 \sim 10^2$, which is similar to the critical Reynolds number for droplet–droplet collisions.

We acknowledge, however, that the physics of droplet–solid collisions is still not well-understood. Therefore, we roughly evaluate the sticking/splashing criteria of droplet–solid collision by using Equation (3.35) instead of Equation (3.57), and our estimate is no more than an order estimation. We will study droplet–solid collisions by using hydrodynamics simulations in the future.

Chapter 4

Thermal conductivity of porous aggregates

Sota Arakawa, Hidekazu Tanaka, Akimasa Kataoka, and Taishi Nakamoto
Astronomy & Astrophysics **608**, L7 (2017).

Abstract

Context. The thermal conductivity of highly porous dust aggregates is a key parameter for many subjects in planetary science; however, it is not yet fully understood.
Aims. In this study, we investigate the thermal conductivity of fluffy dust aggregates with filling factors of less than 10^{-1}.
Methods. We determine the temperature structure and heat flux of the porous dust aggregates calculated by N-body simulations of static compression in the periodic boundary condition.
Results. We derive an empirical formula for the thermal conductivity through the solid network $k_{\rm sol}$ as a function of the filling factor of dust aggregates ϕ. The results reveal that $k_{\rm sol}$ is approximately proportional to ϕ^2, and the thermal conductivity through the solid network is significantly lower than previously assumed. In light of these findings, we must reconsider the thermal histories of small planetary bodies.

4.1 Introduction

Understanding the physical parameters of dust aggregates is important in planetary science. Specifically, the thermal conductivity of dust aggregates is key for determining the thermal evolution of planetary bodies, influencing the thermal evolution pathways of both rocky and icy planetesimals (e.g., Henke et al., 2012a; Sirono, 2017). The thermal evolution and activity of cometary nuclei also depend on the thermal conductivity of icy aggregates (e.g., Haruyama et al., 1993; Guilbert-Lepoutre and Jewitt, 2011).

Dust aggregate thermal conductivity depends on many parameters, and many previous experimental studies have researched the thermal conductivity of dust aggregates with filling factors above 10^{-1}. The thermal conductivity of porous aggregates in vacuum is given by two terms: the thermal conductivity through the solid network $k_{\rm sol}$ and the thermal conductivity owing to radiative transfer $k_{\rm rad}$. Krause et al. (2011) showed that the thermal conductivity through the solid network $k_{\rm sol}$ is exponentially dependent on the filling factor of dust aggregates ϕ for $0.15 < \phi < 0.54$, and concluded that the coordination number of monomer grains C influences the efficiency of heat flux within the aggregates. Sakatani et al. (2016) revealed that $k_{\rm sol}$ is also dependent on the contact radius between monomers $r_{\rm c}$. The thermal conductivity owing to radiative transfer $k_{\rm rad}$ is affected by the temperature of dust aggregates T and the mean free path of photons $l_{\rm p}$ (e.g., Schotte, 1960; Merrill, 1969). Moreover, $l_{\rm p}$ depends on R and ϕ when we apply the geometrical optics approximation for the evaluation of $l_{\rm p}$ (e.g., Skorov et al., 2011; Gundlach and Blum, 2012).

There are also several theoretical studies on the thermal conductivity of dust aggregates (e.g., Chan and Tien, 1973; Sirono, 2014; Sakatani et al., 2017). However, no previous research has been conducted on the thermal conductivity of porous aggregates with filling factors of less than 10^{-1}, although Kataoka et al. (2013a) and Arakawa and Nakamoto (2016b) revealed that the collisional growth of dust aggregates leads to planetesimal formation via highly porous aggregates with filling factors of much less than 10^{-1}. Therefore, the purpose of this study is to investigate the thermal conductivity and thermal evolution of fluffy dust aggregates in protoplanetary disks.

In this letter, we calculate thermal conductivity through the solid network $k_{\rm sol}$ for highly porous aggregates with filling factors in the range of 10^{-2} to 10^{-1}. We use the snapshot data of Kataoka et al. (2013b) for calculation of $k_{\rm sol}$. We then validate our results through a comparison with the experimental data of Krause et al. (2011). We also derive the thermal conductivity owing to radiative transfer $k_{\rm rad}$ for porous aggregates of submicron-sized monomers. Our results show that the thermal conductivity of highly porous aggregates is significantly lower than previously assumed.

4.2 Method

4.2.1 Arrangement of monomer grains

The arrangement of monomer grains depends on the coagulation history of the aggregates. During initial dust aggregate coagulation in protoplanetary disks, both experimental (e.g., Wurm and Blum, 1998) and theoretical (e.g., Kempf et al., 1999) studies have shown that hit-and-stick collisions lead to the formation of fractal aggregates with a fractal dimension $D \sim 2$, which is called ballistic cluster-cluster aggregation (BCCA; Meakin, 1991). Furthermore, Kataoka et al. (2013b) performed three-dimensional numerical simulations of static compression of BCCA aggregates constituted from 16384 spherical grains using a periodic boundary condition. In this study, we use snapshots of the compressed BCCA aggregates calculated by Kataoka et al. (2013b).

4.2.2 Temperature structure of the dust aggregate

To calculate the thermal conductivity through the solid network of an aggregate $k_{\rm sol}$, we have to determine the temperature of each grain in a cubic periodic boundary. We calculate the temperature of each grain using the method of Sirono (2014). Here, we consider one-dimensional heat flow from the lower boundary plane to the upper boundary plane. There are three choices regarding the pair of lower and upper planes, and we calculate $k_{\rm sol}$ from three directions. Then, we average these values for each snapshot.

We define R as the monomer radius and L^3 as the volume of each cubic space. The location of the i-th grain (x_i, y_i, z_i) satisfies $|x_i| < L/2$, $|y_i| < L/2$, and $|z_i| < L/2$ for $i = 1, 2, ..., N$, where $N = 16384$ is the number of grains in the periodic boundary. A sketch of a dust aggregate in a cubic periodic boundary is shown in Fig. 4.1. Here, we assume that heat flow occurs along the z-direction. The grains located in $-L/2 < z_i < -(L/2 - R)$ are on the lower boundary (#1 in Fig. 4.1), and the grains located in $+(L/2 - R) < z_i < +L/2$ are on the upper boundary (#40 in Fig. 4.1). If the i-th grain is located on the lower (upper) boundary, we add a new grain on the upper (lower) boundary. The location of the new grain is $(x_i, y_i, z_i + L)$ if the i-th grain is located on the lower boundary (#X in Fig. 4.1) and $(x_i, y_i, z_i - L)$ if the i-th grain is located on the upper boundary (#Y in Fig. 4.1). We set the temperature of grains located on the lower (#1 and #Y in Fig 4.1) and upper (#40 and #X in Fig 4.1) boundary as $T_0 + \Delta T/2$ and $T_0 - \Delta T/2$, respectively.

Heat flows through the monomer-monomer contacts, and for steady state conditions, the equation of heat balance at the ith grain is given by

$$\sum_j F_{i,j} = 0, \tag{4.1}$$

where $F_{i,j}$ is the heat flow from the jth grain to the ith grain, given by

$$F_{i,j} = H_{\rm c}(T_j - T_i), \tag{4.2}$$

where $H_{\rm c}$ is the heat conductance at the contact of two grains, and T_i and T_j are the temperatures of the ith and jth grains, respectively. We consider the contacts not only inside the periodic boundary but also on the side boundaries (e.g., the contacts between #9 and #10 and between #21 and #22 in Fig. 4.1). The heat conductance at the contact of two grains $H_{\rm c}$ is (Cooper et al., 1969)

$$H_{\rm c} = 2k_{\rm mat}r_{\rm c}, \tag{4.3}$$

where $k_{\rm mat}$ is the material thermal conductivity and $r_{\rm c}$ is the contact radius of monomer grains. The contact radius $r_{\rm c}$ depends on the monomer radius R and the material parameters (Johnson et al., 1971). The heat conductance within a grain $H_{\rm g}$ is also given by (Sakatani et al., 2017)

$$H_{\rm g} = \left(\frac{4\pi}{3}\right)^{1/3} k_{\rm mat}R. \tag{4.4}$$

However, we neglect the effect of $H_{\rm g}$ because $H_{\rm g}$ is sufficiently larger than $H_{\rm c}$ for (sub)micron-sized grains. Therefore, the temperature structure of the aggregate in the cubic periodic boundary can be calculated by solving Eq. (4.1) simultaneously for all N grains except lower and upper boundary grains.

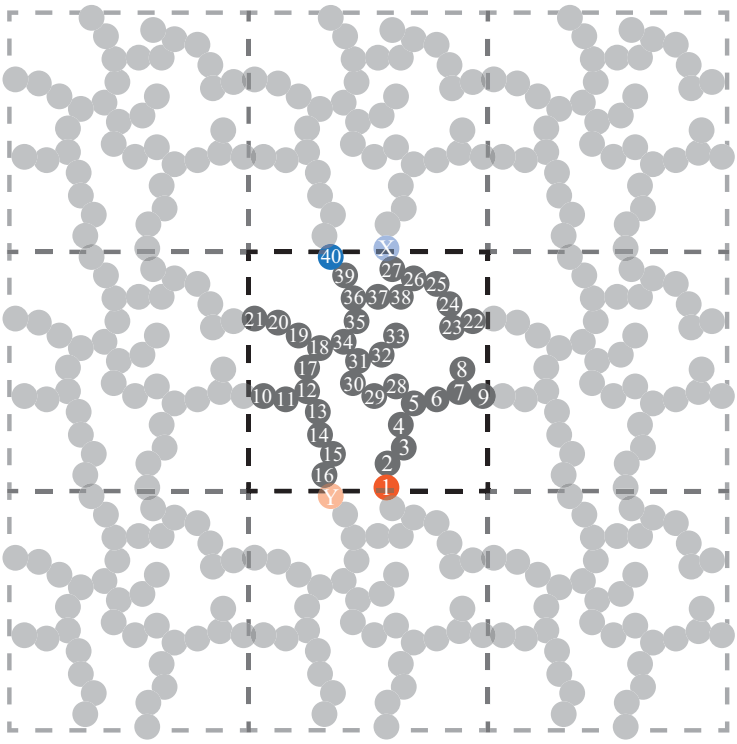

Figure 4.1: Sketch of a dust aggregate in a cubic periodic boundary. The temperature of grains located on the lower (#1 and #Y) and upper (#40 and #X) boundary is set to $T_0 + \Delta T/2$ and $T_0 - \Delta T/2$, respectively. The temperature of each grain is calculated by solving Eq. (4.1) simultaneously for each grain.

4.2.3 Thermal conductivity through the solid network

Once the temperature structure is obtained, we can calculate the total heat flow at the upper boundary $\sum_{\rm upper} F_{i,j}$, where we take the sum of contacts between the upper boundary ith grain and internal jth grain (for the case of Fig. 4.1, $\sum_{\rm upper} F_{i,j} = F_{X,27} + F_{40,39}$). The total heat flow at the upper boundary $\sum_{\rm upper} F_{i,j}$ can be rewritten using the thermal conductivity through the solid network $k_{\rm sol}$ as

$$\sum_{\rm upper} F_{i,j} = k_{\rm sol} \frac{\Delta T}{L} L^2. \tag{4.5}$$

In this study, we discuss $k_{\rm sol}$ as a function of the filling factor ϕ, and rewrite L using ϕ as

$$L = \left(\frac{4\pi N}{3\phi} \right)^{1/3} R. \tag{4.6}$$

Therefore, we obtain $k_{\rm sol}$ as a function of ϕ as follows:

$$\begin{aligned} k_{\rm sol} &= \frac{1}{L\Delta T}\sum_{\rm upper} F_{i,j}, \\ &= 2k_{\rm mat}\frac{r_{\rm c}}{R}\cdot\left(\frac{3\phi}{4\pi N}\right)^{1/3}\sum_{\rm upper}\frac{T_j - T_i}{\Delta T}, \\ &\equiv 2k_{\rm mat}\frac{r_{\rm c}}{R}\cdot f(\phi), \end{aligned} \tag{4.7}$$

where $f(\phi)$ is a dimensionless function of ϕ. Note that the total heat flow at the lower boundary $-\sum_{\rm lower} F_{i,j}$ is clearly equal to $\sum_{\rm upper} F_{i,j}$ considering the heat balance.

4.3 Results

Here, we present the dimensionless function $f(\phi)$ for nine snapshots from three runs and three densities (Table 4.1). We calculated $f(\phi)$ in three directions for each snapshot and took the arithmetic mean values. Note that the compressed BCCA aggregates might be isotropic if the number of monomer grains is sufficiently large; thus, we only discuss the mean values of $f(\phi)$.

Table 4.1: Numerical calculation results.

run	ϕ	$f(\phi)$
□	1.01×10^{-2}	1.44×10^{-4}
□	3.02×10^{-2}	1.12×10^{-3}
□	9.91×10^{-2}	1.04×10^{-2}
△	1.00×10^{-2}	3.86×10^{-5}
△	3.00×10^{-2}	5.24×10^{-4}
△	1.00×10^{-1}	6.24×10^{-3}
○	9.98×10^{-3}	4.14×10^{-5}
○	2.99×10^{-2}	5.15×10^{-4}
○	9.99×10^{-2}	9.05×10^{-3}

Figure 4.2 shows the dimensionless function $f(\phi)$ as a function of the filling factor ϕ. The best-fit line given by the least-squares method (green dashed line) is

$$f(\phi) = 1.18\phi^{2.14}. \tag{4.8}$$

Hereafter, we utilize the following more simple relationship between $f(\phi)$ and ϕ (magenta solid line)

$$f(\phi) = \phi^2. \tag{4.9}$$

Sakatani et al. (2017) predicted that $f(\phi) = (2/\pi^2)C\phi$, where C is the coordination number. For highly porous aggregates, the coordination number C is approximately two, and the filling factor dependence on C is weak. Hence, $f(\phi)$ would be proportional to ϕ in the model of Sakatani et al. (2017); however, in reality, $f(\phi)$ is approximately proportional to ϕ^2.

In the context of the thermal conductivity of colloidal nanofluid and nanocomposites, Evans et al. (2008) revealed that thermal conductivity is

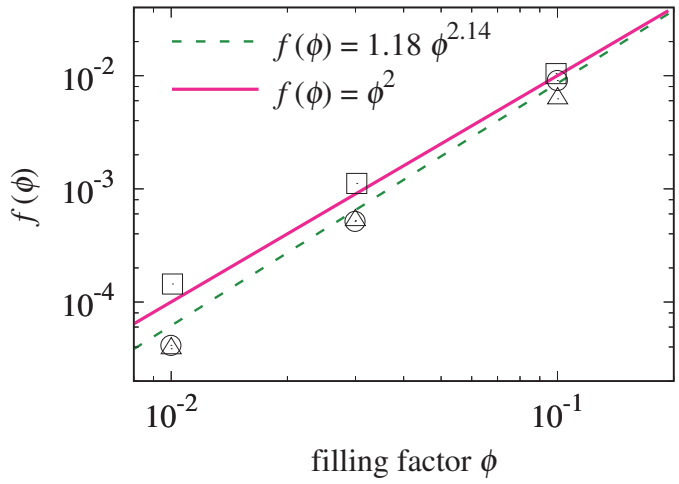

Figure 4.2: Fitting of the dimensionless function of thermal conductivity $f(\phi)$ as a function of the filling factor ϕ. The green dashed line is the best-fit line and the magenta solid line represents the simple function $f(\phi) = \phi^2$.

strongly affected by the fraction of linear chains that contribute to heat flow in the aggregates. The contributing grains are called backbone grains, and non-contributing grains are called dead-end grains (#8, #32, and #33 in Fig. 4.1; Shih et al., 1990). We will discuss the effects of different fractions of backbone and dead-end grains on the thermal conductivity in future research.

By comparing our model to the experimental data of Krause et al. (2011), we can confirm the validity of our model (Fig. 4.3). The magenta line in Fig. 4.3 represents the calculated thermal conductivity from Eqs. (4.7) and (4.9), the blue curve is the exponential fitting of experimental data, $k_{\rm sol} = 1.4e^{7.91(\phi-1)}$ W m^{-1} K^{-1} (Krause et al., 2011), and the black dashed line is a model commonly used to study the thermal evolution of planetary bodies, that is, $k_{\rm sol} = \phi k_{\rm mat}$ (e.g., Sirono, 2017). Both experimental (crosses) and numerical (squares, triangles, and circles) data are plotted.

When we consider the dust aggregates of (sub)micron-sized monomers, the contact radius between monomers $r_{\rm c}$ is given by (Johnson et al., 1971)

$$r_{\rm c} = \left(\frac{9\pi\gamma(1-\nu^2)}{2YR} \right)^{1/3} R, \tag{4.10}$$

where $\gamma = 25$ mJ m^{-2}, $\nu = 0.17$, and $Y = 54$ GPa are the surface energy, Poisson's ratio, and Young's modulus of SiO_2 grains, respectively (Wada et al., 2007). We set $R = 0.75$ μm and $k_{\rm mat} = 1.4$ W m^{-1} K^{-1} to the same values as Krause et al. (2011). Figure 4.3 clearly shows that our empirical model is applicable to the $k_{\rm sol}$ of porous aggregates with filling factors of $\phi \sim 0.1$. Moreover, our model is applicable not only for $\phi \lesssim 0.1$ but also for the range $0.1 \lesssim \phi \lesssim 0.5$.

Note that most of the experimental data of $k_{\rm sol}$ are fitted using exponential functions of ϕ, which pass the material thermal conductivities (e.g., Krause

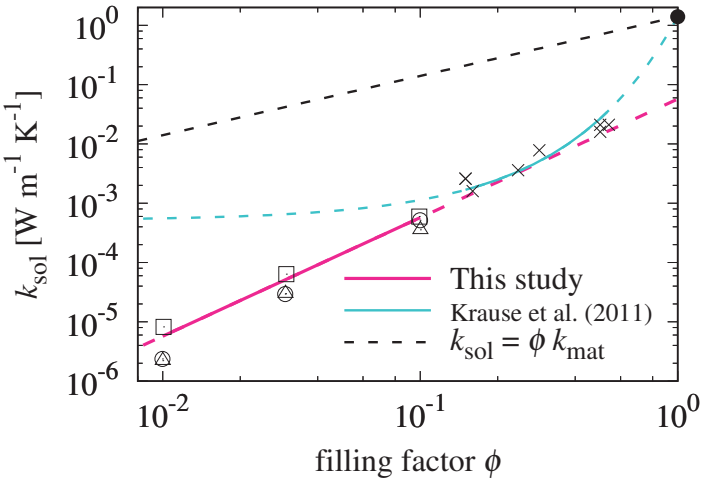

Figure 4.3: Experimental (crosses) and numerical (squares, triangles, and circles) data of thermal conductivity through the solid network $k_{\rm sol}$. Our model (magenta line) was compared to the experimental fitting data of Krause et al. (2011, blue curve).

et al., 2011; Henke et al., 2013). However, when we consider the thermal conductivity through the solid network, i.e., thermal conductivity limited by the necks between two monomers, $k_{\rm sol}$ must be given by $k_{\rm sol} \sim (r_{\rm c}/R)k_{\rm mat}$, even for dense dust aggregates whose filling factors are close to unity (e.g., Chan and Tien, 1973).

4.4 Discussion

Finally, we evaluate the total thermal conductivity of porous icy aggregates under vacuum conditions. Thermal conductivity through the solid network $k_{\rm sol}$ is given by

$$k_{\rm sol} = 2k_{\rm mat}\frac{r_{\rm c}}{R}\phi^2, \tag{4.11}$$

and thermal conductivity owing to radiative transfer $k_{\rm rad}$ is given by (Merrill, 1969)

$$k_{\rm rad} = \frac{16}{3}\sigma_{\rm SB}T^3 l_{\rm p}, \tag{4.12}$$

where $\sigma_{\rm SB} = 5.67 \times 10^{-8}$ W m^{-2} K^{-4} is the Stefan-Boltzmann constant. We calculate the mean free path of photons in fluffy aggregates of submicron-sized grains $l_{\rm p}$ as follows:

$$l_{\rm p} = \frac{1}{(\kappa_{\rm abs} + \kappa_{\rm sca})\rho_{\rm mat}\phi}, \tag{4.13}$$

where $\kappa_{\rm abs}$ and $\kappa_{\rm sca}$ are the absorption and scattering mass opacities of monomers, respectively, and $\rho_{\rm mat} = 1.68 \times 10^3$ kg m^{-3} is the material density. Here, the composition of icy dust aggregates is consistent with Pollack et al. (1994). The total mass opacity of submicron-sized monomers $\kappa_{\rm abs} + \kappa_{\rm sca}$ is hardly dependent on the wavelength of the thermal radiation

$\lambda = 2.9 \times 10^{-3}\ (T/\mathrm{K})^{-1}$ m for 10^{-6} m $< \lambda < 10^{-4}$ m, and $\kappa_{\mathrm{abs}} + \kappa_{\mathrm{sca}}$ is on the order of 10^2 m^2 kg^{-1} (e.g., Kataoka et al., 2014). Then we set $l_{\mathrm{p}} = 10^{-5}\phi^{-1}$ m in this study. Note that, for the case of fluffy aggregates of submicron-sized monomers, the wavelength λ is larger than the monomer radius R, even if the temperature is on the order of 10^3 K. Hence, we cannot apply the geometrical optics approximation for the evaluation of l_{p}.

Figure 4.4 shows the k_{sol} of crystalline and amorphous icy aggregates, $k_{\mathrm{sol,cr}}$ and $k_{\mathrm{sol,am}}$, and the thermal conductivity owing to radiative transfer k_{rad} for aggregates composed of icy monomers with a radius of $R = 0.1$ μm and temperature of $T = 40$ K. We set $\gamma = 100$ mJ m^{-2}, $\nu = 0.25$, and $Y = 7$ GPa for icy grains (Wada et al., 2007). The material thermal conductivities of crystalline and amorphous grains, $k_{\mathrm{mat,cr}}$ and $k_{\mathrm{mat,am}}$, are given by $k_{\mathrm{mat,cr}} = 5.67 \times 10^2\ (T/\mathrm{K})^{-1}$ W m^{-1} K^{-1} and $k_{\mathrm{mat,am}} = 7.1 \times 10^{-8}\ (T/\mathrm{K})$ W m^{-1} K^{-1}, respectively (Haruyama et al., 1993).

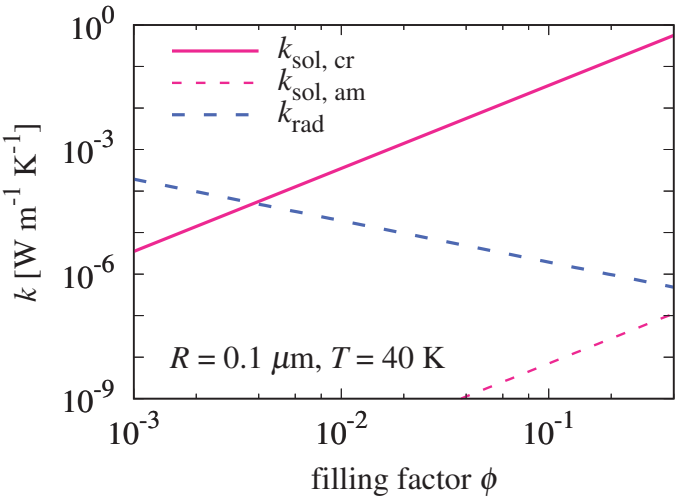

Figure 4.4: Comparison between k_{sol} (magenta solid line for crystalline icy aggregates and magenta dashed line for amorphous) and k_{rad} (blue dashed line). The monomer radius is $R = 0.1$ μm and the temperature is $T = 40$ K.

For the case of $\phi < 4 \times 10^{-3}$, the thermal conductivity owing to radiative transfer k_{rad} is larger than the thermal conductivity through the solid network of crystalline icy aggregates $k_{\mathrm{sol,cr}}$, even if the temperature is sufficiently low ($T = 40$ K). If the total thermal conductivity $k_{\mathrm{sol}} + k_{\mathrm{rad}}$ does not change substantially when crystallization occurs, then the internal temperature of icy planetesimals could still increase after crystallization, which might cause runaway crystallization due to latent heat. In addition, when the temperature of an icy planetesimal increases, sintering can proceed inside the icy aggregate before monomer grains evaporate or melt (e.g., Sirono, 2017). We cannot evaluate the contact radius r_{c} from Eq. (4.10) when aggregates are sintered, and k_{sol} increases linearly as a consequence of the increase of r_{c}. Sintering might also affect the mechanical strength of aggregates (e.g., Omura and Nakamura, 2017) and the critical velocity for collisional growth (e.g., Sirono and Ueno, 2017). Therefore, the growth pathways of icy planetesimals might be altered by sin-

tering of icy aggregates. Not only icy planetesimals but also rocky aggregates could experience sintering before growing into dm-sized bodies, which might explain the retainment of chondrules inside fluffy aggregates (Arakawa, 2017). Note also that the total thermal conductivity might be controlled by the thermal conductivity due to gas diffusion for the case of fluffy aggregates in high gas density environments (e.g., the innermost region of protoplanetary disks and/or planetary surfaces; Piqueux and Christensen, 2009).

In conclusion, we have revealed the filling factor dependence of the thermal conductivity of porous aggregates. We showed that the thermal conductivity of highly porous aggregates is significantly lower than previously assumed. In future work, we will reexamine the growth pathways of planetesimals in protoplanetary disks, and combine this with a density and thermal evolution analysis.

Chapter 5

Thermal conductivity and coordination number of compressed dust aggregates

Sota Arakawa, Misako Tatsuuma, Naoya Sakatani, and Taishi Nakamoto
Icarus **324**, 8–14 (2019).

Abstract

Understanding the heat transfer mechanism within dust aggregates is of great importance for many subjects in planetary science. We calculated the coordination number and the thermal conductivity through the solid network of compressed dust aggregates. We found a simple relationship between the coordination number and the filling factor and revealed that the thermal conductivity through the solid network of aggregates is represented by a power-law function of the filling factor and the coordination number.

5.1 Introduction

Understanding the thermal conductivity of dust aggregates and powdered media is important in numerous scientific and engineering fields. In the context of planetary sciences, for example, the thermal evolution of planetesimals is affected by the thermal conductivity of dust aggregates because they were formed from micron-sized grains in the solar nebula (e.g., Henke et al., 2013; Sirono, 2017). The near-surface temperature distribution of comets and asteroids also depends on the thermal conductivity of surface grains called regolith (e.g., Blum et al., 2017; Okada et al., 2017). Moreover, the radial motion of dust aggregates in a protoplanetary disk is induced by photophoresis, and the efficiency of this process is controlled by the thermal conductivity (e.g., Wurm and Haack, 2009; Loesche and Wurm, 2012).

The thermal conductivity of dust aggregates depends on many physical parameters, and there are many experimental and numerical studies on the thermal conductivity of dust aggregates. The thermal conductivity of porous aggregates under a vacuum condition is given by two terms: the thermal conductivity through the solid network $k_{\rm sol}$ and the thermal conductivity owing to radiative transfer $k_{\rm rad}$. It is usually thought that the coordination number of monomer grains (i.e., the average number of contacts per grain) Z influences the thermal conductivity through the solid network $k_{\rm sol}$ (e.g., Gusarov et al., 2003; Sirono, 2014). Sakatani et al. (2016) revealed that $k_{\rm sol}$ is dependent on the contact radius between monomers $r_{\rm c}$ normalized by the monomer radius R as well. The thermal conductivity owing to radiative transfer $k_{\rm rad}$ is affected by the temperature of dust aggregates T and the mean free path of photons $l_{\rm p}$ (e.g., Gundlach and Blum, 2012; Arakawa et al., 2017), and the mean free path of photons $l_{\rm p}$ depends on the monomer radius R, the filling factor ϕ, and optical properties of dust aggregates.

Arakawa et al. (2017) revealed that the thermal conductivity through the solid network $k_{\rm sol}$ is proportional to the square of the filling factor ϕ for highly porous aggregates with filling factors below 10^{-1}. The coordination number Z hardly changes with changing of ϕ for highly porous aggregates and the effect of Z on $k_{\rm sol}$ would be invisible. In contrast, for compressed aggregates with filling factors above 10^{-1}, the coordination number Z could be dependent on the filling factor ϕ and the effect of the coordination number on the thermal conductivity is expected to be observed.

In this study, we calculate the coordination number Z and the thermal conductivity through the solid network $k_{\rm sol}$ for compressed dust aggregates with filling factors in a wide range of $\phi \lesssim 1$. These snapshot data of compressed dust aggregates are prepared in the same way as Kataoka et al. (2013b). We examine filling factor dependences of the coordination number Z and the thermal conductivity through the solid network $k_{\rm sol}$, and we derive empirical formulae of $Z = Z(\phi)$ and $k_{\rm sol} = k_{\rm sol}(\phi, Z(\phi))$. Then we confirm the validity of the results by comparison with the experimental data of Sakatani et al. (2017). Our findings are expected to be competent tools for many fields of study related to dust aggregates and powdered media.

5.2 Methods

We perform three-dimensional numerical calculations of dust aggregates using the model described by Arakawa et al. (2017). Here we briefly summarize our numerical methods.

5.2.1 Arrangement of monomer grains

The arrangement of monomer grains depends on the coagulation history of the aggregates. At the initial stage of coagulation of dust aggregates in protoplanetary disks, both experimental (e.g., Wurm and Blum, 1998) and theoretical (e.g., Kempf et al., 1999) studies have shown that hit-and-stick collisions without compression lead to the formation of highly porous aggregates with the fractal dimension close to two, which is called ballistic cluster-cluster aggregation (BCCA; Meakin, 1991). In this study, we prepare snapshots of the

compressed BCCA aggregates comprised of $2^{14} = 16384$ spherical monomer grains using three-dimensional numerical simulations of static compression as Kataoka et al. (2013b). Figure 5.1 is an example snapshot of a compressed dust aggregate.

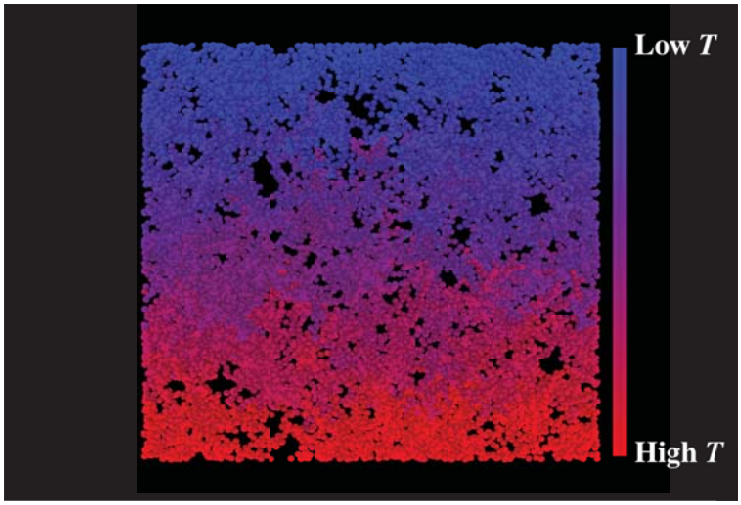

Figure 5.1: Example snapshot of a compressed dust aggregate. The filling factor of the presented aggregate is $\phi = 10^{-1.5}$. The colors of monomers, corresponding to the temperature of each monomer grains, are given by Eq. (5.1).

5.2.2 Temperature structure of the dust aggregate

In order to calculate the thermal conductivity through the solid network of an aggregate $k_{\rm sol}$, we determine the temperature of each monomer grain in a cubic periodic boundary (Sirono, 2014; Arakawa et al., 2017). We calculate the temperature of each grain using the method of Arakawa et al. (2017). Here, we consider one-directional heat flow from the lower boundary plane to the upper boundary plane (see Fig. 5.2). There are three choices regarding the pair of the lower and the upper planes, and we calculate $k_{\rm sol}$ from three directions.

We define R as the monomer radius and L^3 as the volume of each cubic space. The location of the i-th grain (x_i, y_i, z_i) satisfies $|x_i| < L/2$, $|y_i| < L/2$, and $|z_i| < L/2$ for $i = 1, 2, ..., N$, where $N = 16384$ is the number of grains in the periodic boundary (see Fig. 5.2). The grains located in $-L/2 < z_i < -(L/2 - R)$ are on the lower boundary, and the grains located in $+(L/2 - R) < z_i < +L/2$ are on the upper boundary. When the i-th grain is located on the lower (upper) boundary, we add a new grain on the upper (lower) boundary. The location of the new grain is $(x_i, y_i, z_i + L)$ for the case when the i-th grain is located on the lower boundary and $(x_i, y_i, z_i - L)$ for the case when the i-th grain is located on the upper boundary. We set the temperature of grains located on the lower and the upper boundary as $T_0 + \Delta T/2$ and $T_0 - \Delta T/2$, respectively.

Heat flows through the monomer-monomer contacts, and for the case of the steady state, the equation of heat balance at the internal i-th grain is given

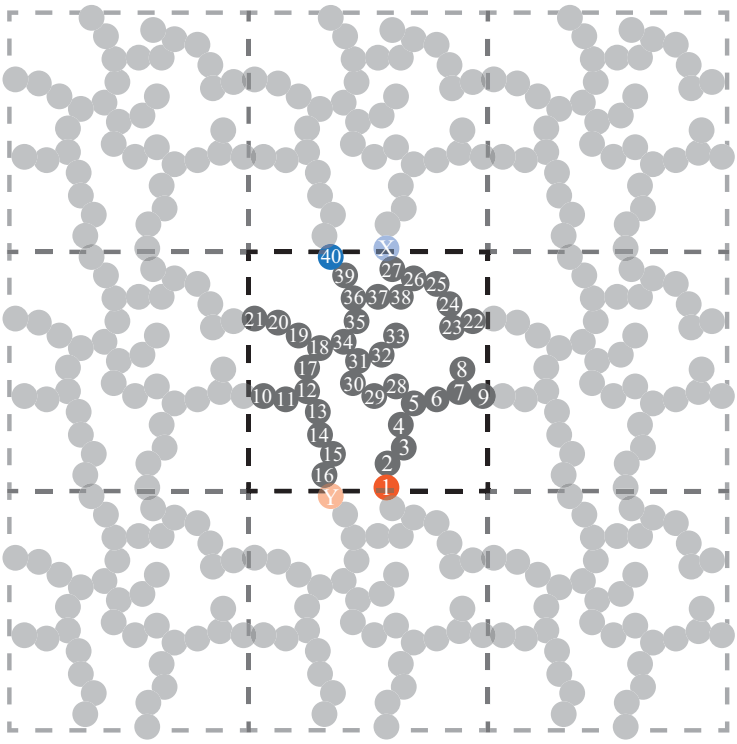

Figure 5.2: Sketch of a dust aggregate in a cubic periodic boundary. The temperature of grains located on the lower (number 1 and location Y) and upper (number 40 and location X) boundary is set to $T_0 + \Delta/2$ and $T_0 + \Delta/2$, respectively. The temperature of each grain is calculated by solving the equation of heat balance (Eq. 5.1) simultaneously for each grain (from Arakawa et al., 2017).

by

$$\sum_j F_{i,j} = 0, \tag{5.1}$$

where $F_{i,j}$ is the heat flow from the j-th grain to the i-th grain. The heat flow from the j-th grain to the i-th grain $F_{i,j}$ is given by

$$F_{i,j} = H_c(T_j - T_i), \tag{5.2}$$

where H_c is the heat conductance at the contact of two grains and T_i and T_j are the temperatures of the i-th and j-th grains. We consider the contacts not only inside the periodic boundary but also on the side boundaries. The heat conductance at the contact of two grains H_c is (Cooper et al., 1969)

$$H_c = 2k_{\rm mat} r_c, \tag{5.3}$$

where $k_{\rm mat}$ is the material thermal conductivity and r_c is the contact radius of monomer grains. The contact radius r_c depends on the monomer radius R and the material parameters (see, e.g., Wada et al., 2007);

$$r_c = \left(\frac{9\pi\gamma(1-\nu_{\rm P}{}^2)}{2YR} \right)^{1/3} R, \tag{5.4}$$

where γ, $\nu_{\rm P}$, and Y are the surface energy, the Poisson's ratio, and Young's modulus of monomer grains, respectively. The temperature structure of the aggregate in the cubic periodic boundary can be calculated by solving the Eq. (5.1) simultaneously for all N monomer grains, except lower and upper boundary grains, as shown in Fig. 5.1.

5.2.3 Thermal conductivity through the solid network

Once the temperature structure is obtained, we calculate the total heat flow at the upper boundary $\sum_{\rm upper} F_{i,j}$, where we take the sum of contacts between the upper boundary i-th grain and internal j-th grain (for the case of Fig. 5.2, $\sum_{\rm upper} F_{i,j} = F_{X,27} + F_{40,39}$). The total heat flow at the upper boundary $\sum_{\rm upper} F_{i,j}$ can be rewritten using the thermal conductivity through the solid network $k_{\rm sol}$ as

$$\sum_{\rm upper} F_{i,j} = k_{\rm sol} \frac{\Delta T}{L} L^2. \tag{5.5}$$

We discuss $k_{\rm sol}$ as a function of the filling factor ϕ in this study, and rewrite L using ϕ as

$$L = \left(\frac{4\pi N}{3\phi} \right)^{1/3} R. \tag{5.6}$$

Therefore we obtain $k_{\rm sol}$ as a function of ϕ as follows:

$$\begin{aligned} k_{\rm sol} &= \frac{1}{L\Delta T} \sum_{\rm upper} F_{i,j}, \\ &= 2k_{\rm mat} \frac{r_{\rm c}}{R} \cdot \left(\frac{3\phi}{4\pi N} \right)^{1/3} \sum_{\rm upper} \frac{T_j - T_i}{\Delta T}, \\ &\equiv 2k_{\rm mat} \frac{r_{\rm c}}{R} \cdot f(\phi), \end{aligned} \tag{5.7}$$

where $f(\phi)$ is a dimensionless function of ϕ.

5.3 Numerical Results

We carried out 10 runs of numerical simulations of static compression with different initial shape of the BCCA aggregate. Then we took 20 snapshot data for each run of compression simulation. The filling factors of compressed dust aggregates range from $\phi = 10^{-2}$ to $10^{-0.4}$ with logarithmic steps of $10^{0.1}$ and from $10^{-0.4}$ to $10^{-0.25}$ with logarithmic steps of $10^{0.05}$. We investigate the filling factor dependence of $Z(\phi)$ and $f(\phi)$ from 10 snapshot data for each ϕ obtained from different runs of compression simulations.

5.3.1 Coordination number

The coordination number (i.e., the average number of contacts per grain) Z increases as an aggregate is compressed. The initial coordination number of an

uncompressed BCCA aggregate is approximately $Z \simeq 2$, so we define ζ as the deviation of the coordination number from the initial condition;

$$\zeta \equiv Z - 2. \tag{5.8}$$

Figure 5.3 shows the deviation of the coordination number from the initial condition $\zeta(\phi)$ as a function of the filling factor ϕ. The magenta circles represent the geometric mean of 10 snapshots from different runs with vertical error bars of twice the standard error. We found that a power-law function well fits the filling factor dependence of $\zeta(\phi)$ at least in the range of $10^{-2} < \phi < 10^{-0.25}$, and the best-fit curve given by the weighted least-squares method is (blue dashed curve),

$$\zeta(\phi) = 9.38\phi^{1.62}. \tag{5.9}$$

Therefore the coordination number $Z(\phi)$ is given by,

$$Z(\phi) = 2 + 9.38\phi^{1.62}. \tag{5.10}$$

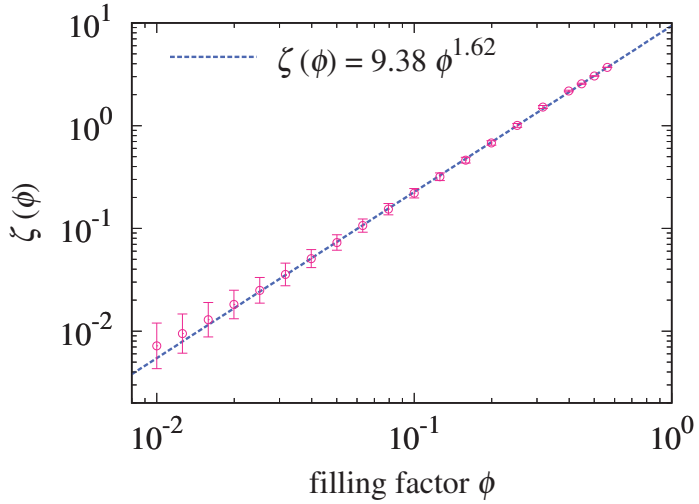

Figure 5.3: Fitting of the deviation of the coordination number from two $\zeta \equiv Z - 2$ as a function of the filling factor ϕ. The magenta circles represent the averaged data with vertical error bars of twice the standard error. The blue dashed curve is the best-fit obtained from the weighted least-squares method.

The coordination number and the filling factor are the key parameters not only for the thermal conductivity but also for the outcome of the collision between dust aggregates (e.g., Wada et al., 2011; Seizinger and Kley, 2013). Bouncing collisions of dust aggregates within a protoplanetary disk might prevent dust aggregates from growing into planetesimals via direct aggregation (Zsom et al., 2010). The results from numerical simulations of aggregate collisions indicate that dust aggregates can stick to each other only when the coordination number is $Z \lesssim 6$ (Wada et al., 2011), or a filling factor of $\phi \lesssim 0.5$ might be the condition for collisional growth (Seizinger and Kley, 2013).

5.3.2 Thermal conductivity

Previous studies (e.g., Sakatani et al., 2017) predicted that thermal conductivity depends on both the filling factor ϕ and the coordination number Z. For highly porous aggregates, however, $Z(\phi)$ is approximately two and behaves as a constant, hence $f(\phi)$ would only depend on ϕ for highly porous aggregates. Arakawa et al. (2017) revealed that $f(\phi)$ is approximately proportional to the square of ϕ for highly porous aggregates with filling factors below 10^{-1}. In this study, we calculate the dimensionless function of the thermal conductivity $f(\phi)$ for both loose (i.e., $Z \simeq 2$) and close (i.e., $Z > 2$) dust aggregates.

Figure 5.4 shows the dimensionless function $f(\phi)$ as a function of the filling factor ϕ. The magenta circles represent the geometric mean of 30 calculation results of the temperature structure from 3 directions and 10 different runs, with vertical error bars of twice the standard error. Here we assume that $f(\phi)$ is given by the power-law function of ϕ and $Z(\phi)$, and the best-fit curve given by the weighted least-squares method is (blue dashed curve),

$$f(\phi) = 0.784\phi^{1.99}\left(\frac{Z(\phi)}{2}\right)^{0.556}. \tag{5.11}$$

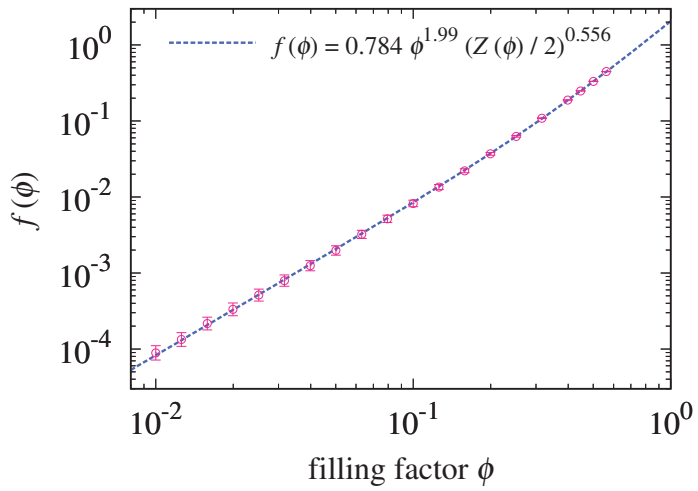

Figure 5.4: Fitting of the dimensionless function of thermal conductivity $f(\phi)$ as a function of the filling factor ϕ. The magenta circles represent the averaged data with vertical error bars of twice the standard error. The blue dashed curve is the best-fit obtained from the weighted least-squares method.

For highly porous dust aggregates with filling factors in the range from 10^{-2} to 10^{-1}, Arakawa et al. (2017) obtained a relationship between $f(\phi)$ and ϕ as $f(\phi) \simeq \phi^2$. Our novel formula of $f(\phi)$ approximately coincides with the result of Arakawa et al. (2017) for highly porous aggregates, and we numerically reveal the effect of the coordination number Z on the dimensionless function of the thermal conductivity f using highly compressed aggregates.

5.4 Comparison with experimental data

5.4.1 Comparison with Sakatani et al. (2017)

The thermal conductivity of dust aggregates in a vacuum is the sum of $k_{\rm sol}$ and $k_{\rm rad}$, and the contributions of $k_{\rm sol}$ and $k_{\rm rad}$ are distinguishable by measuring the temperature dependence of the total thermal conductivity (e.g., Sakatani et al., 2016, 2017). Sakatani et al. (2017) obtained the filling factor dependence of $k_{\rm sol}$ for dust aggregates composed of micron-sized glass grains. Therefore, by comparison with the experimental data of Sakatani et al. (2017), we can verify our model (Fig. 5.5). The blue dashed curve is the calculated thermal conductivity from Eqs. (5.7) and (5.11), and the magenta circles represents the experimental data of dust aggregates (Sakatani et al., 2017).

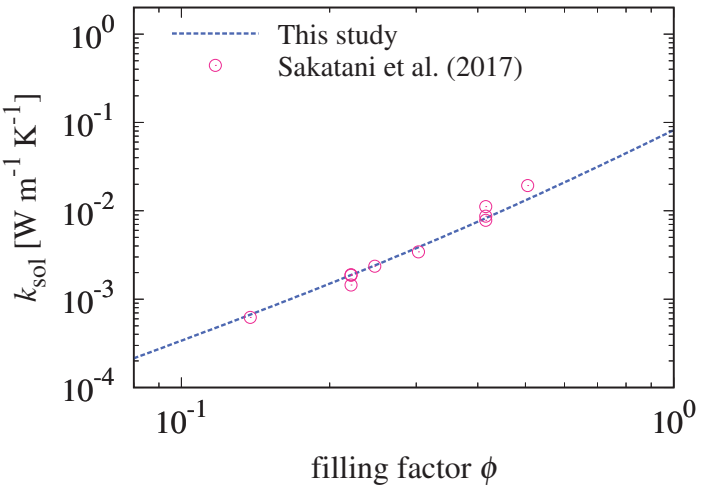

Figure 5.5: The thermal conductivity through the solid network $k_{\rm sol}$ of dust aggregates composed of SiO_2 glass grains. We compare experimental data of Sakatani et al. (2017, magenta circles) with our empirical model (blue dashed curve). The monomer radius is $R = 2.5$ μm and the material thermal conductivity $k_{\rm mat}$ at a temperature of 300 K is $k_{\rm mat} = 1.57$ W m^{-1} K^{-1} (Sakatani et al., 2017).

When we consider the dust aggregates of micron-sized monomers, the contact radius between monomers $r_{\rm c}$ is given by Eq. (5.4). The material properties of SiO_2 glass grains are listed as follows: the surface energy $\gamma = 20$ mJ m^{-2}, the Poisson's ratio $\nu_{\rm P} = 0.17$, and Young's modulus $Y = 54$ GPa (Seizinger and Kley, 2013). The monomer radius used in Sakatani et al. (2017) is $R = 2.5$ μm. The material thermal conductivity $k_{\rm mat}$ depends on the temperature, and at a temperature of 300 K, the material thermal conductivity is $k_{\rm mat} = 1.57$ W m^{-1} K^{-1} (Sakatani et al., 2017). Figure 7.5 shows that our empirical model of $k_{\rm sol}$ reproduces the experimental results with a relative difference of 30% or less for a wide range of filling factors.

5.4.2 Comparison with Krause et al. (2011)

The thermal conductivity of porous dust aggregates composed of micron-sized SiO_2 glass grains is obtained by Krause et al. (2011), using a combination of laboratory experiments and numerical simulations. Krause et al. (2011) reported the filling factor dependence of the thermal conductivity of dust aggregates as Sakatani et al. (2017), although Krause et al. (2011) did not resolve the contributions of the thermal conductivity through the solid network $k_{\rm sol}$ and the thermal conductivity owing to radiative transfer $k_{\rm rad}$. For dust aggregates composed of micron-sized monomers, however, we can calculate $k_{\rm rad}$ using the Rossland diffusion approximation (e.g., Arakawa et al., 2017), and we can also calculate $k_{\rm sol}$ by using Eqs. (5.7) and (5.11). Therefore, by comparison with the experimental data of Krause et al. (2011), we can test the validity of our novel models for both $k_{\rm sol}$ and $k_{\rm rad}$.

The thermal conductivity through the solid network $k_{\rm sol}$ is calculated from Eqs. (5.7) and (5.11). In the experiments by Krause et al. (2011), each sample was heated by the laser beam, and the temperature of dust aggregates temporally changes during their thermal conductivity measurements. Krause et al. (2011) reported that the surface temperature of heated dust samples varied from 300 K to 450 K. Therefore we take into account the temperature dependence of the contact radius $r_{\rm c}$ and the material thermal conductivity $k_{\rm mat}$. We consider the temperature dependence of the material thermal conductivity $k_{\rm mat}$ and the surface energy γ. Gundlach and Blum (2012) assumed that $k_{\rm mat}$ and γ increase with temperature as follows:

$$k_{\rm mat} = c_1 + c_2 T, \tag{5.12}$$

and

$$\gamma = c_3 T, \tag{5.13}$$

with $c_1 = 9.94 \times 10^{-1}$ W K^{-1} m^{-1}, $c_2 = 1.26 \times 10^{-3}$ W K^{-2} m^{-1}, and $c_3 = 6.67 \times 10^{-5}$ J m^{-2} K^{-1}. We apply these temperature dependences of $k_{\rm mat}$ and γ to the calculation of $k_{\rm sol}$. The monomer radius used in Krause et al. (2011) is $R = 0.75$ μm, and we assume the Poisson's ratio $\nu_{\rm P} = 0.17$ and Young's modulus $Y = 54$ GPa (Seizinger and Kley, 2013) as constant values for the calculation of the contact radius $r_{\rm c}$.

We also calculate the thermal conductivity owing to radiative transfer $k_{\rm rad}$. The thermal conductivity owing to radiative transfer is proportional to the mean free path of photons $l_{\rm p}$. In addition, when the monomer radius is smaller than the thermal emission wavelength, $l_{\rm p}$ is inversely proportional to the Rossland mean opacity $\kappa_{\rm R}$. Therefore we calculate the Rossland mean opacity of SiO_2 glass grains whose radius is $R = 0.75$ μm and we obtain the temperature-dependent $\kappa_{\rm R}$ (see 7.A).

Figure 5.6 shows the filling factor dependence of the thermal conductivity through of dust aggregates composed of SiO_2 glass grains. The solid curves are the sum of the thermal conductivity through the solid network and the thermal conductivity owing to radiative transfer, $k_{\rm sol} + k_{\rm rad}$, whereas the dashed curves represent the thermal conductivity through the solid network $k_{\rm sol}$. The blue curves correspond to the thermal conductivity at $T = 450$ K, and the red curves correspond to the thermal conductivity at $T = 300$ K. By comparison with experimental data of Krause et al. (2011, magenta crosses) and our numerical result of $k_{\rm sol} + k_{\rm rad}$ (blue and orange solid curves), we found that our

novel model well reproduces the experimental results for a wide range of filling factors. In addition, the experimental results can only be explained when we take into consideration the effect of radiative transfer when we consider highly porous aggregates (see the experimental data of $\phi = 0.15$ in Fig. 5.6). This conclusion about the contribution of $k_{\rm rad}$ is qualitatively consistent with the claim of Gundlach and Blum (2012). We also stress that our model has no free parameter to fit the numerical calculations to the experimental results.

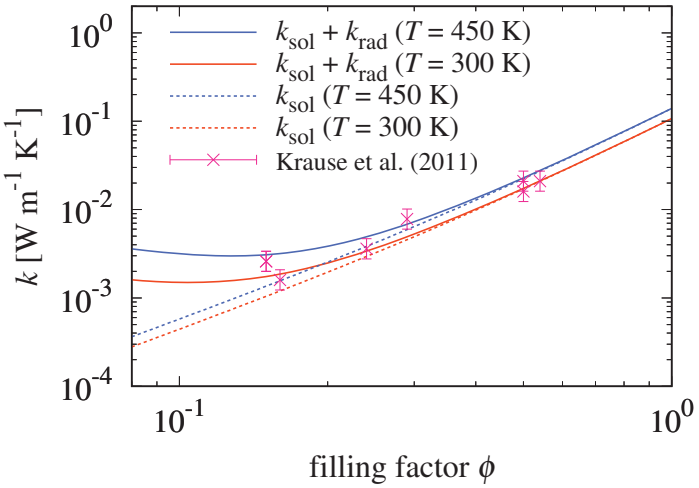

Figure 5.6: The thermal conductivity of dust aggregates composed of SiO_2 glass grains. We compare the experimental data of Krause et al. (2011, magenta crosses with 30% error bars) with our empirical model (blue and red curves). The solid curves represent the sum of the thermal conductivity through the solid network and the thermal conductivity owing to radiative transfer, $k_{\rm sol} + k_{\rm rad}$, whereas the dashed curves represent the thermal conductivity through the solid network $k_{\rm sol}$. The blue curves correspond to the thermal conductivity at $T = 450$ K, and the red curves correspond to the thermal conductivity at $T = 300$ K. The monomer radius is $R = 0.75$ μm, and the temperature-dependence of the material thermal conductivity $k_{\rm mat}$ and the surface energy γ is considered (Gundlach and Blum, 2012). The thermal conductivity owing to radiative transfer $k_{\rm rad}$ is calculated from Eqs. (5.15) and (5.16).

5.5 Discussion

5.5.1 Contributions of $k_{\rm sol}$ and $k_{\rm rad}$

As shown in Fig. 5.6, the contribution of $k_{\rm rad}$ becomes important when the filling factor of dust aggregates becomes lower, whereas the contribution of $k_{\rm sol}$ is much important when the filling factor is higher. Here we define the transition filling factor $\phi_{\rm sol-rad}$ by solving the equation $k_{\rm sol} = k_{\rm rad}$. Assuming $f(\phi) \simeq \phi^2$ for simplicity, we obtain the following relation:

$$\phi_{\rm sol-rad} \simeq \left(\frac{8\sigma_{\rm SB}}{3\rho_{\rm mat}} \frac{R}{r_{\rm c}} \frac{1}{k_{\rm mat}\kappa_{\rm R}} \right)^{1/3} T. \tag{5.14}$$

For the case of SiO_2 glass grains with $T = 300$ K and $R = 0.75$ μm, the transition filling factor $\phi_{\rm sol-rad}$ is given by $\phi_{\rm sol-rad} = 0.13$. The transition filling factor $\phi_{\rm sol-rad}$ is a strong function of T because of the strong temperature dependence of $k_{\rm rad}$; when the temperature is $T \ll 100$ K, then the transition filling factor is $\phi_{\rm sol-rad} \ll 10^{-1}$ for dust aggregates composed of micron-sized SiO_2 glass grains. This fact implies that the thermal conductivity through the solid network $k_{\rm sol}$ might be the dominant term for the heat conduction within cold small bodies, such as comets and trans-Neptunian objects.

5.5.2 Estimation of monomer properties

As seen above, both $k_{\rm sol}$ and $k_{\rm rad}$ depend on the chemical composition and the monomer radius of dust aggregates, because $k_{\rm mat}$, $\kappa_{\rm R}$, and $r_{\rm c}/R$ are strongly dependent on these monomer properties. Therefore, it is possible to give some constraints on the chemical composition and the monomer radius of small bodies by measuring the thermal conductivity of the surface regolith of small bodies. Determining these fundamental properties is of course exceedingly important for understanding the collisional growth process of the planetesimal formation (e.g., Blum and Wurm, 2008; Arakawa and Nakamoto, 2016b; Musiolik et al., 2016b). For the case of comets, the thermal inertia of comets 9P/Tempel 1 and 67P/Churyumov-Gerasimenko are observed by the *Deep Impact* mission and the *Rosetta* mission (e.g. Davidsson et al., 2013; Spohn et al., 2015; Marshall et al., 2018). The thermal inertia I is given by $I = \sqrt{(k_{\rm sol} + k_{\rm rad})\rho_{\rm mat} C_{\rm heat} \phi}$, where $C_{\rm heat}$ is the specific heat. Then we can evaluate the $(k_{\rm sol} + k_{\rm rad})\rho_{\rm mat} C_{\rm heat}$ when I and ϕ are known from observations, and the product $(k_{\rm sol} + k_{\rm rad})\rho_{\rm mat} C_{\rm heat}$ is a parameter directly related to the chemical composition and the monomer radius. We will discuss the nature of the building block of comets by using thermal conductivity calculations.

5.5.3 Pebble-pile hypothesis

In this study, we consider the heat conduction within homogeneous dust aggregates. However, several studies (e.g., Blum et al., 2017; Wahlberg Jansson et al., 2017) proposed that comets were formed via collapse of gravitationally bound clouds of millimeter- to centimeter-sized compactified dust aggregates so-called pebbles, and pebble clouds might collapse into porous pebble-pile bodies. For pebble-pile bodies comprised of millimeter- to centimeter-sized pebbles, the thermal conductivity owing to radiative transfer would be the dominant term for the heat conduction due to the large mean free path of photons inside the voids between pebbles (Gundlach and Blum, 2012). We will address the issue of "pebble-pile hypothesis" in future.

5.6 Conclusion

In this study, we conducted numerical simulations to determine the filling factor dependence of the thermal conductivity of compressed dust aggregates. The initial arrangements of aggregates are given by BCCA and numerical simulations of static compression are done in a cubic periodic boundary. We found

a simple relationship between the coordination number Z and the filling factor ϕ, $Z(\phi) = 2 + 9.38\phi^{1.62}$. This relationship is practical in a wide range of filling factors. It is also revealed that the thermal conductivity through the solid network $k_{\rm sol}$ is given by a power-law function of the filling factor ϕ and the coordination number $Z(\phi)$ as $k_{\rm sol} \propto \phi^{1.99} Z(\phi)^{0.556}$. Although what these indices come from is still unclear, this empirical formula well explains the experimental data of the thermal conductivity measured by Sakatani et al. (2017). In addition, when we consider the contributions of both the thermal conductivity through the solid network and the thermal conductivity owing to radiative transfer, our novel model can reproduce the experimental results of Krause et al. (2011) without any free parameters to fit the numerical calculations to the experimental results.

By using our novel relations, we can determine the thermal conductivity of dust aggregates from a given set of physical parameters. Conversely, we can also constrain the physical parameters of a specific sample by measuring the thermal conductivity. Therefore, our findings are expected to be competent tools for many fields of study related to dust aggregates and powdered media.

Appendix

5.A Thermal conductivity owing to radiative transfer

In this study, we consider the thermal conductivity owing to radiative transfer within fluffy aggregates composed of micron-sized grains. The thermal conductivity owing to radiative transfer $k_{\rm rad}$ is given by (e.g., Merrill, 1969)

$$k_{\rm rad} = \frac{16}{3}\sigma_{\rm SB}T^3 l_{\rm p}, \tag{5.15}$$

where $\sigma_{\rm SB} = 5.67 \times 10^{-8}$ W m^{-2} K^{-4} is the Stefan-Boltzmann constant. We calculated the mean free path of photons in fluffy aggregates of micron-sized grains $l_{\rm p}$ as follows:

$$l_{\rm p} = \frac{1}{\kappa_{\rm R}\rho_{\rm mat}\phi}, \tag{5.16}$$

where $\kappa_{\rm R}$ is the Rossland mean opacity and $\rho_{\rm mat}$ is the material density. We also note that when the wavelength of the thermal radiation is shorter than the monomer radius and monomer grains are considered as opaque, we can apply the geometrical optics approximation for the evaluation of $l_{\rm p}$ (e.g., Schotte, 1960).

The wavelength-averaged mean free path of photons $l_{\rm p}$ is given by a mean opacity averaged over all wavelengths called the Rossland mean opacity $\kappa_{\rm R}$:

$$\frac{1}{\kappa_{\rm R}} \equiv \frac{\int {\rm d}\nu\ {\kappa_{\rm ext}}^{-1}(\partial B_\nu/\partial T)}{\int {\rm d}\nu\ (\partial B_\nu/\partial T)}, \tag{5.17}$$

where ν is the frequency of photons, $\kappa_{\rm ext}$ is the wavelength-dependent extinction opacity, and B_ν is the Planck function. The frequency ν can be rewritten as $\nu = c/\lambda$, where $c = 3.00 \times 10^8$ m s^{-1} is the speed of light and λ is the wavelength. We integrated Eq. (5.17) from $\lambda = 0.1$ μm to 100 μm. The Planck function B_ν is given by,

$$B_\nu = \frac{2h\nu^3}{c^2}\frac{1}{\exp\left[(h\nu)/(k_{\rm B}T)\right]-1}, \tag{5.18}$$

where $h = 6.63 \times 10^{-34}$ J s is the Planck constant and $k_{\rm B} = 1.38 \times 10^{-23}$ J K^{-1} is the Boltzmann constant, respectively. With the assumption of spherical homogeneous particles, the extinction cross section $C_{\rm ext}$ and opacity $\kappa_{\rm ext}$ are given by the Mie theory (Mie, 1908; Bohren and Huffman, 1983):

$$C_{\rm ext} = \frac{2\pi R^2}{x^2}\sum_{n=1}^{\infty}(2n+1){\rm Re}(a_n + b_n), \tag{5.19}$$

and

$$\kappa_{\rm ext} = \frac{C_{\rm ext}}{(4\pi/3)R^3\rho_{\rm mat}}, \tag{5.20}$$

where $x = 2\pi R/\lambda$ is called the size parameter, and a_n and b_n are the Lorenz-Mie coefficients. Then we can calculate the Lorenz-Mie coefficients from the

size parameter x and the wavelength-dependent complex refractive index m from the size parameter x and the wavelength-dependent complex refractive index m (see, e.g., Bohren and Huffman, 1983, for details). We took the wavelength-dependent complex refractive index of SiO_2 amorphous grains from Kitzmann and Heng (2018). The calculated Rossland mean opacity of SiO_2 glass grains is shown in Fig. 5.7.

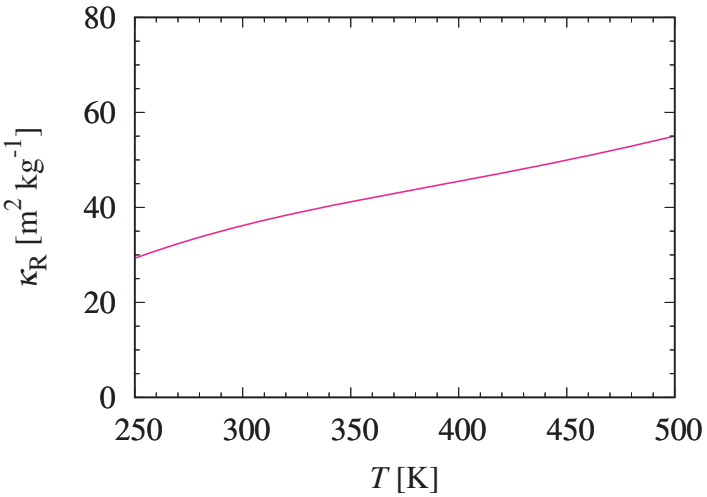

Figure 5.7: The Rossland mean opacity of SiO_2 glass grains. The monomer radius is $R = 0.75$ μm and the material density is $\rho_{\rm mat} = 2.0 \times 10^3$ kg m^{-3}. The refractive index of SiO_2 amorphous grains is taken from Kitzmann and Heng (2018).

Chapter 6

Geometrical structure and thermal conductivity of dust aggregates formed via ballistic cluster–cluster aggregation

Sota Arakawa, Masaki Takemoto, and Taishi Nakamoto
Progress of Theoretical and Experimental Physics **2019**, 093E02 (2019).

Abstract

We herein report a theoretical study of the geometrical structure of porous dust aggregates formed via ballistic cluster–cluster aggregation (BCCA). We calculated the gyration radius $R_{\rm gyr}$ and the graph-based geodesic radius $R_{\rm geo}$ as a function of the number of constituent particles N. We found that $R_{\rm gyr}/r_0 \sim N^{0.531\pm0.011}$ and $R_{\rm geo}/r_0 \sim N^{0.710\pm0.013}$, where r_0 is the radius of constituent particles. Furthermore, we defined two constants that characterize the geometrical structure of fractal aggregates: $D_{\rm f}$ and α. The definition of $D_{\rm f}$ and α are $N \sim (R_{\rm gyr}/r_0)^{D_{\rm f}}$ and $R_{\rm geo}/r_0 \sim (R_{\rm gyr}/r_0)^{\alpha}$, respectively. Our study revealed that $D_{\rm f} \simeq 1.88$ and $\alpha \simeq 1.34$ for the clusters of the BCCA.

In addition, we also studied the filling factor dependence of thermal conductivity of statically compressed fractal aggregates. From this study, we reveal that the thermal conductivity of statically compressed aggregates k is given by $k \sim 2k_{\rm mat}(r_{\rm c}/r_0)\phi^{(1+\alpha)/(3-D_{\rm f})}$, where $k_{\rm mat}$ is the material thermal conductivity, $r_{\rm c}$ is the contact radius of constituent particles, and ϕ is the filling factor of dust aggregates.

6.1 Introduction

The study of the aggregation of small dust particles into larger aggregates is crucial for understanding the fundamental processes in astrophysics and geophysics. For example, the growth of aerosol or haze particles in the atmosphere causes the scattering and absorption of the sunlight (e.g., Sorensen, 2001). In addition to this, the aggregation of dust particles also occurs in the mineral clouds of exoplanets and hence understanding the fundamental processes involved in the formation process of dust aggregates in exoplanets is imperative to interpret the transmission spectra (e.g., Ohno and Okuzumi, 2018; Ohno et al., 2019). In addition, the aggregation of dust particles in the solar nebula is the first step towards the formation of the planets (e.g., Adachi et al., 1976; Dominik and Tielens, 1997; Wada et al., 2008; Tanaka et al., 2012), and the density evolution of dust aggregates is considered to be the key to understanding the evolution from nm- or μm-sized dust grains to km-sized small bodies (e.g., Okuzumi et al., 2012; Arakawa and Nakamoto, 2016b; Tsukamoto et al., 2017; Tatsuuma et al., 2018). The resulting aggregates frequently have a complex and fractal structure with an extremely low filling factor (e.g., Meakin, 1987, 1991; Blum and Wurm, 2008). Therefore, understanding the geometrical structure of these fractal aggregates and its influence on the physical properties such as the thermal conductivity and the compressive strength is of immense current interest.

For porous dust aggregates composed of micron-sized SiO_2 glass grains, the thermal conductivity is obtained by several experimental studies (e.g., Krause et al., 2011; Sakatani et al., 2017), and it is empirically known that the thermal conductivity is approximately proportional to the square of the filling factor (Kobayashi et al., 2013; Arakawa et al., 2017, 2019c). However, the theoretical explanation of the dependence of thermal conductivity on the filling factor is still lacking.

In contrast to the thermal conductivity, the filling factor dependence of the tensile strength of porous dust aggregates is well understood (Tatsuuma et al., 2019). The tensile strength of porous dust aggregates is evaluated from the fractal structure of dust aggregates and the maximum force required to separate two sticking particles. The compression strength would also be evaluated from the fractal structure of dust aggregates and the rolling energy needed to rotate a constituent particle around its connecting points (Kataoka et al., 2013b).

In this paper, we describe the geometrical structure of porous dust aggregates formed in astrophysical environments. We present the calculation of the gyration radius (which is defined in Section 6.2.1) and the graph-based geodesic radius (which is defined in Section 6.2.2) of porous dust aggregates. Subsequently, we present the interpretations of the filling factor dependence of thermal conductivity from the geometrical structure, and we also confirm the validity of our theoretical understanding by comparing it with the result of direct numerical calculations in Section 6.3. Finally, we also present the modified interpretation of the filling factor dependence of compression strength and the average coordination number of dust aggregates in Section 6.4.

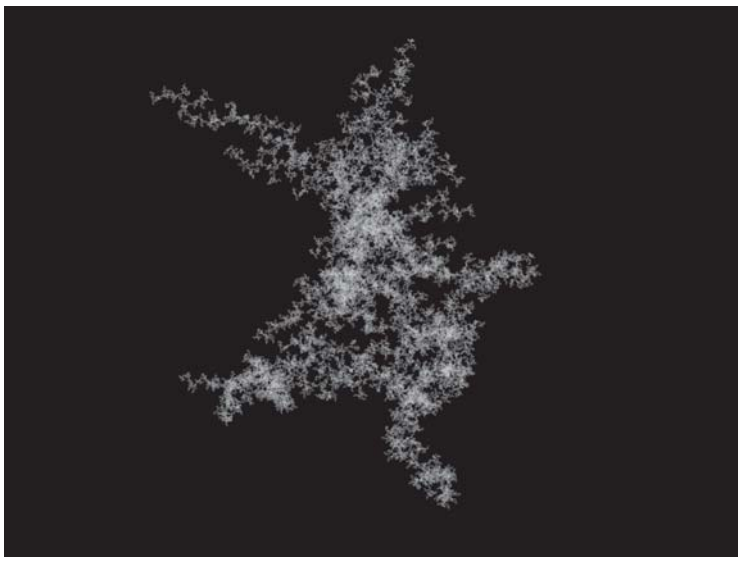

Figure 6.1: Projection of a three-dimensional dust aggregate formed via ballistic cluster-cluster aggregation (BCCA). The number of constituent particles is $N = 2^{16} = 65536$.

6.2 Ballistic cluster-cluster aggregation

In the early stage of dust growth in astrophysical environments such as protoplanetary disks and circumplanetary disks, the collision velocity is sufficiently low to avoid collisional compaction and collisions between similar-sized dust aggregates are dominant (e.g., Wurm and Blum, 1998; Kempf et al., 1999). Therefore, the shape of dust aggregates in astrophysical environments is expected to resemble the clusters of ballistic cluster-cluster aggregation (BCCA). The BCCA clusters are formed by the sticking of two equal sized BCCA clusters with no restructuring (see Figure 3(a) of Okuzumi et al., 2009). We prepare BCCA clusters in the following procedure: (1) prepare an aggregate composed of 2^i particles (initially $i = 0$), (2) copy this aggregate and change the orientation of the copy randomly, (3) by ballistic sticking of these two aggregates with a randomly chosen offset, make a new aggregate composed of 2^{i+1} particles, (4) continue the procedure (1)–(3). As shown in Figure 6.1, a BCCA cluster has a highly porous structure. In this study, we assumed that all constituent particles (hereinafter referred to as "monomers") are spherical and have the same radius r_0.

6.2.1 Gyration radius

For the quantitative analysis of the structure of porous aggregates, we need to define a typical cluster radius. Here, we use the gyration radius $R_{\rm gyr}$, which is customary in aggregation studies (e.g., Kempf et al., 1999; Okuzumi et al., 2009; Mukai et al., 1992) defined by

$$R_{\rm gyr} \equiv \left(\frac{1}{2N^2} \sum_i^N \sum_j^N (\boldsymbol{x}_i - \boldsymbol{x}_j)^2 \right)^{1/2} \equiv \left(\frac{1}{N} \sum_i^N (\boldsymbol{x}_i - \boldsymbol{x}_{\rm o})^2 \right)^{1/2}, \qquad (6.1)$$

where N is the number of constituent monomers, $\boldsymbol{x}_i$ is the coordinate of the ith monomer, and $\boldsymbol{x}_\mathrm{o}$ is the coordinate of the center of mass.

We carried out 20 growth sequences of N-body simulations of BCCA as previous studies (Okuzumi et al., 2009; Mukai et al., 1992). Here we show the geometric mean of the gyration radius R_gyr as the function of the number of monomers N in Figure 6.2(a). We found that the gyration radius R_gyr is given by

$$\log_{10}\frac{R_\mathrm{gyr}}{r_0} = (0.531 \pm 0.011)\log_{10} N + (-0.012 \pm 0.006), \tag{6.2}$$

and given uncertainties are the standard errors. The structure of BCCA clusters is therefore described in terms of the fractal dimension D_f, which is defined as

$$N \sim \left(\frac{R_\mathrm{gyr}}{r_0}\right)^{D_\mathrm{f}}. \tag{6.3}$$

Our numerical data shows that D_f is

$$D_\mathrm{f} \simeq \frac{1}{0.531} \simeq 1.88, \tag{6.4}$$

or $1.85 < D_\mathrm{f} < 1.92$ when we take uncertainty into consideration. This result is consistent with previous studies (Okuzumi et al., 2009; Mukai et al., 1992; Tazaki et al., 2016).

The effective volume of BCCA clusters V is evaluated as $V \sim 4\pi {R_\mathrm{gyr}}^3/3$ and the volume of monomers is $V_0 = 4\pi {r_0}^3/3$. The filling factor of BCCA clusters ϕ is given by

$$\phi = \frac{NV_0}{V} \sim \frac{N}{\left(R_\mathrm{gyr}/r_0\right)^3} \sim N^{1-3/D_\mathrm{f}}. \tag{6.5}$$

Therefore, we can calculate the filling factor of BCCA clusters from the number of monomers.

6.2.2 Graph-based geodesic radius

Granular materials and dust aggregates transmit compressive stresses via a network of force chains (e.g., Liu et al., 1995). Further, the chains of monomers also conduct heat (e.g., Sirono, 2014). Therefore, understanding the chain structure within dust aggregates is essential, especially for the study of the mechanical and heat transfer properties. Here, we introduce *the graph geodesic* and *the graph-based geodesic radius*. Figure 7.3 schematically illustrates a BCCA cluster. The distance between ith and jth particles is $|\boldsymbol{x}_i - \boldsymbol{x}_j|$, and we define the graph geodesic between ith and jth particles as $d_{i,j}$ in Figure 6.3. Considering the graph structure of BCCA cluster, which is a tree (i.e., a connected acyclic graph), we can uniquely determine the graph geodesic $d_{i,j}$.

The typical length of the chain of monomers is obtained using the same method as the definition of R_gyr. We define the graph-based geodesic radius R_geo as

$$R_\mathrm{geo} \equiv \left(\frac{1}{2N^2}\sum_i^N\sum_j^N {d_{i,j}}^2\right)^{1/2}. \tag{6.6}$$

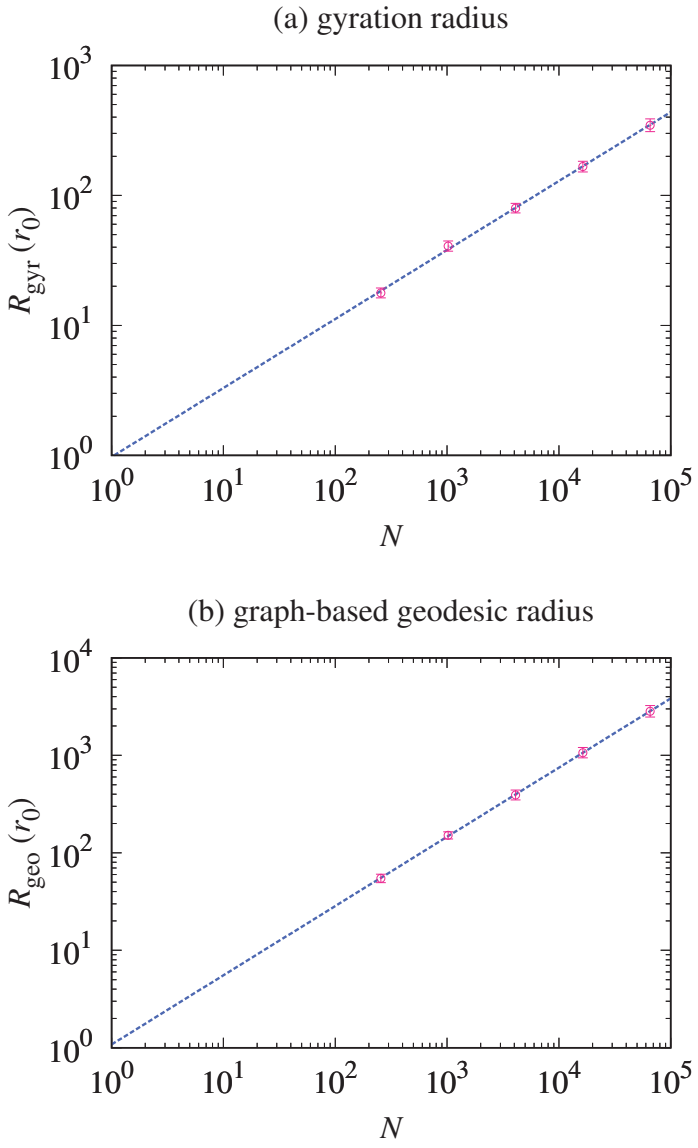

Figure 6.2: (a) Fitting of the gyration radius of BCCA clusters R_{gyr} as a function of the number of monomers N. (b) Fitting of the graph-based geodesic radius of BCCA clusters R_{geo} as a function of N. The circles represent the averaged data with vertical error bars of twice the standard error. The dashed line is the best-fit obtained from the weighted least-squares method.

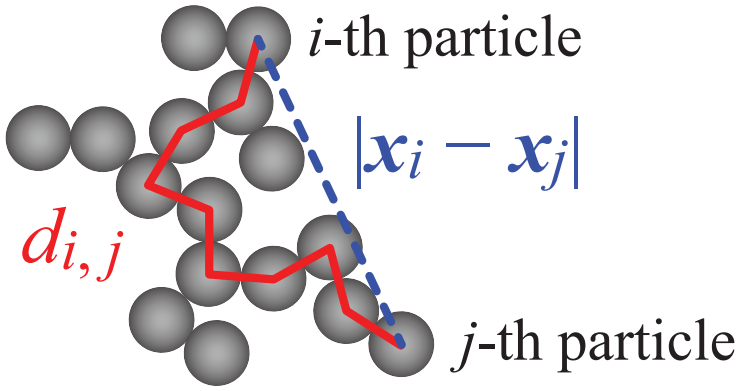

Figure 6.3: Schematic description of the distance between ith and jth particles, $|\boldsymbol{x}_i - \boldsymbol{x}_j|$, and the graph geodesic between ith and jth particles, $d_{i,j}$. It is clear that the graph geodesic $d_{i,j}$ is larger than the distance $|\boldsymbol{x}_i - \boldsymbol{x}_j|$.

It is clear that ${d_{i,j}}^2 \geq \left(\boldsymbol{x}_i - \boldsymbol{x}_j\right)^2$ and then $R_{\rm geo} \geq R_{\rm gyr}$ by definition. Here we show the geometric mean of the graph-based geodesic radius $R_{\rm geo}$ as a function of the number of monomers N over 20 runs in Figure 7.2(b). We found that the graph-based geodesic radius $R_{\rm geo}$ is given by

$$\log_{10} \frac{R_{\rm geo}}{r_0} = (0.710 \pm 0.013) \log_{10} N + (0.034 \pm 0.007), \tag{6.7}$$

and given uncertainties are the standard errors.

Here, we consider the ratio of $R_{\rm geo}$ and $R_{\rm gyr}$. The ratio of $R_{\rm geo}$ and $R_{\rm gyr}$ is given by

$$\frac{R_{\rm geo}}{r_0} \sim \left(\frac{R_{\rm gyr}}{r_0}\right)^{\alpha}, \tag{6.8}$$

where α is the dimensionless constant and the constant α must depend on the aggregation process of clusters. For BCCA clusters, we found that

$$\alpha \simeq \frac{0.710}{0.531} \simeq 1.34, \tag{6.9}$$

or $1.29 < \alpha < 1.39$ when we take uncertainty into consideration.

6.2.3 Bifractality of statically compressed BCCA clusters

In the early stage of dust growth, the fractal dimension of dust aggregates is $D_{\rm f} \simeq 1.9$. When the dust aggregates grow into cm-sized cluster, BCCA clusters are dynamically compressed by dust-dust collisions (e.g., Suyama et al., 2008) and/or statically compressed by ram pressure of the disk gas (e.g., Kataoka et al., 2013a). Although it depends on the physical properties of the disk and the monomers, the compression mechanism for icy aggregates composed of submicron-size monomers in the minimum mass solar nebula (Weidenschilling, 1977; Hayashi, 1981) is the static compression by ram pressure (Kataoka et al., 2013a). In this study, we focus on the geometrical structure of statically compressed BCCA clusters.

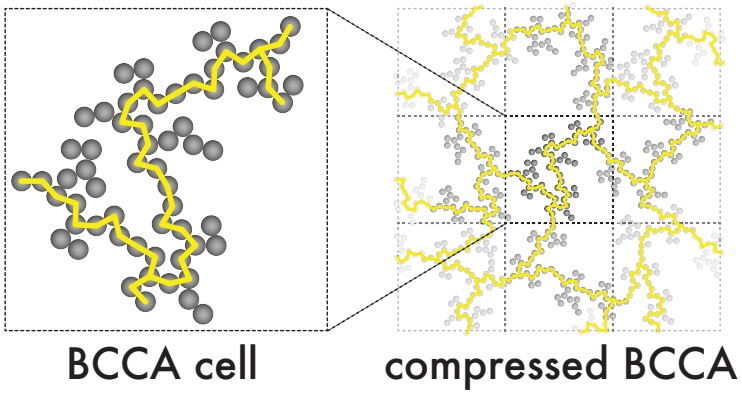

Figure 6.4: Schematic description of a BCCA cell in the compressed BCCA cluster. The yellow lines represent the possible heat paths.

The geometrical structure of statically compressed BCCA clusters is characterized by bifractality. Kataoka et al. (2013b) calculated the average number of particles in spheres of radii $r_{\rm in}$, $N_{\rm in}$. For statically compressed BCCA clusters, $N_{\rm in}$ is approximately given by

$$N_{\rm in} \sim \left(\frac{r_{\rm in}}{r_0}\right)^{D_{\rm f}} \quad (r_{\rm in} \ll r_{\rm tr}), \tag{6.10}$$

$$N_{\rm in} \sim \phi\left(\frac{r_{\rm in}}{r_0}\right)^{3} \quad (r_{\rm in} \gg r_{\rm tr}), \tag{6.11}$$

and the transition radius $r_{\rm tr}$ is evaluated as $r_{\rm tr} \sim \phi^{1/(D_{\rm f}-3)} r_0$. In other words, the fractal dimension becomes three on a large scale, while it remains 1.9, i.e., $D_{\rm f}$ of BCCA, on a small scale. This structure evolution suggests that the static compression reconstructs the fractal aggregate first on a large scale, because of the weak compressive strength on a large scale (Kataoka et al., 2013b). Therefore, we can imagine that it is possible to understand the physical properties of statically compressed BCCA clusters from the geometrical structure of small BCCA clusters preserved in compressed aggregates (hereinafter referred to as "BCCA cells"). Figure 6.4 shows the schematic description of a BCCA cell in the compressed BCCA cluster.

It is important to note that the geometrical structure of dynamically compressed BCCA clusters is also characterized by bifractality (e.g., Wada et al., 2008). The resulting fractal dimension is approximately 2.5 on a large scale and it remains $D_{\rm f}$ of BCCA on a small scale. Therefore, bifractality is a common characteristic of compressed BCCA clusters. We also hypothesize that this bifractality is a common structure for compressed fractal aggregates although the initial cluster is not originated from BCCA but other aggregation processes, for example, diffusion-limited cluster aggregation (e.g., Meakin, 1983) or reaction-limited cluster aggregation (e.g., Jullien and Kolb, 1984). We will, however, need to confirm this hypothesis in the future.

6.3 Thermal conductivity

In this section, we calculate the thermal conductivity of compressed BCCA clusters and demonstrate the manner in which the geometrical structure affects the thermal conductivity.

6.3.1 Methods

We calculate the thermal conductivity of compressed BCCA clusters composed of 16384 ($= 2^{14}$) monomers. The snapshots used in this study and used in our previous study (Arakawa et al., 2019c) are the same and were prepared by Tatsuuma et al. (2019). The methods of the thermal conductivity calculation are described in our previous studies (Arakawa et al., 2017, 2019c), which we briefly summarize it here.

Dust aggregates are statically compressed in a cubic periodic boundary (see Figure 1 of Arakawa et al., 2017). We consider one-directional heat flow from the lower to the upper boundary plane. The thermal conductivity of a dust aggregate in a cubic periodic boundary k is given by

$$k = 2k_{\rm mat}\frac{r_{\rm c}}{r_0}f, \tag{6.12}$$

where f is a dimensionless function of ϕ, $k_{\rm mat}$ is the material thermal conductivity, and $r_{\rm c}$ is the contact radius of monomer grains. The normalized thermal conductivity f is given by

$$f \equiv \frac{r_0 L}{S}\sum_{\rm upper}\frac{T_j - T_i}{\Delta T}, \tag{6.13}$$

where L is the length of the side of the cube, $S = L^2$ is the area of the upper and lower boundaries, T_i is the temperature of ith monomer, and ΔT is the temperature difference between the upper and lower boundaries. We took the sum of contacts between the ith grain on the upper boundary and jth grain inside the boundaries (see Arakawa et al., 2017, for details).

In this study, we also consider the series connection of dust aggregates in a cubic periodic boundary (see Figure 6.5). It is expected that the series connection of dust aggregates would reduce the artificial effects of the boundary condition on the thermal conductivity calculations.

6.3.2 Filling factor dependence

Figure 6.6 shows the projection of three-dimensional compressed BCCA cluster in a cubic periodic boundary. The blue monomers are on the upper boundary and the reds are on the lower boundary. The yellow monomers represent the heat paths and the grays are the non-contributing monomers. The filling factor of the aggregates is $\phi = 10^{-1.5}$. It is clear that not all monomers contribute to the heat transfer within the dust aggregate.

It is predicted that the normalized thermal conductivity of dust aggregates in a series connection of n cubes, f_n, is given by

$$\frac{1}{f_n} \simeq \frac{1}{n}\left(\frac{1}{f_1} + \frac{n-1}{f_\infty}\right), \tag{6.14}$$

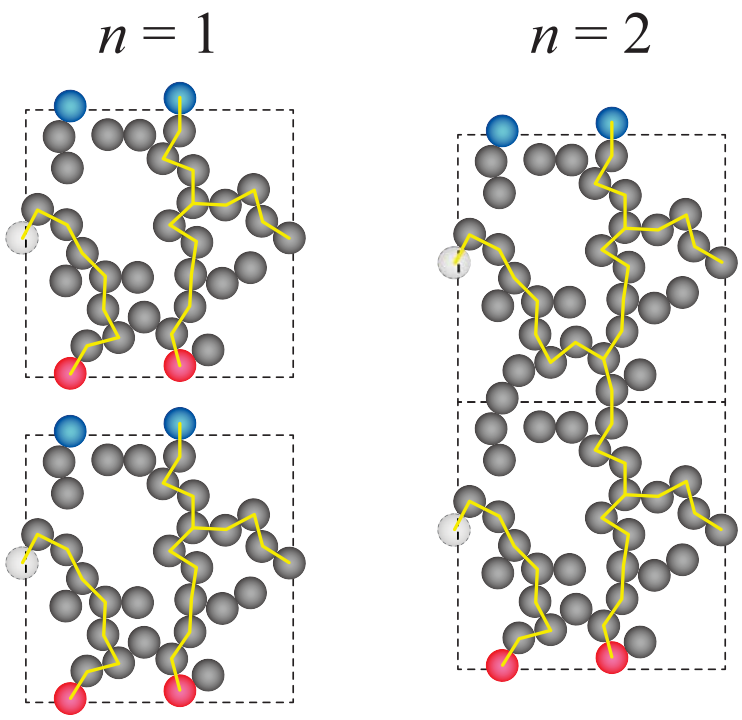

Figure 6.5: Schematic description of the series connection of dust aggregates in a cubic periodic boundary. The blue monomers are on the upper boundary and the reds are on the lower boundary, and the yellow lines represent the heat paths. The series connection of dust aggregates would reduce the artificial effects of the boundary condition.

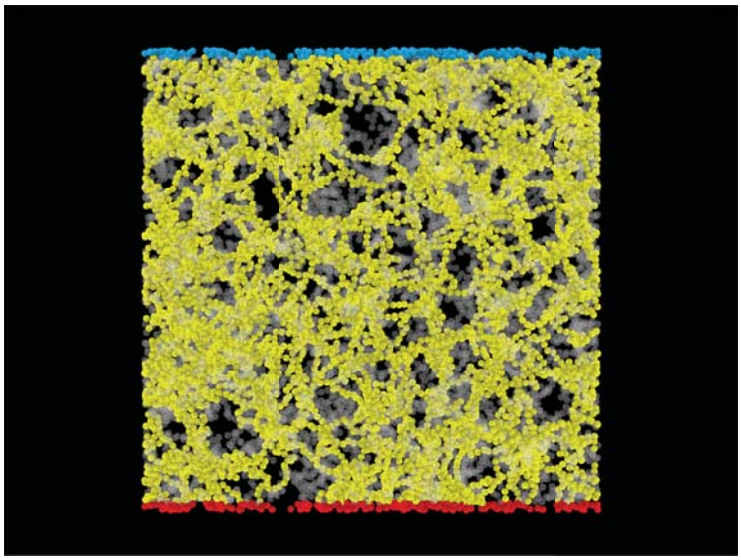

Figure 6.6: An example snapshot of a compressed BCCA cluster in a cubic periodic boundary. The blue monomers are on the upper boundary and the reds are on the lower boundary. The yellow monomers represent the heat paths and the grays are the non-contributing monomers. The filling factor of the aggregates is $\phi = 10^{-1.5}$.

where f_∞ is defined as

$$f_\infty = \lim_{n\to\infty} f_n. \tag{6.15}$$

We can rewrite Equation (6.14) as

$$\frac{f_1}{f_n} - 1 \simeq \left(\frac{f_1}{f_\infty} - 1\right)\left(1 - \frac{1}{n}\right), \tag{6.16}$$

and we found that $(f_1/f_n) - 1$ is approximately proportional to $1 - (1/n)$. In Figure 6.7(a), we confirmed that the relation between $(f_1/f_n) - 1$ and $1 - (1/n)$ works well. Therefore, we can evaluate f_∞ using f_4 and f_8 as follows:

$$f_\infty \simeq \left(\frac{2}{f_8} - \frac{1}{f_4}\right)^{-1}. \tag{6.17}$$

Figure 6.8(a) shows the normalized thermal conductivity for the limiting case of $n \to \infty$, f_∞, as a function of the filling factor ϕ. We used 10 snapshot data for each ϕ obtained from different compression simulations (Tatsuuma et al., 2019) and calculated f_∞ from three directions. The circles represent the geometric mean of 30 calculation results of the temperature structure, with vertical error bars of twice the standard error. We found that f_∞ is given by

$$\log_{10} f_\infty = (2.068 \pm 0.034)\log_{10}\phi + (-0.022 \pm 0.007), \tag{6.18}$$

and given uncertainties are the standard errors. This result is consistent with those of previous studies (Arakawa et al., 2017, 2019c).

6.3.3 Surface density of heat paths

The thermal conductivity of dust aggregates must be affected by the typical length of the chain of monomers $R_{\rm geo}$ and the surface density of heat paths σ. Here, we introduce the number of heat paths at the temperature T, $\mathcal{N}_{\rm path}(T)$. We define $\mathcal{N}_{\rm path}(T)$ as the number of contacts between two monomers whose temperatures are T_i and T_j with $T_i < T < T_j$. Thereafter, the average number of heat paths $\overline{\mathcal{N}_{\rm path}}$ is given by

$$\overline{\mathcal{N}_{\rm path}} \equiv \frac{1}{\Delta T}\int_{-\Delta T/2}^{+\Delta T/2} {\rm d}T \mathcal{N}_{\rm path}(T), \tag{6.19}$$

where the temperature at the upper and lower boundaries are $-\Delta T/2$ and $+\Delta T/2$, respectively. The surface density of heat paths σ is given by

$$\sigma \equiv \frac{\overline{\mathcal{N}_{\rm path}}}{S}. \tag{6.20}$$

The average number of heat paths $\overline{\mathcal{N}_{\rm path}}$ depends on the number of connected cubes, n. In Figure 6.5, $\overline{\mathcal{N}_{\rm path}} = 3/2$ for the case of $n = 1$ and $\overline{\mathcal{N}_{\rm path}} = 409/281$ for the case of $n = 2$. As well as f_∞, we evaluated the surface density of heat paths for the limiting case of $n \to \infty$, σ_∞. In Figure 6.7(b), we confirmed that σ_∞ can be predicted as follows:

$$\sigma_\infty \simeq \left(\frac{2}{\sigma_8} - \frac{1}{\sigma_4}\right)^{-1}, \tag{6.21}$$

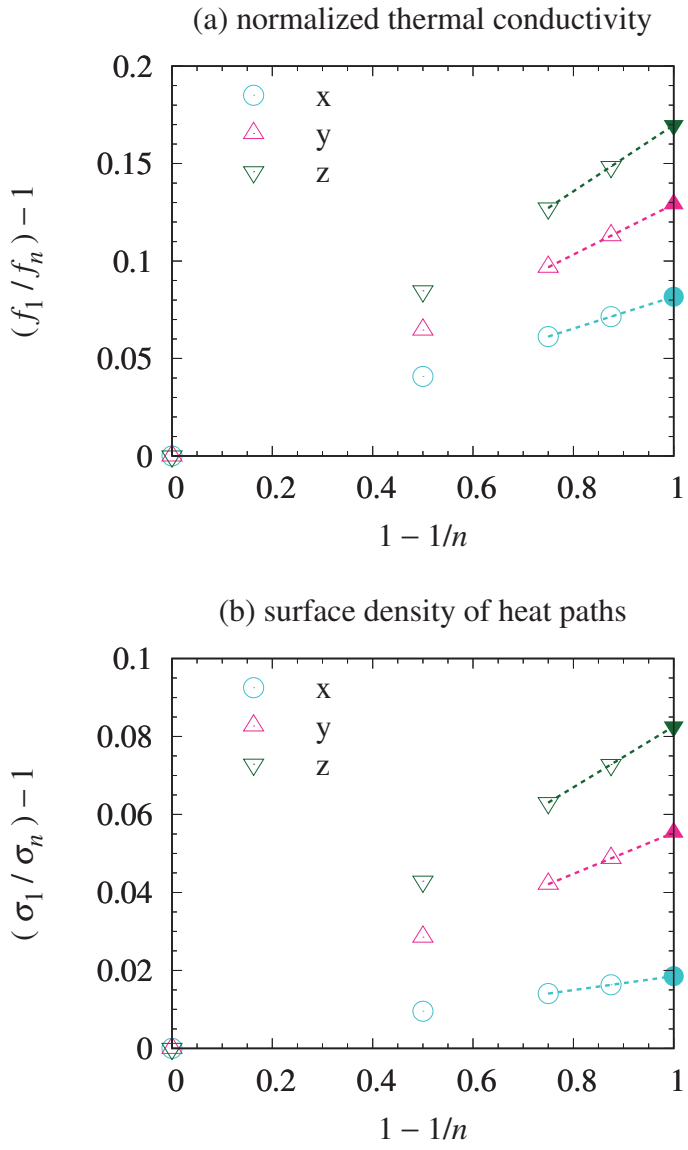

Figure 6.7: (a) Example calculation of f_∞ (filled marker) using f_1, f_2, f_4, and f_8 (open markers). (b) Example calculation of σ_∞ (filled marker) by using σ_1, σ_2, σ_4, and σ_8 (open markers). The aggregate used in this calculation is the same that used in Figure 6.6. We calculated f_∞ and σ_∞ from three directions (x, y, and z).

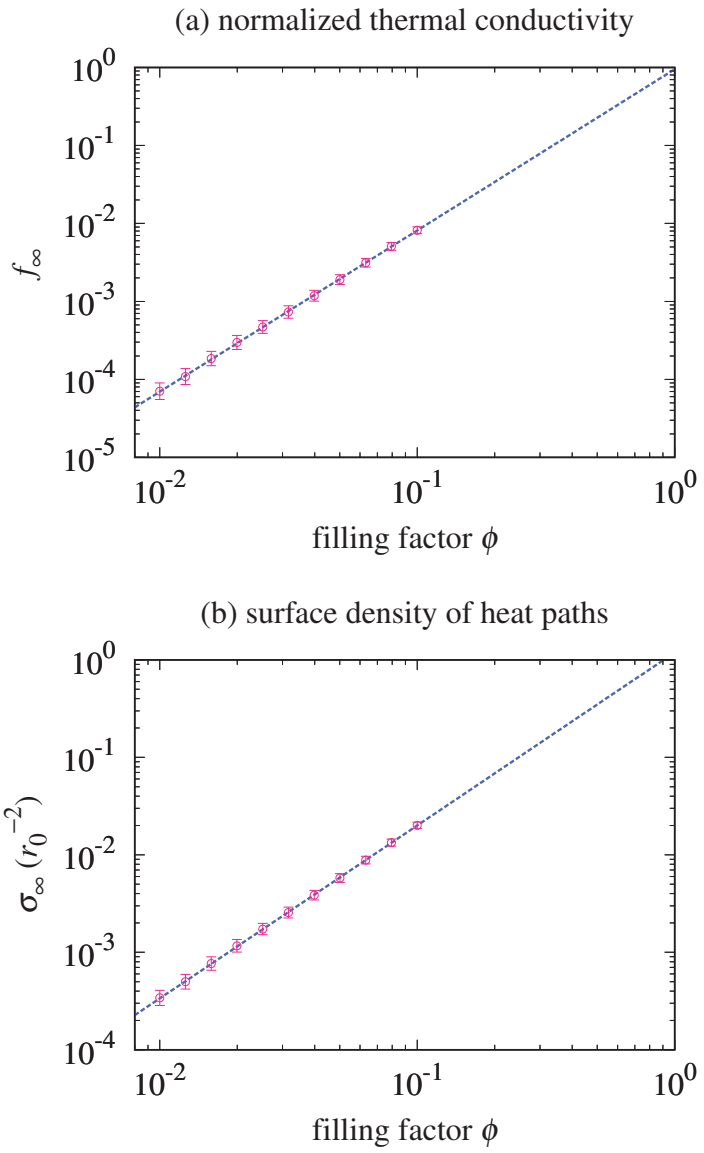

Figure 6.8: (a) Fitting of the normalized thermal conductivity for the limiting case of $n \to \infty$, f_∞, as a function of the filling factor ϕ. (b) Fitting of the surface density of heat paths for the limiting case of $n \to \infty$, σ_∞, as a function of ϕ. The circles represent the averaged data with vertical error bars of twice the standard error. The dashed line is the best-fit obtained from the weighted least-squares method.

where σ_n is the surface density of heat paths within a dust aggregate in a series connection of n cubes. Figure 6.8(b) shows the surface density of heat paths for the limiting case of $n \to \infty$, σ_∞, as a function of the filling factor ϕ. We found that

$$\log_{10} \frac{\sigma_\infty}{{r_0}^{-2}} = (1.775 \pm 0.025) \log_{10} \phi + (0.076 \pm 0.005), \tag{6.22}$$

and given uncertainties are the standard errors.

For a BCCA cell, we can imagine that the average number of heat paths is

$$\overline{\mathcal{N}_{\rm path}} \sim \mathcal{O}(1). \tag{6.23}$$

Thereafter, the surface density of heat paths within a BCCA cell is given by

$$\sigma = \frac{\overline{\mathcal{N}_{\rm path}}}{S} \sim {R_{\rm gyr}}^{-2}. \tag{6.24}$$

The relation between the gyration radius $R_{\rm gyr}$ and the filling factor ϕ is

$$\frac{R_{\rm gyr}}{r_0} \sim N^{1/D_{\rm f}} \sim \phi^{1/(D_{\rm f}-3)}, \tag{6.25}$$

and we obtain the relation between σ and ϕ:

$$\sigma \sim \phi^{2/(3-D_{\rm f})} {r_0}^{-2}. \tag{6.26}$$

We found that $1.85 < D_{\rm f} < 1.92$ in Section 6.2.1, therefore, we obtain $1.74 < 2/(3-D_{\rm f}) < 1.85$. The range of $2/(3-D_{\rm f})$ matches the numerical result, $\sigma \sim \phi^{1.775\pm0.025} {r_0}^{-2}$. This fact validates the assumption that $\overline{\mathcal{N}_{\rm path}} \sim \mathcal{O}(1)$ for BCCA cells.

We note that the tensile strength of compressed BCCA clusters, $P_{\rm t}$, is approximately given by $P_{\rm t} \sim \sigma F_{\rm c}$, where $F_{\rm c} = 3\pi\gamma r_0/2$ is the maximum force required to separate two sticking monomers and γ is the surface energy Dominik and Tielens (1997). Therefore, the tensile strength is given by

$$P_{\rm t} \sim \gamma {r_0}^{-1} \phi^{1.775\pm0.025}, \tag{6.27}$$

which is consistent with the numerical result of Tatsuuma et al. (2019), $P_{\rm t} \simeq 0.6\gamma {r_0}^{-1} \phi^{1.8}$. The coincidence of the filling factor dependence may indicate not only the number of heat paths but the number of force chains is also on the order of unity for BCCA cells.

6.3.4 Understanding the filling factor dependence of the thermal conductivity

Here, we demonstrate the manner in which the filling factor dependence of the thermal conductivity is derived from the geometrical structure. For compressed BCCA clusters, the fractal dimension is three on a large scale, then the thermal conductivity of compressed BCCA clusters should be the same as the thermal conductivity of BCCA cells.

The spatial scale of BCCA cells is $L \sim R_{\rm gyr}$ and the area of the BCCA cells is $S \sim {R_{\rm gyr}}^2$, where $R_{\rm gyr} \sim N^{1/D_{\rm f}} r_0$ is the gyration radius of a BCCA cell and N

is the number of monomers in a BCCA cell. The surface density of heat paths is approximately given by $\sigma \sim {R_{\rm gyr}}^{-2}$. The typical temperature difference between two contacting monomers, δT, is also given by

$$\delta T \sim \frac{\Delta T}{R_{\rm geo}/r_0}, \tag{6.28}$$

where ΔT is the temperature difference between the upper and lower region of a BCCA cell. The heat conductance at the contact of two monomers, H, is (e.g., Luikov et al., 1968; Cooper et al., 1969)

$$H = 2k_{\rm mat}r_{\rm c}, \tag{6.29}$$

and the heat flow at the contact of two monomers, I, is $I \sim H\delta T$. Therefore, the heat flow density within the BCCA cell is

$$k\frac{\Delta T}{L} \sim \sigma H \delta T, \tag{6.30}$$

and the thermal conductivity k is rewritten as follows:

$$k \sim 2k_{\rm mat}\frac{r_{\rm c}}{r_0}\frac{{r_0}^2}{R_{\rm gyr}R_{\rm geo}}. \tag{6.31}$$

The normalized thermal conductivity f of the BCCA cell (and the compressed BCCA cluster) is therefore given by

$$f \sim \frac{{r_0}^2}{R_{\rm gyr}R_{\rm geo}} \sim N^{-(1+\alpha)/D_{\rm f}}. \tag{6.32}$$

The relation between N and ϕ is $N \sim \phi^{D_{\rm f}/(D_{\rm f}-3)}$, then we obtain the following equation:

$$f \sim \phi^{(1+\alpha)/(3-D_{\rm f})} \sim \phi^{2.09}. \tag{6.33}$$

The derived relation shows excellent coincidence with our numerical result, $f \sim \phi^{2.068\pm0.034}$.

6.4 Discussion

6.4.1 Reinterpretation of the filling factor dependence of the compressive strength

We can also derive the filling factor dependence of the compressive strength of compressed BCCA clusters from the geometrical structure. In this section, we evaluate the compressive strength $P_{\rm c}$ as Kataoka et al. (2013b) did.

The compressive force on the surface area of the BCCA cell $F_{\rm c}$ and the compressive strength $P_{\rm c}$ are given by

$$F_{\rm c} \sim P_{\rm c}{R_{\rm gyr}}^2. \tag{6.34}$$

The length of the force chain within the BCCA cell is $R_{\rm geo}$. Since the compression is accompanied by the rolling of pairs of monomers in the force chain, the work required for compression can be given by

$$F_{\rm c}R_{\rm geo} \sim E_{\rm roll}, \tag{6.35}$$

where $E_{\rm roll} = 6\pi^2\gamma r_0\xi_{\rm cr}$ is the energy needed to rotate a monomer around its connection point by $\pi/2$ rad called the rolling energy, and $\xi_{\rm cr}$ is the critical rolling displacement (Dominik and Tielens, 1997). Subsequently, we found that the compressive strength $P_{\rm c}$ is given by

$$P_{\rm c} \sim \frac{E_{\rm roll}}{{R_{\rm gyr}}^2 R_{\rm geo}} \sim \frac{E_{\rm roll}}{{r_0}^3}\phi^{(2+\alpha)/(3-D_{\rm f})}, \tag{6.36}$$

and $(2+\alpha)/(3-D_{\rm f}) \simeq 2.99$ for compressed BCCA clusters. The derived relation shows an excellent agreement with the numerical results of Kataoka et al. (2013b), i.e., $P_{\rm c} \sim (E_{\rm roll}/{r_0}^3)\phi^3$.

We note that the original explanation by Kataoka et al. (2013b) might not be accurate. Kataoka et al. (2013b) evaluated the work required for compression as

$$F_{\rm c} R_{\rm gyr} \sim E_{\rm roll}, \tag{6.37}$$

and the filling factor dependence of the compressive strength was obtained as

$$P_{\rm c} \sim \frac{E_{\rm roll}}{{R_{\rm gyr}}^3} \sim \frac{E_{\rm roll}}{{r_0}^3}\phi^{3/(3-D_{\rm f})}. \tag{6.38}$$

This estimate was based on the assumption that the compression is accompanied by the rolling of single pair of monomers in a BCCA cell. In this derivation, $3/(3-D_{\rm f}) \simeq 2.69$ and it might not reproduce their numerical results. Although our findings suggest that the α parameter associated with the chain length plays a significant role on the compression of dust aggregates, further studies on the force distribution within compressed fractal aggregates are required.

6.4.2 Revisiting the average coordination number of compressed aggregates

The average coordination number (i.e., the average number of contacts per monomer) Z increases as an aggregate is compressed. Arakawa et al. (2019c) found that, for compressed BCCA clusters, the filling factor dependence of Z is given by $Z = 2 + 9.38\phi^{1.62}$. Here, we derive this equation from the geometrical structure.

Considering the graph structure of BCCA cluster, which is a tree (i.e., a connected acyclic graph), the average coordination number of a compressed BCCA clusters is

$$Z \sim \frac{2N + C}{N}, \tag{6.39}$$

where the constant C is the number of the inter-cell contacts per BCCA cell. The number of the faces, edges, and corners within a cube is 6, 12, and 8, respectively. Subsequently, we assume that the number of the inter-cell contacts per BCCA cell is $C \sim 9$.

We define the deviation of the coordination number from two, $\zeta \equiv Z - 2$. The deviation ζ is given by

$$\zeta \sim \frac{C}{N} \sim C\phi^{D_{\rm f}/(3-D_{\rm f})}, \tag{6.40}$$

and $1.60 < D_\mathrm{f}/(3 - D_\mathrm{f}) < 1.79$ when we take the uncertainty of D_f into consideration. Therefore, we obtain the following equation:

$$Z = 2 + C\phi^{D_\mathrm{f}/(3-D_\mathrm{f})}, \tag{6.41}$$

which is consistent with the numerical result of Arakawa et al. (2019c), although the uncertainty of $D_\mathrm{f}/(3 - D_\mathrm{f})$ is large and future studies on both the fractal dimension analysis and the average coordination number are essential. We note that the fractal dimension D_f depends on the formation process of dust aggregates. Therefore, the average coordination number Z also depends on the formation process of dust aggregates, as reported in Seizinger and Kley (2013).

The compressive strength P_c is also affected by the average coordination number Z. If the average coordination number is $Z \simeq 2$, nearly all the monomers can roll when they are compressed. Therefore, the interparticle force is close to the rolling friction force and the compressive strength is given by Equation (6.36). On the other hand, in the high-density region ($\phi \gg 0.1$ and $Z \gg 2$), most of the particles cannot roll freely and the compressive strength is larger than the evaluated value for the case of $Z \simeq 2$ (e.g., Güttler et al., 2009; Seizinger et al., 2012; Omura and Nakamura, 2017, 2018). Then, we expect that the compressive strength would be given by the sliding friction force in the high-density limit (Omura and Nakamura, 2017), although future studies are required to understand this in detail.

6.5 Summary

In this study, we conducted the numerical simulations of the BCCA of small dust particles and calculated the geometrical structure of the fractal dust aggregates. Additionally, we derived the filling factor dependence of the physical properties of porous dust aggregates. Our key findings are summarized as follows.

1. We calculated the gyration radius R_gyr and the graph-based geodesic radius R_geo as the functions of the number of constituent particles N. We found that $R_\mathrm{gyr}/r_0 \sim N^{0.531\pm0.011}$ and $R_\mathrm{geo}/r_0 \sim N^{0.710\pm0.013}$, where r_0 is the radius of constituent particles. Thereafter, we defined two constants which characterize the geometrical structure of fractal aggregates: D_f and α. The definition of D_f and α are $N \sim (R_\mathrm{gyr}/r_0)^{D_\mathrm{f}}$ and $R_\mathrm{geo}/r_0 \sim (R_\mathrm{gyr}/r_0)^{\alpha}$, respectively. We revealed that $D_\mathrm{f} \simeq 1.88$ and $\alpha \simeq 1.34$ for BCCA clusters.

2. Kataoka et al. (2013b) found that the geometrical structure of statically compressed BCCA clusters is characterized by bifractality. This structure evolution suggests that the static compression reconstructs the fractal aggregate first on a large scale because of the weak compressive strength on a large scale. Therefore, we can imagine that it is possible to understand the physical properties of statically compressed BCCA clusters from the geometrical structure of small BCCA clusters preserved in compressed aggregates ("BCCA cells").

3. We investigated the filling factor dependence of thermal conductivity of statically compressed aggregates. We found that the filling factor dependence can be interpreted from the geometrical structure of dust aggregates. The thermal conductivity of statically compressed aggregates k is given by $k \sim 2k_{\rm mat}(r_{\rm c}/r_0)\phi^{(1+\alpha)/(3-D_{\rm f})}$, where $k_{\rm mat}$ is the material thermal conductivity, $r_{\rm c}$ is the contact radius of constituent particles, and ϕ is the filling factor of dust aggregates.

4. The compressive strength $P_{\rm c}$ is also derived from the geometrical structure as $P_{\rm c} \sim (E_{\rm roll}/{r_0}^3)\phi^{(2+\alpha)/(3-D_{\rm f})}$, where $E_{\rm roll}$ is the energy needed to rotate a monomer around its connection point by $\pi/2$ rad. Our finding suggests that the α parameter associated with the chain length plays a significant role in the compression of dust aggregates. In addition, the average coordination number Z is derived from the geometrical structure as $Z = 2 + C\phi^{D_{\rm f}/(3-D_{\rm f})}$, where $C \sim 9$ is the number of the inter-cell contacts per BCCA cell.

Chapter 7

Comet 67P/Churyumov–Gerasimenko is a hierarchical aggregate

Sota Arakawa and Kazumasa Ohno

Abstract

The *Rosetta* mission to comet 67P/Churyumov–Gerasimenko has provided plenty of data to understand what comets are made of. The thermal and mechanical properties of dust aggregates depend on their internal structure, i.e., whether homogeneous or hierarchical. In this study, we calculated the thermal inertia, tensile strength, and compressive strength of homogeneous dust aggregates using theoretically derived formulae. We found that we cannot explain the tensile strength of the comet if it is a homogeneous aggregate of μm-sized dust grains. We also derived the formulae for the physical properties of hierarchical dust aggregates. We found that the thermal inertia, tensile strength, and compressive strength of the comet is consistent with the hierarchical aggregate of cm- or dm-sized constituent aggregates. These findings indicate that the icy planetesimals may form via accretion of cm- or dm-sized compressed dust aggregates in the solar nebula.

7.1 Introduction

Comets are small and irregular-shaped objects composed of ices, organics, and refractory materials. We thought that comets formed in the outer region of the early solar nebula, where the disk temperature is much lower than the sublimation temperature of H_2O ice. Observations of the abundances of CO and CO_2 in various comets indicate that they might form between the CO and CO_2 ice lines (e.g., A'Hearn et al., 2012). Because comets spent a long time under cold conditions since their formation, they would be pristine objects and provide

precious clues about the environment of the early solar system. For example, the chemical composition of comets is the key to understanding the time evolution of the disk temperature and chemical abundances (e.g., Willacy et al., 2015; Eistrup et al., 2019). The physical properties also give us plenty of information.

Understanding the physical properties of cometary dust is essential to construct the planet formation scenario. There are numerous studies on the thermal and mechanical properties of comets constrained from observations and explorations (see, e.g., Groussin et al., 2019). Thermal properties are useful for understanding the physical characteristics of constituent particles of the surface dust layer (e.g., Blum et al., 2017; Hu et al., 2017). The mechanical strengths, e.g., compressive and tensile strength, are thought to reflect the information from the subsurface of cometary nuclei (e.g., Groussin et al., 2015; Basilevsky et al., 2016).

Experimental studies about the thermal conductivity of dust aggregates (e.g., Krause et al., 2011; Sakatani et al., 2017, 2018) revealed that the thermal conductivity depends on the porosity of the dust aggregates and the size and composition of constituent particles. We note that numerical studies about the thermal conductivity of dust aggregates (e.g., Sirono, 2014; Arakawa et al., 2017, 2019c) can reproduce the results from laboratory experiments, and Arakawa et al. (2019b) gave a theoretical explanation. Therefore, it could be possible to retrieve the nature of the constituent particles of comets using thermo-physical modeling and observations.

There are also several experimental studies about the tensile strength (e.g., Blum et al., 2006; Meisner et al., 2012; Gundlach et al., 2018) and compressive strength (e.g., Güttler et al., 2009; Schräpler et al., 2015; Omura and Nakamura, 2018) of dust aggregates. Using the numerical simulations of dust aggregates, Tatsuuma et al. (2019) obtained the theoretical formula to predict the tensile strength, and Kataoka et al. (2013b) obtained the formula of the compressive strength for fluffy aggregates (see also Seizinger et al., 2012; Seizinger and Kley, 2013; Arakawa et al., 2019b). Thus we could constrain the porosity and the size of constituent particles of comets when the cometary dust particles are pristine and preserved as dust aggregates even in the subsurface of cometary nuclei.

The *Rosetta* mission to comet 67P/Churyumov–Gerasimenko (hereinafter referred to as *comet 67P/C–G*) has provided plenty of data to understand what comets are made of. In the context of planetesimal formation, the direct aggregation hypothesis was proposed for the origin of small icy bodies (e.g., Okuzumi et al., 2012). In this model, dust aggregates turn into km-sized comets via collisional growth and static compression (Kataoka et al., 2013a), and the resulting comets would be porous and homogeneous aggregates composed of μm-sized grains. On the other hand, if comets formed via the gravitational collapse of a clump of mm- to dm-sized compressed dust aggregates called pebbles (e.g., Johansen and Youdin, 2007; Yang et al., 2017), then the internal structure of comets would be described by hierarchical aggregates (e.g., Gundlach and Blum, 2012; Skorov and Blum, 2012; Blum et al., 2017). The thermal and mechanical properties must be dependent on the structure of dust aggregates, i.e., whether homogeneous or hierarchical. These physical properties also depend on the nature of the constituent particles, e.g., the size and chemical composition.

In this study, we calculated the thermal inertia, tensile strength, and compressive strength of homogeneous dust aggregates using theoretically derived

formulae (e.g., Arakawa et al., 2019b; Tatsuuma et al., 2019). We found that we cannot explain thermal inertia, tensile strength, and compressive strength simultaneously if we assumed that comet 67P/C–G is a homogeneous aggregate of μm-sized dust grains. Then we discussed the physical properties of hierarchical dust aggregates of cm- or dm-sized constituting aggregates. For the case of comet 67P/C–G, we found that the thermal properties of constituting aggregates determine the diurnal temperature variation. In contrast, the tensile strength strongly depends on whether the structure of dust aggregates is homogeneous or hierarchical, and the hierarchical aggregate of cm- or dm-sized aggregates might be the best solution to explain the low tensile strength of comet 67P/C–G. These findings indicate that the icy planetesimals in the solar nebula might form via the gravitational collapse of dust clumps in the disk, and dust aggregates in the solar nebula were cm-sized and highly compressed.

7.2 Mechanical models

7.2.1 Organic-mantled grains (OMGs)

The surface dust layer of comets is composed of (complex) organics and refractory minerals. From the cometary secondary ion mass analyzer instrument measurements during the *Rosetta* mission, cometary dust particles ejected from the surface of comet 67P/C–G are the mixture of anhydrous silicates and organics (Bardyn et al., 2017). The organic matter also exists in chondritic porous interplanetary dust particles, which come from comets (e.g., Flynn et al., 2013). This organic matter is thought to form via grain-surface reactions by cosmic-rays and ultraviolet photons (e.g., Piani et al., 2017). The chondritic porous interplanetary dust particles are the cometary origin and represent the pristine materials in the solar nebula (e.g., Ishii et al., 2008), and individual (sub)μm-sized grains are mantled by organic matter (e.g., Flynn et al., 2013). Thus, we assumed that the individual grains (hereinafter refereed to as *monomer grains*) are the organic-mantled grains (OMGs). Homma et al. (2019) recently introduced the particle interaction model for OMGs, and we summarize their model.

7.2.2 Particle interaction model

An adhesion model for two sticking homogeneous and spherical grains was proposed by Johnson, Kendall and Roberts (1971), called JKR contact theory (see also Johnson, 1987; Dominik and Tielens, 1997; Wada et al., 2007). In JKR theory, the contact radius of two sticking spherical monomers, a_c, is given by

$$a_c = \left(\frac{9\pi\gamma}{2Y^*R}\right)^{1/3} R, \tag{7.1}$$

where γ is the surface energy, Y^* is the reduced Young's modulus, and R is the monomer radius. The reduced Young's modulus is defined as

$$Y^* = \frac{Y}{1-\nu^2}, \tag{7.2}$$

where Y_{org} is Young's modulus, and ν_{org} is the Poisson's ratio.

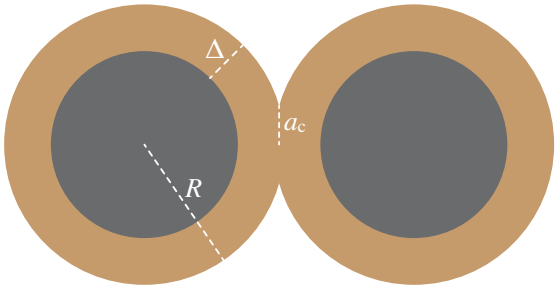

Figure 7.1: Schematic illustration of the two contacting organic-mantled grains (OMGs). In case of the contact radius a_c is much smaller than the thickness of organic mantles Δ, the silicate cores have no effect on the adhesion of the OMGs.

The stress distribution in contacting monomers around the contacting area is given in Johnson (1987), and the spatial scale of the stress distribution is a_c. Therefore, for the case of two contacting OMGs, the contact radius a_c is determined by the material properties of the organic mantle When the thickness of mantle, Δ, is larger than the contact radius a_c. The schematic figure of two contacting OMGs is shown in Figure 7.1.

In this study, we assumed that the mechanical properties of the organic mantle are the same as the analogs of organic aerosols in Titan called tholin (Yu et al., 2017): $\gamma_{org} = 70.9$ mJ m^{-2}, $Y_{org} = 3.0$ GPa, and $\nu_{org} = 0.3$, respectively. The typical value of the surface energy of organic is of the order of 10–100 mJ m^{-2} (e.g., Fowkes, 1964), Young's modulus of organics below the glass transition temperature is of the order of 1–10 GPa (e.g., Yu et al., 2018), and the Poisson's ratio is in the range of 0.3–0.4 (e.g., Sanditov, 2016). Thus our assumptions for γ_{org}, Y_{org}, and ν_{org} are reasonable.

We assumed that the material density of organic mantles is $\rho_{org} = 1000$ kg m^{-3}, which is equal to the density of polystyrene latex (Krijt et al., 2014). The material density of silicate cores is $\rho_{sil} = 3000$ kg m^{-3}. The observationally suggested mass fractions of organic matter and refractory silicates are $f_{org} = 0.45$ and $f_{sil} = 0.55$ (Bardyn et al., 2017), then the volume fractions of the organic mantle and silicate core are assumed to be

$$\chi_{org} = \frac{f_{org}/\rho_{org}}{f_{org}/\rho_{org} + f_{sil}/\rho_{sil}} = 0.71, \tag{7.3}$$

and

$$\chi_{sil} = \frac{f_{sil}/\rho_{sil}}{f_{org}/\rho_{org} + f_{sil}/\rho_{sil}} = 0.29, \tag{7.4}$$

respectively. The mean material density of OMGs is

$$\rho_{mat} = \left(\frac{f_{org}}{\rho_{org}} + \frac{f_{sil}}{\rho_{sil}}\right)^{-1} = 1.58 \times 10^3 \text{ kg m}^{-3}. \tag{7.5}$$

The thickness of the organic mantle is therefore given by

$$\Delta = \left(1 - \chi_{sil}{}^{1/3}\right) R = 0.34R, \tag{7.6}$$

and the condition for using the JKR theory is

$$a_{\rm c} < \Delta. \tag{7.7}$$

When we assume $\gamma = \gamma_{\rm org}$, $Y = Y_{\rm org}$, and $\nu = \nu_{\rm org}$, the contact radius between two sticking OMGs is

$$a_{\rm c} = 6.7 \times 10^{-2} \left(\frac{R}{1\ \mu{\rm m}} \right)^{-1/3} R, \tag{7.8}$$

and the condition for using the JKR theory is fulfilled for μm-sized OMGs.

The critical pulling force to separate two sticking monomers, $F_{\rm c}$, is given by (Johnson et al., 1971)

$$F_{\rm c} = \frac{3}{2} \pi \gamma R, \tag{7.9}$$

and the critical pulling force does not depend on the elastic property of contacting monomers. The rolling energy needed to rotate a monomer around its contacting point by 90° (hereinafter referred to as *rolling energy*), $E_{\rm roll}$, is described as (Dominik and Tielens, 1997)

$$E_{\rm roll} = 6\pi^2 \gamma R \xi_{\rm c}, \tag{7.10}$$

where $\xi_{\rm c}$ is the critical rolling displacement. Krijt et al. (2014) found that $\xi_{\rm c}$ is given by

$$\xi_{\rm c} = \frac{a_{\rm c}}{12} \left(\frac{\Delta\gamma}{\gamma} \right), \tag{7.11}$$

where $(\Delta\gamma/\gamma)$ is the fixed adhesion hysteresis, and $(\Delta\gamma/\gamma) \simeq 3$ for polystyrene latex.

7.2.3 Structures of dust aggregates

The structure of dust aggregates depends on their accretion and compression history. Figure 7.2 shows the schematic illustrations of homogeneous and hierarchical aggregates (see also Gundlach and Blum, 2012; Skorov and Blum, 2012).

Homogeneous aggregates are thought to form via static compression of fluffy dust aggregates (e.g., Kataoka et al., 2013b,a). Thus, if comets formed via accretion of fluffy aggregates, the internal structure of comets would be a homogeneous aggregate due to the static compression caused by self-gravity. In contrast, the comets formed via accretion of compressed aggregates would become hierarchical aggregates when the compressive strength of constituting aggregates is much higher than the self-gravity inside the comets.

7.2.4 Mechanical strengths of homogeneous aggregates

The tensile strength of homogeneous OMG aggregates, $P_{\rm t}$, is given by Tatsuuma et al. (2019) as follows:

$$P_{\rm t} = 0.12 \frac{F_{\rm c}}{R^2} \phi^{1.8} = 2.2 \times 10^3 \left(\frac{R}{1\ \mu{\rm m}} \right)^{-1} \left(\frac{\phi}{0.2} \right)^{1.8} {\rm Pa}. \tag{7.12}$$

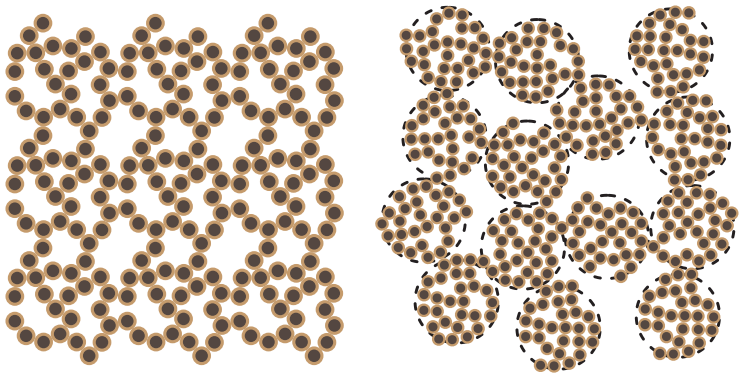

(a) homogeneous aggregate (b) hierarchical aggregate

Figure 7.2: Schematic illustrations of a homogeneous aggregate and a hierarchical aggregate used in this study. (a) A homogeneous aggregate formed via static compression of fluffy dust aggregates (e.g., Kataoka et al., 2013a,b). The radius of each monomer is R and we assume that the constituting monomers are monodisperse. The filling factor of aggregates is ϕ. (b) A hierarchical aggregate formed via accretion of constituting aggregates (surrounded by dashed circles). The constituting aggregates are described by homogeneous aggregates of the aggregate radius of $R_{\rm agg}$ and monomer radius of R, while the physical properties of bulk hierarchical aggregates are different from that of homogeneous aggregates (e.g., Gundlach and Blum, 2012; Skorov and Blum, 2012). The filling factor inside constituting aggregates is $\phi_{\rm agg}$, and the packing fraction of constituting aggregates is $\phi_{\rm p}$, thus the total filling factor of a hierarchical aggregate is given by $\phi = \phi_{\rm agg}\phi_{\rm p}$.

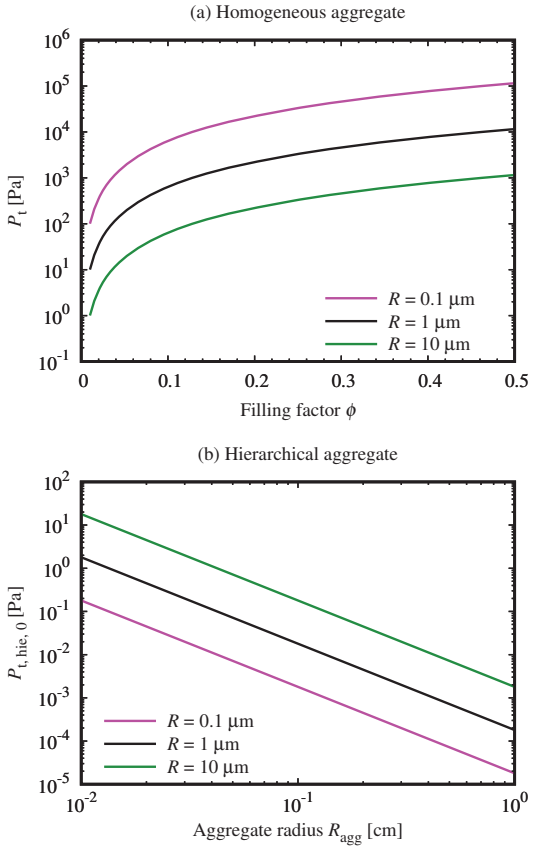

Figure 7.3: The tensile strength of homogeneous aggregates and hierarchical aggregates. (a) The tensile strength of homogeneous aggregates, P_t, as a function of the filling factor ϕ. Magenta: for the case of $R = 0.1$ μm. Black: for the case of $R = 1$ μm. Green: for the case of $R = 10$ μm. (b) The tensile strength of uncompressed hierarchical aggregates, $P_{t,hie,0}$, as a function of the aggregate radius R_{agg}. Magenta: for the case of $R = 0.1$ μm. Black: for the case of $R = 1$ μm. Green: for the case of $R = 10$ μm.

The compressive strength P_c is also given by Kataoka et al. (2013b):

$$P_c = \frac{E_{roll}}{R^3}\phi^3 = 5.6 \times 10^2 \left(\frac{R}{1\ \mu\mathrm{m}}\right)^{-4/3} \left(\frac{\phi}{0.2}\right)^3 \mathrm{Pa}, \tag{7.13}$$

where ϕ is the filling factor of the aggregate (see also Arakawa et al., 2019b). The tensile strength of homogeneous aggregates, P_t, is shown in Figure 7.3(a).

This is because most of the particles cannot roll freely when $\phi \gtrsim 0.2$, and thus the compressive strength of well-compressed aggregates cannot be evaluated from Equation (7.13). Although there is no theoretical model that can predict the compressive strength of dust aggregates of arbitrary monomer radius and filling factor, there are numerous experimental studies of the compression of dust aggregates. Figure 7.4(a) shows the filling factor dependence of the compressive strength of homogeneous dust aggregates composed of

monodisperse spherical particles (see Omura and Nakamura, 2018, and references therein).

7.2.5 Mechanical strengths of hierarchical aggregates

Critical pulling force

The critical pulling force to separate two sticking 0.1 mm-sized aggregates, $F_{\rm c,agg}$, is experimentally studied by Brisset et al. (2016). In their experiments, the statistical threshold velocity between sticking and bouncing is measured. Then the critical pulling force $F_{\rm c,agg}$ was evaluated from the threshold velocity between sticking and bouncing. Figure 7.5 shows the experimental results of $F_{\rm c,agg}$ for various aggregate radius $R_{\rm agg}$. The monomers used in Brisset et al. (2016) are $R \simeq 1$ μm-sized SiO_2 grains. The physical properties of SiO_2 grains are listed in Dominik and Tielens (1997): $\gamma_{\rm sil} = 25$ mJ m^{-2}, $Y_{\rm sil} = 54$ GPa, and $\nu_{\rm sil} = 0.17$.

Monomer-monomer contact model. Here we propose a simple model of $F_{\rm c,agg}$ for uncompressed sticking aggregates. Figure 7.6 shows the schematic illustration. When there is no external pressure, the number of inter-aggregate contacts, n, would be $n \sim 1$. Then the critical pulling force for uncompressed sticking aggregates is given by

$$F_{\rm c,agg} = n \cdot \frac{3}{2}\pi\gamma R = 1.2 \times 10^{-7} \left(\frac{\gamma}{25\ {\rm mJm^{-2}}}\right)\left(\frac{R}{1\ \mu{\rm m}}\right) {\rm N}, \tag{7.14}$$

which is equal to the $F_{\rm c}$ of two sticking monomers when we assume $n = 1$. We can explain the experimental results (Brisset et al., 2016) by using the monomer-monomer contact model (see Figure 7.6).

Effective surface energy model. We also note that the effective surface energy model (Weidling et al., 2012; Brisset et al., 2016) cannot explain the experimental results. Weidling et al. (2012) introduced the "effective surface energy" $\gamma_{\rm eff}$ as follows:

$$\gamma_{\rm eff} = \gamma\phi_{\rm agg}\frac{{a_{\rm c}}^2}{R^2}. \tag{7.15}$$

The critical pulling force for uncompressed sticking aggregates would be given by

$$\left(F_{\rm c,agg}\right)_{\rm ESE} = n \cdot \frac{3}{2}\pi\gamma_{\rm eff}R_{\rm agg}, \tag{7.16}$$

in the framework of the effective surface energy model. Assuming that $\phi_{\rm agg} = 0.37$ (Brisset et al., 2016) and $n = 1$, the critical pulling force will be (see Figure 7.5)

$$\left(F_{\rm c,agg}\right)_{\rm ESE} = 1.5 \times 10^{-9} \left(\frac{R_{\rm agg}}{0.1\ {\rm mm}}\right) {\rm N}; \tag{7.17}$$

however, the experimental results suggest that $F_{\rm c,agg} \simeq 10^{-7}$ N for 0.1 mm-sized aggregates*. Since the condition that $n \sim 10^2$ seems to be unrealistic (because the average coordination number of aggregates is much lower than 12,

* Note that Brisset et al. (2016) calculated the surface energy γ from the effective surface energy $\gamma_{\rm eff}$ (see Table 4 of Brisset et al., 2016). However, we found that their calculation contains errors:

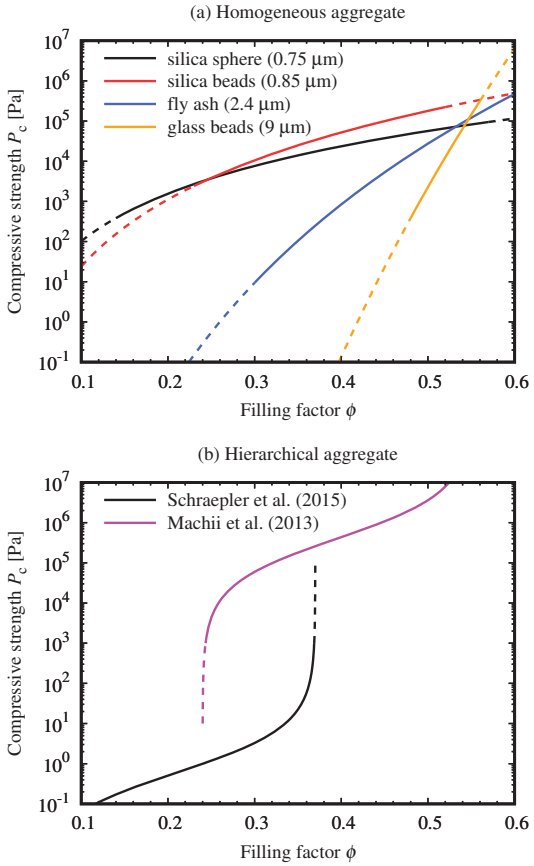

Figure 7.4: (a) Filling factor dependence of the compressive strength of homogeneous aggregates composed of monodisperse spherical particles. Experiments are done by Güttler et al. (2009, black) for dust aggregates of $R = 0.75$ μm silica spheres, Omura and Nakamura (2018, magenta) for $R = 0.85$ μm silica beads, Omura et al. (2016, blue) for $R = 2.4$ μm fly ash, and Omura and Nakamura (2017, green) for $R = 9$ μm glass beads, respectively. Experimental data were fitted using a polytropic relation by Omura and Nakamura (2018), and dashed lines are the extrapolation of experimental results. (b) Filling factor dependence of the compressive strength of hierarchical aggregates. Experiments are done by Schräpler et al. (2015, black) for hierarchical aggregates of $R = 0.75$ μm and $R_{\rm agg} \simeq 0.09$ mm and Machii et al. (2013, maghenta) for hierarchical aggregates of $R = 0.4$ μm and $R_{\rm agg} \simeq 0.5$ mm. Experimental data were fitted using a empirical function proposed by Güttler et al. (2009). The fitting coefficients are listed in Table 1 of Schräpler et al. (2015).

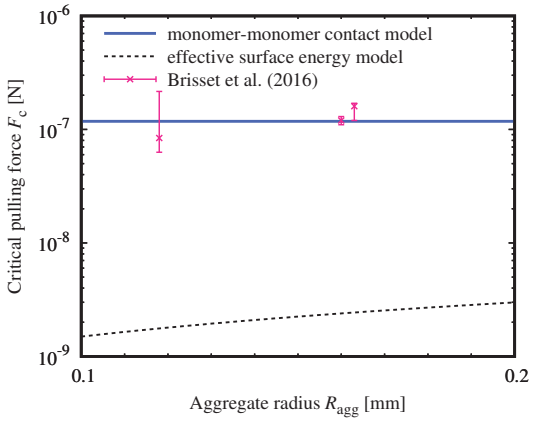

Figure 7.5: The critical pulling force for sticking aggregates $F_{c,agg}$. Magenta crosses with a vertical error bar are the experimental results of Brisset et al. (2016). The blue solid line is the prediction of monomer-monomer contact model proposed in this study. We assumed the number of inter-aggregate contacts is $n = 1$. The black dashed line is the prediction of effective surface energy model (Weidling et al., 2012; Brisset et al., 2016).

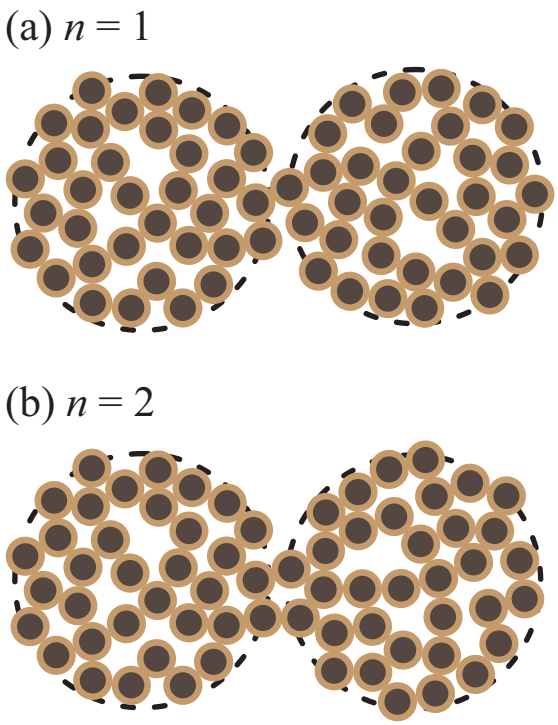

Figure 7.6: Schematic illustrations of two contacting aggregates. (a) Two contacting aggregates with the number of inter-aggregate contacts of $n = 1$. (b) Two contacting aggregates with the number of inter-aggregate contacts of $n = 2$. We assume that $n \sim 1$ for the contacts between uncompressed sticking aggregates, and n increases with compression of hierarchical aggregates.

i.e., the maximum coordination number for monodispersed grains), we conclude that the effective surface energy model (Weidling et al., 2012) might contain a critical error.

Tensile strength

We can theoretically derive the tensile strength of uncompressed hierarchical aggregates, $P_{\rm t,hie,0}$, using Equation (7.16) as follows:

$$P_{\rm t,hie,0} = 0.12 \frac{F_{\rm c,agg}}{{R_{\rm agg}}^2} {\phi_{\rm p}}^{1.8}, \\ = 0.63 \left(\frac{R}{1\ \mu{\rm m}} \right) \left(\frac{R_{\rm agg}}{0.1\ {\rm mm}} \right)^{-2} \left(\frac{\phi_{\rm p}}{0.64} \right)^{1.8} {\rm Pa}. \tag{7.18}$$

Here we assumed the monomers are spherical SiO_2 grains. The tensile strength of uncompressed hierarchical aggregates, $P_{\rm t,hie,0}$, is shown in Figure 7.3(b). We assumed $\phi_{\rm agg} = 0.64$ in Figure 7.3(b).

Although there are no experimental studies on the tensile strength of uncompressed hierarchical aggregates, Blum et al. (2014) studied the tensile strength of compressed hierarchical aggregates, $P_{\rm t,hie}(P)$, as a function of the compression pressure P. Figure 7.7 shows their experimental results, and we found that the tensile strength of uncompressed hierarchical aggregates,

$$P_{\rm t,hie,0} \equiv \lim_{P \to 0} P_{\rm t,hie}(P), \tag{7.19}$$

must be lower than 5 Pa for the case of $R \simeq 1\ \mu$m and 0.1 mm $< R_{\rm agg} <$ 1 mm. Thus our estimate (Equation 7.18) is consistent with the experimental results of Blum et al. (2014), although future precise measurements of $P_{\rm t,hie,0}$ and $P_{\rm t,hie}(P)$ are needed.

Compressive strength

Schräpler et al. (2015) studies the compressive strength of hierarchical aggregates. The monomer radius and aggregate radius used in Schräpler et al. (2015) are $R = 0.75\ \mu$m and $R_{\rm agg} \simeq 0.09$ mm, and the filling factor inside constituting aggregates is $\phi_{\rm agg} = 0.35$ (Weidling et al., 2012). We can imagine that hierarchical aggregates are initially compressed from a large scale ($\sim R_{\rm agg}$) because the compressive strength for the inter-aggregate structure is lower than that of intra-aggregate structure. Then the compaction stops when the packing fraction of constituting aggregates, $\phi_{\rm p}$, reaches $\phi_{\rm p} \simeq 0.6$. Figure 7.4(b) shows the filling factor dependence of the compressive strength of hierarchical aggregates.

Machii et al. (2013) also studied the compressive strength of hierarchical aggregates. The measured compressive strength in Machii et al. (2013) is much

when we assumed $Y = 5.4 \times 10^{10}$ Pa, the measured surface energy scaled down to a monomer particle would be $\gamma = 4.5 \times 10^{-2}$ J m^{-2} for aggregates composed of monodisperse grains and 5.3×10^{-2} J m^{-2} for aggregates composed of polydisperse grains. These values are much larger than their results: $\gamma = 1.7 \times 10^{-2}$ J m^{-2} for aggregates composed of monodisperse grains and 2.0×10^{-2} J m^{-2} for aggregates composed of polydisperse grains. Indeed, we can reproduce their calculation if we applied $Y = 5.4 \times 10^{9}$ Pa, which is ten times lower than the canonical value (Dominik and Tielens, 1997).

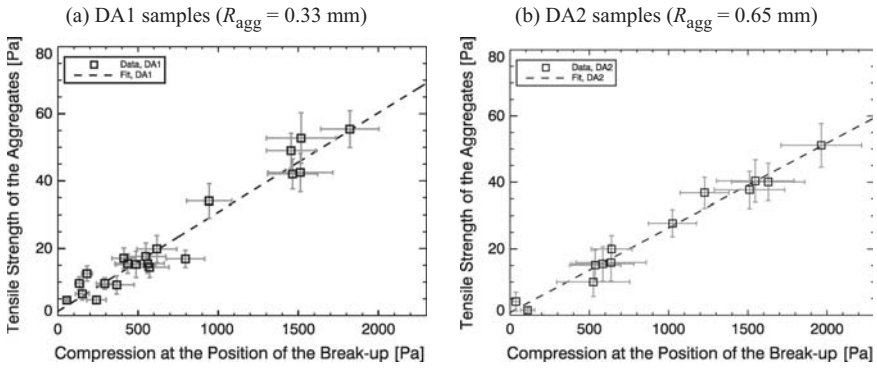

Figure 7.7: Tensile strengths of hierarchical aggregates as a function of the compression pressure at the position of the break-up (squares). (a) The DA1 samples are hierarchical aggregates, and the mean radius of the aggregates is $R_{agg} = 0.33$ mm. (b) The DA2 samples are also hierarchical aggregates, and the mean radius of the aggregates is $R_{agg} = 0.65$ mm. The monomer particles of both DA1 and DA2 samples are micron-sized SiO_2 particles, and the mean particle radius is $R = 1$ μm. The dashed line shows the least-squares linear fit applied to the data. The uncertainties of the tensile strength measurements are denoted by the gray error bars. Experimental results shows that $P_{t,hie,0}$ of both DA1 and DA2 samples is 0–5 Pa. (Figures taken from Figures 7 and 8 of Blum et al., 2014)

higher than that of Schräpler et al. (2015); thus, Machii et al. (2013) observed the compression of constituent aggregates in this stage. The hierarchical aggregates are prepared by using sieves with mesh sizes of 1.0 mm and 1.6 mm. The monomer radius and aggregate radius used in Schräpler et al. (2015) are $R = 0.4$ μm and $R_{agg} \simeq 0.5$ mm. Note that the data of Machii et al. (2013) start at $\phi = 0.24$, whereas the data of Schräpler et al. (2015) end at $\phi = 0.37$. This discrepancy might be originated from the different preparation methods of the hierarchical aggregates (Schräpler et al., 2015), or due to the different monomer and aggregate radii. Future studies on this point are needed to understand the compressive strength of hierarchical aggregates.

7.3 Mechanical strengths of comet 67P/C–G

In this section, we consider estimates for the material strength of the nucleus of comet 67P/C–G. Then we discuss the structure of the nucleus. The main issues in this study are; (1) whether cometary building blocks are consolidated rocks or unconsolidated aggregates, (2) if the comet is an unconsolidated aggregate, whether the internal structure is homogeneous or hierarchical, and (3) how large the constituting aggregates and monomer grains are.

7.3.1 Tensile strength

The tensile strength of the nucleus of comet 67P/C–G is measured in various spatial scales. Figure 7.8(a) is the summary of estimates of P_t. Hirabayashi et al. (2016) calculated the tensile strength at the neck region of comet 67P/C–G. Groussin et al. (2015) and Attree et al. (2018) estimated the tensile strength of

10–100 m-scale overhangs and collapsed structures observed on the surface of the comet. These estimates based on the observation and numerical calculations suggest that (i) the tensile strength of comet 67P/C–G is lower than 10^2 Pa across all spatial scales, and (ii) P_t for km-scale is not larger than that for 10 m-scale.

According to our calculation shown in Figure 7.3, the tensile strength of homogeneous aggregates is $P_t \gtrsim 10^3$ Pa when the monomer radius is $R < 1$ μm and the filling factor is $\phi > 0.1$. Therefore homogeneous dust aggregates of (sub)μm-sized monomers cannot explain the weak tensile strength of comet 67P/C–G, as mentioned in previous studies (e.g., Tatsuuma et al., 2019).

The mechanical strength of consolidated rocks is usually dependent on the spatial scale (e.g., Petrovic, 2003; Xu, 2005). The tensile strength decreases with increasing size, and the Weibull statistical theory (Weibull, 1951) explains this phenomenon: $P_t \sim L^{-0.5}$, where L is the size of consolidated materials. However, the spatial scale dependence of the tensile strength suggests that cometary dust may not be consolidated because the tensile strength for a small scale ($L \lesssim 10$ m) is not larger than that for a large scale ($L \gtrsim 10^3$ m). Thus the nucleus of comet 67P/C–G would be neither consolidated rocks/ices nor homogeneous dust aggregates.

In contrast, the tensile strength of the comet can be explained by hierarchical aggregate model. Gundlach et al. (2015) shows that the maximum gas pressures driven by the outgassing of volatiles (e.g., H_2O and CO_2 ice) is on the order of 0.1 Pa, thus the tensile strength at the cometary surface should be lower than $\simeq 0.1$ Pa to explain the dust activity of comet 67P/C–G. Christou et al. (2018) also performed numerical simulations of gas flow through comet analogue porous medium, and they found that the gas pressure near the surface is $\sim 10^{-2}$ Pa. In Equation (7.18), we derived the the tensile strength of uncompressed hierarchical aggregates:

$$P_{t,hie,0} = 1.8 \times 10^{-2} \left(\frac{R}{1\ \mu\mathrm{m}} \right) \left(\frac{R_{agg}}{1\ \mathrm{mm}} \right)^{-2} \mathrm{Pa}. \tag{7.20}$$

Therefore a hierarchical aggregate constituted of mm-sized (or much larger) aggregates of OMGs can explain the tensile strength at the surface.

The tensile strengths for ≥ 10 m-scale would also be consistent with the hierarchical aggregate model. The tensile strength $P_{t,hie}$ increases with increasing the applied pressure P (see Figure 7.7). Assuming that the filling factor inside the nucleus is uniform (Pätzold et al., 2016), the pressure is given by (e.g., Groussin et al., 2015)

$$P(r) = \frac{4\pi G {\rho_{mat}}^2 r_{67P}}{3} \phi^2 \left(1 - \frac{d}{2r_{67P}} \right) d, \tag{7.21}$$

where G is the gravitational constant, $r_{67P} \sim 1$ km is the radius of the comet, and d is the distance from the surface, i.e., the depth. Since $P(r)$ is approximately proportional to the depth d, and $P_{t,hie}(P)$ is proportional to the applied pressure (Blum et al., 2014), we expect that $P_{t,hie}$ is proportional to the depth d when $P_{t,hie}(P) \gg P_{t,hie,0}$. Assuming that $L \sim d$, the tensile strength $P_{t,hie}$ would also be proportional to the spatial scale L.

For the case of hierarchical aggregates of $R \simeq 1$ μm and $R_{agg} \simeq 0.5$ mm, the pressure dependence of $P_{t,hie}$ is $P_{t,hie}(P) \simeq 0.03P$ (see Figure 7.7). The pressure

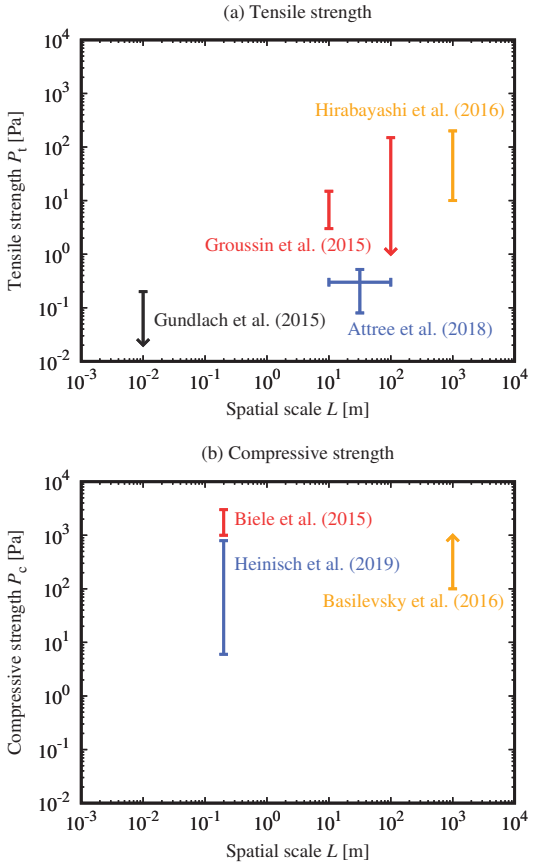

Figure 7.8: The estimates for mechanical strengths of comet 67P/C–G in various spatial scales. (a) Tensile strength P_t. Hirabayashi et al. (2016, orange): P_t at the neck region of comet 67P/C–G (1 km-scale). Groussin et al. (2015, magenta): P_t estimated from 10–100 m-scale overhangs and collapsed structures observed on the surface of the comet. Attree et al. (2018, green): P_t of 10–100 m-scale overhangs calculated from their shape profiles. Gundlach et al. (2015, grey): the maximum gas pressure at the ice-dust interface caused by the sublimation of H_2O and CO_2. (b) Compressive strength P_c. Basilevsky et al. (2016, orange): the lower limit of P_c at the bottom of a 1 km-sized cliff. Biele et al. (2015, magenta): P_c estimated from the mechanical response of the first touchdown of *Philae*. Heinisch et al. (2019, green): P_c estimated from the rebound trajectory at collision and second touchdown of *Philae*.

at the center of the larger lobe of comet 67P/C–G is $P(r_{67P}) \simeq 86$ Pa (Blum et al., 2017), then the expected pressure at the depth d is

$$P(d) \simeq 170\left(\frac{d}{r_{67P}}\right) \text{ Pa}, \tag{7.22}$$

and the tensile strength is also given by a function of the spatial scale L:

$$P_{\text{t,hie}}(L) \sim 5\left(\frac{L}{r_{67P}}\right) \text{ Pa}. \tag{7.23}$$

This estimate is in agreement with the observational results shown in Figure 7.8(a). Note that we still do not know $P_{\text{t,hie}}(P)$ for $R \ll 1$ μm or $R_{\text{agg}} \gg 1$ mm. Future studies of the measurement of $P_{\text{t,hie}}$ for various R and R_{agg} are necessary.

7.3.2 Compressive strength

The compressive strength of the nucleus of comet 67P/C–G is also studied by the *Rosetta* mission. Figure 7.8(b) is the summary of estimates of P_{c}. Results from compressive strength measurements by Basilevsky et al. (2016), Biele et al. (2015), and Heinisch et al. (2019) are consistent with both consolidated and unconsolidated materials when the filling factor inside the nucleus is uniform.

Although the compressive strength of hierarchical aggregates is not yet completely understood, the experimental studies (Schräpler et al., 2015; Machii et al., 2013) suggest that the compressive strength is on the order of 10–10^5 Pa when the total filling factor, $\phi = \phi_{\text{agg}}\phi_{\text{p}}$, is in the range of 0.25–0.35, as shown in Figure 7.4(b). Thus the hierarchical aggregate model is consistent with the observational constraint on P_{c}.

Note that the compressive strength of $P_{\text{c}} \gtrsim 10$ Pa at the depth of $d \lesssim 1$ m could be the evidence that comets did not form from fluffy aggregates with filling factor of $\phi \ll 0.1$. According to Figure 7.3, the compressive strength of fluffy aggregates is

$$P_{\text{c}} \sim 10^{-1}\left(\frac{R}{1\ \mu\text{m}}\right)^{-4/3}\left(\frac{\phi}{10^{-2}}\right)^{2} \text{ Pa}. \tag{7.24}$$

At the depth d, the accreted fluffy aggregates on the comet will be compressed when the compressive strength of the original fluffy aggregates is lower than $P(d)$. The filling factor of compressed aggregates is determined by the following equation, $P_{\text{c}} = P(d)$. The pressure at the depth of $d \sim 1$ m would be only $P \sim 10^{-1}$ Pa, however. Thus the compressive strength of $P_{\text{c}} \gtrsim 10$ Pa at the depth of $d \sim 1$ m cannot be reproduced when comets formed via accretion of fluffy aggregates with the filling factor of $\phi \ll 0.1$.

7.3.3 Impacts of chemical composition on mechanical strengths

In Figure 7.3, we calculated both P_{t} and P_{c} under the condition that monomer grains are OMGs. However, in reality, monomers in the deeper region of

comets are likely to be mantled by ices. Thus, we should evaluate the impacts of ices on P_t and P_c.

The tensile strength P_t is proportional to the surface energy γ (Tatsuuma et al., 2019, see also Eqs. 7.9 and 7.12), and it is independent of the elastic property of monomers, Y^*. The surface energy of organics used in this study is $\gamma_{org} = 70.9$ mJ m^{-2} (Yu et al., 2017), and the surface energy of H_2O ice is $\gamma_{H_2O} = 100$ mJ m^{-2} (Wada et al., 2007). The surface energy of CO_2 ice, γ_{CO_2}, would be about ten times lower than γ_{H_2O} (Musiolik et al., 2016a,b). Therefore, the expected surface energy of ice-mantled grains is in the range of 10–100 mJ m^2, and the tensile strength also changes an order of magnitude by chemical composition of the ice mantle of monomers; although the effects of R and R_{agg} on the tensile strength would be more important than the effect of chemical composition.

The compressive strength P_t also depends on the chemical composition. The dependence of P_t on γ and Y^* is $P_t \sim \gamma^{4/3} Y^{*-1/3}$ (see Eqs. 7.10 and 7.13) when the filling factor is lower than $\phi < 0.2$. The reduced Young's modulus of CO_2 ice is $\sim$ 10 GPa (Musiolik et al., 2016a), which is close to that of H_2O ice (Wada et al., 2007) and organics below the glass transition temperature ($\sim$ 300 K; Yu et al., 2018). Then the compressive strength might also change only an order of magnitude by the chemical composition of the ice mantle of monomers.

7.4 Thermal properties

7.4.1 Thermal conductivity

The thermal conductivity of homogeneous dust aggregates, k, is given by the sum of three terms:

$$k = k_{sol} + k_{rad} + k_{gas}, \tag{7.25}$$

where k_{sol} is the thermal conductivity through the solid network, k_{rad} is he thermal conductivity owing to radiative transfer, and k_{gas} is the thermal conductivity due to gas diffusion. However, the effect of k_{gas} is negligible for the case of airless bodies (see Appendix 7.A), and we only consider k_{sol} and k_{rad} in this study.

Thermal conductivity through the solid network

Arakawa et al. (2017) found that the thermal conductivity through the solid network k_{sol} is given by

$$k_{sol} = 2 k_{mat} \frac{a_c}{R} f(\phi), \tag{7.26}$$

where $f(\phi)$ is the dimensionless function of ϕ, and k_{mat} is the material thermal conductivity. The dimensionless function and $f(\phi)$ is thought to be a function of the filling factor ϕ and the average coordination number Z, and Z is also dependent on ϕ. The numerical simulations by Arakawa et al. (2019c) revealed that $f(\phi)$ and Z are given by

$$f(\phi) = 0.784 \phi^{1.99} \left(\frac{Z}{2} \right)^{0.556}, \tag{7.27}$$

and

$$Z = 2 + 9.38\phi^{1.62}. \tag{7.28}$$

Heat flows through the monomer-monomer contacts, and the heat conductance at the contact determines the heat flow within two monomers. A contact between two monomers disturbs the temperature profiles inside the grains only in a spatial scale of a_c, as in the case of stress distribution described in Section 7.2.2 (see also Gusarov et al., 2003). For the case of OMG aggregates, the material thermal conductivity of organic mantle, k_{org}, determines the thermal conductivity through the solid network when $a_c < \Delta$ is satisfied.

Thermal properties of organic polymers are in general dependent of the temperature, T. We assume that the thermal conductivity of organic mantle is the same as that of polymethyl methacrylate (see Figure 7.16):

$$\frac{1}{k_{org}} = \sqrt{\left(k_{org,1}\left(\frac{T}{100\ \mathrm{K}}\right)^{\alpha_{org,1}}\right)^{-2} + \left(k_{org,2}\left(\frac{T}{100\ \mathrm{K}}\right)^{\alpha_{org,2}}\right)^{-2}}, \tag{7.29}$$

where $k_{org,1} = 0.173\ \mathrm{W\ K^{-1}\ m^{-1}}$, $\alpha_{org,1} = 0.227$, $k_{org,2} = 0.458\ \mathrm{W\ K^{-1}\ m^{-1}}$, and $\alpha_{org,2} = 1.21$ are the fitting coefficients. We note that the thermal conductivity of organic matter is lower than those of refractory minerals and H_2O ice (see Appendix 7.B).

7.4.2 Thermal conductivity owing to radiative transfer

The thermal conductivity owing to radiative transfer is given by

$$k_{rad} = \frac{16}{3}\sigma_{SB}T^3 l_p, \tag{7.30}$$

where σ_{SB} is the Stefan-Boltzmann constant and l_p is the mean free path of photons. We evaluate the mean free path of photons as follows (e.g., Gundlach and Blum, 2012):

$$l_p = \frac{1-\phi}{\kappa_R \rho_{mat}\phi}. \tag{7.31}$$

The Rosseland mean opacity, κ_R, is defined as

$$\frac{1}{\kappa_R} = \frac{\int d\nu\ {\kappa_{eff}}^{-1}(\partial B_\nu/\partial T)}{\int d\nu\ (\partial B_\nu/\partial T)}, \tag{7.32}$$

where B_ν is the Plank function. Here, we introduce the effective absorption coefficient κ_{eff} defined as (e.g., Rybicki and Lightman, 1979)

$$\kappa_{eff} \equiv \sqrt{\kappa_{abs}(\kappa_{abs} + \kappa_{sca})}, \tag{7.33}$$

where κ_{abs} is the absorption opacity and κ_{sca} is the scattering opacity.

We calculate κ_{abs} and κ_{sca} of constituting spherical monomers with Mie theory (Bohren and Huffman, 1983) using a publicly available code LX-MIE (Kitzmann and Heng, 2018). The code is optimized to calculate the opacity of large particles and thus suitable for this study that examines a wide parameter space to large monomer sizes. The refractive index of OMGs is calculated by the effective medium theory with the Bruggeman mixing rule (Bruggeman, 1935),

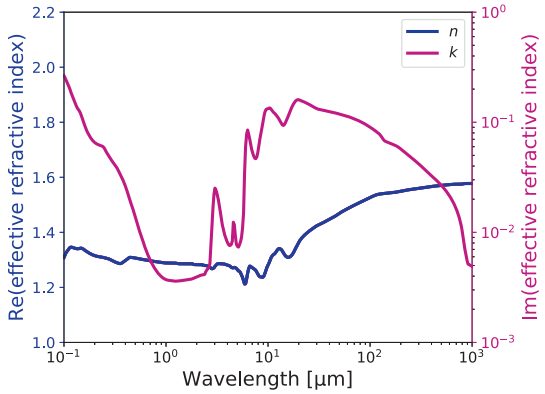

Figure 7.9: Effective refractive index assumed in this study. The horizontal axis is the wavelength. The blue and red lines show the real and imaginary parts of the calculated refractive index (see text).

where the effective dielectric function $\epsilon_{\rm eff}$ is given by (see e.g., Lee et al., 2015; Helling et al., 2019, for applications to exoplanetary clouds)

$$\chi_{\rm org}\frac{\epsilon_{\rm org}-\epsilon_{\rm eff}}{\epsilon_{\rm org}+2\epsilon_{\rm eff}}+\chi_{\rm sil}\frac{\epsilon_{\rm sil}-\epsilon_{\rm eff}}{\epsilon_{\rm sil}+2\epsilon_{\rm eff}}=0. \tag{7.34}$$

Here, $\epsilon_{\rm org}$ and $\epsilon_{\rm sil}$ are the dielectric function of organic and silicate materials. Note that the dielectric function is written as $\epsilon = m^2$, where $m = n + ik$ is the complex refractive index. To obtain the effective refractive index of OMGs, we solve Equation (7.34) with the Newton-Raphson iteration using the refractive index of astronomical silicate (Draine, 2003) and tholin (Khare et al., 1984) for cometary organics. The optical property of tholin reasonably explains the low reflectivity of 67P/C–G (Stern et al., 2015b). Figure 7.9 shows the calculated effective refractive index of OMGs. We calculate the Rosseland mean opacity integrating Equation (7.32) from $\lambda = 0.1$ μm to 1000 μm. The obtained Rosseland mean opacity is shown in Figure 7.10 as a function of temperature for various monomer sizes.

Here we note that the heat transfer within constituting aggregates is dominated by the heat conduction through the solid network. Figure 7.11 shows the contribution of $k_{\rm sol}$ on the total thermal conductivity $k = k_{\rm sol} + k_{\rm rad}$ inside the homogeneous aggregates. From our calculations, $k_{\rm sol}/k \gtrsim 0.9$ for the case of $R \simeq 1$ μm and $\phi \gtrsim 0.2$.

In contrast, the thermal conductivity of hierarchical aggregates is dominated by radiative transfer within inter-aggregate voids (e.g., Gundlach and Blum, 2012). The thermal conductivity of hierarchical aggregates, $k_{\rm hie}$, is given by

$$k_{\rm hie} = \frac{16}{3}\sigma_{\rm SB}T^3 l_{\rm p,hie}, \tag{7.35}$$

where $l_{\rm p,hie}$ is the mean free path of photons within the inter-aggregate structure of hierarchical aggregates. Since $R_{\rm agg}$ is orders of magnitude larger than the thermal radiation wavelength ($\lambda_{\rm th} = 30$ μm at $T = 100$ K), the mean free path $l_{\rm p,hie}$ is given by geometric optical approximation (Skorov et al., 2011;

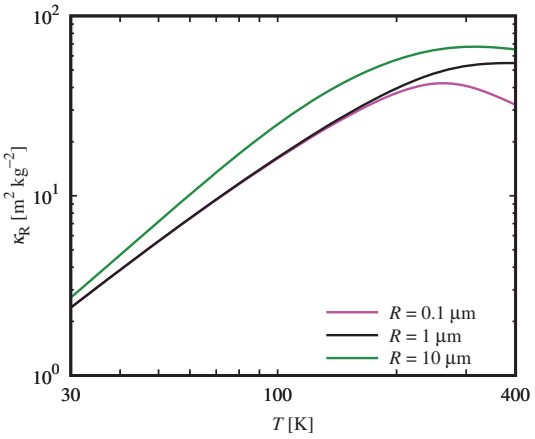

Figure 7.10: The Rosseland mean opacity of OMGs as a function of the temperature and monomer radius.

Gundlach and Blum, 2012):

$$l_{\mathrm{p,hie}} = \frac{1-\phi_{\mathrm{p}}}{(\sigma_{\mathrm{hie}}/V_{\mathrm{hie}})\phi_{\mathrm{p}}} = \frac{4}{3}\frac{1-\phi_{\mathrm{p}}}{\phi_{\mathrm{p}}} R_{\mathrm{agg}}, \tag{7.36}$$

where $\sigma_{\mathrm{hie}} = \pi {R_{\mathrm{agg}}}^2$ and $V_{\mathrm{hie}} = (4\pi/3){R_{\mathrm{agg}}}^3$ are the cross section and volume of a constituting aggregate, respectively. Assuming that $\phi_{\mathrm{p}} = 0.64$, we obtain k_{hie} as a function of T and R_{agg}:

$$k_{\mathrm{hie}} = 2.3 \times 10^{-4} \left(\frac{T}{100\ \mathrm{K}}\right)^3 \left(\frac{R_{\mathrm{agg}}}{1\ \mathrm{mm}}\right) \mathrm{W\ K^{-1}\ m^{-1}}. \tag{7.37}$$

7.4.3 Diurnal thermal skin depth

The diurnal thermal skin depth d_{s} is the e-folding depth of the diurnal variation of temperature, and the definition is

$$d_{\mathrm{s}} = \sqrt{\frac{kP_{\mathrm{rot}}}{\pi c_{\mathrm{heat}} \rho_{\mathrm{mat}} \phi}}, \tag{7.38}$$

where $P_{\mathrm{rot}} = 12.4$ h is the rotation period of comet 67P/C–G (e.g., Jorda et al., 2016) and c_{heat} is the specific heat of OMGs. The specific heat of OMGs is given by

$$c_{\mathrm{heat}} = f_{\mathrm{org}} c_{\mathrm{org}} + f_{\mathrm{sil}} c_{\mathrm{sil}}, \tag{7.39}$$

where c_{org} and c_{sil} are the specific heat of organic materials and silicates, respectively.

We assume that the specific heat of organic mantle c_{org} is the same as that of polymethyl methacrylate (see Figure 7.18):

$$\frac{1}{c_{\mathrm{org}}} = \sqrt{\left(c_{\mathrm{org},1}\left(\frac{T}{100\ \mathrm{K}}\right)^{\beta_{\mathrm{org},1}}\right)^{-2} + \left(c_{\mathrm{org},2}\left(\frac{T}{100\ \mathrm{K}}\right)^{\beta_{\mathrm{org},2}}\right)^{-2}}, \tag{7.40}$$

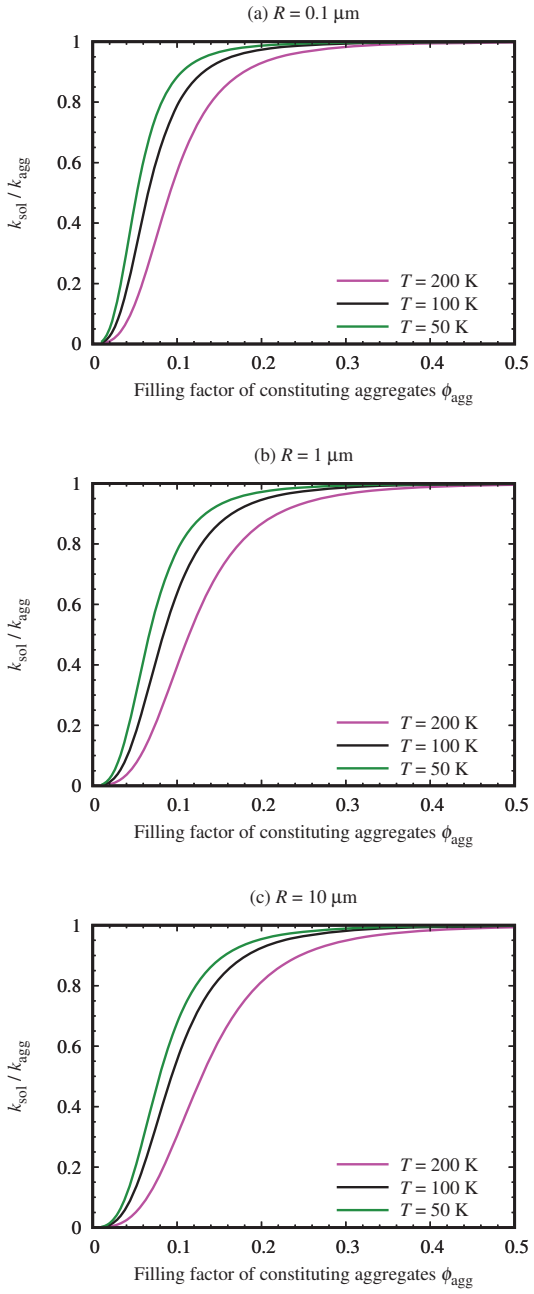

Figure 7.11: The contribution of solid thermal conductivity k_{sol} on the total thermal conductivity within homogeneous aggregates k, as a function of monomer particle radius R and the filling factor ϕ. (a) For the case that the monomer radius is $R = 0.1$ μm. (b) For the case that the monomer radius is $R = 1$ μm. (c) For the case that the monomer radius is $R = 10$ μm.

where $c_{\mathrm{org},1} = 556$ J K^{-1} kg^{-1}, $\beta_{\mathrm{org},1} = 0.829$, $c_{\mathrm{org},2} = 4890$ J K^{-1} kg^{-1}, and $\beta_{\mathrm{org},2} = 2.59$ are the fitting coefficients. We also use the specific heat of amorphous SiO_2 for c_{sil} (see Figure 7.18):

$$\frac{1}{c_{\mathrm{sil}}} = \sqrt{\left(c_{\mathrm{sil},1}\left(\frac{T}{100\ \mathrm{K}}\right)^{\beta_{\mathrm{sil},1}}\right)^{-2} + \left(c_{\mathrm{sil},2}\left(\frac{T}{100\ \mathrm{K}}\right)^{\beta_{\mathrm{sil},2}}\right)^{-2}}, \tag{7.41}$$

where $c_{\mathrm{sil},1} = 771$ J K^{-1} kg^{-1}, $\beta_{\mathrm{sil},1} = 0.197$, $c_{\mathrm{sil},2} = 281$ J K^{-1} kg^{-1}, and $\beta_{\mathrm{sil},2} = 1.30$ are the fitting coefficients.

Figure 7.12 shows the diurnal thermal skin depth of homogeneous dust aggregates, d_{s}, as a function of monomer particle radius R and the filling factor ϕ. We found that $d_{\mathrm{s}} \simeq 1$ cm for $0.1\ \mu\mathrm{m} \lesssim R \lesssim 1\ \mu$m and $0.1 \lesssim \phi \lesssim 0.5$. This indicates that the diurnal temperature variation reflects the thermophysical property of constituent aggregates when the aggregate radius R_{agg} is larger than 1 cm. On the other hand, if $R_{\mathrm{agg}} \ll 1$ cm, then the diurnal temperature variation reflects the radiative transfer process within the inter-aggregate structure (e.g., Gundlach and Blum, 2012; Blum et al., 2017).

7.4.4 Thermal inertia

The diurnal temperature variation is inversely proportional to the thermal inertia I. The definition of I is

$$I = \sqrt{k c_{\mathrm{heat}} \rho_{\mathrm{mat}} \phi}. \tag{7.42}$$

Figure 7.13 shows the thermal inertia of homogeneous dust aggregates, I, as a function of monomer particle radius R and the filling factor ϕ. In the following section, we discuss the size of constituting aggregates of comet 67P/C–G using the temperature dependence of the thermal inertia.

7.5 Thermal inertia of comet 67P/C–G and its interpretation

7.5.1 Observational data

The thermal inertia of the surface of comet 67P/C–G is measured in various temperatures. Marshall et al. (2018) developed a thermal model of the surface and subsurface of the nucleus, and their methods are applied to brightness temperature measurements at wavelength of mm and sub-mm obtained by the Microwave Instrument for the Rosetta Orbiter, MIRO. The observations were done in September 2014, and the typical temperature of observed regions is 150–200 K, and the diurnal temperature variation is consistent with the thermal inertia of $I = 40$–160 J m^{-2} K^{-1} s$^{-1/2}$.

Spohn et al. (2015) measured the temperature variation at the *Philae* landing site in November 2014. The landing site of the *Rosetta*'s lander, Abydos, is surrounded by huge rocks, thus the illumination period is only 40 minutes per day (12.4 hours; Spohn et al., 2015). The temperature of Abydos was 90–130 K, and the diurnal temperature variation indicates that $I = 85 \pm 35$ J m^{-2} K^{-1} s$^{-1/2}$.

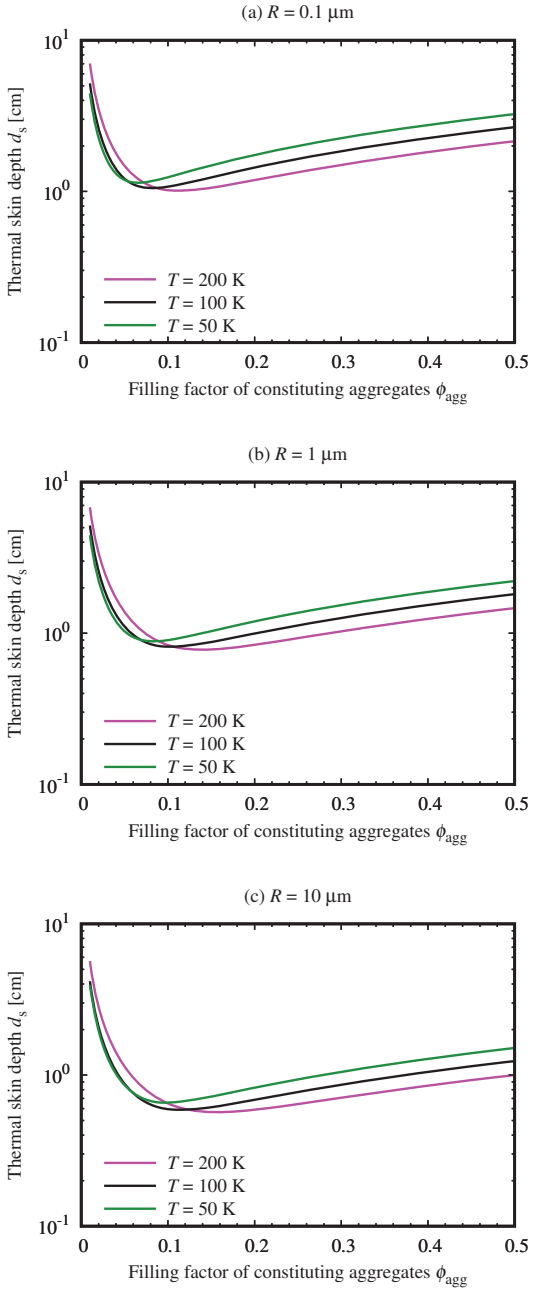

Figure 7.12: The thermal skin depth of homogeneous aggregates d_s as a function of monomer particle radius R and the filling factor ϕ (a) For the case that the monomer radius is $R = 0.1$ μm. (b) For the case that the monomer radius is $R = 1$ μm. (c) For the case that the monomer radius is $R = 10$ μm.

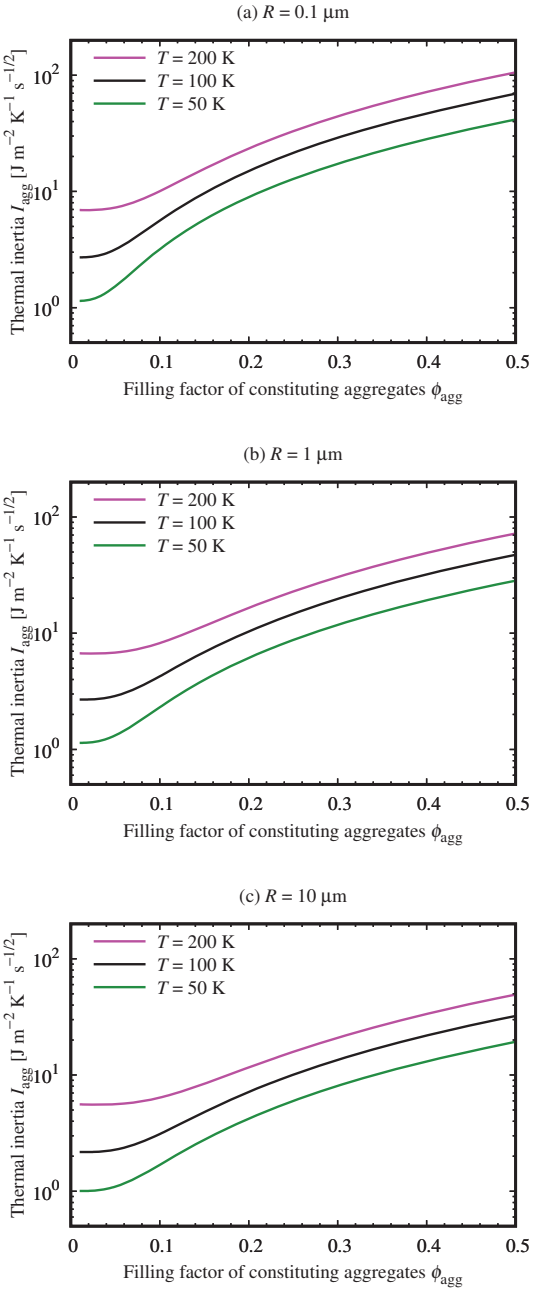

Figure 7.13: Thermal inertia of homogeneous aggregates I as a function of monomer particle radius R and the filling factor ϕ. (a) For the case that the monomer radius is $R = 0.1$ μm. (b) For the case that the monomer radius is $R = 1$ μm. (c) For the case that the monomer radius is $R = 10$ μm.

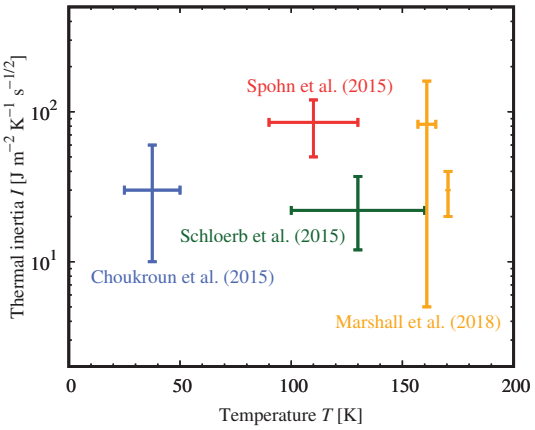

Figure 7.14: Thermal inertia of the surface of comet 67P/C–G, I, as a function of the temperature T. Marshall et al. (2018, orange) reported the estimates of the thermal inertia measured by MIRO in September 2014. The typical temperature at the observed regions is in the range of 150–200 K. Spohn et al. (2015, magenta) observed the temperature at the *Philae* landing site in November 2014. The diurnal temperature to vary between 90–130 K. Choukroun et al. (2015, blue) observed the long-lasting polar night region during the period August to October 2014 using MIRO. The subsurface temperatures are in the range of 25–50 K.

Choukroun et al. (2015) observed the long-lasting polar night region of comet 67P/C–G during the period from August to October 2014 using MIRO. The subsurface temperatures in the range of 25–50 K were observed and the thermal model calculations suggest that the thermal inertia at the polar night region is in the range of $I = 10$–60 J m^{-2} K^{-1} s$^{-1/2}$. Figure 7.14 is the summary of estimates of I in various (sub)surface temperature.

7.5.2 Thermal inertia of hierarchical aggregates

The mechanical strength of the nucleus of the comet suggests that the comet is likely to be a hierarchical aggregate. In this section, we discuss the size of constituting aggregates using the observational data of the thermal inertia.

Here we consider the thermal inertia of hierarchical aggregates. When the diurnal thermal skin depth is comparable to or larger than the aggregate radius, $R_{\rm agg} \gtrsim d_{\rm s}$, the diurnal temperature variation reflects the thermal inertia of constituting aggregates:

$$I = \sqrt{k_{\rm agg} c_{\rm heat} \rho_{\rm mat} \phi_{\rm agg}}, \tag{7.43}$$

where $k_{\rm agg}$ is the thermal conductivity of constituting aggregates. Assuming $\phi_{\rm agg} = 0.4$ and $R = 0.1$ μm, the thermal inertia is in the range of $I = 15$–64 J m^{-2} K^{-1} s$^{-1/2}$ when the temperature is 50 K $< T <$ 200 K (see Figure 7.13). This is good agreement with observations.

On the other hand, when $R_{\rm agg} \lesssim d_{\rm s}$, the diurnal temperature variation is determined by the radiative transfer within the inter-aggregate structure, and

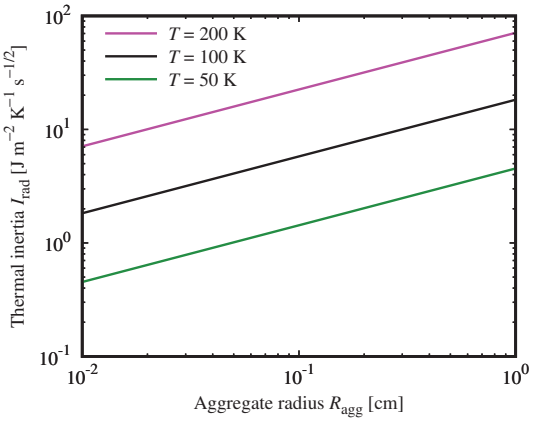

Figure 7.15: Thermal inertia of hierarchical aggregates I_{hie} for the case of $R_{agg} \lesssim d_s$. In this case, the diurnal temperature variation is determined by the radiative transfer within the inter-aggregate structure, and I_{hie} is given by Eq. (7.44).

the thermal inertia of hierarchical aggregates, I_{hie}, is given by

$$I_{hie} = \sqrt{k_{hie} c_{heat} \rho_{mat} \phi}. \tag{7.44}$$

Figure 7.15 shows the thermal inertia of hierarchical aggregates I_{hie} for the case of $R_{agg} \lesssim d_s$. The thermal inertia of hierarchical aggregates I_{hie} is approximately proportional to the square of the temperature T, however, observations suggest that the temperature dependence of the thermal inertia would be weak (see Figure 7.14). The expected thermal inertia at $T < 100$ K from Equation (7.44) is also inconsistent with the observational data. We therefore conclude that the thermal inertia of comet 67P/C–G reflects the thermal inertia of constituting aggregates.

7.5.3 High thermal inertia at the *Philae* landing site Abydos

Rosetta released the *Philae* lander onto the comet's surface in November 2014. The temperature of the landing site, Abydos, is low enough to maintain H_2O ice near its surface layer, because this site is surrounded by cliffs. As shown in Figure 7.14, the thermal inertia at Abydos seems to be higher than that of other regions. Here we discuss the effect of large thermal conductivity and specific heat of H_2O ice on the thermal inertia at the site.

The thermal conductivity and the specific heat of crystalline H_2O ice, k_{H_2O} and c_{H_2O}, are given by (Haruyama et al., 1993)

$$k_{H_2O} = 5.67 \left(\frac{T}{100\ \mathrm{K}} \right)^{-1} \mathrm{W\ K^{-1}\ m^{-1}}, \tag{7.45}$$

and

$$c_{H_2O} = 8.9 \times 10^2 \left(\frac{T}{100\ \mathrm{K}} \right) \mathrm{J\ K^{-1}\ kg^{-1}}. \tag{7.46}$$

The mechanical properties of H_2O ice grains are $\gamma_{H_2O} = 100$ mJ m^{-2}, $Y_{H_2O} = 7$ GPa, $\nu_{H_2O} = 0.25$, and $\rho_{H_2O} = 1000$ kg m^{-3} (Wada et al., 2007). Then the

Aggregate structure	Homogeneous aggregate		Hierarchical aggregate		Consolidated
	$\phi(d) = \text{const.}$	$P_c(\phi) = P(d)$	$R_{agg} \gtrsim 1$ cm	$R_{agg} \lesssim 1$ mm	material
Tensile strength	×	?	✓	✓	×
Compressive strength	✓	×	?	✓	✓
Thermal inertia	✓	×	✓	×	?

Table 7.1: Summary of the observational constraints on the aggregate structure of comet 67P/C–G. The red crosses are the critical disagreements of theoretical prediction and observational constraint we focused on.

contact radius of two sticking icy monomers is

$$a_{c,H_2O} = 0.057 \left(\frac{R}{1\ \mu\text{m}} \right)^{-1/3} R, \tag{7.47}$$

The thermal conductivity of icy dust aggregates is approximately given by the thermal conductivity through the solid network:

$$\begin{aligned} k_{sol,H_2O} &\simeq 2 k_{H_2O} \frac{a_c}{R} \phi^2 \\ &\simeq 5.9 \times 10^{-2} \left(\frac{\phi}{0.3} \right)^2 \left(\frac{T}{100\ \text{K}} \right)^{-1} \text{W K}^{-1}\ \text{m}^{-1}, \end{aligned} \tag{7.48}$$

and the thermal inertia of dust aggregates constituted of crystalline H_2O ice monomers is

$$I_{H_2O} \simeq 1.25 \times 10^2 \left(\frac{\phi}{0.3} \right)^{3/2} \text{J m}^{-2}\ \text{K}^{-1}\ \text{s}^{-1/2}. \tag{7.49}$$

Thus the thermal inertia of $\sim 10^2\ (\phi/0.3)^{3/2}$ J m^{-2} K^{-1} s$^{-1/2}$ at the *Philae* landing site could be explained by the effect of H_2O ice.

7.6 Summary of mechanical and thermal constraints

Table 7.1 is the summary of the observational constraints on the aggregate structure of comet 67P/C–G. We considered three possibility for the structure of the comet: homogeneous aggregate, hierarchical aggregate, and consolidated material. For the case of homogeneous aggregate model, we also consider two possibility: the filling factor profile in the depth direction is uniform, $\phi(d) = \text{const.}$, or the filling factor is determined by the equation $P_c(\phi) = P(d)$. If the comet is homogeneous aggregate and $\phi(d) = \text{const.}$, the tensile strength at the surface and at the 10–100 m-scale is several orders of magnitude higher than the observational estimates (see Figures 7.3 and 7.8a). If the filling factor profile is given by $P_c(\phi) = P(d)$, the observed compressive strength at 0.1–1 m-scale ($P_c \gg 1$ Pa) cannot be reproduced. Thus the homogeneous aggregate model is not suitable for the aggregate structure of comet 67P/C–G.

The consolidated material model (i.e., comets are well-sintered rocks-ice mixtures) is also inconsistent with the observational constraints. The tensile strength of consolidated materials increases with decreasing the spatial scale (Weibull, 1951; Petrovic, 2003; Xu, 2005). However, the observational results of

Rosetta indicate that the tensile strength increases with increasing the spatial scale (see Figure 7.8a). Thus we conclude that comet 67P/C–G is not a consolidated rocks-ice mixture.

The hierarchical aggregate model explains the weak tensile strength and moderate compressive strength of the comet (e.g., Blum et al., 2017, and references therein). We modified the tensile strength model (Section 7.2.5) based on the results from recent numerical and theoretical studies (Tatsuuma et al., 2019; Arakawa et al., 2019b). The compressive strength may also be consistent with observational results, although both theoretical and experimental studies on the compressive strength of hierarchical aggregates are still limited. Thus we should reveal the dependence on the monomer and aggregate radii of the compressive strength in the future.

The thermal conductivity of dust aggregates are studied by our previous studies (Arakawa et al., 2017, 2019b,c). Using the result of Arakawa et al. (2019c), we calculated the thermal skin depth of the surface dust layer of comet 67P/C–G. We found that the diurnal thermal skin depth is $d_\mathrm{s} \simeq 1$ cm. Therefore, the thermal inertia I is given by that of constituting aggregates when the aggregate radius is comparable to or larger than the thermal skin depth, $R_\mathrm{agg} \gtrsim 1$ cm. The calculated thermal inertia is consistent with the observations in the wide temperature range when the filling factor of constituting aggregates is $\phi_\mathrm{agg} \sim 0.4$ (e.g., Weidling et al., 2009). On the other hand, if the aggregate radius is significantly smaller than the thermal skin depth, $R_\mathrm{agg} \ll 1$ cm, the thermal inertia of hierarchical aggregates is determined by the radiative transfer in inter-aggregate voids (see Eq. 7.44). In this case, however, we cannot explain the thermal inertia in low-temperature regions (see Figure 7.14). Therefore, the hierarchical aggregate of cm- or dm-sized constituting aggregates is the only solution to explain both the mechanical and thermal properties of the comet simultaneously.

7.7 Other constraints on the size of constituent aggregates

Note that our conclusion is consistent with the constraint on the physical homogeneity of comet 67P/C–G (Kofman et al., 2015; Pätzold et al., 2016). Kofman et al. (2015) investigated radiowave transmission measurements of the interior of the comet. From the propagation time and form of the signals, they found that the interior is fairly homogeneous on a spatial scale of 10 m. The gravity field observations also support that the nucleus is homogeneous in density down to scales of meters (Pätzold et al., 2016). Moreover, the size-frequency distribution of dust aggregates emitted from the nucleus (see Figure 7 of Blum et al., 2017) suggests that the constituting aggregates of comet 67P/C–G would be cm- to dm-sized aggregates.

Gundlach et al. (2015) estimated the maximum radius of constituent aggregates which can be released from the cometary surface, $R_\mathrm{agg,max}$. The ejected aggregates are lifted up by the gas-friction force, F_gas, and F_gas must overcome the gravitational force, F_grav. The gas-friction force at the cometary surface is approximately given by

$$F_\mathrm{gas} = \pi {R_\mathrm{agg}}^2 p_\mathrm{gas}, \tag{7.50}$$

Constraint on $R_{\rm agg}$	Evidence	Reference
$R_{\rm agg} > 1$ mm	Tensile strength at the cometary surface	This study
$R_{\rm agg} > 1$ cm	Thermal inertia at low temperature regions	This study
$R_{\rm agg} < 10$ m	Radiowave transmission measurement	Kofman et al. (2015)
1 cm $< R_{\rm agg} <$ 1 m	Size distribution of the emitted dust aggregates	Blum et al. (2017)
$R_{\rm agg} < 0.3$ m (at ~ 2 au)	Largest aggregates which can ejected from the comet	Gundlach et al. (2015)

Table 7.2: Summary of the constraints on the size of constituent aggregates.

where $p_{\rm gas}$ is the gas pressure at the ice sublimation interface. The gravitational force is

$$F_{\rm grav} = \frac{GM_{\rm agg}m_{67\rm P}}{{r_{67\rm P}}^2}, \tag{7.51}$$

where $M_{\rm agg} = (4\pi/3){R_{\rm agg}}^3\rho_{\rm agg}$ and $m_{67\rm P} = (4\pi/3){r_{67\rm P}}^3\rho_{67\rm P}$ are the mass of constituent aggregates and comet 67P/C–G. The density of aggregates is $\rho_{\rm agg} = \rho_{\rm mat}\phi_{\rm agg}$ and the density of comet 67P/C–G is $\rho_{67\rm P}$. Then the maximum radius of constituent aggregates $R_{\rm agg,max}$ is given by (Gundlach et al., 2015)

$$R_{\rm agg,max} = \frac{9p_{\rm gas}}{16\pi G\rho_{\rm agg}\rho_{67\rm P}r_{67\rm P}}. \tag{7.52}$$

Gundlach et al. (2015) also derived a simple analytic formula of the gas pressure at the ice sublimation interface:

$$p_{\rm gas} = (1-A)\frac{S_\odot (D_{67\rm P}/1\ {\rm au})^{-2}}{\Lambda}\sqrt{\frac{2\pi k_{\rm B}T_{\rm ice}}{m_{\rm g}}}, \tag{7.53}$$

where A is the Bond albedo of the cometary surface, $S_\odot = 1.37\times10^3$ W m^{-2} is the solar constant, $D_{67\rm P}$ is the heliocentric distance of the comet, Λ is the latent heat of sublimation, and $T_{\rm ice}$ is the temperature of the evaporating ice.

The maximum radius of constituent aggregates is $R_{\rm agg,max} \sim 1\ (D_{67\rm P}/1\ {\rm au})^{-2}$ m for both H_2O and CO_2 activities (see Figure 3 of Gundlach et al., 2015). The estimated value is consistent with the size-frequency distribution of dust aggregates emitted from the nucleus. Table 7.2 is the summary of the constraints on the size of constituent aggregates.

7.8 Mass loss and thermal alteration near the cometary surface

In this section, we briefly discuss the effect of mass loss and thermal evolution of the cometary nucleus. The mass of the nucleus of the comet changed during the *Rosetta* mission (from 2014 to 2016), and the lost mass is $\Delta m_{67\rm P} = (1.0\pm0.3)\times10^{-3}m_{67\rm P}$ (Pätzold et al., 2019). The radius of the comet is ~ 1 km, then the equivalent depth of the lost dust layer is ~ 30 cm. This depth is comparable to the thermal skin depth for seasonal temperature variation (see, e.g., Guilbert-Lepoutre et al., 2016). Therefore, whether the cometary surface we see is thermally altered or not is still controversial.

Most of the mass loss occurred near the perihelion (~ 1.3 au, Pätzold et al., 2019). Comet 67P/C–G has a chaotic orbit and the perihelion distance was

larger than 2 au before the recent close encounter with Jupiter in 1959 (Maquet, 2015). This suggests that the comet experienced the approaching to the sun within 1.5 au less than ten times since its birth. Therefore the cumulative depth of the lost dust layer is only a few meters, and the global shape of the comet hardly changed by the mass loss.

7.9 Comparison with previous works

Previous works on the dust structure of comets (e.g., Skorov and Blum, 2012; Blum et al., 2014; Gundlach et al., 2015; Blum et al., 2017) already proposed the hierarchical dust aggregate model. The main differences between our model and their original model are the equation of tensile strength (Eq. 7.18 in our model) and how observed thermal inertia is determined.

In our model, the tensile strength of uncompressed hierarchical aggregates is $6.3 \times 10^{-3}\ (R/1\ \mu\mathrm{m})(R_\mathrm{agg}/1\ \mathrm{cm})^{-2}$ Pa, which is based on the critical pulling force for uncompressed sticking aggregates (see Eq. 7.18). On the other hand, Skorov and Blum (2012) and Blum et al. (2017) estimated the tensile strength of hierarchical aggregates using the effective surface energy model:

$$(P_\mathrm{t,hie})_\mathrm{ESE} = 0.21 \left(\frac{R_\mathrm{agg}}{1\ \mathrm{cm}} \right)^{-2/3} \mathrm{Pa}. \tag{7.54}$$

Note, however, that the effective surface energy model used in previous works may lack validity (see Figure 7.5) and their model would overestimate the tensile strength of hierarchical aggregates composed of cm- or dm-sized aggregates.

The thermal inertia reflects the thermophysical property of constituting aggregates in our model because the diurnal thermal skin depth d_s is smaller than the aggregate radius R_agg. On the other hand, in the model proposed by Blum et al. (2017), the thermal inertia of comet 67P/C–G is determined by the inter-aggregate radiation and the diurnal thermal skin depth is larger than the aggregate radius. Both models can explain the observed thermal inertia at the regions where the temperature is higher than 100 K; however, the thermal inertia of low-temperature ($T \ll 100$ K) can only be reproduced by our model (see Figures 7.13 and 7.15).

Previous works (e.g., Skorov and Blum, 2012; Blum et al., 2014; Gundlach et al., 2015; Blum et al., 2017) calculated the temperature and gas pressure at the depth where ice molecules sublimate, and they discussed how comets would be active. They also gave upper and lower limits of the aggregate radius. We borrowed their estimate of the gas pressure to evaluate the tensile strength at the cometary surface and we did not calculate the gas pressure in this study. Although Blum et al. (2014) showed that the maximum gas pressure hardly depends on the aggregate radius, the thermophysical properties of dust aggregates assumed in this study are different from that of their previous works. We will check whether the vertical structures under the cometary surface strongly depend on the aggregate model or not in future.

7.10 Conclusion

In conclusion, the mechanical and thermal properties of nucleus of comet 67P/C–G is consistent with the hypothesis that cometary nuclei were hierarchical aggregates of cm- or dm-sized compressed aggregates. This scenario is previously proposed by Blum et al. (2017), and the scenario is also consistent with the activity of comet 67P/C–G (e.g., Skorov and Blum, 2012; Gundlach et al., 2015; Fulle et al., 2019). Our key findings are summarized as follows.

1. We theoretically derived the tensile strength of uncompressed hierarchical aggregates, and our result is consistent with previous experiments (Brisset et al., 2016; Blum et al., 2014). The obtained tensile strength is low enough to explain the dust activity of comet 67P/C–G driven by sublimation of H_2O, CO, and CO_2 ices (e.g., Gundlach et al., 2015).

2. The compressive strength would also be consistent with the hypothesis that comets were formed via accretion of compressed aggregates, although further studies on the compressive strength of hierarchical aggregates and construction of a theoretical explanation are needed.

3. The thermal skin depth of the surface dust layer on comet 67P/C–G is approximately 1 cm. Thus the thermal inertia estimated from observations reflects the thermal properties of constituting aggregates when the aggregate radius is larger than the thermal skin depth. We found that the thermal inertia calculated from the thermal conductivity of constituting aggregates is consistent with *Rosetta* observations in the wide temperature range. In contrast, if the inter-aggregate radiative transfer controls the thermal inertia, we cannot reproduce the observed thermal inertia in low-temperature regions.

4. Therefore, we conclude that the nucleus of comet 67P/C–G is a hierarchical aggregate of cm- or dm-sized compressed aggregates. Our model explains both mechanical and thermal properties of the comet and suggests that comets might form through the gravitational collapse of dust clumps in the solar nebula (e.g., Johansen and Youdin, 2007). The dust compression mechanism in the disk is unknown, but the collisional compression near the bouncing barrier (e.g., Weidling et al., 2009) may be the key.

Appendix

7.A Thermal conductivity due to gas diffusion

In the free molecular flow limit, the thermal conductivity due to gas diffusion, $k_{\rm gas}$, is given by

$$k_{\rm gas} = h_{\rm g} l_{\rm g}, \tag{7.55}$$

where $h_{\rm g}$ is the heat transfer coefficient and $l_{\rm g}$ is the length of monomer-monomer voids. The heat transfer coefficient is (Gusarov and Kovalev, 2009)

$$h_{\rm g} = \frac{1}{8}\frac{\kappa+1}{\kappa-1}\frac{P_{\rm gas} v_{\rm th}}{T}, \tag{7.56}$$

where $\kappa = 4/3$ is the specific heat ratio of H_2O gas molecules, $P_{\rm gas}$ is the gas pressure, and $v_{\rm th}$ is the mean molecular velocity, given by

$$v_{\rm th} = \sqrt{\frac{8 k_{\rm B} T}{\pi m_{\rm g}}} = 485 \left(\frac{T}{200\ {\rm K}}\right)^{1/2} {\rm m\ s^{-1}}, \tag{7.57}$$

where $m_{\rm g} = 18 \times (1.66 \times 10^{-27})$ kg is the molecular mass of H_2O. The length of monomer-monomer voids is given by (Skorov et al., 2011; Gundlach and Blum, 2012)

$$l_{\rm g} = \frac{4}{3}\frac{1-\phi}{\phi} R. \tag{7.58}$$

When we assume $\phi = 0.4$ and $R = 0.1$ μm, the thermal conductivity due to gas diffusion is

$$k_{\rm gas} = 4.2 \times 10^{-8} \left(\frac{P_{\rm gas}}{0.1\ {\rm Pa}}\right)\left(\frac{T}{200\ {\rm K}}\right)^{-1/2} {\rm W\ K^{-1}\ m^{-1}}, \tag{7.59}$$

and this $k_{\rm gas}$ is orders of magnitude lower than $k_{\rm sol}$ and $k_{\rm rad}$.

7.B Thermal properties of matter

7.B.1 Thermal conductivity

Cahill and Pohl (1987) measured the thermal conductivity of amorphous polymethyl methacrylate from 30 K to 300 K, and we obtained a fitting equation (Eq. 7.29). Cahill (1990) measured the thermal conductivity of amorphous SiO_2 from 30 K to 750 K, and the fitting equation is,

$$\frac{1}{k_{\rm sil}} = \sqrt{\left(k_{\rm sil,1}\left(\frac{T}{100\ {\rm K}}\right)^{\alpha_{\rm sil,1}}\right)^{-2} + \left(k_{\rm sil,2}\left(\frac{T}{100\ {\rm K}}\right)^{\alpha_{\rm sil,2}}\right)^{-2}}, \tag{7.60}$$

where $k_{\rm sil,1} = 1.02$ W K^{-1} m^{-1}, $\alpha_{\rm sil,1} = 0.283$, $k_{\rm sil,2} = 0.889$ W K^{-1} m^{-1}, and $\alpha_{\rm sil,2} = 1.28$ are the fitting coefficients. Figure 7.16 shows the temperature dependence of material thermal conductivity.

Thermal conductivities of other amorphous organic polymers are shown in Figure 2 of Kommandur and Yee (2017) (see Figure 7.17). The measured thermal conductivity around 100 K is in general 0.1–0.3 W K^{-1} m^{-1} and the thermal conductivity of organic polymers can be represented by that of polymethyl methacrylate.

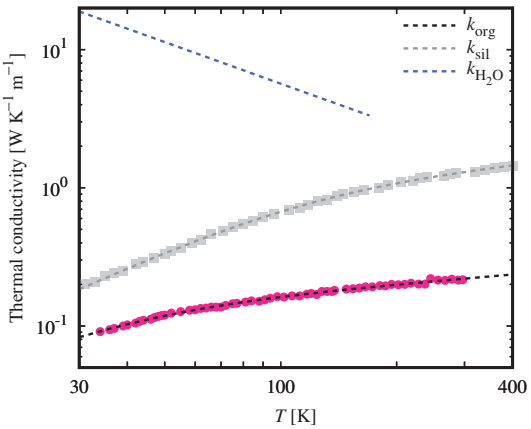

Figure 7.16: Thermal conductivity of amorphous polymethyl methacrylate (k_{org}), amorphous SiO_2 (k_{sil}), and crystalline H_2O ice (k_{H_2O}). Filled circles and squares are experimental data and dashed lines are fitting equations.

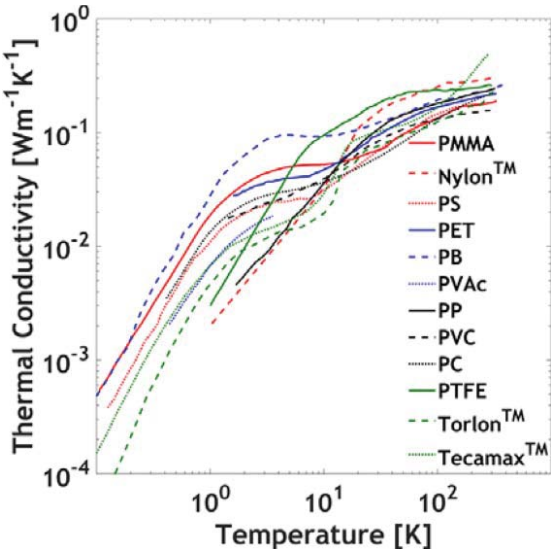

Figure 7.17: Thermal conductivities of amorphous organic polymers. (Figure taken from Figure 2 of Kommandur and Yee, 2017)

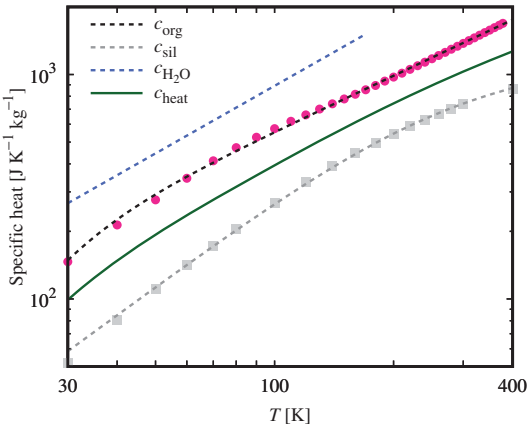

Figure 7.18: Specific heat of amorphous polymethyl methacrylate (c_{org}), amorphous SiO_2 (c_{sil}), and crystalline H_2O ice (c_{H_2O}). Filled circles and squares are experimental data and dashed lines are fitting equations. The solid line is the specific heat of OMGs, $c_{heat} = f_{org}c_{org} + f_{sil}c_{sil}$.

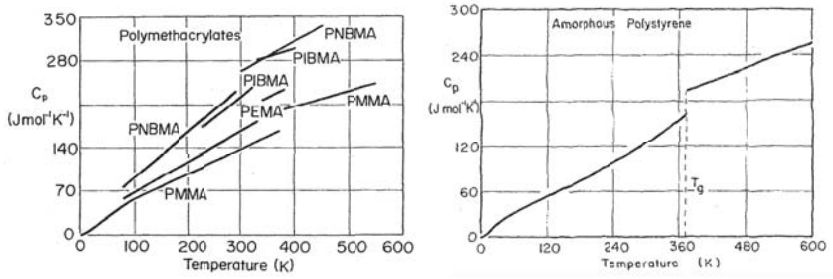

Figure 7.19: Molar specific heat of amorphous organic polymers. (Upper panel) For the case of polymethacrylates (Figure taken from Gaur et al., 1982). The formula weight of methyl methacrylate is 100.12. (Lower panel) For the case of polystyrene (Figure taken from Gaur and Wunderlich, 1982). The formula weight of styrene is 104.15.

7.B.2 Specific heat

The specific heat of polymethyl methacrylate and amorphous SiO_2 are reported by Gaur et al. (1982) (from 0.2 K to 378 K) and Lord and Morrow (1957) (from 10 K to 900 K), and we derived empirical equations of c_{org} and c_{sil} (see Eqs. 7.40 and 7.41, respectively). Figure 7.18 shows the temperature dependence of specific heats.

The molar specific heat of numerous amorphous organic polymers are reported (see Figure 7.19). The measured specific heat around 100 K is in general ~ 500 J K^{-1} kg^{-1} and the specific heat of organic polymers can be represented by that of polymethyl methacrylate.

Chapter 8

Early formation of moons around large trans-Neptunian objects via giant impacts

Sota Arakawa, Ryuki Hyodo, and Hidenori Genda
Nature Astronomy **3**, 802–807 (2019).

Abstract

Recent studies have revealed that all large (over 1000 km in diameter) trans-Neptunian objects (TNOs) form satellite systems. Although the largest Plutonian satellite, Charon, is thought to be an intact fragment of an impactor directly formed via a giant impact, whether giant impacts can explain the variations in secondary-to-primary mass ratios and spin/orbital periods among all large TNOs remains to be determined. Here we find that hydrodynamic simulations of giant impacts can reproduce the secondary-to-primary mass ratio of the satellite systems of large TNOs when the impact velocity is approximately the same as the escape velocity. We also reveal that the satellite systems' current distribution of spin/orbital periods and small eccentricity can be most easily explained when their spins and orbits tidally evolve, initially as fluid-like bodies, and finally as rigid bodies. The preferred duration of fluid-like behavior is $\sim 10^4$–10^6 years, although it depends on the secondary-to-primary mass ratio and the initial orbital elements. These results suggest that all satellites of large TNOs were formed via giant impacts before the outward migration of Neptune, and that they were fully or partially molten during the giant impact era.

8.1 Giant impact simulations

Six known TNOs have diameters larger than 1000 km, with secondary-to-primary mass ratio, $\gamma_{\rm sp}$, varying from $\sim 10^{-1}$ to 10^{-3} (e.g., Parker et al., 2016;

Kiss et al., 2017, see Supplementary Table 8.1). In our simulations, we consider two scenarios for satellite formation via giant impact: (1) accretion from an impact-generated debris disk, forming what we call hereafter "disk-origin moons", or (2) direct formation from the largest intact fragment(s) of the impactor ("intact moons").

Here, we use standard smoothed particle hydrodynamics (SPH) methods to simulate the giant impacts, and calculated the subsequent tidal evolutions for the satellites formed. We performed 434 runs for 1000 km-sized planetary bodies (see Methods), of which 141 resulted in the intact moon formation. Figure 8.1 shows an example result of a giant impact between differentiated bodies that forms a large intact moon. The impactor and target separated after the first oblique impact (Fig. 8.1a), but they were gravitationally bound. During the second impact, the smaller impactor received an angular momentum, and transferred its mass to the larger target (Fig. 8.1b). A small fragment of the impactor was then ejected because of its high specific angular momentum (Fig. 8.1c), leading finally to the formation of a single intact moon with $\gamma_{\rm sp} = 0.13$ (Fig. 8.1d).

The collisional outcome strongly depends on $\theta_{\rm imp}$ and $v_{\rm imp}$, resulting in the formation of either an intact moon with or without a rocky core (Fig. 8.1 or Supplementary Fig. 8.S1), a disk without an intact moon (Supplementary Fig. 8.S2), or a hit-and-run collision (Supplementary Fig. 8.S3). For giant impacts between two differentiated bodies with $M_{\rm tar} = 4 \times 10^{21}$ kg and $M_{\rm imp} = 2 \times 10^{21}$ kg, large intact moons with $\gamma_{\rm sp}$ values higher than 10^{-1} are formed when $\theta_{\rm imp} = 75^\circ$ and $v_{\rm imp} = 1.05 v_{\rm esc}$. Smaller intact moons with $10^{-3} < \gamma_{\rm sp} < 10^{-1}$ were formed in wide parameter space in $\theta_{\rm imp}$–$v_{\rm imp}$ (Fig. 8.2a). We found that when the typical $v_{\rm imp}$ was $\lesssim 1.1 v_{\rm esc}$, the probability of an intact moon being formed for a single giant impact reached 50%, and $\gamma_{\rm sp}$ ranged from 10^{-3} to 10^{-1}, approximately consistent with the observed $\gamma_{\rm sp}$ ranges of the satellite systems of large TNOs.

Similarly, for the case of giant impacts with two undifferentiated icy bodies (with $M_{\rm tar} = 4 \times 10^{21}$ kg and $M_{\rm imp} = 2 \times 10^{21}$ kg), large intact moons with $\gamma_{\rm sp} \simeq 10^{-1}$ formed during some grazing impacts with $\theta_{\rm imp}$ values of 60° or larger. In addition, we also found that intact moons with $10^{-3} < \gamma_{\rm sp} < 10^{-1}$ formed via giant impacts in wide parameter space where $\theta_{\rm imp}$–$v_{\rm imp}$ (Fig. 8.2b). These SPH simulations agree with those of previous studies (Canup, 2005; Sekine et al., 2017), although these previous studies focused only on the formation of Charon assuming the total angular momentum of the system as that of the current Pluto-Charon system. In contrast, we surveyed various $\theta_{\rm imp}$ and $v_{\rm imp}$ values in this paper.

We found that intact moons were formed via giant impacts when $\theta_{\rm imp} \gtrsim 45^\circ$ and $v_{\rm imp} \lesssim 1.2 v_{\rm esc}$ for both undifferentiated and differentiated cases. Supplementary Figs. 8.S4a–c show the outcomes of giant impacts for different total masses, different compositions, and different impactor-to-target mass ratios. In these conditions, intact moons were formed in almost all cases where $\theta_{\rm imp} \gtrsim 45^\circ$ and $v_{\rm imp} \lesssim 1.2 v_{\rm esc}$.

The Pluto–Charon system might have formed via a giant impact between undifferentiated or partially differentiated bodies (Canup, 2005, 2011). Actually, in our calculations, the formation probability of large intact moons with $\gamma_{\rm sp} \geq 10^{-1}$ is higher for the case of undifferentiated bodies than it is for dif-

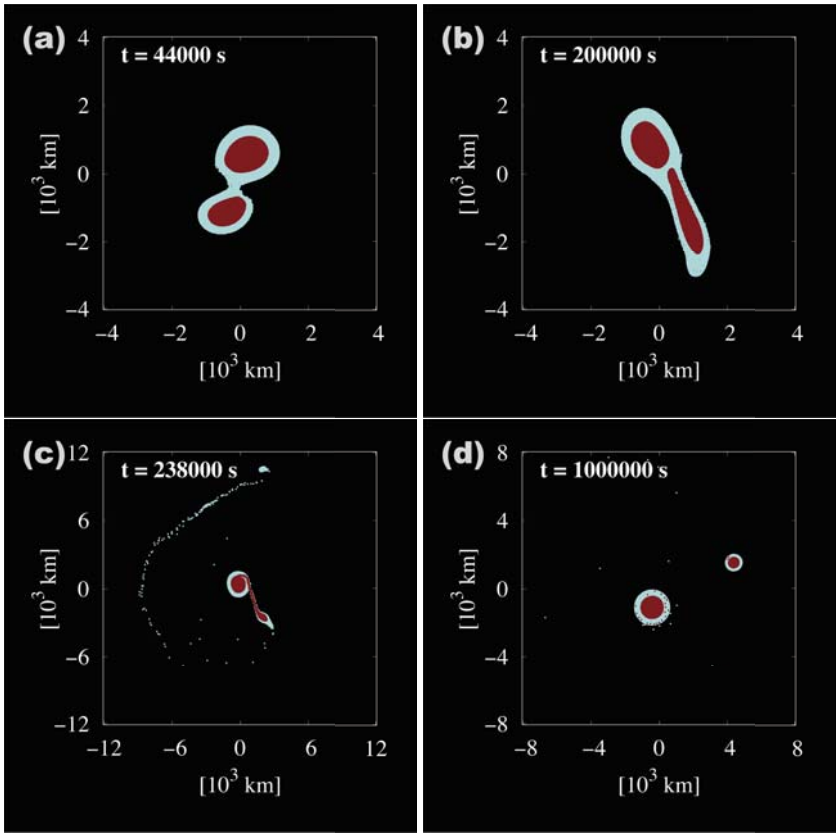

Figure 8.1: Snapshots of a giant impact between two differentiated bodies. Both the target and the impactor were differentiated bodies with ice mass fractions, f_{ice}, of 0.5 (50 wt.% ice and 50 wt.% basalt). The target mass, M_{tar}, and the impactor mass, M_{imp}, were $M_{\mathrm{tar}} = 4 \times 10^{21}$ kg and $M_{\mathrm{imp}} = 2 \times 10^{21}$ kg, respectively. The impact velocity, v_{imp}, was $1.05 v_{\mathrm{esc}}$, and the impact angle, θ_{imp}, was 75° (where 0° represents a head-on impact). This simulation directly formed a satellite with a $\gamma_{\mathrm{sp}} = 0.13$.

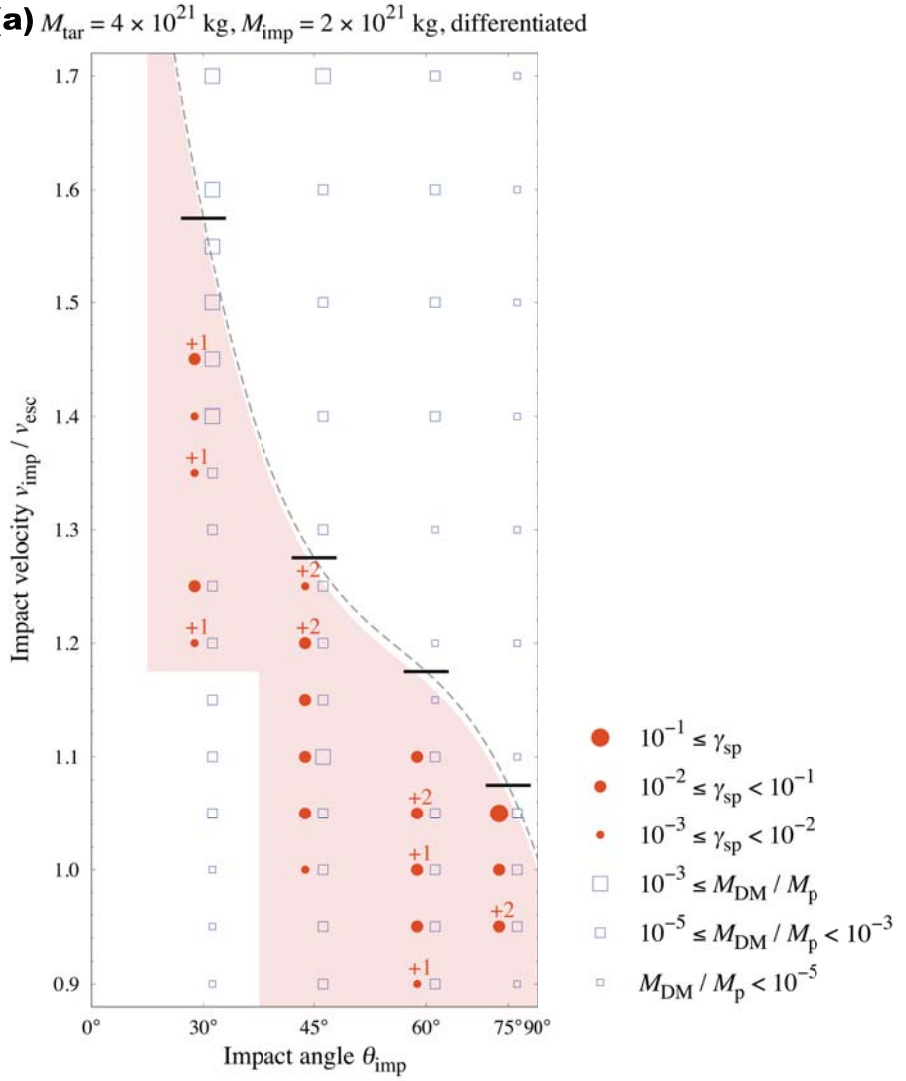

Figure 8.2: Summary of the range of outcomes for the simulated giant impacts. (a) outcomes for giant impacts between differentiated planetary bodies with masses of 4×10^{21} kg and 2×10^{21} kg. Both the impactor and target were differentiated with a f_{ice} of 0.5. (b) outcomes for giant impacts between icy undifferentiated planetary bodies with masses of 4×10^{21} kg and 2×10^{21} kg. The size (large, medium, or small) of each red filled circle represents the mass of the intact moon (if any), and the size of each blue open square represents the estimated mass of the disk-origin moon (the mass of the debris disk is calculated for all simulations).

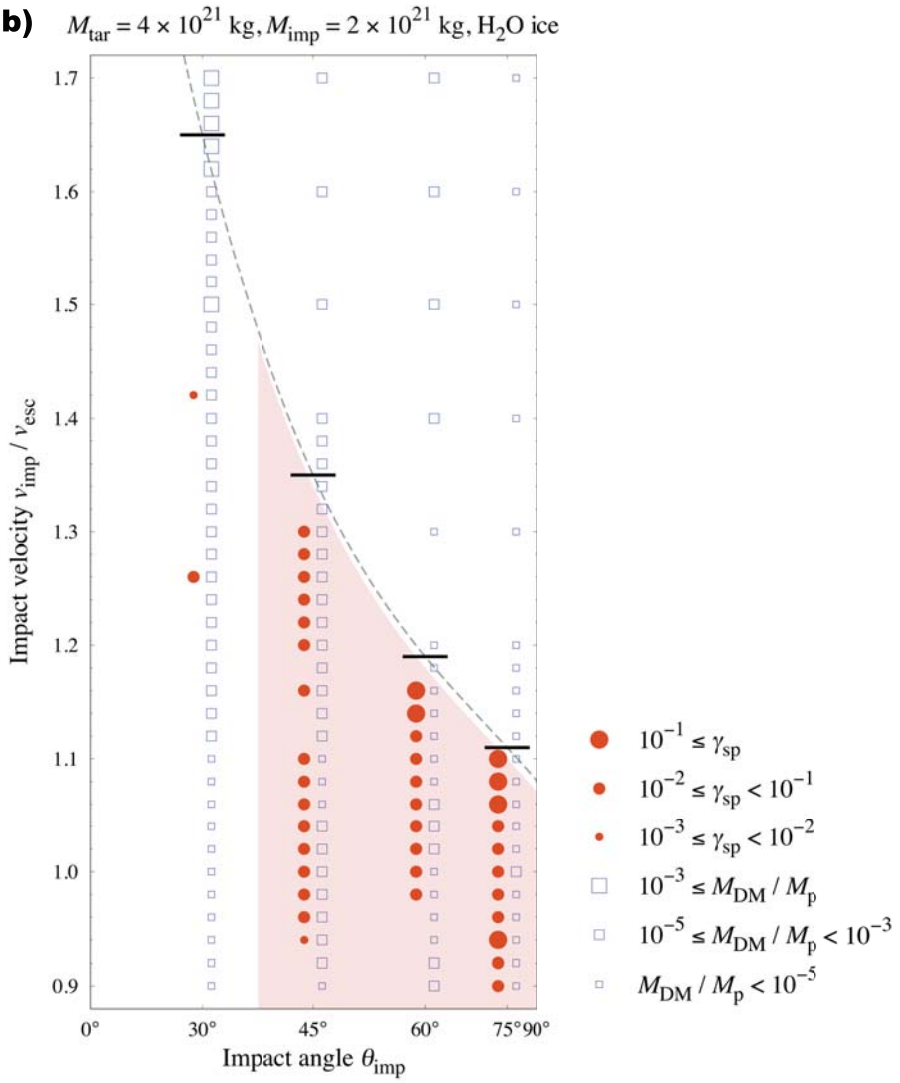

Figure 8.2: (continued) Numbers above red filled circles ("+1" and "+2") signify that multiple intact moons were formed during the single impact ("+1" implies the formation of one large intact moon and another small intact moon, and "+2" imply the formation of one large intact moon and two other small intact moons). We regarded clumps that had more than 24 particles as intact moons. The black solid lines represent the criteria for hit-and-run collisions (Genda et al., 2012), and the grey curve is a fit calculated using a cubic function. The pink-tinted region is a rough estimation of the parameter range for intact moon formation.

ferentiated bodies. Note, however, that the formation probability of the Pluto–Charon analogue is non-zero even for differentiated bodies.

Assuming that the probability distribution of the impact angle, $P(\theta_{\rm imp})$, is given by $P(\theta_{\rm imp}) = \sin(2\theta_{\rm imp})$, then statistically, half of the giant impacts had an impact angle larger than 45°. Typical impact velocities among large (> 1000 km in diameter) TNOs are given by

$$v_{\rm imp} \simeq \sqrt{\left({e_{\rm hel}}^2 + {i_{\rm hel}}^2\right){v_{\rm K}}^2 + {v_{\rm esc}}^2}, \tag{8.1}$$

where $e_{\rm hel}$ and $i_{\rm hel}$ are the heliocentric eccentricity and the inclination respectively, and $v_{\rm K}$ and $v_{\rm esc}$ are the heliocentric Kepler velocity and the escape velocity of the TNOs, respectively (Canup, 2005). When $e_{\rm hel}$ and $i_{\rm hel} \ll 0.1$ in the giant impact era, the relative velocity of large TNOs at infinity, $v_\infty \sim \left({e_{\rm hel}}^2 + {i_{\rm hel}}^2\right)^{1/2} v_{\rm K}$, will be smaller than $v_{\rm esc}$ (~ 1 km s^{-1} for large TNOs), and the impact velocity will be $v_{\rm imp} \sim v_{\rm esc}$. Although the current heliocentric eccentricities of large TNOs are much higher than 0.1 (e.g., currently $e_{\rm hel} = 0.25$ for Pluto), we note that the v_∞ of large TNOs might be small during the giant impact era. This is because $e_{\rm hel}$ and $i_{\rm hel}$ are smaller than 0.1 for the cold classical TNOs, which were thought to be formed locally (Batygin et al., 2011), and large TNOs can also be formed locally, in a similar way to the smaller cold classical TNOs (Shannon et al., 2016).

In order to occur with reasonable frequency, giant impacts between large TNOs must be gravitationally focused (Canup, 2005). When v_∞ was smaller than the Hill velocity, $v_{\rm H} \sim (M_{\rm TNO}/M_\odot)^{1/3} v_{\rm K}$, the collision timescale was ~ 6 Myr ($M_{\rm TNO}$ and $M_\odot$are the masses of the large TNO and the solar mass, respectively; Noll et al., 2008a). If the $e_{\rm hel}$ and the $i_{\rm hel}$ of the TNOs were on the order of 10^{-3}, then they were gravitationally focused (i.e., $v_\infty < v_{\rm H}$; Shannon et al., 2016). In this case, the typical impact velocity was $\sim 1.0 v_{\rm esc}$, consistent with the formation of intact moons via giant impacts. The small v_∞ value is also suggested in the context of the formation of trans-Neptunian binaries (Noll et al., 2008a).

Concerning the possibility of the formation of disk-origin moons by giant impacts (Hyodo et al., 2015), we analyzed the disk mass around the primary at 10^6 seconds after the start of calculation and then estimated the mass of the disk-origin moon using the empirical relation between disk mass ($M_{\rm disk}$) and the mass of the disk-origin moons ($M_{\rm DM}$) (see Methods). As a result of this analysis, we found that large satellites for which $M_{\rm DM}/M_{\rm p} > 10^{-3}$ ($M_{\rm p}$ is the mass of the primary) were very rarely formed via the viscous spreading of a debris disk, except for the case of high-speed impacts of $v_{\rm imp} \gtrsim 1.4 v_{\rm esc}$ (Figs. 8.2a, 8.2b, and Supplementary Figs. 8.S4a–c). Note that the estimated $M_{\rm DM}/M_{\rm p}$ is smaller than 4×10^{-3} for all giant impacts between two differentiated bodies (Supplementary Fig. 8.S5). Therefore, we cannot explain the secondary-to-primary mass ratio of the Pluto–Charon ($\gamma_{\rm sp} = 0.12$) and Eris–Dysnomia ($\gamma_{\rm sp} = 3 \times 10^{-2}$) systems if Charon and Dysnomia were formed as disk-origin moons. This result might indicate that most of the secondaries around large TNOs, which have $\gamma_{\rm sp}$ ranges from 10^{-3}–10^{-1}, are intact moons, not disk-origin moons, although some satellite systems with low $\gamma_{\rm sp}$ values (e.g., Quaoar–Weywot; $\gamma_{\rm sp} = 4 \times 10^{-4}$) might have originated from impact-

generated disks.

The $f_{\rm ice}$ values of satellites formed after giant impacts from differentiated bodies showed a strong correlation with $\gamma_{\rm sp}$ (Supplementary Fig. 8.S5). The $f_{\rm ice}$ values of the resulting intact moons were similar to that of the pre-impact targets and impactors ($f_{\rm ice} = 0.5$) when $\gamma_{\rm sp} \gtrsim 10^{-2}$. In contrast, for small intact moons and disk-origin moons with $\gamma_{\rm sp} \lesssim 10^{-2}$, $f_{\rm ice} \simeq 1$. These values can be compared to observations on the density of both primary and secondary satellites for two systems (Pluto–Charon and Haumea–Hi'iaka). For Pluto–Charon ($\gamma_{\rm sp} = 0.12$), the bulk density of Pluto (1860 kg m^{-3}; Stern et al., 2015a) is similar to that of Charon (1700 kg m^{-3}; Stern et al., 2015a), suggesting that both Pluto and Charon have a similar $f_{\rm ice}$. On the other hand, for Haumea–Hi'iaka system ($\gamma_{\rm sp} = 4.5 \times 10^{-3}$), the bulk density of Haumea (1800 kg m^{-3}; Ortiz et al., 2017) is larger than that of Hi'iaka ($\simeq$ 1000 kg m^{-3}; Ragozzine and Brown, 2009). Therefore, the secondary, Hi'iaka, is a pure icy body, while its primary, Haumea, consists of both ice and rock. These observational constraints are consistent with the theory that both large and small satellites around large TNOs are impact moons formed via giant impacts between differentiated bodies, although we do not reject the possibility of the formation of intact moons from undifferentiated bodies.

During simulation of the formation of the intact moon, the periapsis distance $q_{\rm ini}$ was typically 3–4$R_{\rm p}$, where $R_{\rm p}$ is the planetary radius of the primary (Fig. 8.3). The eccentricity ($e_{\rm ini}$) was distributed across all ranges, from zero to one (Fig. 8.3). This is consistent with a previous study that simulated the impact that formed the Pluto-Charon system (Canup, 2005). Note that we did not consider the long-term co-evolution of the debris disk and intact moon(s), such as the accretion of disk materials onto intact moons, tidal interaction of the intact moon and disk, and so on. We should address these issues in the future.

8.2 Tidal evolution of satellites' orbits

We then performed semi-analytical tidal evolution calculations to discern whether intact moons formed via giant impacts can evolve into satellites with circular orbits. Tidal evolution was found to be strongly dependent on the material states, and we found that most of the intact moons turned into eccentric satellites when their planetary bodies always behaved as rigid bodies, while most of all the intact moons ended up with circular orbits when their planetary bodies initially had small rigidity and behaved as fluid-like bodies (see Supplementary Section 8.S1 and Supplementary Fig. 8.S6).

Figure 8.4 shows the final spin and orbital periods of satellite systems formed as intact moons. Among the satellites around large TNOs, only the Pluto–Charon system is in a dual-synchronous state, i.e., the spin periods of satellite ($P_{\rm spin,s}$) and the primary ($P_{\rm spin,p}$) coincide with the orbital period ($P_{\rm orb}$).

We found that the current spin and orbital periods of largest TNOs could be well explained when assuming planetary bodies would behave as fluid-like bodies for 10^4–10^6 years after a giant impact. If the duration of fluid-like behavior was 4.5×10^9 years, however, most of the satellite systems reached a dual-synchronous state, and there were no satellites with spin and orbital pe-

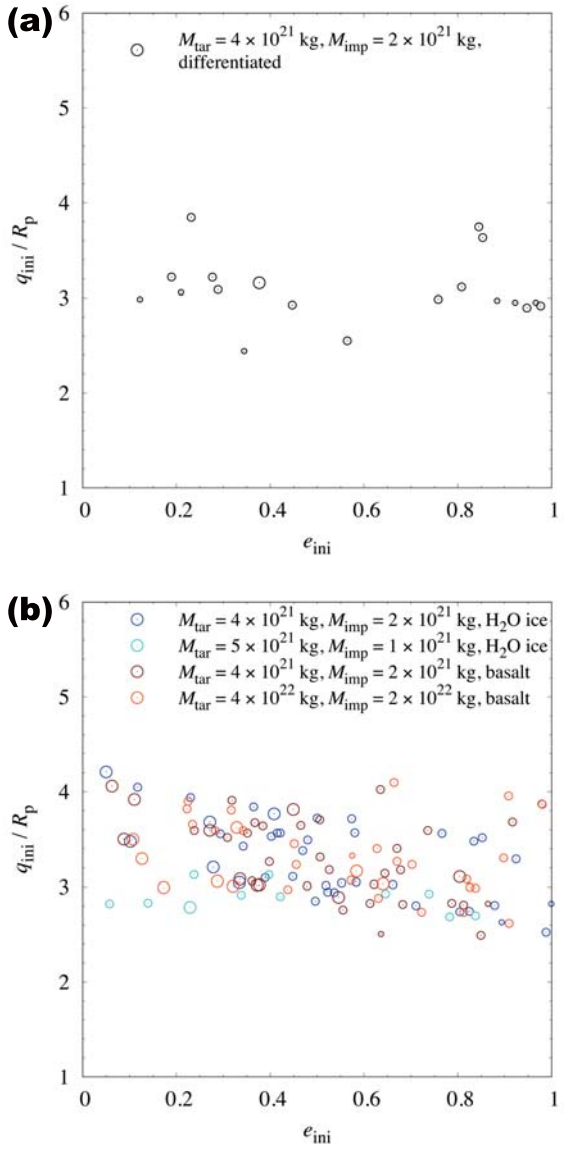

Figure 8.3: Initial distribution of periapsis distance q_{ini} and eccentricity e_{ini} of intact moons before tidal evolution. The size (large, medium, small) of each circle represents γ_{sp} ($10^{-1} \leq \gamma_{sp}$ for large circles, $10^{-2} \leq \gamma_{sp} < 10^{-1}$ for medium-sized circles, and $10^{-3} \leq \gamma_{sp} < 10^{-2}$ for small circles). (a) the case for differentiated bodies. (b) the case for undifferentiated bodies.

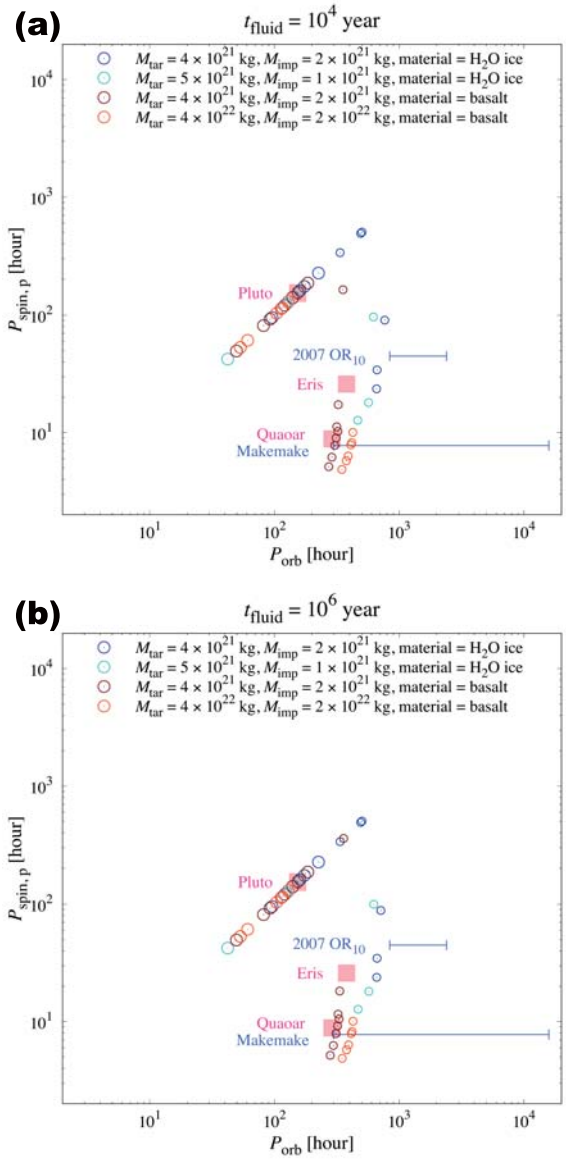

Figure 8.4: Final $P\mathrm{spin,p}$ and P_{orb} values. The observational data of $P\mathrm{spin,p}$ and P_{orb} are represented by pink square markers and blue bars, respectively. The size of each circle represents γ_{sp} as in Fig. 3. Case (a) shows the outcome of tidal evolution when planetary bodies were fluid for the first 10^4 years and became rigid from 10^4 years to 4.5×10^9 years after a giant impact. Case (b) shows the outcome of tidal evolution when planetary bodies were fluid for the first 10^6 years and became rigid from 10^6 years to 4.5×10^9 years after a giant impact. Case (c) shows the outcome of tidal evolution when planetary bodies were fluid for the whole 4.5×10^9 year duration.

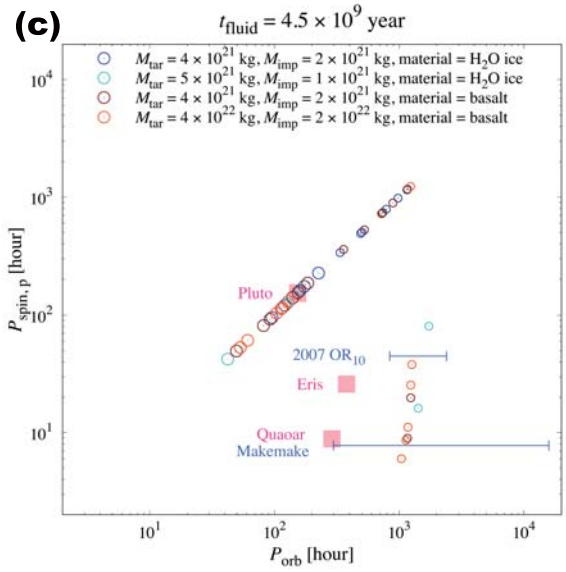

Figure 8.4: (continued)

riods are similar to the Eris–Dysnomia or Quaoar–Weywot systems.

8.3 Discussions and conclusions

We can give some constraints on the thermal evolution of large TNOs from these results. For the case of giant impacts with 1000 km-sized bodies, the effects of impact heating on the internal thermal state of planetary bodies are limited (Canup, 2005). The heat generation from tidal heating can be calculated using the orbital energy of the satellite and the tidal evolution timescale (Supplementary Section 8.S2). We found that, when satellites were initially in solid-state, they could not heat up enough to melt, even if their semimajor axis was as small as their Roche radius.

These results suggest that if all satellites around TNOs have a circular orbit, they were fully or partially molten during the giant impact era. This is consistent with the results of Canup (2011), which suggests that Charon and other small satellites around Pluto were formed via giant impacts with partially differentiated progenitors.

Experimental studies of dust aggregation (e.g., Blum and Wurm, 2008) suggest that micron-sized dust grains aggregate into centimeter-size pebbles in the gaseous solar nebula. In addition, observation of Comet 103P/Hartley (Kelley et al., 2013) shows that its dusty coma is made up of centimeter-sized pebbles. Therefore, kilometer-sized planetesimals with abundant centimeter-sized pebbles may be present at the onset of dwarf planet formation. Shannon et al. (2016) revealed that large TNOs can be formed in situ within a period of a few million years, from a solid belt of kilometer-sized and centimeter-sized bodies. Or, when large TNOs form via accretion of pebbles onto planetesimals in a gaseous solar nebula (e.g., Johansen et al., 2012), the accretion timescale

must be shorter than the lifetime of the solar nebula ($\sim$ 4 Myr: Wang et al., 2017). In these cases, large TNOs that form within a few million years can enter either a partially or fully molten state (Sekine et al., 2017). In addition, when the collision timescale of gravitationally focused large TNOs is also of the order of 10 Myr, then this implies that satellite formation around the TNOs occurred before the outward migration of the outer planets including Neptune (Gomes et al., 2004). This migration is related to the Late Heavy Bombardment ($\sim$ 700 Myr after the formation of the solar system: Gomes et al., 2005), which is thought to have been a favorable epoch for the formation of rings and inner regular satellites around Saturn, Uranus, and Neptune (Hyodo et al., 2017a).

Methods

8.A Numerical code and initial settings for giant impacts

We used the SPH method to perform giant impact simulations (e.g., Monaghan, 1992). The SPH method can easily trace large deformations and shock waves, and has been used in many previous giant impact simulations. Our numerical code is the same as that used in Genda et al. (2015) and it can calculate a purely hydrodynamic flow with self-gravity, but without material strength. We considered three types of pre-impact bodies; undifferentiated basaltic bodies, undifferentiated icy bodies, and differentiated bodies with a basalt core and an icy mantle. We applied the Tillotson equation of state (Tillotson, 1962), which is widely used for giant impact simulations, to calculate the pressure from the internal energy and the density. We note that some previous studies assumed other materials for differentiated/undifferentiated planetary bodies. For example, Canup (2005) used a hydrated silicate, serpentine, for the material of undifferentiated Pluto–Charon progenitors, whereas Sekine et al. (2017) assumed well-mixed mixtures of H_2O ice and basalt as the materials of Pluto-Charon progenitors. A detailed study on the dependence of the outcome of collision on the material chosen should be performed in the future. For our simulations, all SPH particles in the planetary bodies were set to have an equal mass (m_0) and the number of total particles, $N_{\rm total}$ = 24,000. Two impactor-to-target mass ratios ($\gamma_{\rm imp}$) were used in this study, 1/2 and 1/5; the numbers of particles in the target and impactor for these ratios were 16,000 and 8,000 for $\gamma_{\rm imp} = 1/2$, and 20,000 and 4,000 for $\gamma_{\rm imp} = 1/5$. The internal energy of the SPH particles was set to 5.0×10^5 J kg^{-1} and neither the impactor nor the target had pre-impact spin. The method for placement of SPH particles is detailed in Genda et al. (2012).

We prepared 434 sets of initial conditions for the giant impact simulations. The parameters used in this study were the total mass of the target and the impactor ($M_{\rm total}$), the impactor-to-target mass ratio ($\gamma_{\rm imp}$), composition and differentiated state, the impact angle ($\theta_{\rm imp}$), and the impact velocity ($v_{\rm imp}$). We considered two different values for the total mass, $M_{\rm total} = 6 \times 10^{21}$ kg and 6×10^{22} kg. For each case, we varied $\theta_{\rm imp}$ in 15° steps from 30° to 75°, and the $v_{\rm imp}$ in $0.1 v_{\rm esc}$ steps from $0.9 v_{\rm esc}$ to $1.7 v_{\rm esc}$, above the hit-and-run criteria, where $v_{\rm esc}$ is the two-body escape velocity (Agnor and Asphaug, 2004). In order to precisely determine the intact-moon-forming parameter space, we varied $v_{\rm imp}$ with much smaller steps ($0.02 v_{\rm esc}$) below the hit-and-run criteria. The impact parameters $v_{\rm imp}$ and $\theta_{\rm imp}$ are defined when the two planetary bodies are in contact with each other. To prepare the initial condition, we back-calculated the positions of the two planetary bodies until their distance from each other was $3\left(R_{\rm tar} + R_{\rm imp}\right)$ for the cases of $v_{\rm imp} < v_{\rm esc}$ and at $10\left(R_{\rm tar} + R_{\rm imp}\right)$ for the cases of $v_{\rm imp} \geq v_{\rm esc}$, where $R_{\rm tar}$ and $R_{\rm imp}$ are the radius of the target and impactor, respectively, assuming planetary bodies are mass points (see Fig. 1 of Genda et al., 2012). We then performed the SPH simulations over a period of 10^6 s.

8.B Resolution test

We carried out higher-resolution (480,000 particles) simulations for differentiated bodies. First, we confirmed that small (i.e., $10^{-3} \lesssim \gamma_{\rm sp} \lesssim 10^{-2}$) intact moons are formed via giant impacts between differentiated bodies for both lower- and higher-resolution simulations. For the case of $v_{\rm imp} = 1.25 v_{\rm esc}$ and $\theta_{\rm imp} = 30^\circ$, the outcome of the giant impact is the formation of an intact moon without a rocky core ($\gamma_{\rm sp} = 1.0 \times 10^{-2}$ for the lower-resolution simulation and $\gamma_{\rm sp} = 3.4 \times 10^{-3}$ for the higher-resolution simulation). These giant impact also generated a debris disk ($M_{\rm disk}/M_{\rm p} = 8.4 \times 10^{-3}$ for the lower-resolution simulation and $M_{\rm disk}/M_{\rm p} = 1.5 \times 10^{-2}$ for the higher-resolution simulation). The integration time for the higher- and lower-resolution simulations are 5×10^5 s and 1×10^6 s, respectively.

Second, we analyzed the time evolution of the disk mass for both lower- and higher-resolution simulations—for the case of $v_{\rm imp} = 1.05 v_{\rm esc}$ and $\theta_{\rm imp} = 30^\circ$—resulting in the formation of a disk without an intact moon (Supplementary Figure 8.S7). The disk mass decreases with time from $7.1 \times 10^{-2} M_{\rm p}$ at $t = 2 \times 10^5$ s to $3.6 \times 10^{-2} M_{\rm p}$ at $t = 10^6$ s due to unphysical (numerical) viscous spreading (because the physical viscous spreading timescale is 10^7–10^8 s when $M_{\rm p} \simeq 6 \times 10^{21}$ kg and $M_{\rm disk}/M_{\rm p} \simeq 5 \times 10^{-2}$; Daisaka et al., 2001; Takeda and Ida, 2001). A similar trend is also found for a higher-resolution simulation with 480,000 particles. Although we might have underestimated the disk mass by a factor of two, the mass of an intact moon is typically much larger than the mass of a disk-origin moon by an order of magnitude, as long as the intact moon is formed.

In addition, we also carried out three 240,000 particle simulations for undifferentiated icy bodies. We confirmed that large (i.e., $\gamma_{\rm sp} \gtrsim 10^{-1}$) intact moons are formed via giant impacts between undifferentiated bodies for both lower- and higher-resolution simulations. For the case of $v_{\rm imp} = 1.02$–$1.06 v_{\rm esc}$ and $\theta_{\rm imp} = 75^\circ$, the outcome of the giant impact is the formation of an intact moon without a debris disk. For lower-resolution simulations, $\gamma_{\rm sp} = 7.8 \times 10^{-2}$ for $v_{\rm imp} = 1.02 v_{\rm esc}$, $\gamma_{\rm sp} = 9.4 \times 10^{-2}$ for $v_{\rm imp} = 1.04 v_{\rm esc}$, and $\gamma_{\rm sp} = 1.1 \times 10^{-1}$ for $v_{\rm imp} = 1.06 v_{\rm esc}$. For higher-resolution simulations, $\gamma_{\rm sp} = 1.2 \times 10^{-1}$ for $v_{\rm imp} = 1.02 v_{\rm esc}$, $\gamma_{\rm sp} = 6.0 \times 10^{-2}$ for $v_{\rm imp} = 1.04 v_{\rm esc}$, and $\gamma_{\rm sp} = 1.1 \times 10^{-1}$ for $v_{\rm imp} = 1.06 v_{\rm esc}$. The integration time for the higher- and lower-resolution simulations are 5×10^5 s and 1×10^6 s, respectively. We confirmed that intact moons are still widely formed for both lower- and higher-resolution simulations, although changing the number of total particles $N_{\rm total}$ may change the outcomes slightly.

We also performed several additional calculations using the 5-phase equation of state for H_2O (Senft and Stewart, 2008) adapting at Gadget-2 (Springel, 2005) used in previous work (Hyodo and Genda, 2018) with $N_{\rm total}$ = 300,000 (Supplementary Figure 8.S8). We confirmed that changing the resolution and EOS may change the outcomes slightly, but intact moons are still widely formed within the parameter range.

8.C Analysis of the masses of planetary bodies

To obtain the masses of planetary bodies from the collision outcome data, we used a friends-of-friends algorithm (Genda et al., 2012) to identify clumps of SPH particles. If the distance between two particles was less than a critical value ($l_{\rm FOF}$), we defined these particles as belonging to the same clump. $l_{\rm FOF}$ is given by $l_{\rm FOF} = \sqrt{3}(m_0/\rho_0)^{1/3}$, where $m_0 = M_{\rm total}/N_{\rm total}$ is the mass of each SPH particle, and $\rho_{0,\rm basalt} = 2700$ kg m^{-3} and $\rho_{0,\rm ice} = 917$ kg m^{-3} are the typical densities of the basaltic and icy solid bodies (Tillotson, 1962). The value of $l_{\rm FOF}$ is slightly larger than the typical distance between two nearest SPH particles under initial conditions. The distances for all pairs of particles were calculated and we identified clumps.

We regarded clumps that had more than 24 particles as planetary bodies. We termed the largest planetary body the "primary", and the second largest body the "secondary". There were also SPH particles that did not belong to any planetary bodies after collision. We termed these particles isolated particles, and if isolated particles were gravitationally bound to the primary, we identified these particles as disk particles. We calculated the disk mass ($M_{\rm disk}$) from the number of disk particles ($N_{\rm disk}$) as $M_{\rm disk} = N_{\rm disk} m_0$. In this study, we did not calculate the equivalent circular orbital radius (Canup, 2004) nor the pericenter distance of disk particles (Hyodo et al., 2017b), so the disk mass might be slightly overestimated.

In this paper, we mainly focus on the formation of intact moons, but we also discuss satellite formation via impact-generated disks. The dependence of the mass of the disk-origin moon ($M_{\rm DM}$) on the disk mass ($M_{\rm disk}$) is given by Hyodo et al. (2015) and references therein;

$$M_{\rm DM} = \min\left[0.3\frac{M_{\rm disk}}{M_{\rm p}}, 10\left(\frac{M_{\rm disk}}{M_{\rm p}}\right)^2, 2000\left(\frac{M_{\rm disk}}{M_{\rm p}}\right)^3\right], \tag{8.2}$$

where $M_{\rm p}$ is the mass of the primary; although $M_{\rm DM}$ might also be dependent on the disk angular momentum in reality (Kokubo et al., 2000).

8.D Catastrophic disruption of primordal moons and the formation of Haumean moons

Haumea has a short spin period of 3.92 hours (Rabinowitz et al., 2006), and it has two satellites named Hi'iaka and Namaka. The masses of Haumea, Hi'iaka, and Namaka are 4.0×10^{21} kg, 1.8×10^{19} kg, and 1.8×10^{18} kg, respectively (Ragozzine and Brown, 2009), and the secondary-to-primary mass ratio ($\gamma_{\rm sp}$) of the Haumean system is $\sim 4.5 \times 10^{-3}$. If these two satellites were formed close to Haumea, their spins would be expected to have been tidally despun, and they should therefore be rotating synchronously with their own orbital periods. The spin period of Hi'iaka is about 120 times faster than its orbital period (Hastings et al., 2016), however, suggesting that the two current satellites were formed via the catastrophic disruption and re-accretion of a past moon that was located near to the current orbits of the two satellites (Schlichting and Sari, 2009; Ćuk et al., 2013). This mechanism has also been debated in the con-

text of the late formation of Saturn's midsized moons and its rings (Ćuk et al., 2016; Hyodo and Charnoz, 2017).

In our simulations, giant impacts between differentiated bodies sometimes formed multiple intact moons via a single impact (Fig. 8.2a). This indicates the possibility of collision between multiple intact moons. In contrast, no multiple intact moons were formed during simulations of single giant impacts between undifferentiated bodies (Figs. 8.2b and Supplementary Figs. 8.S4a–c). Therefore, the possibility of collisions between multiple intact moons does have the potential to explain the origin of Hi'iaka and Namaka. The question of whether multiple satellites will survive, or instead merge into single large satellite, is beyond the scope of this study.

8.E Orbital evolution of formed satellites

Both the planet and satellite raise tides on each other. The tidal lag caused by friction leads to angular momentum exchange, which also leads to spin and orbital evolution. The tidal evolution of Pluto-Charon has been investigated by several previous studies (Ward and Canup, 2006; Cheng et al., 2014; Woo and Lee, 2018). In this study, we used $\mathcal{O}(e^6)$ tidal evolution equations (Ferraz-Mello, 2013) combined with the constant phase lag model (Goldreich and Peale, 1966, see Supplementary Section 1 for details). Note that if we want to calculate the tidal evolution pathways whose eccentricities are larger than $\sim$ 0.4, we must consider the eccentricity e for a higher order (Goldreich and Peale, 1966). In this study, however, we only calculated tidal evolution where the initial eccentricity was lower than 0.4.

If intact moons were rigid immediately after their formation, they most likely turned into eccentric satellites (Supplementary Fig. 8.S6a). Even when satellites were in a fluid-like state for the first 10^3 years, almost all satellites with $\gamma_{\rm sp}$ values lower than 10^{-1} became eccentric (Supplementary Fig. 8.S6b). These simulations seem to be inconsistent with observations. When the initial eccentricity was smaller than 0.1, the orbit of an intact moon becomes circular whether they were molten or not. However, the initial eccentricity is widely distributed in a range from zero to unity (Fig. 8.3), and long-term eccentricity damping by simultaneously formed debris disk would not be efficient. Therefore, the probability of eccentricity damping might not be so high if the duration of the initial fluid-like state was shorter than 10^3 years. In contrast, when the duration of the initial fluid-like state was longer than 10^4 years, our calculations suggested that almost all intact moons can turn into circular satellites (Supplementary Figs. 8.S6c and d).

Supplementary Material to Chapter 8

8.S1 The equations of tidal evolution

Tides are raised on both the primary and secondary. In this study, we used the $\mathcal{O}(e^6)$ tidal evolution equations1 combined with the constant phase lag model (Goldreich and Peale, 1966). The orbit-averaged evolution of the spin rates of the planet, Ω_p, and satellite, Ω_s, the semimajor axis, a, and the eccentricity, e, are calculated from the following equations:

$$-\frac{1}{n}\frac{\mathrm{d}\Omega_\mathrm{p}}{\mathrm{d}t} = \frac{15n}{4}\frac{{M_\mathrm{s}}^2}{(M_\mathrm{p}+M_\mathrm{s})M_\mathrm{p}}\left(\frac{R_\mathrm{p}}{a}\right)^3\sum_{i=-3}^{+3}\frac{k_{2,\mathrm{p}}}{Q_\mathrm{p}}E_{2,i}^2(e)\,\mathrm{sgn}\big[2\Omega_\mathrm{p}-(2-i)n\big], \tag{8.3}$$

$$-\frac{1}{n}\frac{\mathrm{d}\Omega_\mathrm{s}}{\mathrm{d}t} = \frac{15n}{4}\frac{{M_\mathrm{p}}^2}{(M_\mathrm{p}+M_\mathrm{s})M_\mathrm{s}}\left(\frac{R_\mathrm{s}}{a}\right)^3\sum_{i=-3}^{+3}\frac{k_{2,\mathrm{s}}}{Q_\mathrm{s}}E_{2,i}^2(e)\,\mathrm{sgn}[2\Omega_\mathrm{s}-(2-i)n], \tag{8.4}$$

$$\begin{aligned}\frac{1}{a}\frac{\mathrm{d}a}{\mathrm{d}t} &= \frac{3n}{2}\frac{M_\mathrm{s}}{M_\mathrm{p}}\left(\frac{R_\mathrm{p}}{a}\right)^5\sum_{i=-3}^{+3}\frac{k_{2,\mathrm{p}}}{Q_\mathrm{p}}(2-i)E_{2,i}^2(e)\,\mathrm{sgn}\big[2\Omega_\mathrm{p}-(2-i)n\big]\\ &\quad+\frac{3n}{2}\frac{M_\mathrm{p}}{M_\mathrm{s}}\left(\frac{R_\mathrm{s}}{a}\right)^5\sum_{i=-3}^{+3}\frac{k_{2,\mathrm{s}}}{Q_\mathrm{s}}(2-i)E_{2,i}^2(e)\,\mathrm{sgn}[2\Omega_\mathrm{s}-(2-i)n],\end{aligned} \tag{8.5}$$

$$\begin{aligned}-\frac{1}{e}\frac{\mathrm{d}e}{\mathrm{d}t} &= \frac{3n}{4e^2}\frac{M_\mathrm{s}}{M_\mathrm{p}}\left(\frac{R_\mathrm{p}}{a}\right)^5\sum_{i=-3}^{+3}\frac{k_{2,\mathrm{p}}}{Q_\mathrm{p}}\Big[2\sqrt{1-e^2}-(2-i)(1-e^2)\Big]E_{2,i}^2(e)\,\mathrm{sgn}\big[2\Omega_\mathrm{p}-(2-i)n\big]\\ &\quad+\frac{3n}{4e^2}\frac{M_\mathrm{p}}{M_\mathrm{s}}\left(\frac{R_\mathrm{s}}{a}\right)^5\sum_{i=-3}^{+3}\frac{k_{2,\mathrm{s}}}{Q_\mathrm{s}}\Big[2\sqrt{1-e^2}-(2-i)(1-e^2)\Big]E_{2,i}^2(e)\,\mathrm{sgn}[2\Omega_\mathrm{s}-(2-i)n].\end{aligned} \tag{8.6}$$

148

Here, n is the mean motion, M_p, M_s, R_p, and R_s are the mass and radius of primary and secondary, respectively, and Q_p, Q_s, $k_{2,\mathrm{p}}$, and $k_{2,\mathrm{s}}$ are the dissipation functions and Love numbers of the primary and the secondary, respectively. These equations preserve the total angular momentum1. In this study, we assumed $Q_\mathrm{p} = Q_\mathrm{s} = 100$ (Cheng et al., 2014). The Love number $k_{2,i}$ is given by,

$$k_{2,i} = \frac{3}{2}\left(1 + \frac{38\pi}{3}\frac{\mu_i {R_i}^4}{G{M_i}^2}\right)^{-1}, \tag{8.7}$$

where μ_i is the rigidity of body i (= p for primary and = s for secondary), and G is the gravitational constant. We adopt a μ_i value of 6.5×10^{10} Pa for rigid basalt (Peale and Cassen, 1978) and a μ_i value of 4×10^9 Pa for rigid ice (Hastings et al., 2016). We set $\mu_i = 0$ when the planetary bodies were exhibiting fluid-like behavior, for simplicity. This treatment is used in the tidal evolution calculation of Eris-Dysnomia system (Greenberg and Barnes, 2008). The eccentricity functions $E_{2,i}(e)$ are presented by Efroimsky (2012).

Note that to calculate the tidal evolution pathways with eccentricities where $e \gtrsim 0.4$, we must use the tidal evolution equations that consider the higher-order effects of eccentricity (see Goldreich and Peale, 1966). In this study, however, we only calculated tidal evolution where the initial eccentricity was lower than 0.4.

In this study, we did not consider the effects of a dynamical tide. The dynamical tide can dump eccentricity efficiently when the periapsis distance is small, however, the current dynamical tide model is not suitable for rigid planetary bodies, and this is beyond the scope of this study.

When the primary rotates quickly and the secondary is in synchronous state, i.e., $\Omega_\mathrm{p} \gg (3/2)n$ and $\Omega_\mathrm{s} = n$, the tidal torque caused by the primary increases the orbital eccentricity, while the tidal torque caused by the secondary decreases eccentricity. In this case, the orbit-averaged variation of eccentricity can be simplified as follows:

$$\begin{aligned}
\frac{1}{e}\frac{\mathrm{d}e}{\mathrm{d}t} &= \frac{3n}{4}\frac{M_\mathrm{s}}{M_\mathrm{p}}\left(\frac{R_\mathrm{p}}{a}\right)^5 \frac{k_{2,\mathrm{p}}}{Q_\mathrm{p}}\left(11 + \mathcal{O}(e^2)\right) \\
&\quad -\frac{3n}{4}\frac{M_\mathrm{p}}{M_\mathrm{s}}\left(\frac{R_\mathrm{s}}{a}\right)^5 \frac{k_{2,\mathrm{s}}}{Q_\mathrm{s}}\left(\frac{25}{2} + \mathcal{O}(e^2)\right), \\
&\simeq \frac{33n}{4}\frac{M_\mathrm{s}}{M_\mathrm{p}}\left(\frac{R_\mathrm{p}}{a}\right)^5 \frac{k_{2,\mathrm{p}}}{Q_\mathrm{p}}\left(1 - \frac{25}{22}A\right),
\end{aligned} \tag{8.8}$$

where:

$$A \equiv \frac{k_{2,\mathrm{s}}}{k_{2,\mathrm{p}}}\frac{Q_\mathrm{p}}{Q_\mathrm{s}}\left(\frac{M_\mathrm{p}}{M_\mathrm{s}}\right)^2\left(\frac{R_\mathrm{s}}{R_\mathrm{p}}\right)^5. \tag{8.9}$$

The dimensionless parameter A is the relative rate of tidal dissipation in the planet and satellite (Ward and Canup, 2006). Whether eccentricity increases through tidal evolution can then be determined using the relative rate of tidal dissipation in the planet and satellite; if A is larger than unity, dissipation mainly occurs in the satellite, and eccentricity will decrease (e.g., Cheng et al., 2014).

If we assume that the density and the dissipation function are the same for both the primary and the secondary, the parameter A depends on ratios of the

planetary radii (R_s/R_p) and the Love numbers ($k_{2,s}/k_{2,p}$). For rigid bodies, the Love number of 1000 km-sized solid-like bodies is smaller than unity, and is proportional to the square of the planetary radius. In contrast, for fluid-like bodies (i.e., partially or fully molten bodies), the Love number is approximately 3/2, and does not depend on the planetary radius.

When the primary and the secondary are both in a rigid state, the relative rate A is:

$$A \sim \frac{R_s}{R_p} < 1, \tag{8.10}$$

whereas when both the primary and the secondary are in fluid-like state:

$$A \sim \frac{R_p}{R_s} > 1. \tag{8.11}$$

We found that eccentricity will decrease when both the primary and the secondary are in a fluid-like state.

8.S2 Tidal heating on intact moons

When the primary rotates quickly and the secondary is in synchronous state, the orbit-averaged variation of the semimajor axis can be simplified as follows:

$$\begin{aligned} \frac{1}{a}\frac{da}{dt} &= \frac{3n}{2}\frac{M_s}{M_p}\left(\frac{R_p}{a}\right)^5 \frac{k_{2,p}}{Q_p}\left(2 + 27e^2 + \mathcal{O}(e^4)\right) \\ &\quad - \frac{3n}{2}\frac{M_p}{M_s}\left(\frac{R_s}{a}\right)^5 \frac{k_{2,s}}{Q_s}\left(\frac{73}{2}e^2 + \mathcal{O}(e^4)\right). \end{aligned} \tag{8.12}$$

Here we discuss whether satellites in solid-state can turn into fluid-like bodies through tidal heating. When both the primary and the secondary are in a rigid state, the semimajor axis, a, increases with the timescale, τ_a, which is given by:

$$\begin{aligned} \tau_a &= \frac{1}{3n}\frac{M_p}{M_s}\left(\frac{a}{R_p}\right)^5 \frac{Q_p}{k_{2,p}} \\ &\sim 1 \times 10^5 \left(\frac{a/R_p}{4}\right)^{13/2} \left(\frac{R_s/R_p}{0.2}\right)^{-2} \left(\frac{R_p}{500\ \mathrm{km}}\right)^{-2} \mathrm{year}. \end{aligned} \tag{8.13}$$

The cooling timescale of a satellite due to heat conduction, τ_{cool}, is given by,

$$\tau_{cool} = \frac{\rho c R_s^2}{\lambda} \sim 3 \times 10^8 \left(\frac{R_s}{100\ \mathrm{km}}\right)^2 \mathrm{year}, \tag{8.14}$$

where c is the specific heat ($c = 1.13 \times 10^3$ J kg^{-1} K^{-1}; Sekine et al., 2017) and λ is the thermal conductivity ($\lambda = 2.1$ W K^{-1} m^{-1}; Saxena et al., 2018). In comparison with the cooling timescale and the tidal dissipation timescale, we found that most of the thermal energy generated by tidal dissipation is retained in both the primary and the secondary, which can increase the internal temperature of satellites.

The increase of temperature is given by,

$$\Delta T_s \sim \frac{\Delta E_s}{M_s c}, \tag{8.15}$$

Where ΔE_s is the thermal energy generated by tidal dissipation in the satellite. The thermal energy, ΔE_s, can be estimated from $\Delta E_\mathrm{s} \simeq \dot{E}_\mathrm{s}\tau_a$, where $\dot{E}_\mathrm{s}$ is the heat generation in the satellite per unit time. The heat generation rate, $\dot{E}_\mathrm{s}$, is given by:

$$\dot{E}_\mathrm{s} = \frac{1}{2}\frac{GM_\mathrm{p}M_\mathrm{s}}{a}\tau_\mathrm{s}^{-1}, \tag{8.16}$$

where the energy dissipation timescale of the satellite, τ_e, is given by:

$$\tau_\mathrm{e} = \frac{4}{219n}\frac{1}{e^2}\frac{M_\mathrm{s}}{M_\mathrm{p}}\left(\frac{a}{R_\mathrm{s}}\right)^5\frac{Q_\mathrm{s}}{k_{2,\mathrm{s}}}. \tag{8.17}$$

The increase of the internal temperature of the satellite, ΔT_s, is given by:

$$\begin{aligned}\Delta T_\mathrm{s} &\simeq \frac{73e^2}{8}\left(\frac{R_\mathrm{s}}{R_\mathrm{p}}\right)\frac{GM_\mathrm{p}}{ac} \\ &\sim 5\left(\frac{a/R_\mathrm{p}}{4}\right)^{-1}\left(\frac{e}{0.4}\right)^2\left(\frac{R_\mathrm{s}/R_\mathrm{p}}{0.2}\right)\left(\frac{R_\mathrm{p}}{500\ \mathrm{km}}\right)^2\ \mathrm{K}.\end{aligned} \tag{8.18}$$

Therefore, the effect of tidal dissipation is limited, and it is unlikely that satellites can move into a fluid-like state through tidal heating alone.

8.S3 Rubble-pile satellites

When a small satellite is formed via accretion from an impact-generated debris disk, the internal structure might be a rubble pile. Although the rigidity of rubble-pile bodies should depend on the radius and the composition, the rigidity of the Martian moon Phobos ($\sim$ 11 km in radius) is estimated to be $\mu \sim 6 \times 10^9$ Pa (Yoder, 1982) and this μ value is approximately one-tenth that of monolith rocky bodies. Then the orbit of a satellite becomes circular when the secondary-to-primary radius ratio is much higher than 1/10. Therefore, if some of the 100 km-sized satellites around large TNOs (e.g., Weywot, the satellite around Quaoar) are rubble-pile bodies, then we can explain their circular orbits; although large satellites such as Charon and Dysnomia might not be rubble piles and we need to consider (partially) molten satellites in the initial state of their tidal evolution.

8.S4 Supplementary table and figures

primary (R_p)	secondary (R_s)	$\gamma_{sp} \equiv M_s/M_p$
Pluto (1187 km) (Stern et al., 2015a)	Charon (606 km) (Stern et al., 2015a)	1.2×10^{-1} (Brozović et al., 2015)
Eris (1163 km) (Sicardy et al., 2011)	Dysnomia (350 km) (Brown and Butler, 2018)	3×10^{-2}
Haumea (816 km) (Ortiz et al., 2017)	Hi'iaka (150 km) (Ragozzine and Brown, 2009)	4.5×10^{-3} (Ragozzine and Brown, 2009)
Makemake (715 km) (Ortiz et al., 2012)	(no name) (90 km) (Parker et al., 2016)	2×10^{-3}
2007 OR_{10} (770 km) (Pál et al., 2016)	(no name) (180 km) (Kiss et al., 2017)	1×10^{-2}
Quaoar (535 km) (Fornasier et al., 2013)	Weywot (40 km) (Fornasier et al., 2013)	4×10^{-4}

$P_{spin,p}$ (h)	$P_{spin,s}$ (h)	P_{orb} (h)	e
153.2 (Brozović et al., 2015)	153.2 (Brozović et al., 2015)	153.2 (Brozović et al., 2015)	5×10^{-5} (Brozović et al., 2015)
25.9 (Roe et al., 2008)	(unknown)	379.0 (Brown and Butler, 2018)	$< 4 \times 10^{-3}$ (Brown and Butler, 2018)
3.91 (Rabinowitz et al., 2006)	9.8 (Hastings et al., 2016)	1187 (Ragozzine and Brown, 2009)	5×10^{-2} (Ragozzine and Brown, 2009)
7.77 (Heinze and de Lahunta, 2009)	(unknown)	300–16000 (Parker et al., 2016)	(unknown)
44.8 (Pál et al., 2016)	(unknown)	840–2400 (Kiss et al., 2017)	(unknown)
8.84 (Thirouin et al., 2010)	(unknown)	289.0 (Fraser et al., 2013)	~ 0.15 (Fraser et al., 2013)

Supplementary Table 8.1: Radii of primary and secondary (R_p and R_s), secondary-to-primary mass ratio (γ_{sp}), spin periods of primary and secondary ($P_{spin,p}$ and $P_{spin,s}$), the orbital period (P_{orb}), and the eccentricity (e) of the satellite systems around large trans-Neptunian objects. Note that, except for Pluto–Charon and Haumea–Hi'iaka, we estimated γ_{sp} by assuming that both the primary and the secondary have equal densities.

152

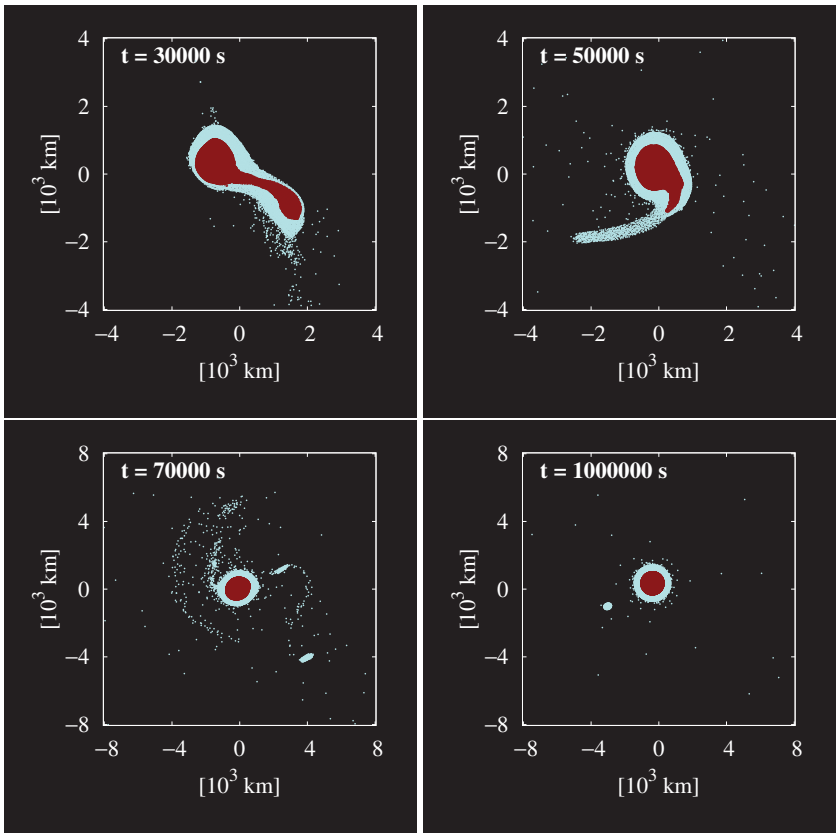

Supplementary Figure 8.S1: Snapshots of a giant impact between two differentiated bodies (as Figure 8.1). The impact velocity, $v_{\rm imp}$, was $1.05 v_{\rm esc}$, and the impact angle, $\theta_{\rm imp}$, was 75°, resulting in formation of an intact moon without a rocky core ($\gamma_{\rm sp} = 1.0 \times 10^{-2}$).

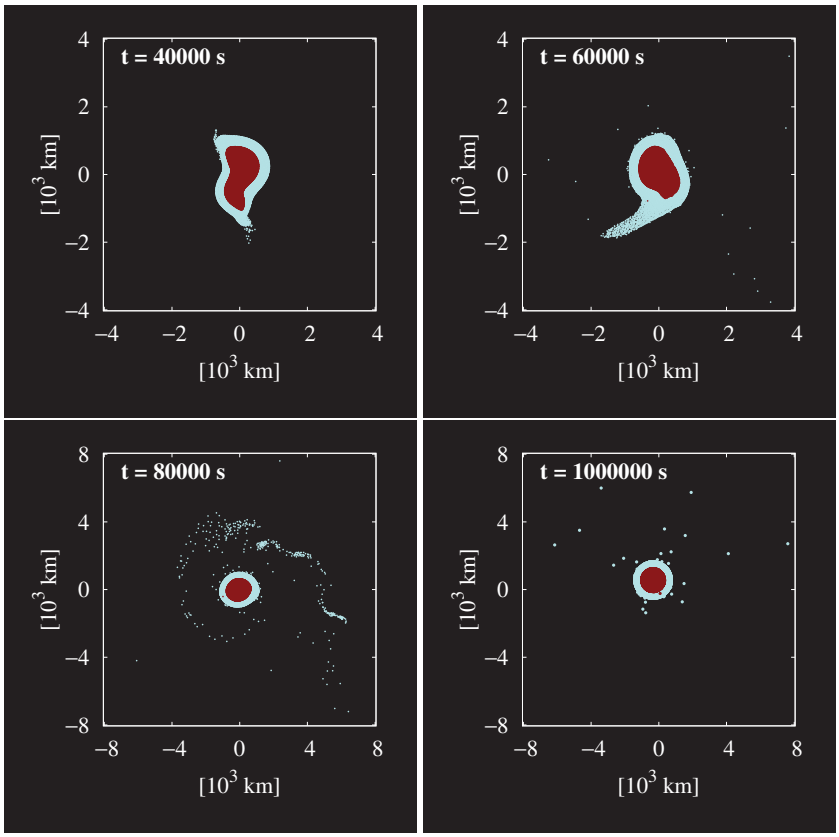

Supplementary Figure 8.S2: Snapshots of a giant impact between two differentiated bodies (as Figure 8.1). The impact velocity, v_{imp}, was $1.05 v_{\mathrm{esc}}$, and the impact angle, θ_{imp}, was 30°, resulting in the formation of a disk without an intact moon ($M_{|rmdisk}/M_{\mathrm{p}} = 3.6 \times 10^{-3}$ and the estimated mass of the disk-origin moon is $M_{\mathrm{DM}}/M_{\mathrm{p}} = 9.0 \times 10^{-5}$).

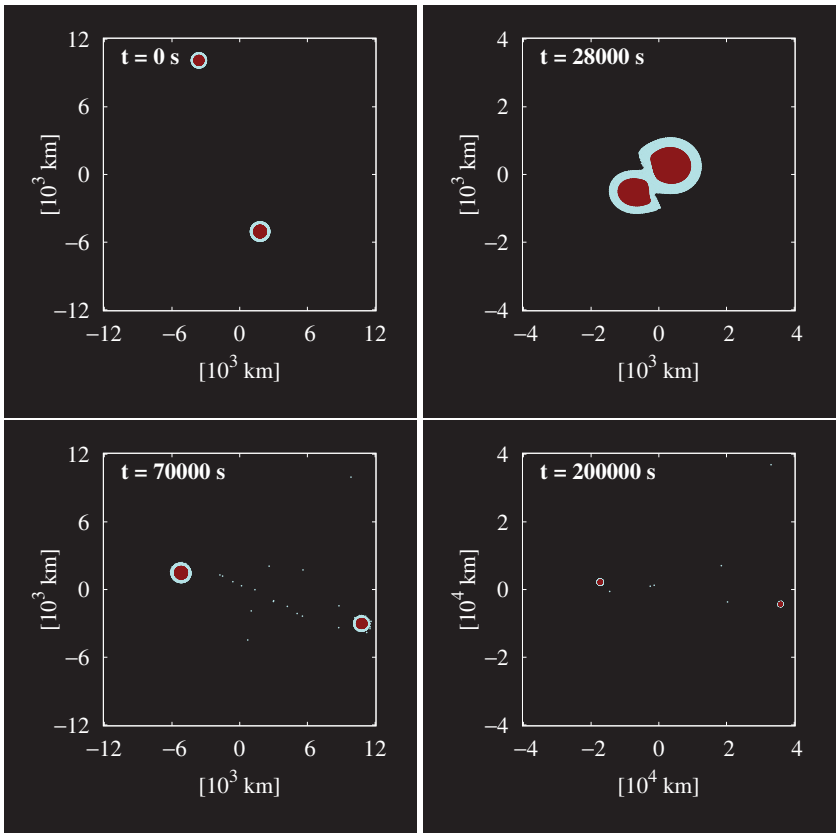

Supplementary Figure 8.S3: Snapshots of a giant impact between two differentiated bodies (as Figure 8.1). The impact velocity, v_{imp}, was $1.2 v_{\mathrm{esc}}$, and the impact angle, θ_{imp}, was 60°, resulting in a hit-and-run collision.

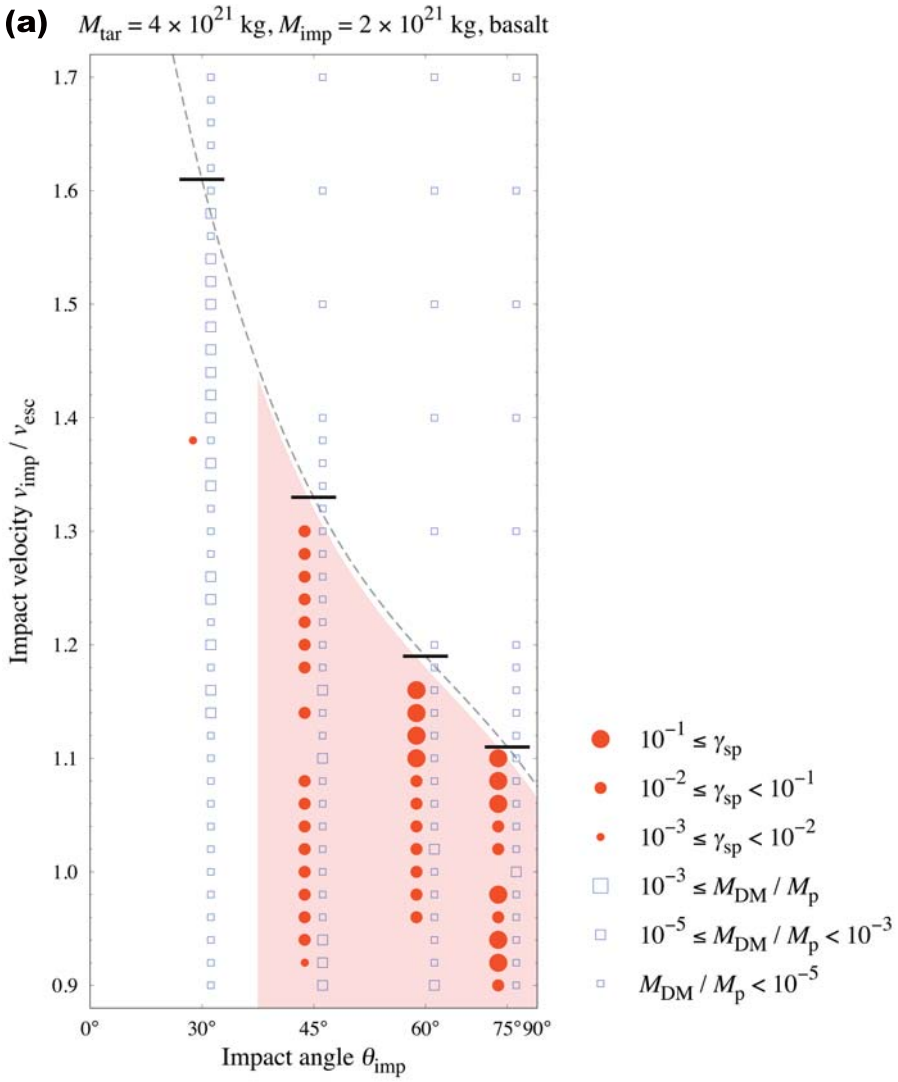

Supplementary Figure 8.S4: Summary of the range of outcomes for giant impacts (as Figure 8.2). (a) outcomes for giant impacts between rocky undifferentiated planetary bodies with masses of 4×10^{21} kg and 2×10^{21} kg. (b) outcomes for giant impacts between rocky undifferentiated planetary bodies with masses of 4×10^{22} kg and 2×10^{22} kg. (c) outcomes for giant impacts between icy undifferentiated planetary bodies with masses of 5×10^{21} kg and 1×10^{21} kg.

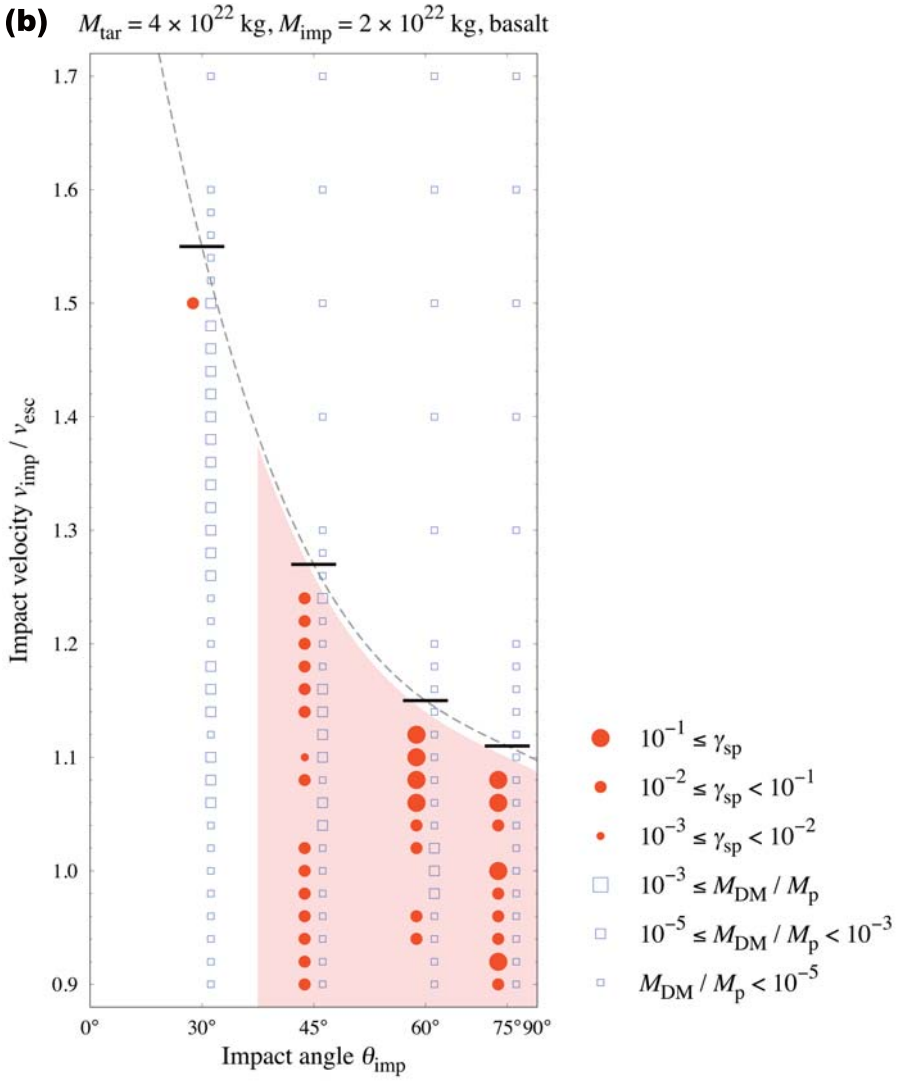

Supplementary Figure 8.S4: (continued)

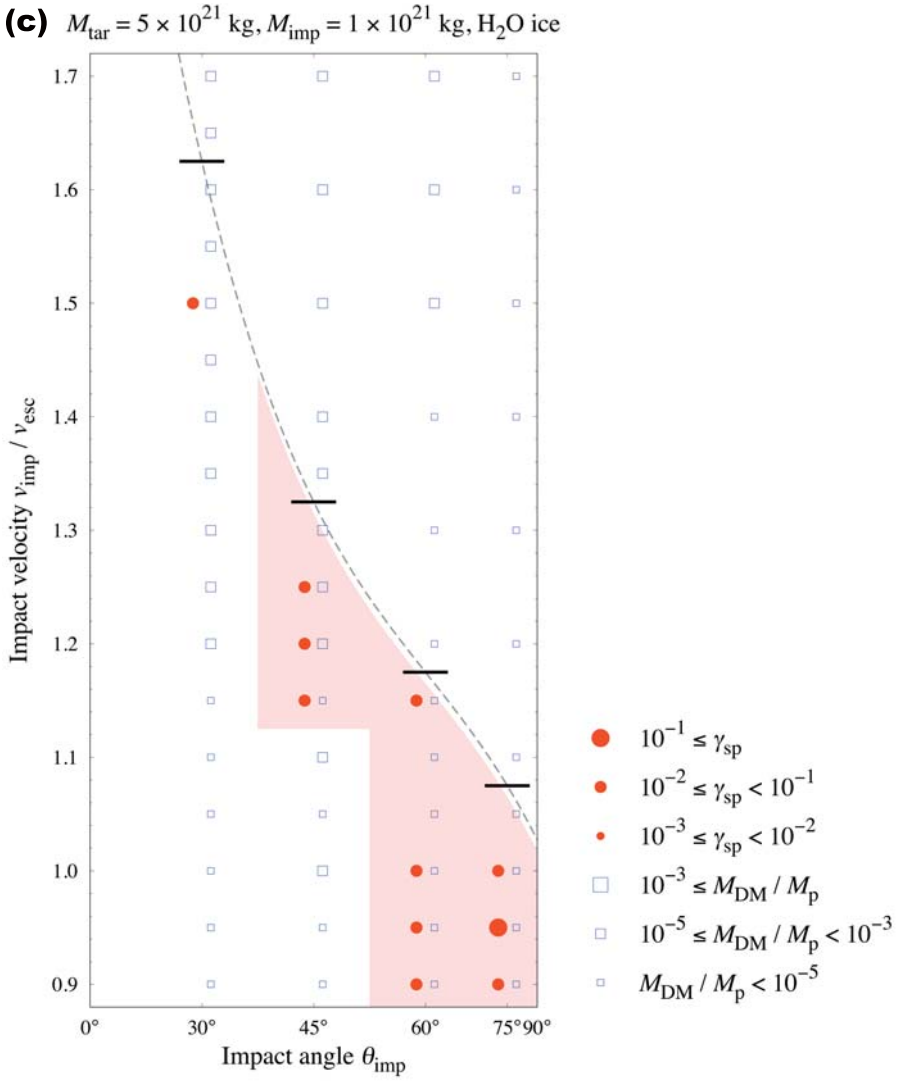

Supplementary Figure 8.S4: (continued)

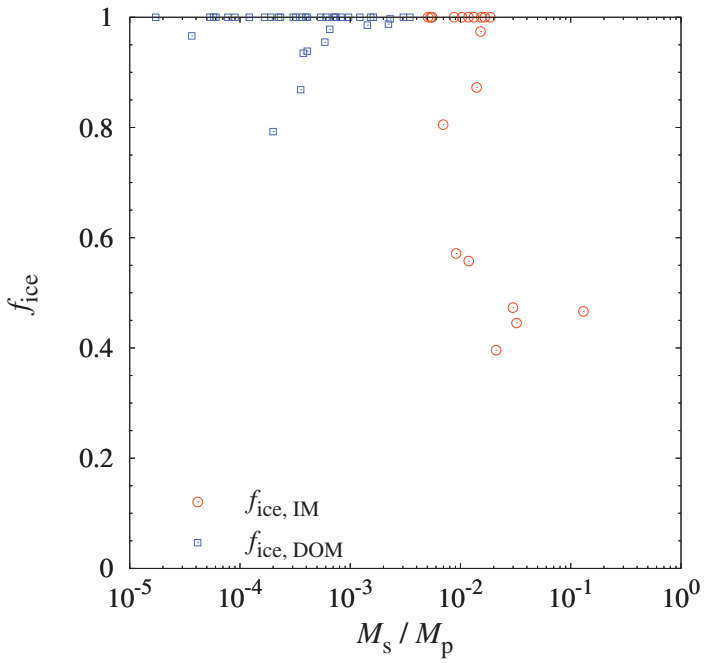

Supplementary Figure 8.S5: The ice mass fraction of intact moons ($f_{ice,IM}$; red circles) vs. the secondary-to-primary mass ratio γ_{sp}. Note that, for cases where multiple intact moons were formed, only the $f_{ice,IM}$ of the largest intact moon is shown. We also plot the ice mass fraction of disk-origin moons ($f_{ice,DM}$; blue squares) vs. the estimated γ_{sp} of the largest disk-origin moon. IM = intact moon, DM = disk-origin moon.

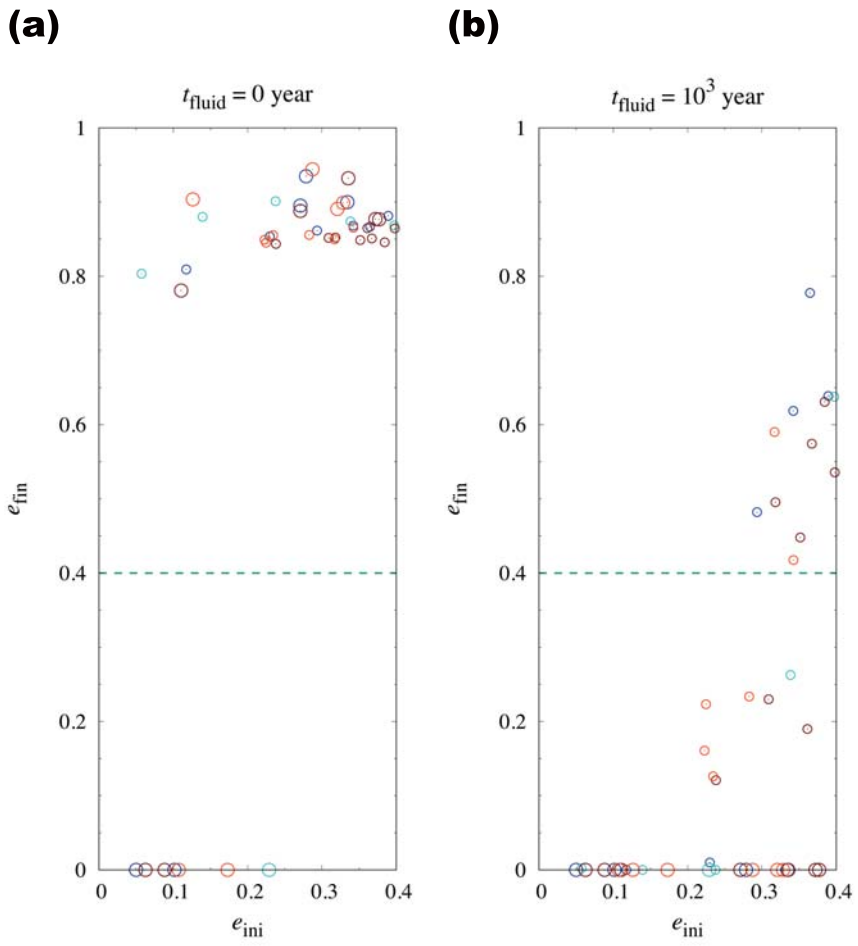

Supplementary Figure 8.S6: Final eccentricity after 4.5 Gyr-tidal evolution (e_{fin}) for different times taken for intact moons to become rigid bodies from fluid bodies (t_{fluid}). The size and color of each circle represents the γ_{sp} value and the mass and composition of the impactor and target, as in Fig. 3 in the main text. The four cases were as follows: (a) $t_{fluid} = 0$ years, in which planetary bodies were rigid for the whole time; (b) $t_{fluid} = 10^3$ years, in which represents that planetary bodies behaved as fluid for the first 10^3 years after the giant impact, before becoming rigid; (c) $t_{fluid} = 10^4$ years; and (d) $t_{fluid} = 10^6$ years. The tidal evolution pathways with e_{ini} values larger than ~ 0.4 could not be precisely calculated for the semi-analytical method that we used; a higher order method in e should be used (see Goldreich and Peale, 1966). Therefore, in this study we only calculated tidal evolution where e_{ini} was lower than 0.4.

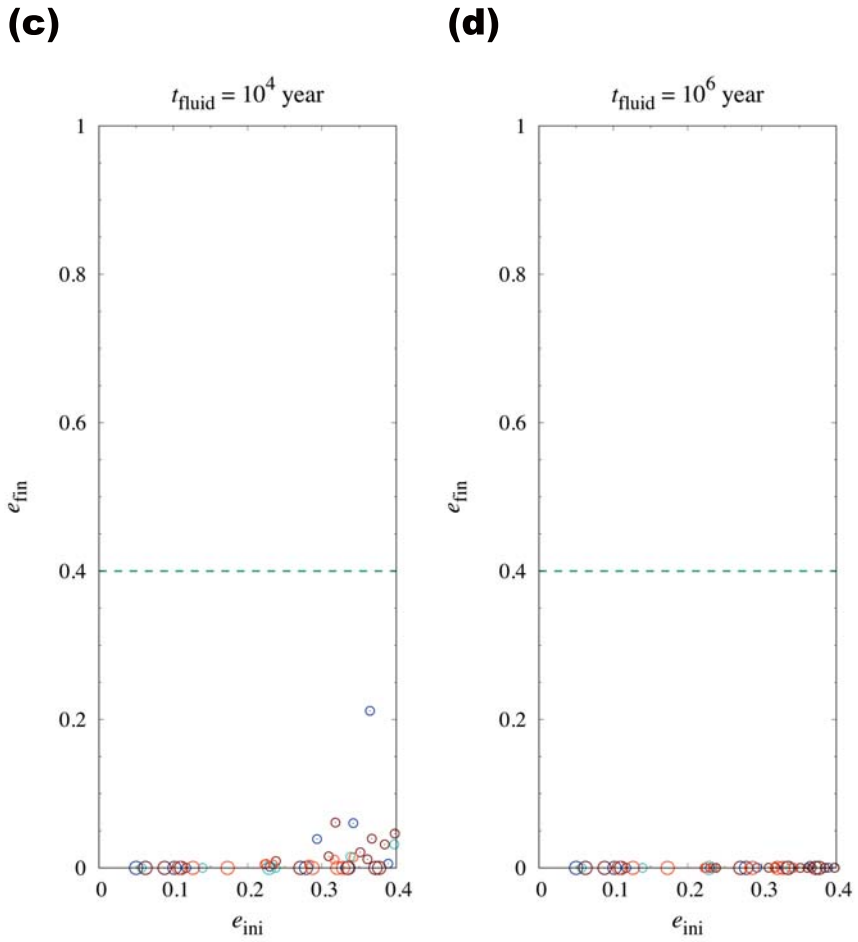

Supplementary Figure 8.S6: (continued)

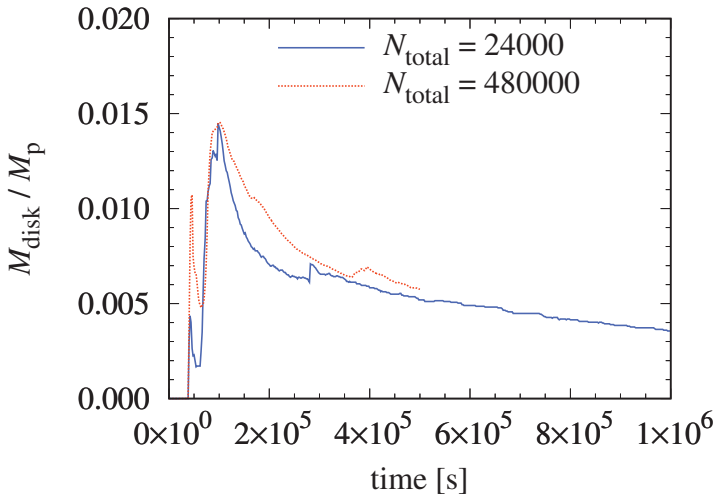

Supplementary Figure 8.S7: Time evolution of the disk mass. This result is for the simulation presented in Supplementary Figure 2(b), resulting in the formation of a disk without an intact moon ($M_{\rm disk}/M_{\rm p} = 3.6 \times 10^{-3}$ at $t = 10^6$ s for the case of $N_{\rm total}$ = 24,000 and $M_{\rm disk}/M_{\rm p} = 5.8 \times 10^{-3}$ at $t = 5 \times 10^5$ s for the case of $N_{\rm total}$ = 480,000). We found that the time evolution of disk mass hardly depends on the resolution.

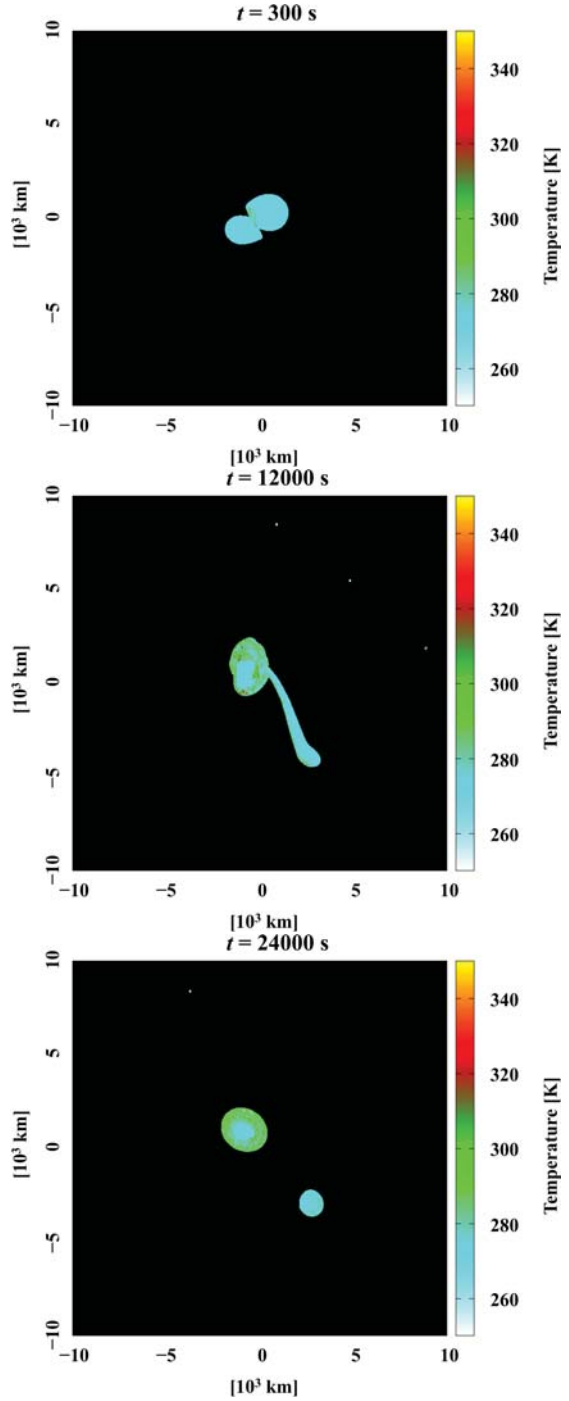

Supplementary Figure 8.S8: Snapshots of giant impacts between two icy undifferentiated bodies using the 5-phase equation of state for H_2O adapting at Gadget-2 with N_{total} = 300,000. The target mass and the impactor mass are 4×10^{21} kg and 2×10^{21} kg, respectively, and $v_{\text{imp}} = 1.00 v_{\text{esc}}$ and $\theta_{\text{imp}} = 75^\circ$. The collisional outcome is the formation of a large intact moon.

Chapter 9

Summary and outlook

9.1 Chondrule formation

Chondrules are millimeter-sized spherical igneous grains contained within chondrites, which are the most common type of meteorites, as a major component. The volume fraction of chondrules in ordinary chondrites is 60–80% (e.g., Rubin, 2000; Scott, 2007) and the ages of chondrules are approximately 4.563–4.567 billion years, i.e., they were formed during the first 4 million years of the solar system (e.g., Connelly et al., 2012; Bollard et al., 2017). Therefore, they must contain a wealth of information regarding the evolution of the solar nebula. In the canonical view, small dust grains in the solar nebula grew into millimeter-sized aggregates, after which chondrules were formed by the melting of these aggregates in the early solar nebula and became spherical owing to their surface tension (e.g., Zanda, 2004); however, their precise origin is still unclear.

Some chondrules, referred to as compound chondrules, are composed of two or more chondrules fused. They comprise a low percentage of all chondrules (e.g., 4% in ordinary chondrites; Gooding and Keil, 1981); however, they may offer crucial information regarding the physical state of solid materials during chondrule formation. Although the formation process of compound chondrules is still under debate, we can interpret the presence of compound chondrules as the result of collisions (e.g., Gooding and Keil, 1981; Ciesla et al., 2004b; Miura et al., 2008b; Bogdan et al., 2019).

In Chapters 2 and 3, we constructed a model for compound chondrule formation (Arakawa and Nakamoto, 2016a, 2019). We examined the possibility of compound chondrule formation via optically thin shock waves. Several features of compound chondrules indicate that compound chondrules formed via the collisions of supercooled precursors (Arakawa and Nakamoto, 2016a). We evaluated whether compound chondrules can be formed via the collision of supercooled chondrule precursors in the framework of the shock-wave heating model by using semi-analytical methods and discuss whether most of the crystallized chondrules can avoid destruction upon collision in the post-shock region (Arakawa and Nakamoto, 2019).

We found that chondrule precursors immediately turn into supercooled

droplets when the shock waves are optically thin, and they can maintain supercooling until the condensation of evaporated fine dust grains. Owing to the large viscosity of supercooled melts, supercooled chondrule precursors can survive high-speed collisions on the order of 1 km s^{-1} when the temperature is below $\sim$ 1400 K. From the perspective of the survivability of crystallized chondrules, shock waves with a spatial scale of $\sim 10^4$ km may be potent candidates for the chondrule formation mechanism.

9.2 Thermal conductivity of dust aggregates

9.2.1 Numerical simulations and theoretical interpretations

Understanding the thermal conductivity of dust aggregates is essential in numerous scientific and engineering fields. In the context of planetary sciences, for example, the thermal evolution of planetesimals is affected by the thermal conductivity of dust aggregates because they formed from micron-sized grains in the solar nebula (e.g., Henke et al., 2013; Sirono, 2017). The near-surface temperature distribution of comets and asteroids also depends on the thermal conductivity of surface grains (e.g., Blum et al., 2017; Okada et al., 2017).

In Chapters 4 and 5, we numerically calculated the thermal conductivity of dust aggregates (Arakawa et al., 2017, 2019c). We found that the thermal conductivity of dust aggregates through the solar network, $k_{\rm sol}$, is approximately given by

$$k_{\rm sol} \simeq 2k_{\rm mat}\frac{a_{\rm c}}{R}\phi^2, \tag{9.1}$$

where $k_{\rm mat}$ is the material thermal conductivity, $a_{\rm c}$ is the contact radius between two sticking monomer grains, R is the monomer radius, and ϕ is the filling factor of aggregates, respectively. We also derived the thermal conductivity due to radiative transfer and gas diffusion (see Chapter 7).

Then we gave a theoretical explanation for the thermal conductivity of dust aggregates from the fractal structure of dust aggregates (see Chapter 6; Arakawa et al., 2019b). In our numerical simulations, we used statically compressed aggregates formed via ballistic cluster–cluster aggregation (BCCA; Meakin, 1987, 1991). We introduced two dimensionless parameters that characterize the structure of fractal aggregates: the fractal dimension $D_{\rm f}$ and the detour parameter α (see Chapter 6 for details). We found that the thermal conductivity of statically compressed fractal aggregates is given by

$$k_{\rm sol} \simeq 2k_{\rm mat}\frac{a_{\rm c}}{R}\phi^{(1+\alpha)/(3-D_{\rm f})}. \tag{9.2}$$

For dust aggregates formed via BCCA, the fractal dimension is $D_{\rm f} \simeq 1.9$ (e.g., Mukai et al., 1992; Okuzumi et al., 2009), and the detour parameter is $\alpha \simeq 1.3$ (Arakawa et al., 2019b). The derived filling factor dependence of the thermal conductivity, $k_{\rm sol} \sim \phi^{2.1}$, is consistent with the numerical results.

We compared our numerical results with experimental data (Krause et al., 2011; Sakatani et al., 2017) and confirmed that the numerically derived formula could reproduce their experimental results without any free parameters (Arakawa et al., 2019c). We note, however, that dust aggregates used in experimental studies are not prepared by static compression of BCCA aggregates,

and the reason why our formula reproduces the experimental results is still unclear. We will survey the geometrical structure and thermal conductivity of various types of aggregates with different values of D_f and α, to understand the thermal conductivity of dust aggregates more deeply.

9.2.2 Photophoresis

Thermal conductivity of dust aggregates would be important not only for the thermal evolution of small bodies but also for the motion of dust aggregates in circumstellar and circumplanetary disks. Photo-irradiated dust particles which exhibit a temperature gradient move in a gaseous disk by momentum transfer with colliding gas molecules (e.g., Krauss and Wurm, 2005; Loesche and Wurm, 2012). This photophoretic force may create a dust-depleted region in the innermost of the disk, resulting in the formation of a pressure maximum around the outer edge of the dust-depleted region (e.g., Arakawa and Shibaike, 2019). This pressure maximum may help the formation of small bodies because dust particles are collected near the pressure maximum (e.g., Haghighipour and Boss, 2003).

Photophoresis may also assist the rapid formation of gas giant planets (Teiser and Dodson-Robinson, 2013). Gas giants formed via accretion of the nebular gas onto solid protoplanets whose mass is about 10 Earth mass (e.g., Mizuno, 1980). The critical mass for mass accretion, however, strongly depends on the opacity of accreting materials, i.e., the mixture of gas and dust particles (e.g., Ikoma et al., 2000). Photophoresis may be a mechanism for pushing the dust out of the planetary atmosphere and accelerate the formation of gas giants by reducing the opacity of accreting materials from the disk (Teiser and Dodson-Robinson, 2013). The rapid formation of Jupiter in the early solar nebula is favored for chondrule formation via shock waves caused by eccentric planetesimals (e.g., Weidenschilling et al., 1998; Nagasawa et al., 2014, 2019).

9.3 Thermal history of icy small bodies

9.3.1 Comets

Understanding the physical properties of cometary dust is essential to construct the planet formation scenario. There are numerous studies on the thermal and mechanical properties of comets constrained from observations and explorations (see, e.g., Groussin et al., 2019). Thermal properties are useful for understanding the physical characteristics of constituent particles of the surface dust layer (e.g., Blum et al., 2017; Hu et al., 2017). The mechanical strengths, e.g., compressive and tensile strength, are thought to reflect the information from the subsurface of cometary nuclei (e.g., Groussin et al., 2015; Basilevsky et al., 2016).

In Chapter 7, we calculated the thermal inertia, tensile strength, and compressive strength of dust aggregates using the results of recent theoretical studies (e.g., Arakawa et al., 2019b), and compared calculations with the *Rosetta* mission's observational results of comet 67P/Churyumov–Gerasimenko. We found that we cannot explain the tensile strength of the comet if it is a homogeneous aggregate of μm-sized dust grains, as pointed out by Tatsuuma

et al. (2019). We also derived the formulae for the physical properties of hierarchical dust aggregates, which are proposed by Skorov and Blum (2012). We found that the thermal inertia, tensile strength, and compressive strength of the comet is consistent with the hierarchical aggregate of cm- or dm-sized constituent aggregates. These findings indicate that the icy planetesimals may form via accretion of cm- or dm-sized compressed dust aggregates in the solar nebula.

The mechanical strength of comet 67P/Churyumov–Gerasimenko is consistent with the non-sintered hierarchical aggregate model. Therefore, the cooling timescale within the comet might be much shorter than the half-life of short-lived radionuclides (e.g., ^{26}Al), or the accretion of the comet is later than the extinction of short-lived radionuclides. The cooling timescale of comets is given by

$$\begin{aligned} \tau_{\rm cool} &= \frac{\rho c_{\rm heat} r^2}{k} \\ &\sim 10^6 \left(\frac{k}{10^{-2}\ {\rm W\ K^{-1}\ m^{-1}}} \right)^{-1} \left(\frac{r}{1\ {\rm km}} \right)^2 {\rm yr}, \end{aligned} \tag{9.3}$$

where $\rho \sim 5 \times 10^2$ kg m^{-3} is the density, $c_{\rm heat} \sim 10^3$ J kg^{-1} K^{-1} is the specific heat, r is the radius of comets, and k is the thermal conductivity. The thermal conductivity within cometary nuclei is given by (see Chapter 7)

$$k \simeq 8 \times 10^{-3} \left(\frac{T}{150\ {\rm K}} \right)^3 \left(\frac{R_{\rm agg}}{1\ {\rm cm}} \right) {\rm W\ K^{-1}\ m^{-1}}, \tag{9.4}$$

where T is the temperature and $R_{\rm agg}$ is the radius of constituent aggregates. The cooling timescale is therefore comparable to (or shorter than) the half-life of ^{26}Al ($= 7.2 \times 10^5$ years), which is the primary heat source of small bodies formed within a few million years from the formation of the sun, when the aggregate radius is $R_{\rm agg} \sim 1$ cm (or $R_{\rm agg} \gg 1$ cm). This rapid cooling of comets might prevent them from severe sintering, and thus they are still pristine dust aggregates that possess the information of the early solar nebula.

9.3.2 Trans-Neptunian objects

Recent observational studies have revealed that all 1000 km-sized large TNOs form satellite systems. However, their origins are still under debate. The largest Plutonian satellite, Charon, is thought to be an intact fragment of an impactor directly formed via a giant impact (e.g., Canup, 2005), although whether giant impacts can explain the characteristics of other satellite systems, e.g., the secondary-to-primary mass ratios, the spin/orbital periods, and their small eccentricities, remains to be determined.

In Chapter 8, we found that hydrodynamic simulations of giant impacts can reproduce the secondary-to-primary mass ratio of the satellite systems of large TNOs when the impact velocity is approximately the same as the escape velocity (Arakawa et al., 2019a). We also revealed that the satellite systems' current distribution of spin/orbital periods and small eccentricity could be explained when their spins and orbits tidally evolve, initially as fluid-like bodies, and finally as rigid bodies. These results suggest that all satellites of large

TNOs formed via giant impacts before the outward migration of Neptune (e.g., Gomes et al., 2004) and that they were fully or partially molten during the giant impact era.

Recent studies (e.g., Johansen et al., 2015; Shannon et al., 2016) proposed that accretion of cm-sized dust aggregates onto pre-existing planetesimals can form 100–1000 km-sized large TNOs within a few million years. The growth of large TNOs via accretion of cm-sized aggregates could also reproduce the size distribution of observed TNOs with the mass peaking around ~ 50 km in radii (e.g., Bernstein et al., 2004; Fuentes and Holman, 2008; Fraser et al., 2014). We also think that the accreting cm-sized dust aggregates may be identical with the building blocks of comets (e.g., Skorov and Blum, 2012; Blum et al., 2017, see also Chapter 7).

The heat source of large TNOs is still unclear. There are two candidates for the primary heat source: short-lived radionuclides (e.g., ^{26}Al) and long-lived radionuclides (e.g., ^{40}K, ^{232}Th, ^{235}U, and ^{238}U). If the primary heat source is ^{26}Al, large TNOs melted and differentiated within the first four million years of the solar system formation (see, e.g., Sekine et al., 2017). On the other hand, the timing of differentiation of 1000 km-sized TNOs would be approximately 100 million years after their accretion if long-lived radionuclides mainly heat them (see, e.g., Robuchon and Nimmo, 2011). We will test these scenarios from the thermal and dynamical evolutions in the future.

9.4 Compression of dust aggregates by shock waves

We found that the building blocks of planetesimals might be cm-sized compressed dust aggregates. Although the compression mechanism of dust aggregates is still unclear, here we propose that shock-waves in the solar nebula may be a potential candidate. The ram pressure of chondrule-forming shock waves considered in Chapter 3 (Arakawa and Nakamoto, 2019) is

$$p_{\rm ram} = \rho_{\rm g} {v_{\rm s}}^2 \sim 10^3 \ {\rm Pa}, \tag{9.5}$$

where $\rho_{\rm g} \sim 10^{-5}$ kg m^{-3} is the gas density of the nebula and $v_{\rm s} \sim 10^4$ m s^{-1} is the shock-wave velocity. The compressive strength of dust aggregates is shown in Figure 7.4(a), and dust aggregates of μm-sized monomer grains can turn into compressed aggregates whose filling factor is larger than 0.2, which is consistent with the conclusion of Arakawa (2017) and Chapter 7. Note that whether this mechanism can work in the outer region of the solar nebula or not is controversial. The source of shock waves is needed to be discussed, and the thermal process of icy dust aggregates after shock heating should be considered. Evaporation and (partial) recondensation of volatiles (e.g., H_2O and CO_2) might change the ice-to-refractory mass ratio in the outer solar system (e.g., Brown, 2012; Pätzold et al., 2019), which is significantly lower than the classical prediction of the ice-to-refractory mass ratio estimated from the solar chemical composition (e.g., Hayashi, 1981).

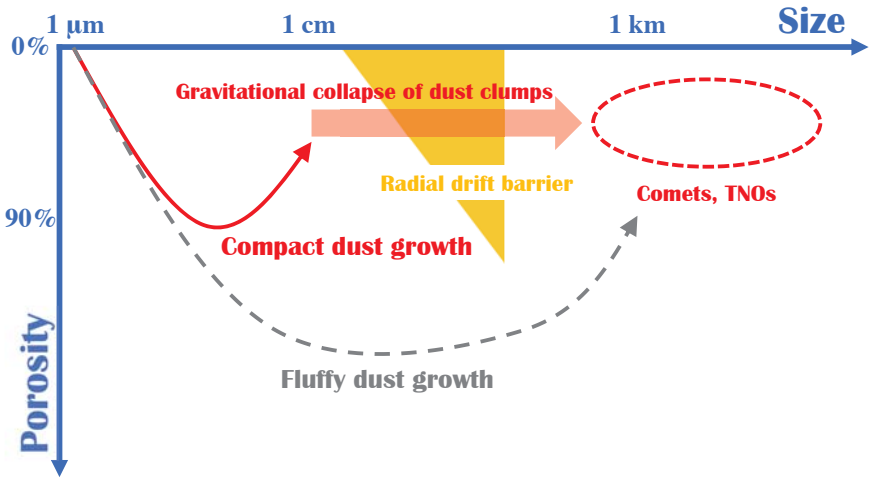

Figure 9.1: Possible planetesimal formation pathways in the early solar system. The red line shows the compact dust growth model which is suggested from laboratory collisional experiments (e.g., Weidling et al., 2009; Zsom et al., 2010). Dust aggregates in the solar nebula are compressed by mutual collisions and compressed cm-sized aggregates formed in the nebula. Then planetesimals would be formed via gravitational collapse of dust clumps (e.g., Johansen and Youdin, 2007; Yang et al., 2017). The grey dashed line shows the evolutional track for the fluffy dust growth model (e.g., Okuzumi et al., 2012; Arakawa and Nakamoto, 2016b) and the yellow triangle is the radial drift barrier (e.g., Adachi et al., 1976; Weidenschilling, 1977).

9.5 Planetesimal formation in the early solar system

Finally, we discuss a possible planetesimal formation history in the early solar system. In this thesis, we discussed what the building blocks of planetesimals are and how planetesimals formed in the solar nebula, from the thermal history of small bodies. The formation pathway of planetesimals is illustrated in Figure 9.1.

Over the last decade, two basic pathways of dust growth toward planetesimals have been proposed. One is the direct growth via collisional sticking of dust aggregates with significant density evolution (e.g., Okuzumi et al., 2012; Arakawa and Nakamoto, 2016b). Another one is that dust aggregates in the nebula are concentrated locally and collapse gravitationally to form planetesimals (e.g., Johansen and Youdin, 2007; Yang et al., 2017). Note that this aerodynamic process is independent of the porosity of dust aggregates and both porous and compressed aggregates can turn into planetesimals via gravitational collapse of dust clumps.

As shown in Chapter 7, the building blocks of icy planetesimals might be cm-sized compressed aggregates, not highly porous aggregates. We note that not only icy planetesimals but also rocky planetesimals may be formed via compressed aggregates. Arakawa (2017) found that chondrules in fluffy aggregates would be lost in the collisional growth sequence; however, chondrules are observed as the major components of meteorites. The minimum filling factor of dust aggregates which can retain chondrules inside is approximately

1–3% (Arakawa, 2017), and this value is between the predicted filling factors from two proposed pathways of dust growth. Therefore, co-accretion of chondrules and fine dust grains may be possible when rocky planetesimals formed via gravitational collapse of dust clumps of compressed aggregates, while the direct growth via collisional sticking of fluffy dust aggregates might be difficult to explain the formation of chondrite parent bodies.

References

Adachi, I., Hayashi, C., Nakazawa, K., 1976. The gas drag effect on the elliptical motion of a solid body in the primordial solar nebula. Progress of Theoretical Physics 56, 1756–1771. doi:10.1143/PTP.56.1756.

Agnor, C., Asphaug, E., 2004. Accretion efficiency during planetary collisions. The Astrophysical Journal 613, L157–L160. URL: https://doi.org/10.1086/425158, doi:10.1086/425158.

A'Hearn, M.F., Feaga, L.M., Keller, H.U., Kawakita, H., Hampton, D.L., Kissel, J., Klaasen, K.P., McFadden, L.A., Meech, K.J., Schultz, P.H., Sunshine, J.M., Thomas, P.C., Veverka, J., Yeomans, D.K., Besse, S., Bodewits, D., Farnham, T.L., Groussin, O., Kelley, M.S., Lisse, C.M., Merlin, F., Protopapa, S., Wellnitz, D.D., 2012. Cometary Volatiles and the Origin of Comets. The Astrophysical Journal 758, 29. doi:10.1088/0004-637X/758/1/29.

Akaki, T., Nakamura, T., 2005. Formation processes of compound chondrules in CV3 carbonaceous chondrites: Constraints from oxygen isotope ratios and major element concentrations. Geochimica et Cosmochimica Acta 69, 2907–2929. doi:10.1016/j.gca.2004.12.025.

Akaki, T., Nakamura, T., Noguchi, T., Tsuchiyama, A., 2007. Multiple Formation of Chondrules in the Early Solar System: Chronology of a Compound Al-rich Chondrule. The Astrophysical Journal Letters 656, L29–L32. doi:10.1086/512100.

Alexander, C.M.O., Grossman, J.N., Ebel, D.S., Ciesla, F.J., 2008. The Formation Conditions of Chondrules and Chondrites. Science 320, 1617. doi:10.1126/science.1156561.

Arakawa, S., 2017. Ejection of Chondrules from Fluffy Matrices. The Astrophysical Journal 846, 118. doi:10.3847/1538-4357/aa8564.

Arakawa, S., Hyodo, R., Genda, H., 2019a. Early formation of moons around large trans-Neptunian objects via giant impacts. Nature Astronomy 3, 802–807. doi:10.1038/s41550-019-0797-9.

Arakawa, S., Nakamoto, T., 2016a. Compound chondrule formation via collision of supercooled droplets. Icarus 276, 102–106. doi:10.1016/j.icarus.2016.04.041.

Arakawa, S., Nakamoto, T., 2016b. Rocky Planetesimal Formation via Fluffy Aggregates of Nanograins. The Astrophysical Journal Letters 832, L19. doi:10.3847/2041-8205/832/2/L19.

Arakawa, S., Nakamoto, T., 2019. Compound Chondrule Formation in Optically Thin Shock Waves. The Astrophysical Journal 877, 84. doi:10.3847/1538-4357/ab1b3e.

Arakawa, S., Shibaike, Y., 2019. Photophoresis in the circumjovian disk and its impact on the orbital configuration of the Galilean satellites. Astronomy & Astrophysics 629, A106. doi:10.1051/0004-6361/201936202.

Arakawa, S., Takemoto, M., Nakamoto, T., 2019b. Geometrical structure and thermal conductivity of dust aggregates formed via ballistic cluster-cluster aggregation. Progress of Theoretical and Experimental Physics 2019, 093E02. doi:10.1093/ptep/ptz102.

Arakawa, S., Tanaka, H., Kataoka, A., Nakamoto, T., 2017. Thermal conductivity of porous aggregates. Astronomy & Astrophysics 608, L7. doi:10.1051/0004-6361/201732182.

Arakawa, S., Tatsuuma, M., Sakatani, N., Nakamoto, T., 2019c. Thermal conductivity and coordination number of compressed dust aggregates. Icarus 324, 8–14. doi:10.1016/j.icarus.2019.01.022.

Ashgriz, N., Poo, J.Y., 1990. Coalescence and separation in binary collisions of liquid drops. Journal of Fluid Mechanics 221, 183–204. doi:10.1017/S0022112090003536.

Asphaug, E., Jutzi, M., Movshovitz, N., 2011. Chondrule formation during planetesimal accretion. Earth and Planetary Science Letters 308, 369–379. doi:10.1016/j.epsl.2011.06.007.

Attree, N., Groussin, O., Jorda, L., Nébouy, D., Thomas, N., Brouet, Y., Kührt, E., Preusker, F., Scholten, F., Knollenberg, J., Hartogh, P., Sierks, H., Barbieri, C., Lamy, P., Rodrigo, R., Koschny, D., Rickman, H., Keller, H.U., A'Hearn, M.F., Auger, A.T., Barucci, M.A., Bertaux, J.L., Bertini, I., Bodewits, D., Boudreault, S., Cremonese, G., Da Deppo, V., Davidsson, B., Debei, S., De Cecco, M., Deller, J., El-Maarry, M.R., Fornasier, S., Fulle, M., Gutiérrez, P.J., Güttler, C., Hviid, S., Ip, W.H., Kovacs, G., Kramm, J.R., Küppers, M., Lara, L.M., Lazzarin, M., Lopez Moreno, J.J., Lowry, S., Marchi, S., Marzari, F., Mottola, S., Naletto, G., Oklay, N., Pajola, M., Toth, I., Tubiana, C., Vincent, J.B., Shi, X., 2018. Tensile strength of 67P/Churyumov-Gerasimenko nucleus material from overhangs. Astronomy & Astrophysics 611, A33. doi:10.1051/0004-6361/201732155.

Balbus, S.A., Hawley, J.F., 1991. A powerful local shear instability in weakly magnetized disks. I - Linear analysis. II - Nonlinear evolution. The Astrophysical Journal 376, 214–233. doi:10.1086/170270.

Bardyn, A., Baklouti, D., Cottin, H., Fray, N., Briois, C., Paquette, J., Stenzel, O., Engrand, C., Fischer, H., Hornung, K., Isnard, R., Langevin, Y., Lehto, H., Le Roy, L., Ligier, N., Merouane, S., Modica, P., Orthous-Daunay, F.R.,

Rynö, J., Schulz, R., Silén, J., Thirkell, L., Varmuza, K., Zaprudin, B., Kissel, J., Hilchenbach, M., 2017. Carbon-rich dust in comet 67P/Churyumov-Gerasimenko measured by COSIMA/Rosetta. Monthly Notices of the Royal Astronomical Society 469, S712–S722. doi:10.1093/mnras/stx2640.

Basilevsky, A.T., Krasil'nikov, S.S., Shiryaev, A.A., Mall, U., Keller, H.U., Skorov, Y.V., Mottola, S., Hviid, S.F., 2016. Estimating the strength of the nucleus material of comet 67P Churyumov-Gerasimenko. Solar System Research 50, 225–234. doi:10.1134/S0038094616040018.

Batygin, K., Brown, M.E., Fraser, W.C., 2011. Retention of a primordial cold classical Kuiper belt in an instability-driven model of Solar System formation. The Astrophysical Journal 738, 13. doi:10.1088/0004-637X/738/1/13.

Beitz, E., Güttler, C., Weidling, R., Blum, J., 2012. Free collisions in a microgravity many-particle experiment - II: The collision dynamics of dust-coated chondrules. Icarus 218, 701–706. doi:10.1016/j.icarus.2011.11.036.

Bernstein, G.M., Trilling, D.E., Allen, R.L., Brown, M.E., Holman, M., Malhotra, R., 2004. The Size Distribution of Trans-Neptunian Bodies. The Astronomical Journal 128, 1364–1390. doi:10.1086/422919.

Biele, J., Ulamec, S., Maibaum, M., Roll, R., Witte, L., Jurado, E., Muñoz, P., Arnold, W., Auster, H.U., Casas, C., Faber, C., Fantinati, C., Finke, F., Fischer, H.H., Geurts, K., Güttler, C., Heinisch, P., Herique, A., Hviid, S., Kargl, G., Knapmeyer, M., Knollenberg, J., Kofman, W., Kömle, N., Kührt, E., Lommatsch, V., Mottola, S., Pardo de Santayana, R., Remetean, E., Scholten, F., Seidensticker, K.J., Sierks, H., Spohn, T., 2015. The landing(s) of Philae and inferences about comet surface mechanical properties. Science 349, 1.9816. doi:10.1126/science.aaa9816.

Bischoff, A., Wurm, G., Chaussidon, M., Horstmann, M., Metzler, K., Weyrauch, M., Weinauer, J., 2017. The Allende multicompound chondrule (ACC)—Chondrule formation in a local super-dense region of the early solar system. Meteoritics & Planetary Science 52, 906–924. doi:10.1111/maps.12833.

Blum, J., 2018. Dust Evolution in Protoplanetary Discs and the Formation of Planetesimals. What Have We Learned from Laboratory Experiments? Space Science Reviews 214, 52. doi:10.1007/s11214-018-0486-5.

Blum, J., Gundlach, B., Krause, M., Fulle, M., Johansen, A., Agarwal, J., von Borstel, I., Shi, X., Hu, X., Bentley, M.S., Capaccioni, F., Colangeli, L., Della Corte, V., Fougere, N., Green, S.F., Ivanovski, S., Mannel, T., Merouane, S., Migliorini, A., Rotundi, A., Schmied, R., Snodgrass, C., 2017. Evidence for the formation of comet 67P/Churyumov-Gerasimenko through gravitational collapse of a bound clump of pebbles. Monthly Notices of the Royal Astronomical Society 469, S755–S773. doi:10.1093/mnras/stx2741.

Blum, J., Gundlach, B., Mühle, S., Trigo-Rodriguez, J.M., 2014. Comets formed in solar-nebula instabilities! - An experimental and modeling attempt to relate the activity of comets to their formation process. Icarus 235, 156–169. doi:10.1016/j.icarus.2014.03.016.

Blum, J., Münch, M., 1993. Experimental investigations on aggregate-aggregate collisions in the early solar nebula. Icarus 106, 151. doi:10.1006/icar.1993.1163.

Blum, J., Schräpler, R., Davidsson, B.J.R., Trigo-Rodríguez, J.M., 2006. The Physics of Protoplanetesimal Dust Agglomerates. I. Mechanical Properties and Relations to Primitive Bodies in the Solar System. The Astrophysical Journal 652, 1768–1781. doi:10.1086/508017.

Blum, J., Wurm, G., 2000. Experiments on Sticking, Restructuring, and Fragmentation of Preplanetary Dust Aggregates. Icarus 143, 138–146. doi:10.1006/icar.1999.6234.

Blum, J., Wurm, G., 2008. The Growth Mechanisms of Macroscopic Bodies in Protoplanetary Disks. Annual Review of Astronomy and Astrophysics 46, 21–56. doi:10.1146/annurev.astro.46.060407.145152.

Blum, J., Wurm, G., Kempf, S., Poppe, T., Klahr, H., Kozasa, T., Rott, M., Henning, T., Dorschner, J., Schräpler, R., Keller, H.U., Markiewicz, W.J., Mann, I., Gustafson, B.A., Giovane, F., Neuhaus, D., Fechtig, H., Grün, E., Feuerbacher, B., Kochan, H., Ratke, L., El Goresy, A., Morfill, G., Weidenschilling, S.J., Schwehm, G., Metzler, K., Ip, W.H., 2000. Growth and Form of Planetary Seedlings: Results from a Microgravity Aggregation Experiment. Physical Review Letters 85, 2426–2429. doi:10.1103/PhysRevLett.85.2426.

Bogdan, T., Teiser, J., Fischer, N., Kruss, M., Wurm, G., 2019. Constraints on compound chondrule formation from laboratory high-temperature collisions. Icarus 319, 133–139. doi:10.1016/j.icarus.2018.09.011.

Bohren, C.F., Huffman, D.R., 1983. Absorption and scattering of light by small particles. Wiley.

Boley, A.C., Durisen, R.H., 2008. Gravitational Instabilities, Chondrule Formation, and the FU Orionis Phenomenon. The Astrophysical Journal 685, 1193–1209. doi:10.1086/591013.

Boley, A.C., Morris, M.A., Desch, S.J., 2013. High-temperature Processing of Solids through Solar Nebular Bow Shocks: 3D Radiation Hydrodynamics Simulations with Particles. The Astrophysical Journal 776, 101. doi:10.1088/0004-637X/776/2/101.

Bollard, J., Connelly, J.N., Whitehouse, M.J., Pringle, E.A., Bonal, L., Jørgensen, J.K., Nordlund, Å., Moynier, F., Bizzarro, M., 2017. Early formation of planetary building blocks inferred from Pb isotopic ages of chondrules. Science Advances 3, e1700407. doi:10.1126/sciadv.1700407.

Boss, A.P., Durisen, R.H., 2005. Chondrule-forming Shock Fronts in the Solar Nebula: A Possible Unified Scenario for Planet and Chondrite Formation. The Astrophysical Journal Letters 621, L137–L140. doi:10.1086/429160.

Bowen, N.L., Andersen, O., 1914. The binary system MgO-SiO_2. American Journal of Science 37, 487–500. doi:10.2475/ajs.s4-37.222.487.

Brisset, J., Heißelmann, D., Kothe, S., Weidling, R., Blum, J., 2016. Submillimetre-sized dust aggregate collision and growth properties. Experimental study of a multi-particle system on a suborbital rocket. Astronomy & Astrophysics 593, A3. doi:10.1051/0004-6361/201527288.

Brown, M.E., 2012. The Compositions of Kuiper Belt Objects. Annual Review of Earth and Planetary Sciences 40, 467–494. doi:10.1146/annurev-earth-042711-105352.

Brown, M.E., Butler, B.J., 2018. Medium-sized Satellites of Large Kuiper Belt Objects. The Astronomical Journal 156, 164. doi:10.3847/1538-3881/aad9f2.

Brown, M.E., van Dam, M.A., Bouchez, A.H., Le Mignant, D., Campbell, R.D., Chin, J.C.Y., Conrad, A., Hartman, S.K., Johansson, E.M., Lafon, R.E., Rabinowitz, D.L., Stomski, P. J., J., Summers, D.M., Trujillo, C.A., Wizinowich, P.L., 2006. Satellites of the Largest Kuiper Belt Objects. The Astrophysical Journal Letters 639, L43–L46. doi:10.1086/501524.

Brozović, M., Showalter, M.R., Jacobson, R.A., Buie, M.W., 2015. The orbits and masses of satellites of Pluto. Icarus 246, 317–329. doi:10.1016/j.icarus.2014.03.015.

Bruggeman, D.A.G., 1935. Berechnung verschiedener physikalischer Konstanten von heterogenen Substanzen. I. Dielektrizitätskonstanten und Leitfähigkeiten der Mischkörper aus isotropen Substanzen. Annalen der Physik 416, 636–664. doi:10.1002/andp.19354160705.

Budde, G., Burkhardt, C., Brennecka, G.A., Fischer-Gödde, M., Kruijer, T.S., Kleine, T., 2016a. Molybdenum isotopic evidence for the origin of chondrules and a distinct genetic heritage of carbonaceous and non-carbonaceous meteorites. Earth and Planetary Science Letters 454, 293–303. doi:10.1016/j.epsl.2016.09.020.

Budde, G., Kleine, T., Kruijer, T.S., Burkhardt, C., Metzler, K., 2016b. Tungsten isotopic constraints on the age and origin of chondrules. Proceedings of the National Academy of Science 113, 2886–2891. doi:10.1073/pnas.1524980113.

Cahill, D.G., 1990. Thermal conductivity measurement from 30 to 750 K: the 3ω method. Review of Scientific Instruments 61, 802–808. doi:10.1063/1.1141498.

Cahill, D.G., Pohl, R.O., 1987. Thermal conductivity of amorphous solids above the plateau. Physical Review B 35, 4067–4073. doi:10.1103/PhysRevB.35.4067.

Canup, R.M., 2004. Simulations of a late lunar-forming impact. Icarus 168, 433–456. doi:10.1016/j.icarus.2003.09.028.

Canup, R.M., 2005. A giant impact origin of Pluto-Charon. Science 307, 546–550. doi:10.1126/science.1106818.

Canup, R.M., 2011. On a giant impact origin of Charon, Nix, and Hydra. The Astronomical Journal 141, 35. doi:10.1088/0004-6256/141/2/35.

Carrera, D., Johansen, A., Davies, M.B., 2015. How to form planetesimals from mm-sized chondrules and chondrule aggregates. Astronomy & Astrophysics 579, A43. doi:10.1051/0004-6361/201425120.

Chan, C.K., Tien, C.L., 1973. Conductance of packed spheres in vacuum. Journal of Heat Transfer 95, 302–308. doi:10.1115/1.3450056.

Chandra, S., Avedisian, C.T., 1991. On the Collision of a Droplet with a Solid Surface. Proceedings of the Royal Society of London Series A 432, 13–41. doi:10.1098/rspa.1991.0002.

Cheng, W.H., Lee, M.H., Peale, S.J., 2014. Complete tidal evolution of Pluto–Charon. Icarus 233, 242–258. doi:10.1016/j.icarus.2014.01.046.

Choukroun, M., Keihm, S., Schloerb, F.P., Gulkis, S., Lellouch, E., Leyrat, C., von Allmen, P., Biver, N., Bockelée-Morvan, D., Crovisier, J., Encrenaz, P., Hartogh, P., Hofstadter, M., Ip, W.H., Jarchow, C., Janssen, M., Lee, S., Rezac, L., Beaudin, G., Gaskell, B., Jorda, L., Keller, H.U., Sierks, H., 2015. Dark side of comet 67P/Churyumov-Gerasimenko in Aug.-Oct. 2014. MIRO/Rosetta continuum observations of polar night in the southern regions. Astronomy & Astrophysics 583, A28. doi:10.1051/0004-6361/201526181.

Christou, C., Dadzie, S.K., Thomas, N., Marschall, R., Hartogh, P., Jorda, L., Kührt, E., Wright, I., Rodrigo, R., 2018. Gas flow in near surface comet like porous structures: Application to 67P/Churyumov-Gerasimenko. Planetary and Space Science 161, 57–67. doi:10.1016/j.pss.2018.06.009.

Ciesla, F.J., 2006. Chondrule collisions in shock waves. Meteoritics & Planetary Science 41, 1347–1359. doi:10.1111/j.1945-5100.2006.tb00526.x.

Ciesla, F.J., Hood, L.L., Weidenschilling, S.J., 2004a. Evaluating planetesimal bow shocks as sites for chondrule formation. Meteoritics & Planetary Science 39, 1809–1821. doi:10.1111/j.1945-5100.2004.tb00077.x.

Ciesla, F.J., Lauretta, D.S., Hood, L.L., 2004b. The frequency of compound chondrules and implications for chondrule formation. Meteoritics & Planetary Science 39, 531–544. doi:10.1111/j.1945-5100.2004.tb00917.x.

Cohen, B.A., Hewins, R.H., Yu, Y., 2000. Evaporation in the young solar nebula as the origin of 'just-right' melting of chondrules. Nature 406, 600–602. doi:10.1038/35020514.

Connelly, J.N., Bizzarro, M., Krot, A.N., Nordlund, Å., Wielandt, D., Ivanova, M.A., 2012. The Absolute Chronology and Thermal Processing of Solids in the Solar Protoplanetary Disk. Science 338, 651. doi:10.1126/science.1226919.

Connolly, Jr., H.C., Hewins, R.H., 1995. Chondrules as products of dust collisions with totally molten droplets within a dust-rich nebular environment: An experimental investigation. Geochimica et Cosmochimica Acta 59, 3231–3246. doi:10.1016/0016-7037(95)00207-G.

Connolly, Jr., H.C., Hewins, R.H., Atre, N., Lofgren, G.E., 1994. Compound chondrules: an experimental investigation. Meteoritics 29, 458.

Connolly, Jr., H.C., Jones, B.D., Hewins, R.H., 1998. The flash melting of chondrules: an experimental investigation into the melting history and physical nature of chondrule precursors. Geochimica et Cosmochimica Acta 62, 2725–2735. doi:10.1016/S0016-7037(98)00176-8.

Connolly, Jr., H.C., Jones, R.H., 2016. Chondrules: The canonical and non-canonical view. Journal of Geophysical Research: Planets 121, 1885–1899. doi:10.1002/2016JE005113.

Cooper, M., Mikic, B., Yovanovich, M., 1969. Thermal contact conductance. International Journal of Heat and Mass Transfer 12, 279–300. doi:10.1016/0017-9310(69)90011-8.

Ćuk, M., Dones, L., Nesvorný, D., 2016. Dynamical evidence for a late formation of Saturn's moons. The Astrophysical Journal 820, 97. doi:10.3847/0004-637X/820/2/97.

Ćuk, M., Ragozzine, D., Nesvorný, D., 2013. On the dynamics and origin of Haumea's moons. The Astronomical Journal 146, 89. doi:10.1088/0004-6256/146/4/89.

Cuzzi, J.N., Hogan, R.C., 2003. Blowing in the wind. I. Velocities of chondrule-sized particles in a turbulent protoplanetary nebula. Icarus 164, 127–138. doi:10.1016/S0019-1035(03)00104-0.

Daisaka, H., Tanaka, H., Ida, S., 2001. Viscosity in a dense planetary ring with self-gravitating particles. Icarus 154, 296–312. doi:10.1006/icar.2001.6716.

Dauphas, N., Chaussidon, M., 2011. A Perspective from Extinct Radionuclides on a Young Stellar Object: The Sun and Its Accretion Disk. Annual Review of Earth and Planetary Sciences 39, 351–386. doi:10.1146/annurev-earth-040610-133428.

Davidsson, B.J.R., Gutiérrez, P.J., Groussin, O., A'Hearn, M.F., Farnham, T., Feaga, L.M., Kelley, M.S., Klaasen, K.P., Merlin, F., Protopapa, S., Rickman, H., Sunshine, J.M., Thomas, P.C., 2013. Thermal inertia and surface roughness of Comet 9P/Tempel 1. Icarus 224, 154–171. doi:10.1016/j.icarus.2013.02.008.

DeMeo, F.E., Carry, B., 2014. Solar System evolution from compositional mapping of the asteroid belt. Nature 505, 629–634. doi:10.1038/nature12908.

Desch, S.J., Connolly, Jr., H.C., 2002. A model of the thermal processing of particles in solar nebula shocks: Application to the cooling rates of chondrules. Meteoritics & Planetary Science 37, 183–207. doi:10.1111/j.1945-5100.2002.tb01104.x.

Desch, S.J., Cuzzi, J.N., 2000. The Generation of Lightning in the Solar Nebula. Icarus 143, 87–105. doi:10.1006/icar.1999.6245.

Desch, S.J., Kalyaan, A., Alexander, C.M.O., 2018. The Effect of Jupiter's Formation on the Distribution of Refractory Elements and Inclusions in Meteorites. The Astrophysical Journals 238, 11. doi:10.3847/1538-4365/aad95f.

Desch, S.J., Morris, M.A., Connolly, Jr., H.C., Boss, A.P., 2012. The importance of experiments: Constraints on chondrule formation models. Meteoritics & Planetary Science 47, 1139–1156. doi:10.1111/j.1945-5100.2012.01357.x.

Dominik, C., Tielens, A.G.G.M., 1997. The Physics of Dust Coagulation and the Structure of Dust Aggregates in Space. The Astrophysical Journal 480, 647–673. doi:10.1086/303996.

Draine, B.T., 2003. Scattering by Interstellar Dust Grains. II. X-Rays. The Astrophysical Journal 598, 1026–1037. doi:10.1086/379123.

Dullemond, C.P., Stammler, S.M., Johansen, A., 2014. Forming Chondrules in Impact Splashes. I. Radiative Cooling Model. The Astrophysical Journal 794, 91. doi:10.1088/0004-637X/794/1/91.

Ebel, D.S., Brunner, C., Konrad, K., Leftwich, K., Erb, I., Lu, M., Rodriguez, H., Crapster-Pregont, E.J., Friedrich, J.M., Weisberg, M.K., 2016. Abundance, major element composition and size of components and matrix in CV, CO and Acfer 094 chondrites. Geochimica et Cosmochimica Acta 172, 322–356. doi:10.1016/j.gca.2015.10.007.

Edgeworth, K.E., 1943. The evolution of our planetary system. Journal of the British Astronomical Association 53, 181–188.

Edgeworth, K.E., 1949. The origin and evolution of the Solar System. Monthly Notices of the Royal Astronomical Society 109, 600–609. doi:10.1093/mnras/109.5.600.

Efroimsky, M., 2012. Bodily tides near spin-orbit resonances. Celestial Mechanics and Dynamical Astronomy 112, 283–330. doi:10.1007/s10569-011-9397-4.

Eisenhour, D.D., 1996. Determining chondrule size distributions from thin-section measurements. Meteoritics & Planetary Science 31, 243–248. doi:10.1111/j.1945-5100.1996.tb02019.x.

Eistrup, C., Walsh, C., van Dishoeck, E.F., 2019. Cometary compositions compared with protoplanetary disk midplane chemical evolution. An emerging chemical evolution taxonomy for comets. Astronomy & Astrophysics 629, A84. doi:10.1051/0004-6361/201935812.

Ennis, B.J., Tardos, G., Pfeffer, R., 1991. A microlevel-based characterization of granulation phenomena. Powder Technology 65, 257–272. doi:10.1016/0032-5910(91)80189-p.

Evans, W., Prasher, R., Fish, J., Meakin, P., Phelan, P., Keblinski, P., 2008. Effect of aggregation and interfacial thermal resistance on thermal conductivity of nanocomposites and colloidal nanofluids. International Journal of Heat and Mass Transfer 51, 1431–1438. doi:10.1016/j.ijheatmasstransfer.2007.10.017.

Fedkin, A.V., Grossman, L., 2013. Vapor saturation of sodium: Key to unlocking the origin of chondrules. Geochimica et Cosmochimica Acta 112, 226–250. doi:10.1016/j.gca.2013.02.020.

Ferraz-Mello, S., 2013. Tidal synchronization of close-in satellites and exoplanets. A rheophysical approach. Celest. Mech. Dyn. Astron. 116, 109–140. doi:10.1007/s10569-013-9482-y.

Finotello, G., Kooiman, R.F., Padding, J.T., Buist, K.A., Jongsma, A., Innings, F., Kuipers, J.A.M., 2018. The dynamics of milk droplet-droplet collisions. Experiments in Fluids 59, 17. doi:10.1007/s00348-017-2471-2.

Finotello, G., Padding, J.T., Deen, N.G., Jongsma, A., Innings, F., Kuipers, J.A.M., 2017. Effect of viscosity on droplet-droplet collisional interaction. Physics of Fluids 29, 067102. doi:10.1063/1.4984081.

Flynn, G.J., Wirick, S., Keller, L.P., 2013. Organic grain coatings in primitive interplanetary dust particles: Implications for grain sticking in the Solar Nebula. Earth, Planets, and Space 65, 1159–1166. doi:10.5047/eps.2013.05.007.

Fornasier, S., Lellouch, E., Müller, T., Santos-Sanz, P., Panuzzo, P., Kiss, C., Lim, T., Mommert, M., Bockelée-Morvan, D., Vilenius, E., Stansberry, J., Tozzi, G.P., Mottola, S., Delsanti, A., Crovisier, J., Duffard, R., Henry, F., Lacerda, P., Barucci, A., Gicquel, A., 2013. TNOs are Cool: A survey of the trans-Neptunian region. VIII. Combined Herschel PACS and SPIRE observations of nine bright targets at 70–500 μm. Astronomy & Astrophysics 555, A15. doi:10.1051/0004-6361/201321329.

Fowkes, F.M., 1964. Attractive forces at interfaces. Industrial & Engineering Chemistry 56, 40–52. doi:10.1021/ie50660a008.

Fraser, W.C., Bannister, M.T., Pike, R.E., Marsset, M., Schwamb, M.E., Kavelaars, J.J., Lacerda, P., Nesvorný, D., Volk, K., Delsanti, A., Benecchi, S., Lehner, M.J., Noll, K., Gladman, B., Petit, J.M., Gwyn, S., Chen, Y.T., Wang, S.Y., Alexand ersen, M., Burdullis, T., Sheppard, S., Trujillo, C., 2017. All planetesimals born near the Kuiper belt formed as binaries. Nature Astronomy 1, 0088. doi:10.1038/s41550-017-0088.

Fraser, W.C., Batygin, K., Brown, M.E., Bouchez, A., 2013. The mass, orbit, and tidal evolution of the Quaoar-Weywot system. Icarus 222, 357–363. doi:10.1016/j.icarus.2012.11.004.

Fraser, W.C., Brown, M.E., Morbidelli, A.r., Parker, A., Batygin, K., 2014. The Absolute Magnitude Distribution of Kuiper Belt Objects. The Astrophysical Journal 782, 100. doi:10.1088/0004-637X/782/2/100.

Fuentes, C.I., Holman, M.J., 2008. A SUBARU Archival Search for Faint Trans-Neptunian Objects. The Astronomical Journal 136, 83–97. doi:10.1088/0004-6256/136/1/83.

Fulcher, G.S., 1925. Analysis of recent measurements of the viscosity of glasses. Journal of the American Ceramic Society 8, 339–355. doi:10.1111/j.1151-2916.1925.tb16731.x.

Fulle, M., Blum, J., Rotundi, A., 2019. How Comets Work. The Astrophysical Journal Letters 879, L8. doi:10.3847/2041-8213/ab2898.

Gail, H.P., Henke, S., Trieloff, M., 2015. Thermal evolution and sintering of chondritic planetesimals. II. Improved treatment of the compaction process. Astronomy & Astrophysics 576, A60. doi:10.1051/0004-6361/201424278.

Gaur, U., Lau, S.f., Wunderlich, B.B., Wunderlich, B., 1982. Heat Capacity and Other Thermodynamic Properties of Linear Macromolecules VI. Acrylic Polymers. Journal of Physical and Chemical Reference Data 11, 1065–1089. doi:10.1063/1.555671.

Gaur, U., Wunderlich, B., 1982. Heat Capacity and Other Thermodynamic Properties of Linear Macromolecules. V. Polystyrene. Journal of Physical and Chemical Reference Data 11, 313–325. doi:10.1063/1.555663.

Genda, H., Fujita, T., Kobayashi, H., Tanaka, H., Abe, Y., 2015. Resolution dependence of disruptive collisions between planetesimals in the gravity regime. Icarus 262, 58–66. doi:10.1016/j.icarus.2015.08.029.

Genda, H., Kokubo, E., Ida, S., 2012. Merging criteria for giant impacts of protoplanets. The Astrophysical Journal 744, 137. doi:10.1088/0004-637X/744/2/137.

Giordano, D., Russell, J.K., Dingwell, D.B., 2008. Viscosity of magmatic liquids: A model. Earth and Planetary Science Letters 271, 123–134. doi:10.1016/j.epsl.2008.03.038.

Gladman, B., Marsden, B.G., Vanlaerhoven, C., 2008. Nomenclature in the Outer Solar System. University of Arizona Press.

Goldreich, P., Lithwick, Y., Sari, R., 2002. Formation of Kuiper-belt binaries by dynamical friction and three-body encounters. Nature 420, 643–646. doi:10.1038/nature01227.

Goldreich, P., Peale, S., 1966. Spin–orbit coupling in the solar system. The Astronomical Journal 71, 425. doi:10.1086/109947.

Gombosi, T.I., Nagy, A.F., Cravens, T.E., 1986. Dust and neutral gas modeling of the inner atmospheres of comets. Reviews of Geophysics 24, 667–700. doi:10.1029/RG024i003p00667.

Gomes, R., Levison, H.F., Tsiganis, K., Morbidelli, A., 2005. Origin of the cataclysmic Late Heavy Bombardment period of the terrestrial planets. Nature 435, 466–469. doi:10.1038/nature03676.

Gomes, R.S., Morbidelli, A., Levison, H.F., 2004. Planetary migration in a planetesimal disk: Why did Neptune stop at 30 AU? Icarus 170, 492–507. doi:10.1016/j.icarus.2004.03.011.

Gooding, J.L., Keil, K., 1981. Relative abundances of chondrule primary textural types in ordinary chondrites and their bearing on conditions of chondrule formation. Meteoritics 16, 17–43.

Gotaas, C., Havelka, P., Jakobsen, H.A., Svendsen, H.F., Hase, M., Roth, N., Weigand, B., 2007. Effect of viscosity on droplet-droplet collision outcome: Experimental study and numerical comparison. Physics of Fluids 19, 102106–102106–17. doi:10.1063/1.2781603.

Greenberg, R., Barnes, R., 2008. Tidal evolution of Dysnomia, satellite of the dwarf planet Eris. Icarus 194, 847–849. doi:10.1016/j.icarus.2007.12.017.

Groussin, O., Attree, N., Brouet, Y., Ciarletti, V., Davidsson, B., Filacchione, G., Fischer, H.H., Gundlach, B., Knapmeyer, M., Knollenberg, J., Kokotanekova, R., Kührt, E., Leyrat, C., Marshall, D., Pelivan, I., Skorov, Y., Snodgrass, C., Spohn, T., Tosi, F., 2019. The Thermal, Mechanical, Structural, and Dielectric Properties of Cometary Nuclei After Rosetta. Space Science Reviews 215, 29. doi:10.1007/s11214-019-0594-x.

Groussin, O., Jorda, L., Auger, A.T., Kührt, E., Gaskell, R., Capanna, C., Scholten, F., Preusker, F., Lamy, P., Hviid, S., Knollenberg, J., Keller, U., Huettig, C., Sierks, H., Barbieri, C., Rodrigo, R., Koschny, D., Rickman, H., A'Hearn, M.F., Agarwal, J., Barucci, M.A., Bertaux, J.L., Bertini, I., Boudreault, S., Cremonese, G., Da Deppo, V., Davidsson, B., Debei, S., De Cecco, M., El-Maarry, M.R., Fornasier, S., Fulle, M., Gutiérrez, P.J., Güttler, C., Ip, W.H., Kramm, J.R., Küppers, M., Lazzarin, M., Lara, L.M., Lopez Moreno, J.J., Marchi, S., Marzari, F., Massironi, M., Michalik, H., Naletto, G., Oklay, N., Pommerol, A., Pajola, M., Thomas, N., Toth, I., Tubiana, C., Vincent, J.B., 2015. Gravitational slopes, geomorphology, and material strengths of the nucleus of comet 67P/Churyumov-Gerasimenko from OSIRIS observations. Astronomy & Astrophysics 583, A32. doi:10.1051/0004-6361/201526379.

Guilbert-Lepoutre, A., Jewitt, D., 2011. Thermal Shadows and Compositional Structure in Comet Nuclei. The Astrophysical Journal 743, 31. doi:10.1088/0004-637X/743/1/31.

Guilbert-Lepoutre, A., Rosenberg, E.D., Prialnik, D., Besse, S., 2016. Modelling the evolution of a comet subsurface: implications for 67P/Churyumov-Gerasimenko. Monthly Notices of the Royal Astronomical Society 462, S146–S155. doi:10.1093/mnras/stw2371.

Gundlach, B., Blum, J., 2012. Outgassing of icy bodies in the Solar System – II: Heat transport in dry, porous surface dust layers. Icarus 219, 618–629. doi:10.1016/j.icarus.2012.03.013.

Gundlach, B., Blum, J., 2015. The Stickiness of Micrometer-sized Water-ice Particles. The Astrophysical Journal 798, 34. doi:10.1088/0004-637X/798/1/34.

Gundlach, B., Blum, J., Keller, H.U., Skorov, Y.V., 2015. What drives the dust activity of comet 67P/Churyumov-Gerasimenko? Astronomy & Astrophysics 583, A12. doi:10.1051/0004-6361/201525828.

Gundlach, B., Schmidt, K.P., Kreuzig, C., Bischoff, D., Rezaei, F., Kothe, S., Blum, J., Grzesik, B., Stoll, E., 2018. The tensile strength of ice and dust aggregates and its dependence on particle properties. Monthly Notices of the Royal Astronomical Society 479, 1273–1277. doi:10.1093/mnras/sty1550.

Gunkelmann, N., Kataoka, A., Dullemond, C.P., Urbassek, H.M., 2017. Low-velocity collisions of chondrules: How a thin dust cover helps enhance the sticking probability. Astronomy & Astrophysics 599, L4. doi:10.1051/0004-6361/201630155.

Gusarov, A., Laoui, T., Froyen, L., Titov, V., 2003. Contact thermal conductivity of a powder bed in selective laser sintering. International Journal of Heat and Mass Transfer 46, 1103–1109. doi:10.1016/s0017-9310(02)00370-8.

Gusarov, A.V., Kovalev, E.P., 2009. Model of thermal conductivity in powder beds. Physical Review B 80, 024202. doi:10.1103/PhysRevB.80.024202.

Güttler, C., Blum, J., Zsom, A., Ormel, C.W., Dullemond, C.P., 2010. The outcome of protoplanetary dust growth: pebbles, boulders, or planetesimals?. I. Mapping the zoo of laboratory collision experiments. Astronomy and Astrophysics 513, A56. doi:10.1051/0004-6361/200912852.

Güttler, C., Krause, M., Geretshauser, R.J., Speith, R., Blum, J., 2009. The Physics of Protoplanetesimal Dust Agglomerates. IV. Toward a Dynamical Collision Model. The Astrophysical Journal 701, 130–141. doi:10.1088/0004-637X/701/1/130.

Güttler, C., Poppe, T., Wasson, J.T., Blum, J., 2008. Exposing metal and silicate charges to electrical discharges: Did chondrules form by nebular lightning? Icarus 195, 504–510. doi:10.1016/j.icarus.2007.11.021.

Haghighipour, N., Boss, A.P., 2003. On Pressure Gradients and Rapid Migration of Solids in a Nonuniform Solar Nebula. The Astrophysical Journal 583, 996–1003. doi:10.1086/345472.

Hansen, B.M.S., 2009. Formation of the Terrestrial Planets from a Narrow Annulus. The Astrophysical Journal 703, 1131–1140. doi:10.1088/0004-637X/703/1/1131.

Haruyama, J., Yamamoto, T., Mizutani, H., Greenberg, J.M., 1993. Thermal history of comets during residence in the Oort cloud - Effect of radiogenic heating in combination with the very low thermal conductivity of amorphous ice. Journal of Geophysics Research 98, 15. doi:10.1029/93JE01325.

Hasegawa, Y., Turner, N.J., Masiero, J., Wakita, S., Matsumoto, Y., Oshino, S., 2016. Forming Chondrites in a Solar Nebula with Magnetically Induced Turbulence. The Astrophysical Journal Letters 820, L12. doi:10.3847/2041-8205/820/1/L12.

Hastings, D.M., Ragozzine, D., Fabrycky, D.C., Burkhart, L.D., Fuentes, C., Margot, J.L., Brown, M.E., Holman, M., 2016. The short rotation period of Hi'iaka, Haumea's largest satellite. The Astronomical Journal 152, 195. doi:10.3847/0004-6256/152/6/195.

Hayashi, C., 1981. Structure of the Solar Nebula, Growth and Decay of Magnetic Fields and Effects of Magnetic and Turbulent Viscosities on the Nebula. Progress of Theoretical Physics Supplement 70, 35–53. doi:10.1143/PTPS.70.35.

Hayashi, C., Nakazawa, K., Nakagawa, Y., 1985. Formation of the solar system., in: Black, D.C., Matthews, M.S. (Eds.), Protostars and Planets II, pp. 1100–1153.

Heinisch, P., Auster, H.U., Gundlach, B., Blum, J., Güttler, C., Tubiana, C., Sierks, H., Hilchenbach, M., Biele, J., Richter, I., Glassmeier, K.H., 2019. Compressive strength of comet 67P/Churyumov-Gerasimenko derived from Philae surface contacts. Astronomy & Astrophysics 630, A2. doi:10.1051/0004-6361/201833889.

Heinze, A.N., de Lahunta, D., 2009. The Rotation Period and Light-Curve Amplitude of Kuiper Belt Dwarf Planet 136472 Makemake (2005 FY9). The Astronomical Journal 138, 428–438. doi:10.1088/0004-6256/138/2/428.

Helling, C., Iro, N., Corrales, L., Samra, D., Ohno, K., Alam, M.K., Steinrueck, M., Lew, B., Molaverdikhani, K., MacDonald, R.J., et al., 2019. Understanding the atmospheric properties and chemical composition of the ultra-hot jupiter hat-p-7b. Astronomy & Astrophysics 631, A79. doi:10.1051/0004-6361/201935771.

Henke, S., Gail, H.P., Trieloff, M., Schwarz, W., 2013. Thermal evolution model for the H chondrite asteroid-instantaneous formation versus protracted accretion. Icarus 226, 212–228. doi:10.1016/j.icarus.2013.05.034.

Henke, S., Gail, H.P., Trieloff, M., Schwarz, W.H., Kleine, T., 2012a. Thermal evolution and sintering of chondritic planetesimals. Astronomy & Astrophysics 537, A45. doi:10.1051/0004-6361/201117177.

Henke, S., Gail, H.P., Trieloff, M., Schwarz, W.H., Kleine, T., 2012b. Thermal history modelling of the H chondrite parent body. Astronomy & Astrophysics 545, A135. doi:10.1051/0004-6361/201219100.

Hewins, R.H., Radomsky, P.M., 1990. Temperature conditions for chondrule formation. Meteoritics 25, 309–318. doi:10.1111/j.1945-5100.1990.tb00715.x.

Hirabayashi, M., Scheeres, D.J., Chesley, S.R., Marchi, S., McMahon, J.W., Steckloff, J., Mottola, S., Naidu, S.P., Bowling, T., 2016. Fission and reconfiguration of bilobate comets as revealed by 67P/Churyumov-Gerasimenko. Nature 534, 352–355. doi:10.1038/nature17670.

Homma, K.A., Okuzumi, S., Nakamoto, T., Ueda, Y., 2019. Rocky Planetesimal Formation Aided by Organics. The Astrophysical Journal 877, 128. doi:10.3847/1538-4357/ab1de0.

Hood, L.L., Horányi, M., 1991. Gas dynamic heating of chondrule precursor grains in the solar nebula. Icarus 93, 259–269. doi:10.1016/0019-1035(91)90211-B.

Horányi, M., Morfill, G., Goertz, C.K., Levy, E.H., 1995. Chondrule formation in lightning discharges. Icarus 114, 174–185. doi:10.1006/icar.1995.1052.

Hu, X., Shi, X., Sierks, H., Blum, J., Oberst, J., Fulle, M., Kührt, E., Güttler, C., Gundlach, B., Keller, H.U., Mottola, S., Pajola, M., Barbieri, C., Lamy, P.L., Rodrigo, R., Koschny, D., Rickman, H., Agarwal, J., A'Hearn, M.F., Barucci, M.A., Bertaux, J.L., Bertini, I., Boudreault, S., Büttner, I., Cremonese, G., Da Deppo, V., Davidsson, B., Debei, S., De Cecco, M., Deller, J., Fornasier, S., Groussin, O., Gutiérrez, P.J., Gutiérrez-Marqués, P., Hall, I., Hofmann, M., Hviid, S.F., Ip, W.H., Jorda, L., Knollenberg, J., Kovacs, G., Kramm, J.R., Küppers, M., Lara, L.M., Lazzarin, M., López-Moreno, J.J., Marzari, F., Naletto, G., Oklay, N., Richards, M.L., Ripken, J., Thomas, N., Tubiana, C., Vincent, J.B., 2017. Thermal modelling of water activity on comet 67P/Churyumov-Gerasimenko with global dust mantle and plural dust-to-ice ratio. Monthly Notices of the Royal Astronomical Society 469, S295–S311. doi:10.1093/mnras/stx1607.

Hubbard, A., 2015. Compound chondrules fused cold. Icarus 254, 56–61. doi:10.1016/j.icarus.2015.02.030.

Hyodo, R., Charnoz, S., 2017. Dynamical evolution of the debris disk after a satellite catastrophic disruption around Saturn. The Astronomical Journal 154, 34. doi:10.3847/1538-3881/aa74c9.

Hyodo, R., Charnoz, S., Ohtsuki, K., Genda, H., 2017a. Ring formation around giant planets by tidal disruption of a single passing large Kuiper belt object. Icarus 282, 195–213. doi:10.1016/j.icarus.2016.09.012.

Hyodo, R., Genda, H., 2018. Implantation of Martian materials in the inner Solar System by a mega impact on Mars. The Astrophysical Journal Letters 856, L36. doi:10.3847/2041-8213/aab7f0.

Hyodo, R., Genda, H., Charnoz, S., Rosenblatt, P., 2017b. On the impact origin of Phobos and Deimos. I. Thermodynamic and physical aspects. The Astrophysical Journal 845, 125. doi:10.3847/1538-4357/aa81c4.

Hyodo, R., Ohtsuki, K., Takeda, T., 2015. Formation of multiple-satellite systems from low-mass circumplanetary particle disks. The Astrophysical Journal 799, 40. doi:10.1088/0004-637X/799/1/40.

Iida, A., Nakamoto, T., Susa, H., Nakagawa, Y., 2001. A Shock Heating Model for Chondrule Formation in a Protoplanetary Disk. Icarus 153, 430–450. doi:10.1006/icar.2001.6682.

Ikoma, M., Nakazawa, K., Emori, H., 2000. Formation of Giant Planets: Dependences on Core Accretion Rate and Grain Opacity. The Astrophysical Journal 537, 1013–1025. doi:10.1086/309050.

Ishii, H.A., Bradley, J.P., Dai, Z.R., Chi, M., Kearsley, A.T., Burchell, M.J., Browning, N.D., Molster, F., 2008. Comparison of Comet 81P/Wild 2 Dust with Interplanetary Dust from Comets. Science 319, 447. doi:10.1126/science.1150683.

Jacquet, E., 2014. The quasi-universality of chondrule size as a constraint for chondrule formation models. Icarus 232, 176–186. doi:10.1016/j.icarus.2014.01.012.

Jacquet, E., Thompson, C., 2014. Chondrule Destruction in Nebular Shocks. The Astrophysical Journal 797, 30. doi:10.1088/0004-637X/797/1/30.

Jewitt, D., Luu, J., 1993. Discovery of the candidate Kuiper belt object 1992 QB_1. Nature 362, 730–732. doi:10.1038/362730a0.

Johansen, A., Mac Low, M.M., Lacerda, P., Bizzarro, M., 2015. Growth of asteroids, planetary embryos, and Kuiper belt objects by chondrule accretion. Science Advances 1, 1500109. doi:10.1126/sciadv.1500109.

Johansen, A., Okuzumi, S., 2018. Harvesting the decay energy of ^{26}Al to drive lightning discharge in protoplanetary discs. Astronomy & Astrophysics 609, A31. doi:10.1051/0004-6361/201630047.

Johansen, A., Youdin, A., 2007. Protoplanetary Disk Turbulence Driven by the Streaming Instability: Nonlinear Saturation and Particle Concentration. The Astrophysical Journal 662, 627–641. doi:10.1086/516730.

Johansen, A., Youdin, A.N., Lithwick, Y., 2012. Adding particle collisions to the formation of asteroids and Kuiper belt objects via streaming instabilities. Astronomy & Astrophysics 537, A125. doi:10.1051/0004-6361/201117701.

Johnson, B.C., Minton, D.A., Melosh, H.J., Zuber, M.T., 2015. Impact jetting as the origin of chondrules. Nature 517, 339–341. doi:10.1038/nature14105.

Johnson, K.L., 1987. Contact Mechanics. Cambridge University Press.

Johnson, K.L., Kendall, K., Roberts, A.D., 1971. Surface Energy and the Contact of Elastic Solids. Proceedings of the Royal Society of London Series A 324, 301–313. doi:10.1098/rspa.1971.0141.

Jorda, L., Gaskell, R., Capanna, C., Hviid, S., Lamy, P., Ďurech, J., Faury, G., Groussin, O., Gutiérrez, P., Jackman, C., Keihm, S.J., Keller, H.U., Knollenberg, J., Kührt, E., Marchi, S., Mottola, S., Palmer, E., Schloerb, F.P., Sierks, H., Vincent, J.B., A'Hearn, M.F., Barbieri, C., Rodrigo, R., Koschny, D., Rickman, H., Barucci, M.A., Bertaux, J.L., Bertini, I., Cremonese, G., Da Deppo, V., Davidsson, B., Debei, S., De Cecco, M., Fornasier, S., Fulle, M., Güttler, C., Ip, W.H., Kramm, J.R., Küppers, M., Lara, L.M., Lazzarin, M., Lopez Moreno, J.J., Marzari, F., Naletto, G., Oklay, N., Thomas, N., Tubiana, C., Wenzel, K.P., 2016. The global shape, density and rotation of Comet 67P/Churyumov-Gerasimenko from preperihelion Rosetta/OSIRIS observations. Icarus 277, 257–278. doi:10.1016/j.icarus.2016.05.002.

Josserand, C., Thoroddsen, S.T., 2016. Drop Impact on a Solid Surface. Annual Review of Fluid Mechanics 48, 365–391. doi:10.1146/annurev-fluid-122414-034401.

Jullien, R., Kolb, M., 1984. Hierarchical model for chemically limited cluster-cluster aggregation. Journal of Physics A: Mathematical and General 17, L639–L643. doi:10.1088/0305-4470/17/12/003.

Kadono, T., Arakawa, M., 2005. Breakup of liquids by high velocity flow and size distribution of chondrules. Icarus 173, 295–299. doi:10.1016/j.icarus.2004.08.014.

Kataoka, A., Okuzumi, S., Tanaka, H., Nomura, H., 2014. Opacity of fluffy dust aggregates. Astronomy & Astrophysics 568, A42. doi:10.1051/0004-6361/201323199.

Kataoka, A., Tanaka, H., Okuzumi, S., Wada, K., 2013a. Fluffy dust forms icy planetesimals by static compression. Astronomy & Astrophysics 557, L4. doi:10.1051/0004-6361/201322151.

Kataoka, A., Tanaka, H., Okuzumi, S., Wada, K., 2013b. Static compression of porous dust aggregates. Astronomy & Astrophysics 554, A4. doi:10.1051/0004-6361/201321325.

Keller, H.U., Barbieri, C., Lamy, P., Rickman, H., Rodrigo, R., Wenzel, K.P., Sierks, H., A'Hearn, M.F., Angrilli, F., Angulo, M., Bailey, M.E., Barthol, P., Barucci, M.A., Bertaux, J.L., Bianchini, G., Boit, J.L., Brown, V., Burns, J.A., Büttner, I., Castro, J.M., Cremonese, G., Curdt, W., da Deppo, V., Debei, S., de Cecco, M., Dohlen, K., Fornasier, S., Fulle, M., Germerott, D., Gliem, F., Guizzo, G.P., Hviid, S.F., Ip, W.H., Jorda, L., Koschny, D., Kramm, J.R., Kührt, E., Küppers, M., Lara, L.M., Llebaria, A., López, A., López-Jimenez, A., López-Moreno, J., Meller, R., Michalik, H., Michelena, M.D., Müller, R., Naletto, G., Origné, A., Parzianello, G., Pertile, M., Quintana, C., Ragazzoni, R., Ramous, P., Reiche, K.U., Reina, M., Rodríguez, J., Rousset, G., Sabau, L., Sanz, A., Sivan, J.P., Stöckner, K., Tabero, J., Telljohann, U., Thomas, N., Timon, V., Tomasch, G., Wittrock, T., Zaccariotto, M., 2007. OSIRIS The Scientific Camera System Onboard Rosetta. Space Science Reviews 128, 433–506. doi:10.1007/s11214-006-9128-4.

Kelley, M.S., Lindler, D.J., Bodewits, D., A'Hearn, M.F., Lisse, C.M., Kolokolova, L., Kissel, J., Hermalyn, B., 2013. A distribution of large particles in the coma of Comet 103P/Hartley 2. Icarus 222, 634–652. doi:10.1016/j.icarus.2012.09.037.

Kempf, S., Pfalzner, S., Henning, T.K., 1999. N-Particle-Simulations of Dust Growth. I. Growth Driven by Brownian Motion. Icarus 141, 388–398. doi:10.1006/icar.1999.6171.

Khare, B.N., Sagan, C., Arakawa, E.T., Suits, F., Callcott, T.A., Williams, M.W., 1984. Optical constants of organic tholins produced in a simulated Titanian atmosphere: From soft x-ray to microwave frequencies. Icarus 60, 127–137. doi:10.1016/0019-1035(84)90142-8.

Kiss, C., Marton, G., Farkas-Takács, A., Stansberry, J., Müller, T., Vinkó, J., Balog, Z., Ortiz, J.L., Pál, A., 2017. Discovery of a satellite of the large trans-Neptunian object (225088) 2007 OR10. The Astrophysical Journal Letters 838, L1. doi:10.3847/2041-8213/aa6484.

Kita, N.T., Ushikubo, T., 2012. Evolution of protoplanetary disk inferred from ^{26}Al chronology of individual chondrules. Meteoritics & Planetary Science 47, 1108–1119. doi:10.1111/j.1945-5100.2011.01264.x.

Kitazato, K., Milliken, R.E., Iwata, T., Abe, M., Ohtake, M., Matsuura, S., Arai, T., Nakauchi, Y., Nakamura, T., Matsuoka, M., Senshu, H., Hirata, N., Hiroi, T., Pilorget, C., Brunetto, R., Poulet, F., Riu, L., Bibring, J.P., Takir, D.,

Domingue, D.L., Vilas, F., Barucci, M.A., Perna, D., Palomba, E., Galiano, A., Tsumura, K., Osawa, T., Komatsu, M., Nakato, A., Arai, T., Takato, N., Matsunaga, T., Takagi, Y., Matsumoto, K., Kouyama, T., Yokota, Y., Tatsumi, E., Sakatani, N., Yamamoto, Y., Okada, T., Sugita, S., Honda, R., Morota, T., Kameda, S., Sawada, H., Honda, C., Yamada, M., Suzuki, H., Yoshioka, K., Hayakawa, M., Ogawa, K., Cho, Y., Shirai, K., Shimaki, Y., Hirata, N., Yamaguchi, A., Ogawa, N., Terui, F., Yamaguchi, T., Takei, Y., Saiki, T., Nakazawa, S., Tanaka, S., Yoshikawa, M., Watanabe, S., Tsuda, Y., 2019. The surface composition of asteroid 162173 Ryugu from Hayabusa2 near-infrared spectroscopy. Science 364, 272–275. doi:10.1126/science.aav7432.

Kitzmann, D., Heng, K., 2018. Optical properties of potential condensates in exoplanetary atmospheres. Monthly Notices of the Royal Astronomical Society 475, 94–107. doi:10.1093/mnras/stx3141.

Kobayashi, H., Kimura, H., Yamamoto, S., 2013. Dust mantle of comet 9P/Tempel 1: dynamical constraints on physical properties. Astronomy & Astrophysics 550, A72. doi:10.1051/0004-6361/201220464.

Kofman, W., Herique, A., Barbin, Y., Barriot, J.P., Ciarletti, V., Clifford, S., Edenhofer, P., Elachi, C., Eyraud, C., Goutail, J.P., Heggy, E., Jorda, L., Lasue, J., Levasseur-Regourd, A.C., Nielsen, E., Pasquero, P., Preusker, F., Puget, P., Plettemeier, D., Rogez, Y., Sierks, H., Statz, C., Svedhem, H., Williams, I., Zine, S., Van Zyl, J., 2015. Properties of the 67P/Churyumov-Gerasimenko interior revealed by CONSERT radar. Science 349, aab0639. doi:10.1126/science.aab0639.

Kokubo, E., Ida, S., 1998. Oligarchic Growth of Protoplanets. Icarus 131, 171–178. doi:10.1006/icar.1997.5840.

Kokubo, E., Ida, S., Makino, J., 2000. Evolution of a Circumterrestrial Disk and Formation of a Single Moon. Icarus 148, 419–436. doi:10.1006/icar.2000.6496.

Kominami, J.D., Makino, J., Daisaka, H., 2011. Binary Formation in Planetesimal Disks. I. Equal Mass Planetesimals. Publications of the Astronomical Society of Japan 63, 1331–1344. doi:10.1093/pasj/63.6.1331.

Kommandur, S., Yee, S.K., 2017. An empirical model to predict temperature-dependent thermal conductivity of amorphous polymers. Journal of Polymer Science B: Polymer Physics 55, 1160–1170. doi:10.1002/polb.24365.

Krause, M., Blum, J., Skorov, Y.V., Trieloff, M., 2011. Thermal conductivity measurements of porous dust aggregates: I. Technique, model and first results. Icarus 214, 286–296. doi:10.1016/j.icarus.2011.04.024.

Krauss, O., Wurm, G., 2005. Photophoresis and the Pile-up of Dust in Young Circumstellar Disks. The Astrophysical Journal 630, 1088–1092. doi:10.1086/432087.

Krijt, S., Dominik, C., Tielens, A.G.G.M., 2014. Rolling friction of adhesive microspheres. Journal of Physics D: Applied Physics 47, 175302. doi:10.1088/0022-3727/47/17/175302.

Krijt, S., Ormel, C.W., Dominik, C., Tielens, A.G.G.M., 2015. Erosion and the limits to planetesimal growth. Astronomy & Astrophysics 574, A83. doi:10.1051/0004-6361/201425222.

Krot, A.N., Rubin, A.E., 1994. Glass-rich chondrules in ordinary chondrites. Meteoritics 29, 697–707. doi:10.1111/j.1945-5100.1994.tb00787.x.

Kruijer, T.S., Burkhardt, C., Budde, G., Kleine, T., 2017. Age of Jupiter inferred from the distinct genetics and formation times of meteorites. Proceedings of the National Academy of Science 114, 6712–6716. doi:10.1073/pnas.1704461114.

Kührt, E.K., Keller, H.U., 1994. The Formation of Cometary Surface Crusts. Icarus 109, 121–132. doi:10.1006/icar.1994.1080.

Kührt, E.K., Keller, H.U., 1996. On the Importance of Dust in Cometary Nuclei. Earth Moon and Planets 72, 79–89. doi:10.1007/BF00117506.

Kuiper, G.P., 1951. On the Origin of the Solar System. Proceedings of the National Academy of Science 37, 1–14. doi:10.1073/pnas.37.1.1.

Langkowski, D., Teiser, J., Blum, J., 2008. The Physics of Protoplanetesimal Dust Agglomerates. II. Low-Velocity Collision Properties. The Astrophysical Journal 675, 764–776. doi:10.1086/525841.

Lee, G., Helling, C., Dobbs-Dixon, I., Juncher, D., 2015. Modelling the local and global cloud formation on HD 189733b. Astronomy & Astrophysics 580, A12. doi:10.1051/0004-6361/201525982.

Leliwa-Kopystynski, J., Taniguchi, T., Kondo, K., Sawaoka, A., 1984. Sticking in moderate velocity oblique impact - Application to planetology. Icarus 57, 280–293. doi:10.1016/0019-1035(84)90073-3.

Li, H., Kuschel, M., Sommerfeld, M., 2016. Experimental Investigation and Modeling of Coalescence and Agglomeration for Spray Drying of Solutions. Springer. doi:10.1007/978-3-319-32370-1_6.

Libourel, G., Portail, M., 2018. Chondrules as direct thermochemical sensors of solar protoplanetary disk gas. Science Advances 4, eaar3321. doi:10.1126/sciadv.aar3321.

Liu, B., Ormel, C.W., 2018. Catching drifting pebbles. I. Enhanced pebble accretion efficiencies for eccentric planets. Astronomy & Astrophysics 615, A138. doi:10.1051/0004-6361/201732307.

Liu, C.h., Nagel, S.R., Schecter, D.A., Coppersmith, S.N., Majumdar, S., Narayan, O., Witten, T.A., 1995. Force Fluctuations in Bead Packs. Science 269, 513–515. doi:10.1126/science.269.5223.513.

Loesche, C., Wurm, G., 2012. Thermal and photophoretic properties of dust mantled chondrules and sorting in the solar nebula. Astronomy & Astrophysics 545, A36. doi:10.1051/0004-6361/201218989.

Lofgren, G., Russell, W.J., 1986. Dynamic crystallization of chondrule melts of porphyritic and radial pyroxene composition. Geochimica et Cosmochimica Acta 50, 1715–1726. doi:10.1016/0016-7037(86)90133-X.

Lord, R.C., Morrow, J.C., 1957. Calculation of the Heat Capacity of α Quartz and Vitreous Silica from Spectroscopic Data. The Journal of Chemical Physics 26, 230–232. doi:10.1063/1.1743274.

Luikov, A., Shashkov, A., Vasiliev, L., Fraiman, Y., 1968. Thermal conductivity of porous systems. International Journal of Heat and Mass Transfer 11, 117–140. doi:10.1016/0017-9310(68)90144-0.

Machii, N., Nakamura, A.M., Güttler, C., Beger, D., Blum, J., 2013. Collision of a chondrule with matrix: Relation between static strength of matrix and impact pressure. Icarus 226, 111–118. doi:10.1016/j.icarus.2013.05.006.

Mai, C., Desch, S.J., Boley, A.C., Weiss, B.P., 2018. Magnetic Fields Recorded by Chondrules Formed in Nebular Shocks. The Astrophysical Journal 857, 96. doi:10.3847/1538-4357/aab711.

Maquet, L., 2015. The recent dynamical history of comet 67P/Churyumov-Gerasimenko. Astronomy & Astrophysics 579, A78. doi:10.1051/0004-6361/201425461.

Marshall, D., Groussin, O., Vincent, J.B., Brouet, Y., Kappel, D., Arnold, G., Capria, M.T., Filacchione, G., Hartogh, P., Hofstadter, M., Ip, W.H., Jorda, L., Kührt, E., Lellouch, E., Mottola, S., Rezac, L., Rodrigo, R., Rodionov, S., Schloerb, P., Thomas, N., 2018. Thermal inertia and roughness of the nucleus of comet 67P/Churyumov-Gerasimenko from MIRO and VIRTIS observations. Astronomy & Astrophysics 616, A122. doi:10.1051/0004-6361/201833104.

Mathis, J.S., Rumpl, W., Nordsieck, K.H., 1977. The size distribution of interstellar grains. The Astrophysical Journal 217, 425–433. doi:10.1086/155591.

Matsumoto, Y., Oshino, S., Hasegawa, Y., Wakita, S., 2017. Chondrule Accretion with a Growing Protoplanet. The Astrophysical Journal 837, 103. doi:10.3847/1538-4357/aa607d.

Meakin, P., 1983. Formation of Fractal Clusters and Networks by Irreversible Diffusion-Limited Aggregation. Physical Review Letters 51, 1119–1122. doi:10.1103/physrevlett.51.1119.

Meakin, P., 1987. Fractal aggregates. Advances in Colloid and Interface Science 28, 249–331. doi:10.1016/0001-8686(87)80016-7.

Meakin, P., 1991. Fractal aggregates in geophysics. Reviews of Geophysics 29, 317–354. doi:10.1029/91RG00688.

Meisner, T., Wurm, G., Teiser, J., 2012. Experiments on centimeter-sized dust aggregates and their implications for planetesimal formation. Astronomy & Astrophysics 544, A138. doi:10.1051/0004-6361/201219099.

Merrill, R.B., 1969. Thermal conduction through an evacuated idealized powder over the temperature range 100° to 500°K. NASA Technical Note D-5063.

Metzler, K., 2018. From 2D to 3D chondrule size data: Some empirical ground truths. Meteoritics & Planetary Science 53, 1489–1499. doi:10.1111/maps.13091.

Mie, G., 1908. Beiträge zur Optik trüber Medien, speziell kolloidaler Metallösungen. Annalen der Physik 330, 377–445. doi:10.1002/andp.19083300302.

Miura, H., Nakamoto, T., 2005. A shock-wave heating model for chondrule formation II. Minimum size of chondrule precursors. Icarus 175, 289–304. doi:10.1016/j.icarus.2004.11.011.

Miura, H., Nakamoto, T., Doi, M., 2008a. Origin of three-dimensional shapes of chondrules. I. Hydrodynamics simulations of rotating droplet exposed to high-velocity rarefied gas flow. Icarus 197, 269–281. doi:10.1016/j.icarus.2008.04.019.

Miura, H., Nakamoto, T., Susa, H., 2002. A Shock-Wave Heating Model for Chondrule Formation: Effects of Evaporation and Gas Flows on Silicate Particles. Icarus 160, 258–270. doi:10.1006/icar.2002.6964.

Miura, H., Tanaka, K.K., Yamamoto, T., Nakamoto, T., Yamada, J., Tsukamoto, K., Nozawa, J., 2010a. Formation of Cosmic Crystals in Highly Supersaturated Silicate Vapor Produced by Planetesimal Bow Shocks. The Astrophysical Journal 719, 642–654. doi:10.1088/0004-637X/719/1/642.

Miura, H., Yamamoto, T., 2014. A New Estimate of the Chondrule Cooling Rate Deduced from an Analysis of Compositional Zoning of Relict Olivine. The Astronomical Journal 147, 54. doi:10.1088/0004-6256/147/3/54.

Miura, H., Yasuda, S., Nakamoto, T., 2008b. Fragment-collision model for compound chondrule formation: Estimation of collision probability. Icarus 194, 811–821. doi:10.1016/j.icarus.2007.11.005.

Miura, H., Yokoyama, E., Nagashima, K., Tsukamoto, K., Srivastava, A., 2010b. Phase-field simulation for crystallization of a highly supercooled forsterite-chondrule melt droplet. Journal of Applied Physics 108, 114912. doi:10.1063/1.3504655.

Miyake, K., Nakagawa, Y., 1993. Effects of particle size distribution on opacity curves of protoplanetary disks around T Tauri stars. Icarus 106, 20. doi:10.1006/icar.1993.1156.

Mizuno, H., 1980. Formation of the Giant Planets. Progress of Theoretical Physics 64, 544–557. doi:10.1143/PTP.64.544.

Monaghan, J.J., 1992. Smoothed particle hydrodynamics. Annual Review of Astronomy and Astrophysics 30, 543–574. doi:10.1146/annurev.aa.30.090192.002551.

Morris, M.A., Boley, A.C., Desch, S.J., Athanassiadou, T., 2012. Chondrule Formation in Bow Shocks around Eccentric Planetary Embryos. The Astrophysical Journal 752, 27. doi:10.1088/0004-637X/752/1/27.

Morris, M.A., Desch, S.J., 2010. Thermal Histories of Chondrules in Solar Nebula Shocks. The Astrophysical Journal 722, 1474–1494. doi:10.1088/0004-637X/722/2/1474.

Mukai, T., Ishimoto, H., Kozasa, T., Blum, J., Greenberg, J.M., 1992. Radiation pressure forces of fluffy porous grains. Astronomy & Astrophysics 262, 315–320.

Mundo, C.H.R., Sommerfeld, M., Tropea, C., 1995. Droplet-wall collisions: experimental studies of the deformation and breakup process. International journal of multiphase flow 21, 151–173. doi:10.1016/0301-9322(94)00069-v.

Muranushi, T., 2010. Dust-dust collisional charging and lightning in protoplanetary discs. Monthly Notices of the Royal Astronomical Society 401, 2641–2664. doi:10.1111/j.1365-2966.2009.15848.x.

Murase, T., McBirney, A.R., 1973. Properties of Some Common Igneous Rocks and Their Melts at High Temperatures. Geological Society of America Bulletin 84, 3563. doi:10.1130/0016-7606(1973)84<3563:POSCIR>2.0.CO;2.

Musiolik, G., Teiser, J., Jankowski, T., Wurm, G., 2016a. Collisions of CO_2 Ice Grains in Planet Formation. The Astrophysical Journal 818, 16. doi:10.3847/0004-637X/818/1/16.

Musiolik, G., Teiser, J., Jankowski, T., Wurm, G., 2016b. Ice Grain Collisions in Comparison: CO2, H2O, and Their Mixtures. The Astrophysical Journal 827, 63. doi:10.3847/0004-637X/827/1/63.

Nagasawa, M., Tanaka, K.K., Tanaka, H., Nakamoto, T., Miura, H., Yamamoto, T., 2014. Revisiting Jovian-resonance Induced Chondrule Formation. The Astrophysical Journal Letters 794, L7. doi:10.1088/2041-8205/794/1/L7.

Nagasawa, M., Tanaka, K.K., Tanaka, H., Nomura, H., Nakamoto, T., Miura, H., 2019. Shock-generating Planetesimals Perturbed by a Giant Planet in a Gas Disk. The Astrophysical Journal 871, 110. doi:10.3847/1538-4357/aaf795.

Nagashima, K., Moriuchi, Y., Tsukamoto, K., Tanaka, K.K., Kobatake, H., 2008. Critical cooling rates for glass formation in levitated Mg_2SiO_4-$MgSiO_3$ chondrule melts. Journal of Mineralogical and Petrological Sciences 103, 204–208. doi:10.2465/jmps.070620c.

Nagashima, K., Tsukamoto, K., Satoh, H., Kobatake, H., Dold, P., 2006. Reproduction of chondrules from levitated, hypercooled melts. Journal of Crystal Growth 293, 193–197. doi:10.1016/j.jcrysgro.2006.01.064.

Nakamoto, T., Miura, H., 2004. Collisional Destruction of Chondrules in Shock Waves and Inferred Dust to Gas Mass Ratio, in: Lunar and Planetary Science Conference Abstracts, p. 1847.

Nakamura, T., Noguchi, T., Tanaka, M., Zolensky, M.E., Kimura, M., Tsuchiyama, A., Nakato, A., Ogami, T., Ishida, H., Uesugi, M., Yada, T., Shirai, K., Fujimura, A., Okazaki, R., Sandford, S.A., Ishibashi, Y., Abe, M.,

Okada, T., Ueno, M., Mukai, T., Yoshikawa, M., Kawaguchi, J., 2011. Itokawa Dust Particles: A Direct Link Between S-Type Asteroids and Ordinary Chondrites. Science 333, 1113. doi:10.1126/science.1207758.

Natta, A., Testi, L., Calvet, N., Henning, T., Waters, R., Wilner, D., 2007. Dust in Protoplanetary Disks: Properties and Evolution, in: Reipurth, B., Jewitt, D., Keil, K. (Eds.), Protostars and Planets V, p. 767.

Naue, G., Bärwolff, G., 1992. Transportprozesse in Fluiden. Deutscher Verlag für Grundstoffindustrie, Leipzig.

Nelson, V.E., Rubin, A.E., 2002. Size-frequency distributions of chondrules and chondrule fragments in LL3 chondrites: Implications for parent-body fragmentation of chondrules. Meteoritics & Planetary Science 37, 1361–1376. doi:10.1111/j.1945-5100.2002.tb01034.x.

Nesvorný, D., Li, R., Youdin, A.N., Simon, J.B., Grundy, W.M., 2019. Trans-Neptunian binaries as evidence for planetesimal formation by the streaming instability. Nature Astronomy 3, 808–812. doi:10.1038/s41550-019-0806-z.

Nesvorný, D., Youdin, A.N., Richardson, D.C., 2010. Formation of Kuiper Belt Binaries by Gravitational Collapse. The Astronomical Journal 140, 785–793. doi:10.1088/0004-6256/140/3/785.

Noll, K.S., Grundy, W.M., Chiang, E.I., Margot, J.L., Kern, S.D., 2008a. Binaries in the Kuiper Belt. University of Arizona Press.

Noll, K.S., Grundy, W.M., Stephens, D.C., Levison, H.F., Kern, S.D., 2008b. Evidence for two populations of classical transneptunian objects: The strong inclination dependence of classical binaries. Icarus 194, 758–768. doi:10.1016/j.icarus.2007.10.022.

Ohno, K., Okuzumi, S., 2018. Microphysical Modeling of Mineral Clouds in GJ1214 b and GJ436 b: Predicting Upper Limits on the Cloud-top Height. The Astrophysical Journal 859, 34. doi:10.3847/1538-4357/aabee3.

Ohno, K., Okuzumi, S., Tazaki, R., 2019. Clouds of Fluffy Aggregates: How They Form in Exoplanetary Atmospheres and Influence Transmission Spectra. The Astrophysical Journal (in press). arXiv:1908.02201.

Okabayashi, S., Yokoyama, T., Nakanishi, N., Iwamori, H., 2019. Fractionation of highly siderophile elements in metal grains from unequilibrated ordinary chondrites: Implications for the origin of chondritic metals. Geochimica et Cosmochimica Acta 244, 197–215. doi:10.1016/j.gca.2018.10.003.

Okada, T., Fukuhara, T., Tanaka, S., Taguchi, M., Imamura, T., Arai, T., Senshu, H., Ogawa, Y., Demura, H., Kitazato, K., Nakamura, R., Kouyama, T., Sekiguchi, T., Hasegawa, S., Matsunaga, T., Wada, T., Takita, J., Sakatani, N., Horikawa, Y., Endo, K., Helbert, J., Müller, T.G., Hagermann, A., 2017. Thermal Infrared Imaging Experiments of C-Type Asteroid 162173 Ryugu on Hayabusa2. Space Science Reviews 208, 255–286. doi:10.1007/s11214-016-0286-8.

Okuzumi, S., 2016. Modeling Dust and Turbulence in Protoplanetary Disks: A New Picture of Planetesimal Formation. The astronomical herald 109, 833–842.

Okuzumi, S., Momose, M., Sirono, S.i., Kobayashi, H., Tanaka, H., 2016. Sintering-induced Dust Ring Formation in Protoplanetary Disks: Application to the HL Tau Disk. The Astrophysical Journal 821, 82. doi:10.3847/0004-637X/821/2/82.

Okuzumi, S., Tanaka, H., Kobayashi, H., Wada, K., 2012. Rapid Coagulation of Porous Dust Aggregates outside the Snow Line: A Pathway to Successful Icy Planetesimal Formation. The Astrophysical Journal 752, 106. doi:10.1088/0004-637X/752/2/106.

Okuzumi, S., Tanaka, H., Sakagami, M.a., 2009. Numerical Modeling of the Coagulation and Porosity Evolution of Dust Aggregates. The Astrophysical Journal 707, 1247–1263. doi:10.1088/0004-637X/707/2/1247.

Omura, T., Kiuchi, M., Güttler, C., Nakamura, A.M., 2016. Centrifugal Experiments with Simulated Regolith: Effects of Gravity, Size Distribution, and Particle Shape on Porosity. Transactions of the Japan Society for Aeronautical and Space Sciences, Aerospace Technology Japan 14, Pk_17–Pk_21. doi:10.2322/tastj.14.pk_17.

Omura, T., Nakamura, A.M., 2017. Experimental study on compression property of regolith analogues. Planetary and Space Science 149, 14–22. doi:10.1016/j.pss.2017.08.003.

Omura, T., Nakamura, A.M., 2018. Estimating the Porosity Structure of Granular Bodies Using the Lane–Emden Equation Applied to Laboratory Measurements of the Pressure–Density Relation of Fluffy Granular Samples. The Astrophysical Journal 860, 123. doi:10.3847/1538-4357/aabe81.

Oort, J.H., 1950. The structure of the cloud of comets surrounding the Solar System and a hypothesis concerning its origin. Bulletin of the Astronomical Institutes of the Netherlands 11, 91–110.

Ormel, C.W., Cuzzi, J.N., 2007. Closed-form expressions for particle relative velocities induced by turbulence. Astronomy & Astrophysics 466, 413–420. doi:10.1051/0004-6361:20066899.

Ortiz, J.L., Santos-Sanz, P., Sicardy, B., Benedetti-Rossi, G., Bérard, D., Morales, N., Duffard, R., Braga-Ribas, F., Hopp, U., Ries, C., Nascimbeni, V., Marzari, F., Granata, V., Pál, A., Kiss, C., Pribulla, T., Komžík, R., Hornoch, K., Pravec, P., Bacci, P., Maestripieri, M., Nerli, L., Mazzei, L., Bachini, M., Martinelli, F., Succi, G., Ciabattari, F., Mikuz, H., Carbognani, A., Gaehrken, B., Mottola, S., Hellmich, S., Rommel, F.L., Fernández-Valenzuela, E., Campo Bagatin, A., Cikota, S., Cikota, A., Lecacheux, J., Vieira-Martins, R., Camargo, J.I.B., Assafin, M., Colas, F., Behrend, R., Desmars, J., Meza, E., Alvarez-Candal, A., Beisker, W., Gomes-Junior, A.R., Morgado, B.E., Roques, F., Vachier, F., Berthier, J., Mueller, T.G., Madiedo, J.M., Unsalan, O., Sonbas, E., Karaman, N., Erece, O., Koseoglu, D.T., Ozisik, T., Kalkan, S., Guney, Y., Niaei, M.S., Satir, O., Yesilyaprak, C., Puskullu, C., Kabas, A., Demircan, O., Alikakos,

J., Charmandaris, V., Leto, G., Ohlert, J., Christille, J.M., Szakáts, R., Takácsné Farkas, A., Varga-Verebélyi, E., Marton, G., Marciniak, A., Bartczak, P., Santana-Ros, T., Butkiewicz-Bąk, M., Dudziński, G., Alí-Lagoa, V., Gazeas, K., Tzouganatos, L., Paschalis, N., Tsamis, V., Sánchez-Lavega, A., Pérez-Hoyos, S., Hueso, R., Guirado, J.C., Peris, V., Iglesias-Marzoa, R., 2017. The size, shape, density and ring of the dwarf planet Haumea from a stellar occultation. Nature 550, 219–223. doi:10.1038/nature24051.

Ortiz, J.L., Sicardy, B., Braga-Ribas, F., Alvarez-Cand al, A., Lellouch, E., Duffard, R., Pinilla-Alonso, N., Ivanov, V.D., Littlefair, S.P., Camargo, J.I.B., Assafin, M., Unda-Sanzana, E., Jehin, E., Morales, N., Tancredi, G., Gil-Hutton, R., de La Cueva, I., Colque, J.P., da Silva Neto, D.N., Manfroid, J., Thirouin, A., Gutiérrez, P.J., Lecacheux, J., Gillon, M., Maury, A., Colas, F., Licandro, J., Mueller, T., Jacques, C., Weaver, D., Milone, A., Salvo, R., Bruzzone, S., Organero, F., Behrend, R., Roland, S., Vieira-Martins, R., Widemann, T., Roques, F., Santos-Sanz, P., Hestroffer, D., Dhillon, V.S., Marsh, T.R., Harlingten, C., Campo Bagatin, A., Alonso, M.L., Ortiz, M., Colazo, C., Lima, H.J.F., Oliveira, A.S., Kerber, L.O., Smiljanic, R., Pimentel, E., Giacchini, B., Cacella, P., Emilio, M., 2012. Albedo and atmospheric constraints of dwarf planet Makemake from a stellar occultation. Nature 491, 566–569. doi:10.1038/nature11597.

Ossenkopf, V., 1993. Dust coagulation in dense molecular clouds : the formation of fluffy aggregates. Astronomy & Astrophysics 280, 617–646.

Pál, A., Kiss, C., Müller, T.G., Molnár, L., Szabó, R., Szabó, G.M., Sárneczky, K., Kiss, L.L., 2016. Large Size and Slow Rotation of the Trans-Neptunian Object (225088) 2007 OR_{10} Discovered from Herschel and K2 Observations. The Astronomical Journal 151, 117. doi:10.3847/0004-6256/151/5/117.

Palme, H., Hezel, D.C., Ebel, D.S., 2015. The origin of chondrules: Constraints from matrix composition and matrix-chondrule complementarity. Earth and Planetary Science Letters 411, 11–19. doi:10.1016/j.epsl.2014.11.033.

Pape, J., Mezger, K., Bouvier, A.S., Baumgartner, L.P., 2019. Time and duration of chondrule formation: Constraints from ^{26}Al-^{26}Mg ages of individual chondrules. Geochimica et Cosmochimica Acta 244, 416–436. doi:10.1016/j.gca.2018.10.017.

Parker, A.H., Buie, M.W., Grundy, W.M., Noll, K.S., 2016. Discovery of a Makemakean Moon. The Astrophysical Journal Letters 825, L9. doi:10.3847/2041-8205/825/1/L9.

Paszun, D., Dominik, C., 2009. Collisional evolution of dust aggregates. From compaction to catastrophic destruction. Astronomy & Astrophysics 507, 1023–1040. doi:10.1051/0004-6361/200810682.

Pätzold, M., Andert, T., Hahn, M., Asmar, S.W., Barriot, J.P., Bird, M.K., Häusler, B., Peter, K., Tellmann, S., Grün, E., Weissman, P.R., Sierks, H., Jorda, L., Gaskell, R., Preusker, F., Scholten, F., 2016. A homogeneous nucleus for comet 67P/Churyumov-Gerasimenko from its gravity field. Nature 530, 63–65. doi:10.1038/nature16535.

Pätzold, M., Andert, T.P., Hahn, M., Barriot, J.P., Asmar, S.W., Häusler, B., Bird, M.K., Tellmann, S., Oschlisniok, J., Peter, K., 2019. The Nucleus of comet 67P/Churyumov-Gerasimenko - Part I: The global view - nucleus mass, mass-loss, porosity, and implications. Monthly Notices of the Royal Astronomical Society 483, 2337–2346. doi:10.1093/mnras/sty3171.

Peale, S.J., Cassen, P., 1978. Contribution of tidal dissipation to lunar thermal history. Icarus 36, 245–269. doi:10.1016/0019-1035(78)90109-4.

Petrovic, J.J., 2003. Mechanical properties of ice and snow. Journal of Materials Science 38, 1–6. doi:10.1023/a:1021134128038.

Piani, L., Tachibana, S., Hama, T., Tanaka, H., Endo, Y., Sugawara, I., Dessimoulie, L., Kimura, Y., Miyake, A., Matsuno, J., Tsuchiyama, A., Fujita, K., Nakatsubo, S., Fukushi, H., Mori, S., Chigai, T., Yurimoto, H., Kouchi, A., 2017. Evolution of Morphological and Physical Properties of Laboratory Interstellar Organic Residues with Ultraviolet Irradiation. The Astrophysical Journal 837, 35. doi:10.3847/1538-4357/aa5ca6.

Pinte, C., Dent, W.R.F., Ménard, F., Hales, A., Hill, T., Cortes, P., de Gregorio-Monsalvo, I., 2016. Dust and Gas in the Disk of HL Tauri: Surface Density, Dust Settling, and Dust-to-gas Ratio. The Astrophysical Journal 816, 25. doi:10.3847/0004-637X/816/1/25.

Piqueux, S., Christensen, P.R., 2009. A model of thermal conductivity for planetary soils: 1. Theory for unconsolidated soils. Journal of Geophysical Research (Planets) 114, E09005. doi:10.1029/2008JE003308.

Pollack, J.B., Hollenbach, D., Beckwith, S., Simonelli, D.P., Roush, T., Fong, W., 1994. Composition and radiative properties of grains in molecular clouds and accretion disks. The Astrophysical Journal 421, 615–639. doi:10.1086/173677.

Pollack, J.B., McKay, C.P., Christofferson, B.M., 1985. A calculation of the Rosseland mean opacity of dust grains in primordial solar system nebulae. Icarus 64, 471–492. doi:10.1016/0019-1035(85)90069-7.

Qian, J., Law, C.K., 1997. Regimes of coalescence and separation in droplet collision. Journal of Fluid Mechanics 331, 59–80. doi:10.1017/s0022112096003722.

Rabinowitz, D.L., Barkume, K., Brown, M.E., Roe, H., Schwartz, M., Tourtellotte, S., Trujillo, C., 2006. Photometric observations constraining the size, shape, and albedo of 2003 EL61, a rapidly rotating, Pluto-sized object in the Kuiper belt. The Astrophysical Journal 639, 1238–1251. doi:10.1086/499575.

Radomsky, P.M., Hewins, R.H., 1990. Formation conditions of pyroxene-olivine and magnesian olivine chondrules. Geochimica et Cosmochimica Acta 54, 3475–3490. doi:10.1016/0016-7037(90)90299-Z.

Ragozzine, D., Brown, M.E., 2009. Orbits and masses of the satellites of the dwarf planet Haumea (2003 EL61). The Astronomical Journal 137, 4766–4776. doi:10.1088/0004-6256/137/6/4766.

Ricci, L., Testi, L., Natta, A., Brooks, K.J., 2010. Dust grain growth in ρ-Ophiuchi protoplanetary disks. Astronomy & Astrophysics 521, A66. doi:10.1051/0004-6361/201015039.

Robuchon, G., Nimmo, F., 2011. Thermal evolution of Pluto and implications for surface tectonics and a subsurface ocean. Icarus 216, 426–439. doi:10.1016/j.icarus.2011.08.015.

Roe, H.G., Pike, R.E., Brown, M.E., 2008. Tentative detection of the rotation of Eris. Icarus 198, 459–464. doi:10.1016/j.icarus.2008.08.001.

Rubin, A.E., 2000. Petrologic, geochemical and experimental constraints on models of chondrule formation. Earth Science Reviews 50, 3–27. doi:10.1016/S0012-8252(99)00067-7.

Rubin, A.E., 2010. Physical properties of chondrules in different chondrite groups: Implications for multiple melting events in dusty environments. Geochimica et Cosmochimica Acta 74, 4807–4828. doi:10.1016/j.gca.2010.05.018.

Rubin, A.E., Grossman, J.N., 1987. Size-frequency distributions of EH3 chondrules. Meteoritics 22, 237–251. doi:10.1111/j.1945-5100.1987.tb00622.x.

Rybicki, G.B., Lightman, A.P., 1979. Radiative processes in astrophysics. Wiley.

Safronov, V.S., 1969. Evolution of the Protoplanetary Cloud and Formation of the Earth and the Planets. Nauka Press.

Sakatani, N., Ogawa, K., Arakawa, M., Tanaka, S., 2018. Thermal conductivity of lunar regolith simulant JSC-1A under vacuum. Icarus 309, 13–24. doi:10.1016/j.icarus.2018.02.027.

Sakatani, N., Ogawa, K., Iijima, Y., Arakawa, M., Honda, R., Tanaka, S., 2017. Thermal conductivity model for powdered materials under vacuum based on experimental studies. AIP Advances 7, 015310. doi:10.1063/1.4975153.

Sakatani, N., Ogawa, K., Iijima, Y.i., Arakawa, M., Tanaka, S., 2016. Compressional stress effect on thermal conductivity of powdered materials: Measurements and their implication to lunar regolith. Icarus 267, 1–11. doi:10.1016/j.icarus.2015.12.012.

Sanders, I.S., Scott, E.R.D., 2012. The origin of chondrules and chondrites: Debris from low-velocity impacts between molten planetesimals? Meteoritics & Planetary Science 47, 2170–2192. doi:10.1111/maps.12002.

Sanditov, D.S., 2016. The origin of the Poisson ratio of amorphous organic polymers and inorganic glasses. Polymer Science, Series A 58, 710–725. doi:10.1134/s0965545x16050175.

Saxena, P., Renaud, J.P., Henning, W.G., Jutzi, M., Hurford, T., 2018. Relevance of tidal heating on large TNOs. Icarus 302, 245–260. doi:10.1016/j.icarus.2017.11.023.

Schlichting, H.E., Sari, R., 2009. The creation of Haumea's collisional family. The Astrophysical Journal 700, 1242–1246. doi:10.1088/0004-637X/700/2/1242.

Schotte, W., 1960. Thermal conductivity of packed beds. AIChE Journal 6, 63–67.

Schräpler, R., Blum, J., 2011. The Physics of Protoplanetesimal Dust Agglomerates. VI. Erosion of Large Aggregates as a Source of Micrometer-sized Particles. The Astrophysical Journal 734, 108. doi:10.1088/0004-637X/734/2/108.

Schräpler, R., Blum, J., Krijt, S., Raabe, J.H., 2018. The Physics of Protoplanetary Dust Agglomerates. X. High-velocity Collisions between Small and Large Dust Agglomerates as a Growth Barrier. The Astrophysical Journal 853, 74. doi:10.3847/1538-4357/aaa0d2.

Schräpler, R., Blum, J., von Borstel, I., Güttler, C., 2015. The stratification of regolith on celestial objects. Icarus 257, 33–46. doi:10.1016/j.icarus.2015.04.033.

Scott, E.R.D., 2007. Chondrites and the Protoplanetary Disk. Annual Review of Earth and Planetary Sciences 35, 577–620. doi:10.1146/annurev.earth.35.031306.140100.

Seizinger, A., Kley, W., 2013. Bouncing behavior of microscopic dust aggregates. Astronomy & Astrophysics 551, A65. doi:10.1051/0004-6361/201220946.

Seizinger, A., Speith, R., Kley, W., 2012. Compression behavior of porous dust agglomerates. Astronomy & Astrophysics 541, A59. doi:10.1051/0004-6361/201218855.

Sekine, Y., Genda, H., Kamata, S., Funatsu, T., 2017. The Charon-forming giant impact as a source of Pluto's dark equatorial regions. Nature Astronomy 1, 0031. doi:10.1038/s41550-016-0031.

Senft, L.E., Stewart, S.T., 2008. Impact crater formation in icy layered terrains on Mars. Meteoritics & Planetary Science 43, 1993–2013. URL: https://doi.org/10.1111/j.1945-5100.2008.tb00657.x, doi:10.1111/j.1945-5100.2008.tb00657.x.

Seto, Y., Suzuki, K., Shoda, N., Ichimura, S., 2017. Reproduction experiments of chondrule textures using an ambient-controlled levitation system embedded in tube furnace, in: The Eighth Symposium on Polar Science, p. OAp7.

Shannon, A., Wu, Y., Lithwick, Y., 2016. Forming the cold classical Kuiper belt in a light disk. The Astrophysical Journal 818, 175. doi:10.3847/0004-637X/818/2/175.

Shih, W.H., Shih, W.Y., Kim, S.I., Liu, J., Aksay, I.A., 1990. Scaling behavior of the elastic properties of colloidal gels. Physical Review A 42, 4772–4779. doi:10.1103/PhysRevA.42.4772.

Sicardy, B., Ortiz, J.L., Assafin, M., Jehin, E., Maury, A., Lellouch, E., Hutton, R.G., Braga-Ribas, F., Colas, F., Hestroffer, D., Lecacheux, J., Roques, F., Santos-Sanz, P., Widemann, T., Morales, N., Duffard, R., Thirouin, A., Castro-Tirado, A.J., Jelínek, M., Kubánek, P., Sota, A., Sánchez-Ramírez, R., Andrei, A.H., Camargo, J.I.B., da Silva Neto, D.N., Gomes, A.R., Martins, R.V., Gillon, M., Manfroid, J., Tozzi, G.P., Harlingten, C., Saravia, S., Behrend, R., Mottola, S., Melendo, E.G., Peris, V., Fabregat, J., Madiedo, J.M., Cuesta, L., Eibe, M.T., Ullán, A., Organero, F., Pastor, S., de Los Reyes, J.A., Pedraz, S., Castro, A., de La Cueva, I., Muler, G., Steele, I.A., Cebrián, M., Montañés-Rodríguez, P., Oscoz, A., Weaver, D., Jacques, C., Corradi, W.J.B., Santos, F.P., Reis, W., Milone, A., Emilio, M., Gutiérrez, L., Vázquez, R., Hernández-Toledo, H., 2011. A Pluto-like radius and a high albedo for the dwarf planet Eris from an occultation. Nature 478, 493–496. doi:10.1038/nature10550.

Sierks, H., Barbieri, C., Lamy, P.L., Rodrigo, R., Koschny, D., Rickman, H., Keller, H.U., Agarwal, J., A'Hearn, M.F., Angrilli, F., Auger, A.T., Barucci, M.A., Bertaux, J.L., Bertini, I., Besse, S., Bodewits, D., Capanna, C., Cremonese, G., Da Deppo, V., Davidsson, B., Debei, S., De Cecco, M., Ferri, F., Fornasier, S., Fulle, M., Gaskell, R., Giacomini, L., Groussin, O., Gutierrez-Marques, P., Gutiérrez, P.J., Güttler, C., Hoekzema, N., Hviid, S.F., Ip, W.H., Jorda, L., Knollenberg, J., Kovacs, G., Kramm, J.R., Kührt, E., Küppers, M., La Forgia, F., Lara, L.M., Lazzarin, M., Leyrat, C., Lopez Moreno, J.J., Magrin, S., Marchi, S., Marzari, F., Massironi, M., Michalik, H., Moissl, R., Mottola, S., Naletto, G., Oklay, N., Pajola, M., Pertile, M., Preusker, F., Sabau, L., Scholten, F., Snodgrass, C., Thomas, N., Tubiana, C., Vincent, J.B., Wenzel, K.P., Zaccariotto, M., Pätzold, M., 2015. On the nucleus structure and activity of comet 67P/Churyumov-Gerasimenko. Science 347, aaa1044. doi:10.1126/science.aaa1044.

Simon, J.B., Armitage, P.J., Li, R., Youdin, A.N., 2016. The Mass and Size Distribution of Planetesimals Formed by the Streaming Instability. I. The Role of Self-gravity. The Astrophysical Journal 822, 55. doi:10.3847/0004-637X/822/1/55.

Simon, J.I., Cuzzi, J.N., McCain, K.A., Cato, M.J., Christoffersen, P.A., Fisher, K.R., Srinivasan, P., Tait, A.W., Olson, D.M., Scargle, J.D., 2018. Particle size distributions in chondritic meteorites: Evidence for pre-planetesimal histories. Earth and Planetary Science Letters 494, 69–82. doi:10.1016/j.epsl.2018.04.021.

Sirono, S.i., 2004. Conditions for collisional growth of a grain aggregate. Icarus 167, 431–452. doi:10.1016/j.icarus.2003.09.018.

Sirono, S.i., 2014. Numerical simulation of heat conduction in a random ballistic deposited grain aggregate. Meteoritics & Planetary Science 49, 109–116. doi:10.1111/maps.12245.

Sirono, S.i., 2017. Heating of Porous Icy Dust Aggregates. The Astrophysical Journal 842, 11. doi:10.3847/1538-4357/aa7389.

Sirono, S.i., Ueno, H., 2017. Collisions between Sintered Icy Aggregates. The Astrophysical Journal 841, 36. doi:10.3847/1538-4357/aa6fad.

Skorov, Y., Blum, J., 2012. Dust release and tensile strength of the non-volatile layer of cometary nuclei. Icarus 221, 1–11. doi:10.1016/j.icarus.2012.01.012.

Skorov, Y.V., van Lieshout, R., Blum, J., Keller, H.U., 2011. Activity of comets: Gas transport in the near-surface porous layers of a cometary nucleus. Icarus 212, 867–876. doi:10.1016/j.icarus.2011.01.018.

Sommerfeld, M., Kuschel, M., 2016. Modelling droplet collision outcomes for different substances and viscosities. Experiments in Fluids 57, 187. doi:10.1007/s00348-016-2249-y.

Sorensen, C.M., 2001. Light Scattering by Fractal Aggregates: A Review. Aerosol Science and Technology 35, 648–687. doi:10.1080/02786820117868.

Spohn, T., Knollenberg, J., Ball, A.J., Banaszkiewicz, M., Benkhoff, J., Grott, M., Grygorczuk, J., Hüttig, C., Hagermann, A., Kargl, G., Kaufmann, E., Kömle, N., Kührt, E., Kossacki, K.J., Marczewski, W., Pelivan, I., Schrödter, R., Seiferlin, K., 2015. Thermal and mechanical properties of the near-surface layers of comet 67P/Churyumov-Gerasimenko. Science 349, 2.464. doi:10.1126/science.aab0464.

Springel, V., 2005. The cosmological simulation code GADGET-2. Monthly Notices of the Royal Astronomical Society 364, 1105–1134. doi:10.1111/j.1365-2966.2005.09655.x.

Srivastava, A., Inatomi, Y., Tsukamoto, K., Maki, T., Miura, H., 2010. In situ visualization of crystallization inside high temperature silicate melts. Journal of Applied Physics 107, 114907–114907. doi:10.1063/1.3406149.

Stebbins, J.F., Carmichael, I.S.E., Moret, L.K., 1984. Heat capacities and entropies of silicate liquids and glasses. Contributions to Mineralogy and Petrology 86, 131–148. doi:10.1007/BF00381840.

Stephens, I.W., Yang, H., Li, Z.Y., Looney, L.W., Kataoka, A., Kwon, W., Fernández-López, M., Hull, C.L.H., Hughes, M., Segura-Cox, D., Mundy, L., Crutcher, R., Rao, R., 2017. ALMA Reveals Transition of Polarization Pattern with Wavelength in HL Tau's Disk. The Astrophysical Journal 851, 55. doi:10.3847/1538-4357/aa998b.

Stern, S.A., Bagenal, F., Ennico, K., Gladstone, G.R., Grundy, W.M., McKinnon, W.B., Moore, J.M., Olkin, C.B., Spencer, J.R., Weaver, H.A., Young, L.A., Andert, T., Andrews, J., Banks, M., Bauer, B., Bauman, J., Barnouin, O.S., Bedini, P., Beisser, K., Beyer, R.A., Bhaskaran, S., Binzel, R.P., Birath, E., Bird, M., Bogan, D.J., Bowman, A., Bray, V.J., Brozovic, M., Bryan, C., Buckley, M.R., Buie, M.W., Buratti, B.J., Bushman, S.S., Calloway, A., Carcich, B., Cheng, A.F., Conard, S., Conrad, C.A., Cook, J.C., Cruikshank, D.P., Custodio, O.S., Dalle Ore, C.M., Deboy, C., Dischner, Z.J.B., Dumont, P., Earle, A.M., Elliott, H.A., Ercol, J., Ernst, C.M., Finley, T., Flanigan, S.H., Fountain, G., Freeze, M.J., Greathouse, T., Green, J.L., Guo, Y., Hahn, M., Hamilton, D.P., Hamilton, S.A., Hanley, J., Harch, A., Hart, H.M., Hersman, C.B., Hill, A., Hill, M.E., Hinson, D.P., Holdridge, M.E., Horanyi, M., Howard, A.D., Howett, C.J.A.,

Jackman, C., Jacobson, R.A., Jennings, D.E., Kammer, J.A., Kang, H.K., Kaufmann, D.E., Kollmann, P., Krimigis, S.M., Kusnierkiewicz, D., Lauer, T.R., Lee, J.E., Lindstrom, K.L., Linscott, I.R., Lisse, C.M., Lunsford, A.W., Mallder, V.A., Martin, N., McComas, D.J., McNutt, R.L., Mehoke, D., Mehoke, T., Melin, E.D., Mutchler, M., Nelson, D., Nimmo, F., Nunez, J.I., Ocampo, A., Owen, W.M., Paetzold, M., Page, B., Parker, A.H., Parker, J.W., Pelletier, F., Peterson, J., Pinkine, N., Piquette, M., Porter, S.B., Protopapa, S., Redfern, J., Reitsema, H.J., Reuter, D.C., Roberts, J.H., Robbins, S.J., Rogers, G., Rose, D., Runyon, K., Retherford, K.D., Ryschkewitsch, M.G., Schenk, P., Schindhelm, E., Sepan, B., Showalter, M.R., Singer, K.N., Soluri, M., Stanbridge, D., Steffl, A.J., Strobel, D.F., Stryk, T., Summers, M.E., Szalay, J.R., Tapley, M., Taylor, A., Taylor, H., Throop, H.B., Tsang, C.C.C., Tyler, G.L., Umurhan, O.M., Verbiscer, A.J., Versteeg, M.H., Vincent, M., Webbert, R., Weidner, S., Weigle, G.E., White, O.L., Whittenburg, K., Williams, B.G., Williams, K., Williams, S., Woods, W.W., Zangari, A.M., Zirnstein, E., 2015a. The Pluto system: Initial results from its exploration by New Horizons. Science 350, aad1815. doi:10.1126/science.aad1815.

Stern, S.A., Feaga, L.M., Schindhelm, E., Steffl, A., Parker, J.W., Feldman, P.D., Weaver, H.A., A'Hearn, M.F., Cook, J., Bertaux, J.L., 2015b. First extreme and far ultraviolet spectrum of a Comet Nucleus: Results from 67P/Churyumov-Gerasimenko. Icarus 256, 117–119. doi:10.1016/j.icarus.2015.04.023.

Stewart, S.T., Leinhardt, Z.M., 2009. Velocity-Dependent Catastrophic Disruption Criteria for Planetesimals. The Astrophysical Journal Letters 691, L133–L137. doi:10.1088/0004-637X/691/2/L133.

Susa, H., Nakamoto, T., 2002. On the Maximal Size of Chondrules in Shock Wave Heating Model. The Astrophysical Journal 564, L57–L60. doi:10.1086/338789.

Suyama, T., Wada, K., Tanaka, H., 2008. Numerical Simulation of Density Evolution of Dust Aggregates in Protoplanetary Disks. I. Head-on Collisions. The Astrophysical Journal 684, 1310–1322. doi:10.1086/590143.

Tachibana, S., Huss, G.R., 2005. Sulfur isotope composition of putative primary troilite in chondrules from Bishunpur and Semarkona. Geochimica et Cosmochimica Acta 69, 3075–3097. doi:10.1016/j.gca.2004.06.025.

Takeda, T., Ida, S., 2001. Angular momentum transfer in a protolunar disk. The Astrophysical Journal 540, 514–533. doi:10.1086/322406.

Tammann, G., Hesse, W., 1926. Die Abhängigkeit der Viscosität von der Temperatur bie unterkühlten Flüssigkeiten. Zeitschrift für anorganische und allgemeine Chemie 156, 245–257. doi:10.1002/zaac.19261560121.

Tanaka, H., Wada, K., Suyama, T., Okuzumi, S., 2012. Growth of Cosmic Dust Aggregates and Reexamination of Particle Interaction Models. Progress of Theoretical Physics Supplement 195, 101–113. doi:10.1143/PTPS.195.101.

Tanaka, K.K., Yamamoto, T., Nagashima, K., Tsukamoto, K., 2008. A new method of evaluation of melt/crystal interfacial energy and activation energy of diffusion. Journal of Crystal Growth 310, 1281–1286. doi:10.1016/j.jcrysgro.2007.06.038.

Tang, C., Zhang, P., Law, C.K., 2012. Bouncing, coalescence, and separation in head-on collision of unequal-size droplets. Physics of Fluids 24, 022101. doi:10.1063/1.3679165.

Tatsuuma, M., Kataoka, A., Tanaka, H., 2019. Tensile Strength of Porous Dust Aggregates. The Astrophysical Journal 874, 159. doi:10.3847/1538-4357/ab09f7.

Tatsuuma, M., Michikoshi, S., Kokubo, E., 2018. Gravitational Instability of a Dust Layer Composed of Porous Silicate Dust Aggregates in a Protoplanetary Disk. The Astrophysical Journal 855, 57. doi:10.3847/1538-4357/aaaccf.

Tazaki, R., Tanaka, H., Kataoka, A., Okuzumi, S., Muto, T., 2019. Unveiling Dust Aggregate Structure in Protoplanetary Disks by Millimeter-wave Scattering Polarization. The Astrophysical Journal 885, 52. doi:10.3847/1538-4357/ab45f0.

Tazaki, R., Tanaka, H., Okuzumi, S., Kataoka, A., Nomura, H., 2016. Light Scattering by Fractal Dust Aggregates. I. Angular Dependence of Scattering. The Astrophysical Journal 823, 70. doi:10.3847/0004-637X/823/2/70.

Teiser, J., Dodson-Robinson, S.E., 2013. Photophoresis boosts giant planet formation. Astronomy & Astrophysics 555, A98. doi:10.1051/0004-6361/201321582.

Testi, L., Birnstiel, T., Ricci, L., Andrews, S., Blum, J., Carpenter, J., Dominik, C., Isella, A., Natta, A., Williams, J.P., Wilner, D.J., 2014. Dust Evolution in Protoplanetary Disks, in: Beuther, H., Klessen, R.S., Dullemond, C.P., Henning, T. (Eds.), Protostars and Planets VI, p. 339. doi:10.2458/azu_uapress_9780816531240-ch015.

Thirouin, A., Ortiz, J.L., Duffard, R., Santos-Sanz, P., Aceituno, F.J., Morales, N., 2010. Short-term variability of a sample of 29 trans-Neptunian objects and Centaurs. Astronomy & Astrophysics 522, A93. doi:10.1051/0004-6361/200912340.

Tillotson, J.H., 1962. Metallic Equations of State for Hypervelocity Impact. Technical Report No. GA-3216 (General Atomic). General Atomic Report.

Toomre, A., 1964. On the gravitational stability of a disk of stars. The Astrophysical Journal 139, 1217–1238. doi:10.1086/147861.

Trujillo, C.A., Jewitt, D.C., Luu, J.X., 2001. Properties of the Trans-Neptunian Belt: Statistics from the Canada-France-Hawaii Telescope Survey. The Astronomical Journal 122, 457–473. doi:10.1086/321117.

Tschermak, G., Wood, J.A., Wood, K.M., 1964. The Microscopic Properties of Meteorites by Gustav Tschermak (Die Mikroskopische Beschaffenheit der Meteoriten, trans lated by John A. Wood and K Mathilde Wood). Smithsonian Contributions to Astrophysics 4, 137–239.

Tsuchiyama, A., Shigeyoshi, R., Kawabata, T., Nakano, T., Uesugi, K., Shirono, S., 2003. Three-Dimensional Structures of Chondrules and Their High-Speed Rotation, in: Lunar and Planetary Science Conference Abstracts, p. 1271.

Tsukamoto, K., Satoh, H., Takamura, Y., Kuribayashi, K., 1999. A new approach for the formation of olivine-chondrules by aero-acoustic levitation. Antarctic Meteorites 24, 179–181.

Tsukamoto, Y., Okuzumi, S., Kataoka, A., 2017. Apparent Disk-mass Reduction and Planetisimal Formation in GravitationallyUnstable Disks in Class 0/I Young Stellar Objects. The Astrophysical Journal 838, 151. doi:10.3847/1538-4357/aa6081.

Ueda, T., Murakami, Y., Ishitsu, N., Kawabe, H., Inoue, R., Nakamura, T., Sekiya, M., Takaoka, N., 2001. Collisional destruction experiment of chondrules and formation of fragments in the solar nebula. Earth, Planets, and Space 53, 927–935. doi:10.1186/bf03351689.

Uesugi, M., Akaki, T., Sekiya, M., Nakamura, T., 2005. Motion of iron sulfide inclusions inside a shock-melted chondrule. Meteoritics & Planetary Science 40, 1103. doi:10.1111/j.1945-5100.2005.tb00175.x.

Uesugi, M., Sekiya, M., Nakamura, T., 2008. Kinetic stability of a melted iron globule during chondrule formation. I. Non-rotating model. Meteoritics & Planetary Science 43, 717–730. doi:10.1111/j.1945-5100.2008.tb00680.x.

Vicsek, T., 1983. Fractal models for diffusion controlled aggregation. Journal of Physics A: Mathematical and General 16, L647–L652. doi:10.1088/0305-4470/16/17/003.

Villeneuve, J., Libourel, G., Soulié, C., 2015. Relationships between type I and type II chondrules: Implications on chondrule formation processes. Geochimica et Cosmochimica Acta 160, 277–305. doi:10.1016/j.gca.2015.03.033.

Vincent, J.B., Farnham, T., Kührt, E., Skorov, Y., Marschall, R., Oklay, N., El-Maarry, M.R., Keller, H.U., 2019. Local Manifestations of Cometary Activity. Space Science Reviews 215, 30. doi:10.1007/s11214-019-0596-8.

Vogel, H., 1921. Das Temperaturabhaengigkeitsgesetz der Viskositaet von Fluessigkeiten. Physikalische Zeitschrift 22, 645–646.

Wada, K., Tanaka, H., Okuzumi, S., Kobayashi, H., Suyama, T., Kimura, H., Yamamoto, T., 2013. Growth efficiency of dust aggregates through collisions with high mass ratios. Astronomy & Astrophysics 559, A62. doi:10.1051/0004-6361/201322259.

Wada, K., Tanaka, H., Suyama, T., Kimura, H., Yamamoto, T., 2007. Numerical Simulation of Dust Aggregate Collisions. I. Compression and Disruption of Two-Dimensional Aggregates. The Astrophysical Journal 661, 320–333. doi:10.1086/514332.

Wada, K., Tanaka, H., Suyama, T., Kimura, H., Yamamoto, T., 2008. Numerical Simulation of Dust Aggregate Collisions. II. Compression and Disruption of Three-Dimensional Aggregates in Head-on Collisions. The Astrophysical Journal 677, 1296–1308. doi:10.1086/529511.

Wada, K., Tanaka, H., Suyama, T., Kimura, H., Yamamoto, T., 2009. Collisional Growth Conditions for Dust Aggregates. The Astrophysical Journal 702, 1490–1501. doi:10.1088/0004-637X/702/2/1490.

Wada, K., Tanaka, H., Suyama, T., Kimura, H., Yamamoto, T., 2011. The Rebound Condition of Dust Aggregates Revealed by Numerical Simulation of Their Collisions. The Astrophysical Journal 737, 36. doi:10.1088/0004-637X/737/1/36.

Wahlberg Jansson, K., Johansen, A., Bukhari Syed, M., Blum, J., 2017. The Role of Pebble Fragmentation in Planetesimal Formation. II. Numerical Simulations. The Astrophysical Journal 835, 109. doi:10.3847/1538-4357/835/1/109.

Wakita, S., Matsumoto, Y., Oshino, S., Hasegawa, Y., 2017. Planetesimal Collisions as a Chondrule Forming Event. The Astrophysical Journal 834, 125. doi:10.3847/1538-4357/834/2/125.

Walsh, K.J., Levison, H.F., 2016. Terrestrial Planet Formation from an Annulus. The Astronomical Journal 152, 68. doi:10.3847/0004-6256/152/3/68.

Walzel, P., 1980. Zerteilgrenze beim tropfenprall. Chemie Ingenieur Technik 52, 338–339. doi:10.1002/cite.330520412.

Wang, H., Weiss, B.P., Bai, X.N., Downey, B.G., Wang, J., Wang, J., Suavet, C., Fu, R.R., Zucolotto, M.E., 2017. Lifetime of the solar nebula constrained by meteorite paleomagnetism. Science 355, 623–627. doi:10.1126/science.aaf5043.

Ward, W.R., Canup, R.M., 2006. Forced resonant migration of Pluto's outer satellites by Charon. Science 313, 1107–1109. doi:10.1126/science.1127293.

Wasson, J.T., 1993. Constraints on chondrule origins. Meteoritics 28, 14–28. doi:10.1111/j.1945-5100.1993.tb00244.x.

Wasson, J.T., 2012. Chondrule Volatile Retention, Dust Enrichments and the Composition of the Nebular Gas. Meteoritics & Planetary Science Supplement 75, 5083.

Wasson, J.T., Kallemeyn, G.W., 1988. Compositions of chondrites. Philosophical Transactions of the Royal Society of London Series A 325, 535–544. doi:10.1098/rsta.1988.0066.

Wasson, J.T., Krot, A.N., Lee, M.S., Rubin, A.E., 1995. Compound chondrules. Geochimica et Cosmochimica Acta 59, 1847–1869. doi:10.1016/0016-7037(95)00087-G.

Wasson, J.T., Rubin, A.E., 2003. Ubiquitous low-FeO relict grains in type II chondrules and limited overgrowths on phenocrysts following the final melting event. Geochimica et Cosmochimica Acta 67, 2239–2250. doi:10.1016/S0016-7037(03)00023-1.

Weibull, W., 1951. A Statistical Distribution Function of Wide Applicability. Journal of Applied Mechanics 18, 293–297.

Weidenschilling, S.J., 1977. Aerodynamics of solid bodies in the solar nebula. Monthly Notices of the Royal Astronomical Society 180, 57–70. doi:10.1093/mnras/180.1.57.

Weidenschilling, S.J., Marzari, F., Hood, L.L., 1998. The Origin of Chondrules at Jovian Resonances. Science 279, 681. doi:10.1126/science.279.5351.681.

Weidling, R., Güttler, C., Blum, J., 2012. Free collisions in a microgravity many-particle experiment. I. Dust aggregate sticking at low velocities. Icarus 218, 688–700. doi:10.1016/j.icarus.2011.10.002.

Weidling, R., Güttler, C., Blum, J., Brauer, F., 2009. The Physics of Protoplanetesimal Dust Agglomerates. III. Compaction in Multiple Collisions. The Astrophysical Journal 696, 2036–2043. doi:10.1088/0004-637X/696/2/2036.

Weingartner, J.C., Draine, B.T., 2001. Dust Grain-Size Distributions and Extinction in the Milky Way, Large Magellanic Cloud, and Small Magellanic Cloud. The Astrophysical Journal 548, 296–309. doi:10.1086/318651.

Willacy, K., Alexander, C., Ali-Dib, M., Ceccarelli, C., Charnley, S.B., Doronin, M., Ellinger, Y., Gast, P., Gibb, E., Milam, S.N., Mousis, O., Pauzat, F., Tornow, C., Wirström, E.S., Zicler, E., 2015. The Composition of the Protosolar Disk and the Formation Conditions for Comets. Space Science Reviews 197, 151–190. doi:10.1007/s11214-015-0167-6.

Willis, K., Orme, M., 2003. Binary droplet collisions in a vacuum environment: an experimental investigation of the role of viscosity. Experiments in Fluids 34, 28–41. doi:10.1007/s00348-002-0526-4.

Windmark, F., Birnstiel, T., Güttler, C., Blum, J., Dullemond, C.P., Henning, T., 2012. Planetesimal formation by sweep-up: how the bouncing barrier can be beneficial to growth. Astronomy & Astrophysics 540, A73. doi:10.1051/0004-6361/201118475.

Woo, J.M.Y., Lee, M.H., 2018. On the early in situ formation of Pluto's small satellites. The Astronomical Journal 155, 175. doi:10.3847/1538-3881/aab367.

Wurm, G., Blum, J., 1998. Experiments on Preplanetary Dust Aggregation. Icarus 132, 125–136. doi:10.1006/icar.1998.5891.

Wurm, G., Haack, H., 2009. Outward transport of CAIs during FU-Orionis events. Meteoritics & Planetary Science 44, 689–699. doi:10.1111/j.1945-5100.2009.tb00763.x.

Wurm, G., Paraskov, G., Krauss, O., 2005. Growth of planetesimals by impacts at $\sim$ 25 m/s. Icarus 178, 253–263. doi:10.1016/j.icarus.2005.04.002.

Xiang, C., Carballido, A., Hanna, R.D., Matthews, L.S., Hyde, T.W., 2019. The initial structure of chondrule dust rims I: Electrically neutral grains. Icarus 321, 99–111. doi:10.1016/j.icarus.2018.10.014.

Xu, Y., 2005. Explanation of scaling phenomenon based on fractal fragmentation. Mechanics Research Communications 32, 209–220. doi:10.1016/j.mechrescom.2003.10.001.

Yang, C.C., Johansen, A., Carrera, D., 2017. Concentrating small particles in protoplanetary disks through the streaming instability. Astronomy & Astrophysics 606, A80. doi:10.1051/0004-6361/201630106.

Yasuda, S., Miura, H., Nakamoto, T., 2009. Compound chondrule formation in the shock-wave heating model: Three-dimensional hydrodynamics simulation of the disruption of a partially-molten dust particle. Icarus 204, 303–315. doi:10.1016/j.icarus.2009.06.014.

Yoder, C.F., 1982. Tidal rigidity of phobos. Icarus 49, 327–346. doi:10.1016/0019-1035(82)90040-9.

Youdin, A.N., Goodman, J., 2005. Streaming Instabilities in Protoplanetary Disks. The Astrophysical Journal 620, 459–469. doi:10.1086/426895.

Youdin, A.N., Lithwick, Y., 2007. Particle stirring in turbulent gas disks: Including orbital oscillations. Icarus 192, 588–604. doi:10.1016/j.icarus.2007.07.012.

Yu, X., Hörst, S.M., He, C., McGuiggan, P., Bridges, N.T., 2017. Direct Measurement of Interparticle Forces of Titan Aerosol Analogs ("Tholin") Using Atomic Force Microscopy. Journal of Geophysical Research (Planets) 122, 2610–2622. doi:10.1002/2017JE005437.

Yu, X., Hörst, S.M., He, C., McGuiggan, P., Crawford, B., 2018. Where Does Titan Sand Come From: Insight From Mechanical Properties of Titan Sand Candidates. Journal of Geophysical Research: Planets 123, 2310–2321. doi:10.1029/2018je005651.

Yurimoto, H., Abe, K.i., Abe, M., Ebihara, M., Fujimura, A., Hashiguchi, M., Hashizume, K., Ireland, T.R., Itoh, S., Katayama, J., Kato, C., Kawaguchi, J., Kawasaki, N., Kitajima, F., Kobayashi, S., Meike, T., Mukai, T., Nagao, K., Nakamura, T., Naraoka, H., Noguchi, T., Okazaki, R., Park, C., Sakamoto, N., Seto, Y., Takei, M., Tsuchiyama, A., Uesugi, M., Wakaki, S., Yada, T., Yamamoto, K., Yoshikawa, M., Zolensky, M.E., 2011. Oxygen Isotopic Compositions of Asteroidal Materials Returned from Itokawa by the Hayabusa Mission. Science 333, 1116. doi:10.1126/science.1207776.

Yurimoto, H., Wasson, J.T., 2002. Extremely rapid cooling of a carbonaceous-chondrite chondrule containing very ^{16}O-rich olivine and a ^{26}Mg-excess. Geochimica et Cosmochimica Acta 66, 4355–4363. doi:10.1016/S0016-7037(02)01218-8.

Zanda, B., 2004. Chondrules. Earth and Planetary Science Letters 224, 1–17. doi:10.1016/j.epsl.2004.05.005.

Zsom, A., Ormel, C.W., Güttler, C., Blum, J., Dullemond, C.P., 2010. The outcome of protoplanetary dust growth: pebbles, boulders, or planetesimals? II. Introducing the bouncing barrier. Astronomy & Astrophysics 513, A57. doi:10.1051/0004-6361/200912976.